Proceedings of
THE SECOND INTERNATIONAL WORKSHOP
on

# CIVILIAN SPACE APPLICATIONS

Edited by: D. Weihs

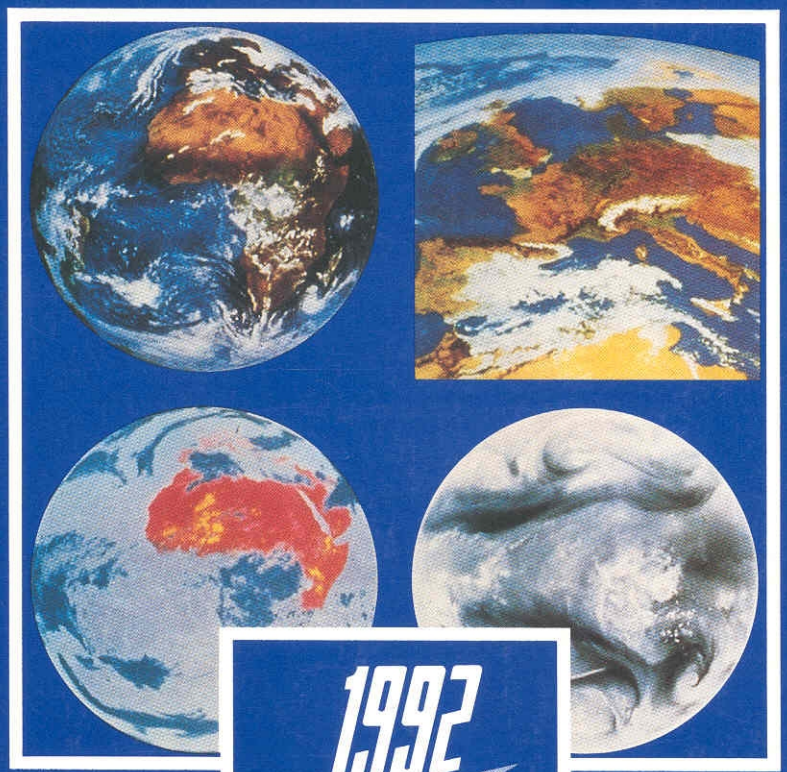

In conjunction with:
The 32nd International Symposium
on Aviation and Astronautics

Technion - Israel Institute of Technology
The S. Neaman Institute for Advanced Studies in Science and Technology

The S. Neaman Institute for Advanced Studies in Science and Technology

Proceedings of

THE SECOND INTERNATIONAL WORKSHOP

on

# CIVILIAN SPACE APPLICATIONS

Edited by: D. Weihs

In conjunction with :
The 32nd International Symposium
on Aviation and Astronautics

Tel-Aviv, February 19, 1992

Printed in Israel by **The S. Neaman Press**, April 1992.

# Contents

## OPENING REMARKS

Prof. D. Weihs, Director, The Samuel Neaman Institute
for Advanced Studies in Science and Technology

I am very happy to open this special symposium, dedicated to civilian applications of space. This is the second time that the Samuel Neaman Institute for Advanced Studies in Science and Technology is holding such a gathering. The first time was in early 1988, when it became clear, in the wake of the Lavi affair, that the Israeli high-tech industry must broaden its base, and develop new "flagship" industries, as well as to move more massively into the civilian market.

The S. Neaman Institute, which is Technion's think-tank for policy research and has as one of its major objectives the encouragement and development of Israeli science and technology, to improve the economy, had by then identified space as one of the more promising areas for development.

In the four years that have passed since then, both of these trends became imperative due to the enormous changes in the political and economic situation in the world. These include the dissolution of the eastern bloc, European approaches towards unity, the Gulf war, the informatics "revolution" and the recession in much of the world market. The Israeli aerospace industry is continually required to show its capability for flexibility in order to prosper in this changing environment. For this to occur, a wide scientific and technological base, perhaps even beyond its natural proportions in a small country must be maintained.

Developments in Israel have been dramatic in this period. Two research satellites were launched (Ofeq 1 in September 1988, and Ofeq 2 in 1990). A communications satellite - Amos, is under construction and rapid growth of the internal and export market for satellite communications has occurred.

Also, 1992 has been declared as the International Space Year, in which the importance of space research and exploitation is being brought to the collective consciousness of the wider public around the world. Thus it was natural that this second symposium be held in conjunction with the 32nd Israel Annual Conference on Aviation and Astronautics.

I am happy that the Organizing Committee of the 32nd Israel Annual Conference has agreed to this union as a sign of inclusion of space into the mainstream of Israeli science and Industry. This Symposium will already have over 10 locally written papers, adn we hope that this will become a regular feature of the Israel Annual Conferences.

## OPENING REMARKS

Professor Yuval Neeman, Chairman, Israel Space Agency

1992 has been proclaimed the Space and Discovery Year, in commemoration of the 500th Anniversary for the Discovery of America - and for us also the 500 anniversary of the Expulsion from Spain. The connection is not incidental, and the part of Jewish scientists in the discoveries of Spain and Portugal in the 15th century is well known.The fact that in the beginning of the century, the International Astronomical Association has named the moon craters in the names of Ibn Ezra, Rabbi Levi (Ben Gershom) and Zakut, are testimony to that effect. Zakut had a very similar job in the court of the sea-faring Prince Henry as Werner von Braun had in NASA. Lately we have all witnessed a considerable progress of Israeli Space projects.

(1) The Amos Communications Satellite, has been launched as a commercial project. I hope that barring difficulties, it will be launched to space in 1993 or 1994.

(2) The Israel Aircraft Industry is continuing to develop OFEQ, hoping to use its economic advantages of our launching facilities, and the accumulated know-how for low-orbit satellites. We have already taken part in international tenders for low-orbit satellites and I am sure success is not far.

(3) The ultraviolet telescope project of the Tel Aviv University and El-Op group has already been launched, with Danish knowhow.
(4) A Technion group is participating in the computational aspects of the Russian Mars Project in 1994.

(5) A student Tech-Tat project is carried out at Technion.

(6) In August we are expecting the launching of the Hornets project of Prof. Ishai of Tel Aviv University, on a Shuttle mission.

As you see we have reached the point where past efforts are about to come to fruition. Let us hope we achieve worthy results!


32
"The
"הסימפוזיון ה
לשימושים
אזרחיים בח
1992

# THE SPACE PROJECTS OF THE EUROPEAN SPACE AGENCY (ESA)

Jean-Marie Luton, ESA Director General
Paris, France

## Introduction

Ladies and Gentlemen, first let me say that it is a great pleasure for me as Director General of the European Space Agency to be here today with you and to take part in this conference on aviation and astronautics and to have this opportunity to see the Israeli space facilities. I believe that I am the first Director General of the European Space Agency to visit Israel and I look forward to continuing the dialogue thus begun.

I should briefly like to run over the beginnings of European cooperation in space and outline the purpose and structure of ESA. Then I shall discuss the objectives of Europe's space programme and describe the successes and future plans of European space policy.

Over the past thirty years, Europe has made substantial progress in developing its capability in space research and technology alongside the USA and the former Soviet Union.

## The European Space Agency

The European Space Agency was formed in 1975 out of two former organizations: the European Space Research Organization (ESRO) which came into being in 1964 and which was concerned with satellite activities for scientific purposes and the European Launcher Development Organization (ELDO), which, as its name implies, was responsible for launcher development. It also started its work in 1964.

If early cooperation in Europe was essentially scientific, member states were soon aware of the political, economic, and technological

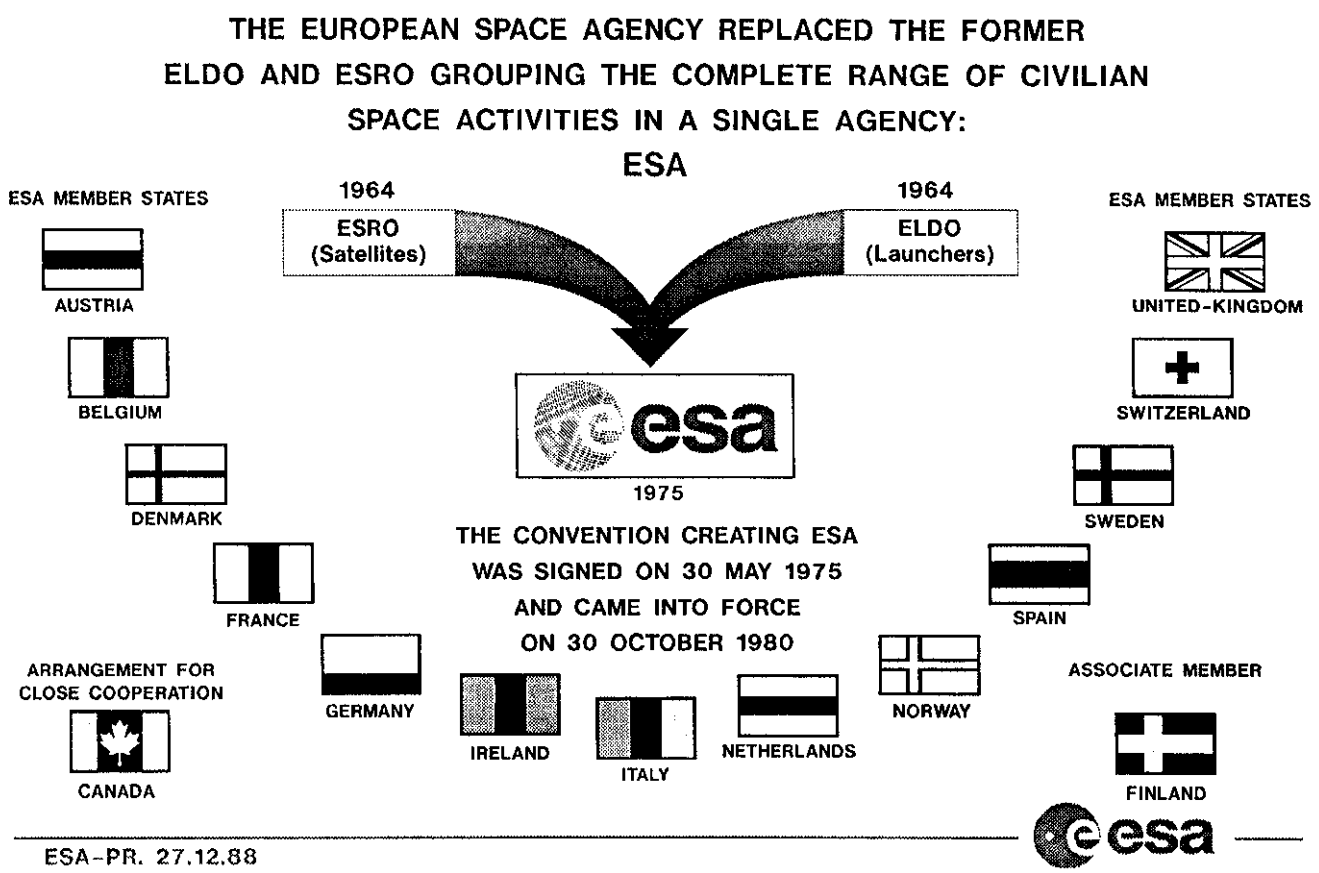

significance of space exploration and exploitation. They also realized that individual national resources and expertise were not sufficient to enable them to go alone.

Today, a large part of space research and development in Europe is carried out under the ESA banner. ESA has currently thirteen member states: Austria, Belgium, Denmark, France, Germany, Ireland, Italy, The Netherlands, Norway, Spain, Sweden, Switzerland and the United Kingdom. Finland is an associate member, and the Agency has a cooperation agreement with Canada, giving them a limited possibility of involvement in the Agency's programmes and representation in its delegate bodies.

ESA's convention sets out the Agency's main objectives, namely to provide for and to promote, for exclusively peaceful purposes, cooperation among European states in space research and space technology and their space applications; to elaborate and implement a long-term space policy and, finally, to elaborate and implement an industrial policy for its member states.

The highest ESA delegate body is its Council consisting of representatives of the member states. For the purpose of drawing up and supervising the individual programmes, Council set up several Programme Boards to which each member state participating in the relevant programme delegates experts. In addition, Council set up an Administrative and Finance Committee to give advice on administrative matters.

The Agency's Director General is aided in the implementation of his executive tasks by directors, of whom there are currently eight, an inspector general and the staff.

# PURPOSE OF ESA
## (Article 2 of ESA Convention)

Provide for and promote, for exclusively peaceful purposes, cooperation among European states in the field of:

Space Research and Technology
Space Applications

for scientific purposes and for operational space applications:

- by elaborating and implementing a long term European space policy
- by elaborating and implementing space activities and programmes
- by coordinating the European space programme and national programmes
- by elaborating and implementing an industrial policy

# ESTABLISHMENTS

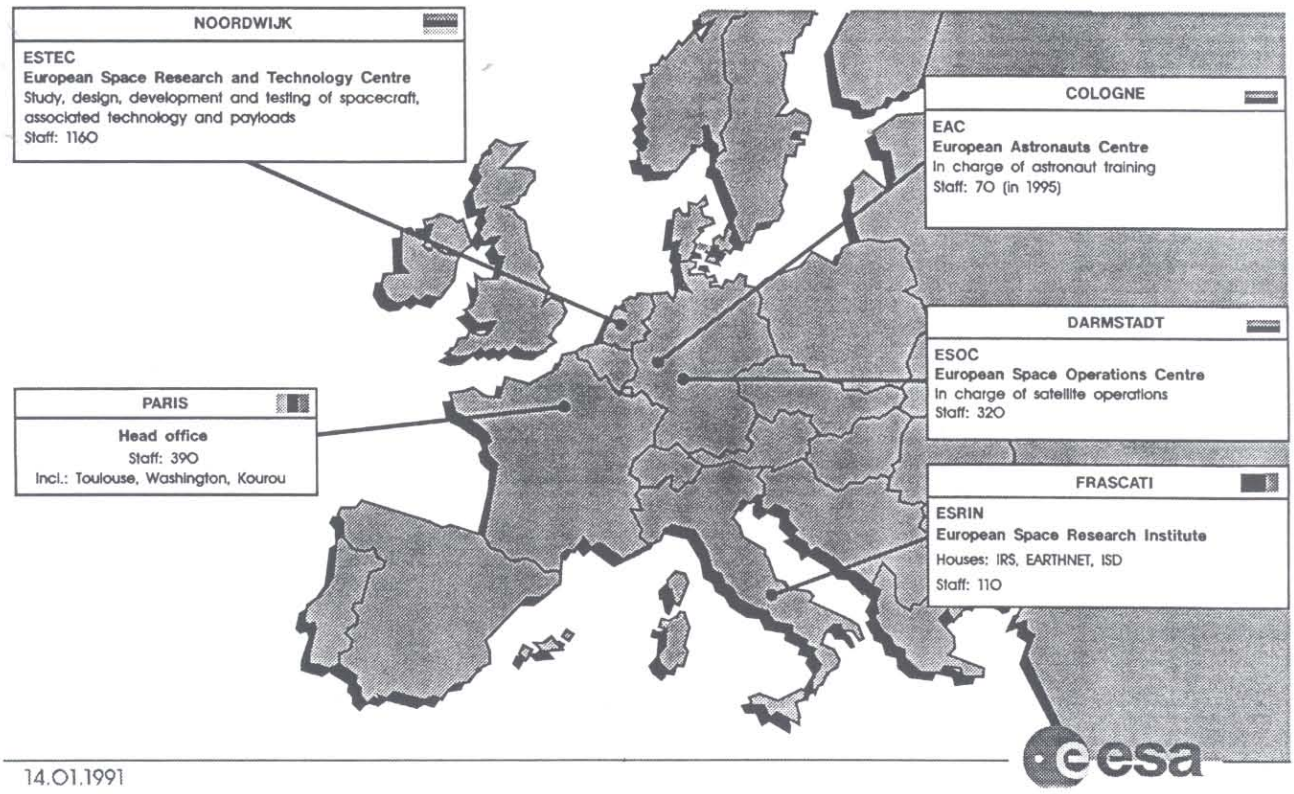


14.01.1991

The Agency has the following establishments:
Its headquarters is in Paris, where some 320 staff are employed and where the political decisions are taken.
The European Space Research and Technology Centre (ESTEC) in Noordwijk in the Netherlands, which employs 1200 people, is Europe's largest centre of expertise in the field of space research and development.It is responsible for the project management for most ESA space projects, including the studies and preparatory programmes and the development phase for future projects. ESTEC also provides the appropriate facilities for testing a spacecraft on Earth under conditions simulating, as closely as possible, those it will encounter from lift-off onwards.

The European Space Operations Centre (ESOC) located in Darmstadt, Germany, which is in charge of all satellite operations and the corresponding ground facilities and communications networks. There are about 300 permanent staff employed.

The European Space Research Institute (ESRIN) at Frascati houses the Earthnet Programme Office for the acquisition, processing and dissemination of data from remote sensing satellites as well as the Information Retrieval Service which provides access to over 200 databases in all fields of science and technology and the European Space Information System (ESIS). On this site there are 120 staff members.

The expansion of European space activities has led ESA to build more facilities.

The most recent establishment is the European Astronaut Centre (EAC), at Porz-Wahn, Germany which coordinates all European astronaut activities including the training of the future European astronauts.

Finally, the Agency is supporting the Kourou launch base in French Guiana.

# ESA PROGRAMMES

## MANDATORY

- **BASIC ACTIVITIES**
  Studies Future Projects, Technological Research, Common Technical Investments (Facilities, Standards, etc.), Earthnet, Education
- **SCIENCE**
  Scientific Satellites, Space Science Activities

## OPTIONAL

- **EARTH OBSERVATION**
  Meteorology, Remote Sensing, Climatology, Geodesy
- **MICROGRAVITY RESEARCH**
  Material Sciences, Life Sciences
- **TELECOMMUNICATIONS**
  Point to Point Communications, Television and Sound Broadcasting, Data Relay
- **SPACE STATION AND PLATFORMS**
  SPACELAB, EURECA, COLUMBUS
- **SPACE TRANSPORTATION SYSTEMS**
  ARIANE HERMES

Oct. '86

esa

## COMPARISONS OF MEMBER STATES' CONTRIBUTIONS TO ESA BUDGETS RELATIVE TO GNP

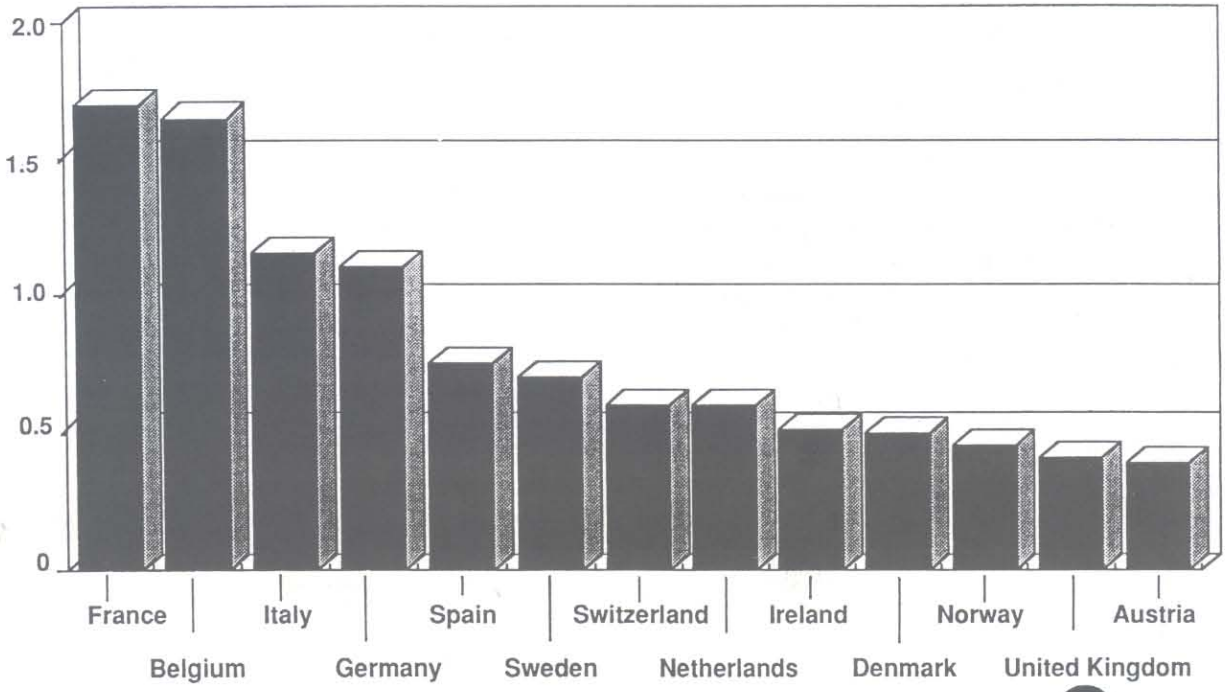


30.09.1991

esa

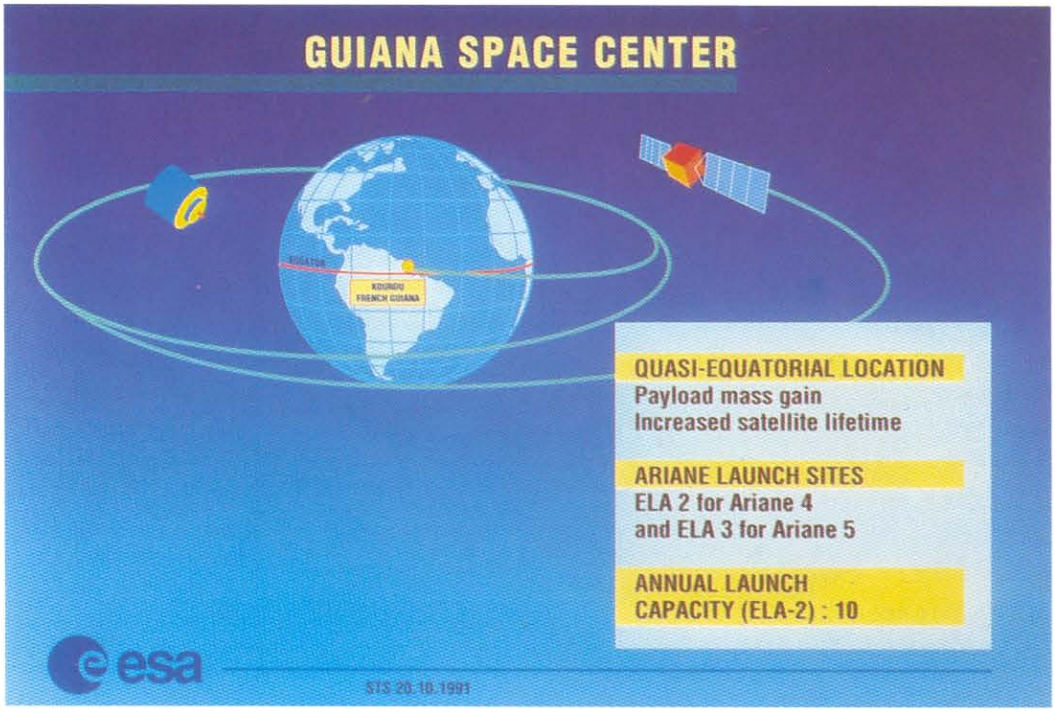


Guiana Space Center

Image of ELA1/ELA2

# BUDGETS FOR 1992*

## INCOME FROM MEMBER STATES AND OTHER SOURCES

APPROVED PROGRAMMES + PROGRAMMES FINANCED BY THIRD PARTIES

TOTAL : 2731.6 MAU

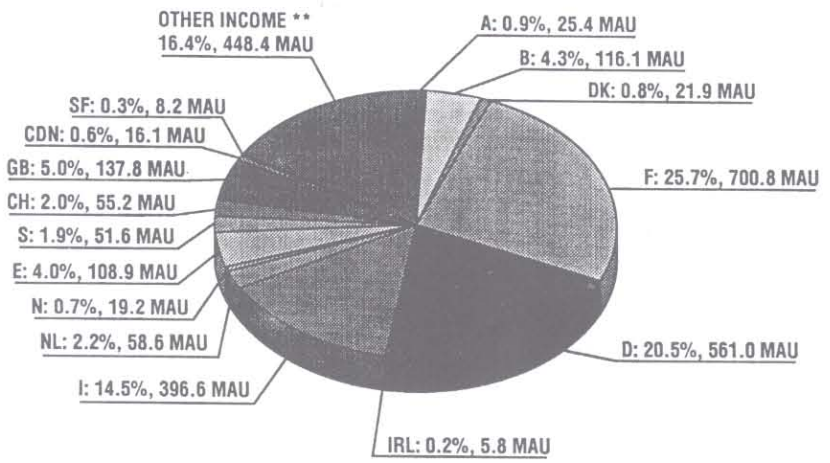


CONTRIBUTIONS 1992

| | MAU | % |
|---|---|---|
| A | 25.4 | 1.1% |
| B | 116.1 | 5.1% |
| DK | 21.9 | 1.0% |
| F | 700.8 | 30.7% |
| D | 561.0 | 24.6% |
| IRL | 5.8 | 0.2% |
| I | 396.6 | 17.4% |
| NL | 58.6 | 2.6% |
| N | 19.2 | 0.8% |
| E | 108.9 | 4.8% |
| S | 51.6 | 2.2% |
| CH | 55.2 | 2.4% |
| GB | 137.8 | 6.0% |
| CDN | 16.1 | 0.7% |
| SF | 8.2 | 0.4% |
| | 2283.2 | 100% |
| OTHER INCOME | 448.4 | |
| | 2731.6 | |

*ESA/AF(91)30 + add 1, 2, 3 and 4 - January 1992
**Income from third parties, Nasa, etc...

MAU : Million of Accounting Units (1 AU = 0,69 British Pounds, 1,15 US Dollars, 1,31 Canadian Dollars - Rates applicable to 1992 budgets)

esa

# BUDGETS FOR 1992*

## APPROVED PROGRAMMES + PROGRAMMES FINANCED BY THIRD PARTIES

TOTAL : 2731 MAU

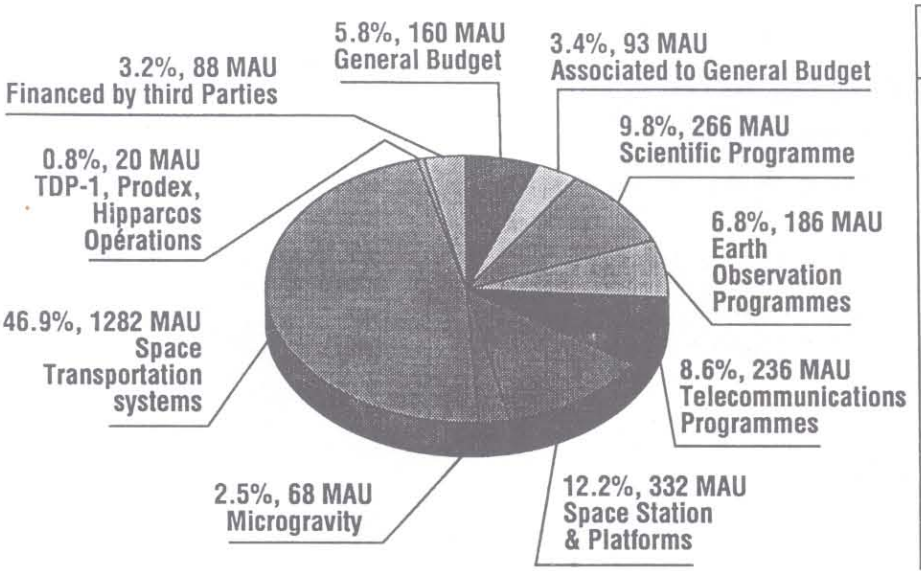


| LIKELY BUDGETS DEVELOPMENTS IN 1992 | MAU |
|---|---|
| • Approved programmes | 2643 |
| • Programmes financed by third parties | 88 |
| Sub total | 2731 |
| • New budgets to be approved in 1992 | 82 |
| Grand total | 2813** |

* ESA/AF(91)30 + add 1, 2, 3, and 4 - January 92
** NOT INCLUDING CARRY FORWARD TO 1992

MAU : Million of Accounting Units (1 AU = 0,69 British Pounds, 1,15 US Dollars, 1,31 Canadian Dollars - Rates applicable to 1992 budgets)

esa

To facilitate collaboration among ESA member states, there are two kinds of programmes: the mandatory programme, in which each country participates at a level corresponding to its GDP, and the optional programmes. The former covers not only the running costs of the Agency but also the science and basic technology programme. The latter are funded by individual member states depending on their interest in a particular programme. This category includes Earth observation, telecommunications and microgravity programmes, as well as the launcher and space infrastructure programmes. Thus, France has concentrated on launchers, Germany has taken the lead in the development of Spacelab. Italy has shown particular interest in telecommunication satellites and Earth observation is the centrepiece of the United Kingdom's space policy.

The 1992 budget of ESA amounts to around 2.8 billion European Accounting Units, which corresponds to roughly 3.2 billion US dollars. In comparison, NASA has a budget of about 14 billion dollars. Of each Accounting Unit spent by ESA, around 90% is spent through the procurement process and the rest for internal costs. As a rule, the distribution of ESA contracts orients itself to the level of financial shares provided by the member states, known under the term of fair return for investment. This has been defined not for individual contracts, but on a cumulative basis.

One of the principal aims of the whole European space programme is to keep European industry competitive in advanced technology development with the United States and Japan. We also need an effective and challenging space programme for Europe to keep European scientists at the forefront of their science.

One can identify several reasons for our member states to take part in ESA's activities: first, participation in ESA programmes is perceived as crucial for their industries, commercial and industrial competitiveness: the potential of space is seen as a mechanism for industrial innovation.

# ESA LONG TERM PROGRAMME

## Its aims are :

1. to expand Europe's autonomous capability in space
2. to maintain and enhance Europe's competitiveness in all space disciplines
3. to strengthen Europe's position as a competent partner for international cooperation and in particular for cooperation with the United States

formulated expressions for the change in time or position of the impulses, which, if executed in small steps, can assure the optimization. As a result of this contribution, the primers of fig. 3 can be interpreted as follows:

- primer b indicates that an intermediate impulse will always reduce the fuel consumption. The time of this impulse should be the time when the primer is maximal and its direction, the direction of the primer vector at this time.
- primer c indicates that an initial coast will always reduce the fuel consumption.
- primer d indicates that a final coast will always reduce the fuel consumption.

The explicit expressions for the change in the time and position of an intermediate waypoint, which appear in ref. [4], are functions of the primer vector's first derivative, thus expressing Lawden's fourth necessary condition.

Several works have used similar methods for fuel optimization:

Prussing [12] and [13] treated minimum fuel fixed-time rendezvous in the proximity of a circular orbit, and separated the maneuvers according to the number of impulses (2, 3 and 4).

Jezewski and Rozendaal [14] treated rendezvous between three dimensional trajectories, with practical application to the Apollo program. They showed that a considerable amount of fuel can be saved by adding impulses.

Gross and Prussing [15] treated free-time rendezvous between circular orbits, where ratio of radiuses is much bigger than unity.

Prussing and Chiu [16] treated fixed time rendezvous, as a function of the phase angle. They showed that if the time is sufficient, than Hohmann transfer is optimal.

None of these works deal with any kind of constraints.

## 3. Problem formulation

The purpose of this research is to develop an interactive graphical tool for planning time-limited rendezvous trajectories between space vehicles that orbit in the proximity of the space station. The resultant trajectories must satisfy the spatial constraints assuring collission avoidance and must have an optimal fuel consumption. Some of the practical applications may be:

transfer of crew between neighbouring vehicles, where the time limitation can originate from the limited amount of oxygen for breathing, batteries, navigation precision, or from the need to perform an urgent operation, such as rescue.

- transfer of equipment, with an unmanned spaceship.
- free flyers maintenance.

The chaser, target and rendezvous trajectories discussed herein are two dimensional and limited to the station's orbital plane, but are not otherwise limited in their shape. Fig. 4 describes graphically a typical testcase in which the location of the chaser and the target at initial task time, $t_0$, and final time, $t_f$, are given, so that their trajectories are fully defined. The mission total task time is $t_{task}=t_f-t_0$. The coordinate system, (s,r), is attached to the space station which is placed in a circular orbit, 480 km above the Earth. The chaser leaves its original trajectory at time $t_1$, when the initial impulse $\Delta V_1$ is applied, adjusts the rendezvous trajectory at $t_2$, with the intermediate impulse $\Delta V_2$, and reaches the target trajectory at $t_3$, where the final impulse $\Delta V_3$ adjusts its velocity, according to the target's velocity. In this case the rendezvous trajectory is composed of an initial coast along the chaser trajectory ($t_0<t<t_1$), two sections, a final coast along the target trajectory ($t_3<t<t_f$), and three impulses. The second section of the rendezvous trajectory does not fulfil the spatial constraint, so that even if this solution is fuel optimal, another one, with a higher fuel consumption, must be found.

Finding a fuel optimal trajectory means finding a trajectory in which the sum of the impulses applied is minimal, including the last one. Taking into account the last impulse is specific to rendezvous maneuvers, while for interception cases, this last impulse is ignored.

An additional demand for the required method is that it must be simple enough to be implemented and used with reasonable hardware, so that it can be operated in each vehicle, in orbit, without the need of a wide academic background in the field.

The basic assumptions made in this research were:

- motion in a central inverse square law gravity field, that yields Keplerian trajectories; no perturbations were considered;
- two dimensional motion, limited to the orbital plane of the space station;
- limited task time;
- propulsion achieved by impulses, with no limitations on their number, magnitude or direction; no disturbing forces (like drag, third body attraction, etc.) were considered;
- motion in almost circular trajectories, with negligible excentricity;
- linear problem in which the fuel consumption [kg] is proportional to the sum of the impulses [m/sec].

## 4. Method of Solution

Planning a complex maneuver, which is fuel optimal and fulfils the spatial constraints, turns out to be a difficult task. Therefore the approach of this method is to use an interactive graphic system, which displays simultaneously the maneuver, the spatial constraints, the cost function (the sum of the impulses applied), together with an optimization pointer and the primer vector distribution. The solution is obtained by means of an iterative process, whose logic flowchart is described in fig. 5.

The optimization method is based on the primer vector theory, which does not take into account any constraints. Due to the extension of the primer vector to non-optimal trajectories, an optimization pointer is built, which indicates the change of time and location of the intermediate waypoints, that assures minimizing the fuel consumption. This pointer exists only when the trajectory is not optimal. The optimal solution is obtained with the interactive aid of the operator, by moving the waypoints, according to the pointer and so that it by-passes the constraints. Although the solution may be composed of up to four waypoints, only one is active each time. This way, finding the constrained optimal solution is a simple and straight-forward process.

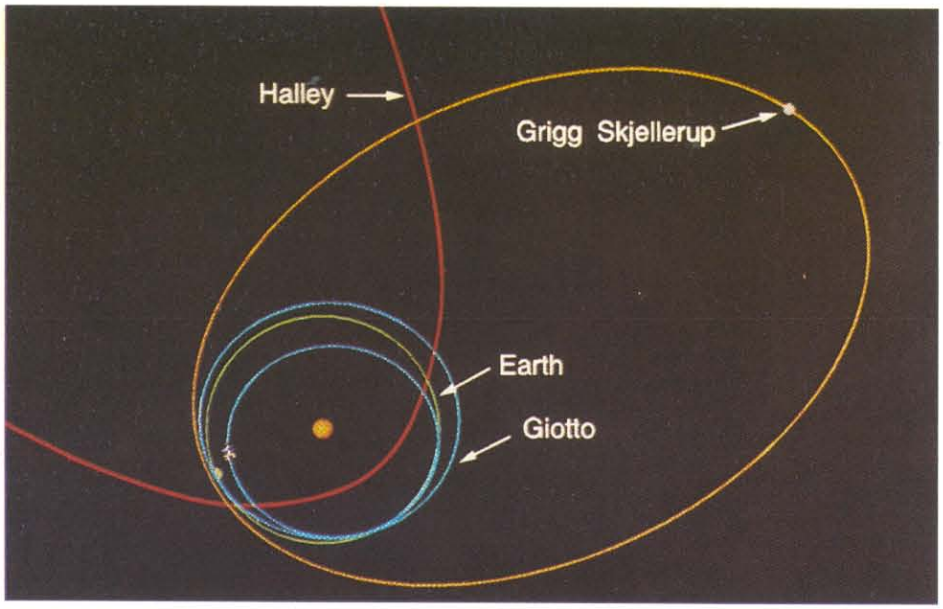


Giotto Extended Mission

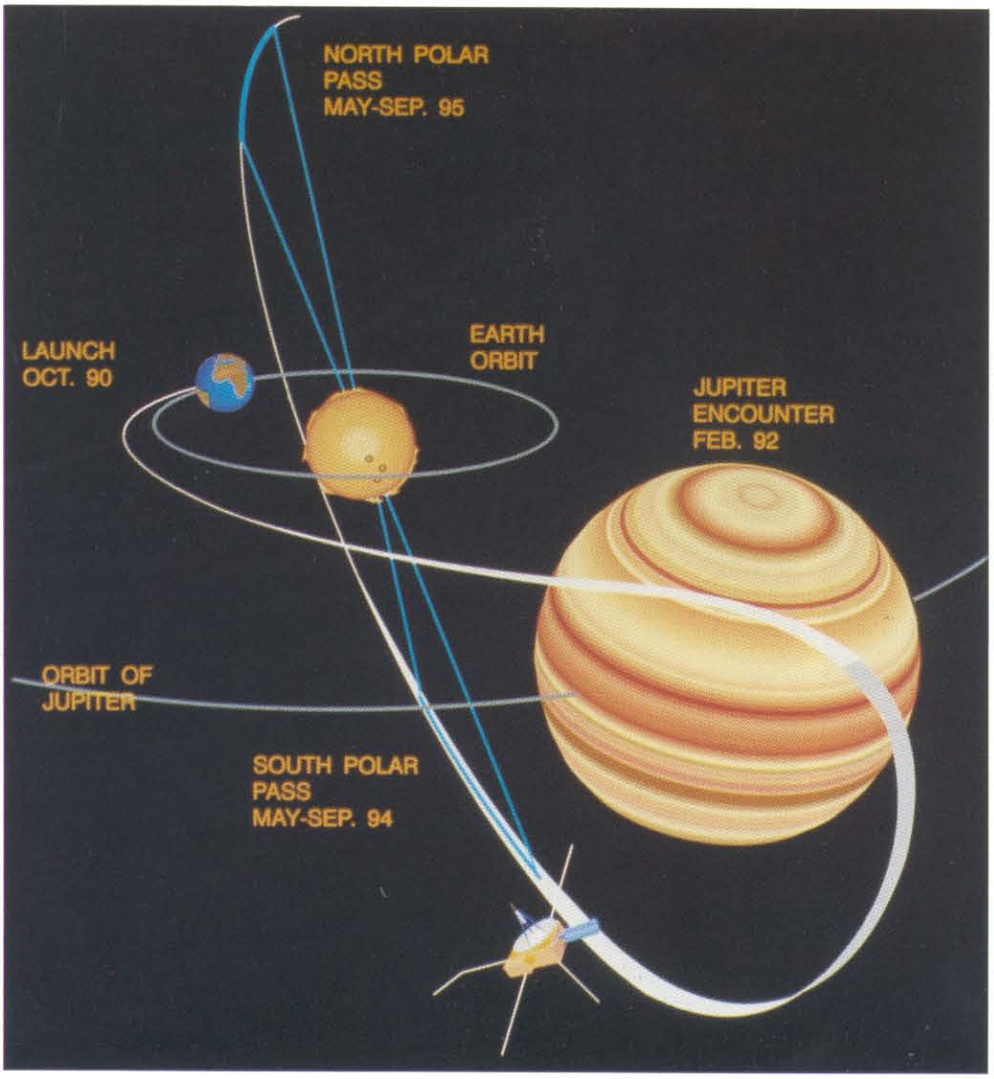


Ulysses' route to the Sun

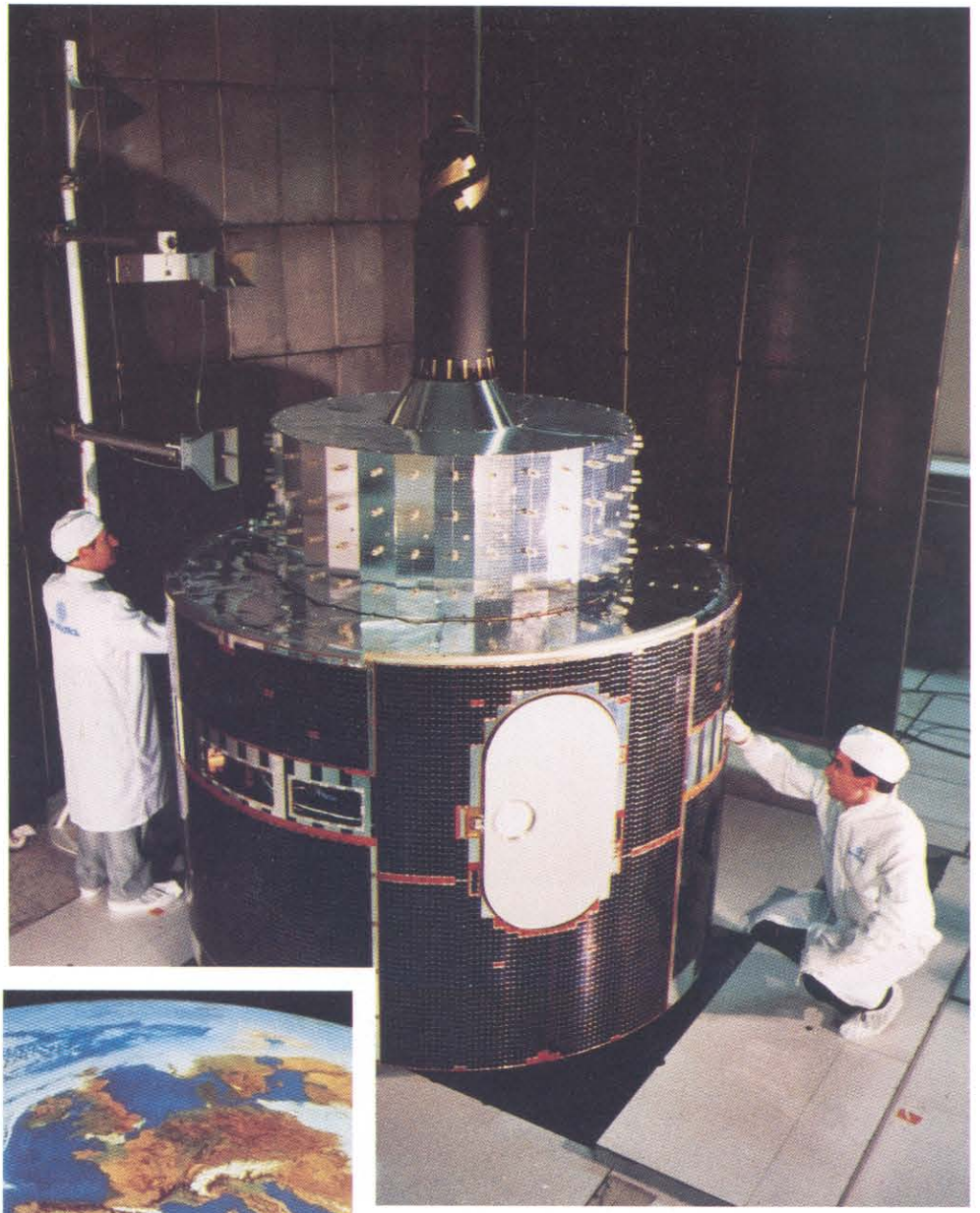

Meteosat (the satellite)

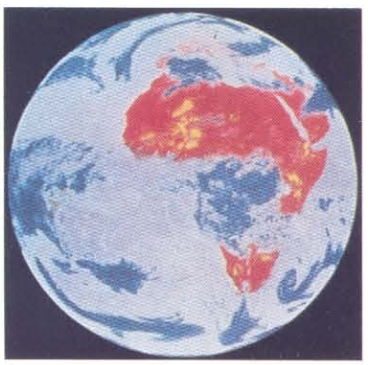

Image of Meteosat

In Munich the ministers endorsed the long-term space plan as the strategic framework for the Agency's activities, in particular in the field of Earth observation and Europe's ambitions for a manned space capability.

However, the ministers instructed the Agency to evaluate further the costs of the large programmes and to look for new ideas and possibilities for wider international cooperation with a view to use the capacities already existing, in nonmember countries in order to put the basis of world-wide cooperation for very ambitious projects.

The ministers also recognised the unique contribution that observations of the Earth from space can make towards a better understanding and management of our environment and approved a major new programme, the first polar orbiting Earth observation mission due for launch in 1998.

At this stage our attention and efforts in the Agency and in our member states are focused on the next ministerial council meeting which will take place at the end of this year in Spain. We are currently in the process of preparing a strategy on how best Europe's ambitions in space should be implemented in the light of the new world situation and the financial constraints of our member states.

**The Science programme**

Since its beginnings, the mandatory science programme has been the backbone of the Agency. In space science, ESA and its predecessor ESRO (European Space Research Organization), have been able to undertake 17 missions. Among them we find the Giotto mission to Comet Halley in 1986 which for the first time made a flyby of a comet nucleus at a distance of about 600 km and obtained pictures of it with less than 100 m in resolution. After having carried out brilliantly its first mission, Giotto will encounter another comet, Grigg-Skjellerup, in July 1992.

The latest in the series of scientific satellites launched was Ulysses, an ESA/NASA collaborative mission to explore the regions of the solar system away from the ecliptic plane, in particular above the solar poles. Ulysses was launched on 6 October 1990 and the spacecraft swung by Jupiter on 8 February 1992 at a distance of about 370.000 km leaving the ecliptic plane to fly above the poles of the Sun in 1994/95, an achievement never accomplished before by a man-made object.

ESA's future science programme called "Horizon 2000" comprises very original and very challenging projects which will further explore the Solar System, bring back cometary samples, and look further than ever before into the secrets which the Universe still holds tight.

Several scientific satellites are at present under development, among them the Infrared Space Observatory (ISO) to be launched in November 1993, the Solar-Terrestrial Science Programme (STSP), consisting of Soho and Cluster and to be launched in July and December 1995, and Huygens/Cassini, a joint mission with NASA to explore Saturn and its moon Titan scheduled for launch in 1995/96.

**Earth Observation**

I now come to Earth observation, an area of space research that is not only of considerable importance for science but one which will become increasingly relevant in fields such as climate research and environmental monitoring. Among ESA's future activities, Earth observation from space will occupy a prominent place in the long-term strategy that is being prepared by the Agency.

The first application programme for observing the Earth which has been undertaken by the Agency and one of the longest ongoing European cooperative efforts starting in the beginning of the seventies as an experimental programme was Meteosat.

As early as 1977, Meteosat 1, started routine observations of the Earth's atmosphere and surface, thus inaugurating a service which has now become not only a major tool to the meteorological community in Europe, but also an essential component of the global observational network which make up the World Weather Watch. The Meteosat family of satellites comprises now 5 satellites and the system has become operational in 1989.

One of the Agency's deliberate limitations is that it concentrates on the pre-operational phase of project development. Once the system has proved operational it is handed over to separate entities for operating the new services and for passing them on to the real end users. Thus, Meteosat is now operated by Eumetsat, the European Organization for the Exploitation of Meteorological Satellites which is based in Darmstadt, Germany.

The Agency's primary responsibility is to conduct innovative research and development for the benefit of its member states. In the field of Earth observation for example the Agency's function is to draw together a coherent policy and to take the lead in research and development in support of future missions. This may include the conception, development and demonstration of new techniques that in the future will replace or enhance existing instruments.

A good example of this is the Agency's first Remote Sensing Satellite (ERS-l) with its unique set of all-weather microwave instruments to monitor ocean and ice processes for scientific research and applications purposes which has been launched on 17 July 1991. The spacecraft which is now fully operational has sent back some impressive results and the scientific community is full of enthusiasm for the first data which have been obtained from this innovative mission so far.

ERS-l is only the forerunner of a new generation of space missions planned for the

# *ERS 1*
## *EUROPE'S FIRST REMOTE SENSING SATELLITE*

**OBJECTIVES :** INCREASE SCIENTIFIC UNDERSTANDING OF COASTAL ZONES AND GLOBAL OCEAN PROCESSES, MONITORING OF THE POLAR REGIONS

**PAYLOAD :** EQUIPPED WITH AN ACTIVE MICROWAVE INSTRUMENT (AMI) FOR ALL-WEATHER RADAR OBSERVATION

**APPLICATIONS :** OFF-SHORE ACTIVITIES, SHIP NAVIGATION, FISHERIES, OIL POLLUTION MONITORING

**LAUNCH :** 1991

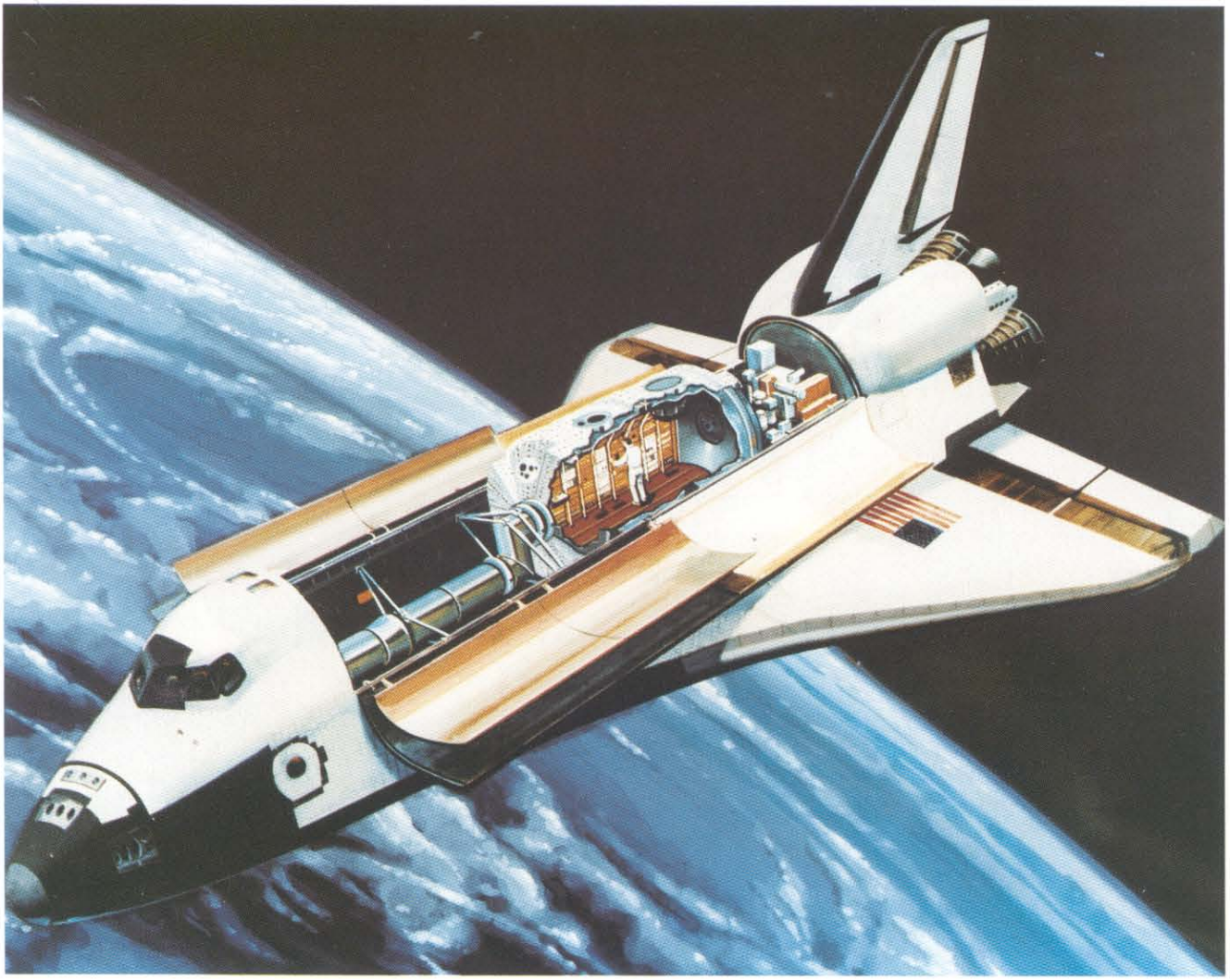

Spacelab

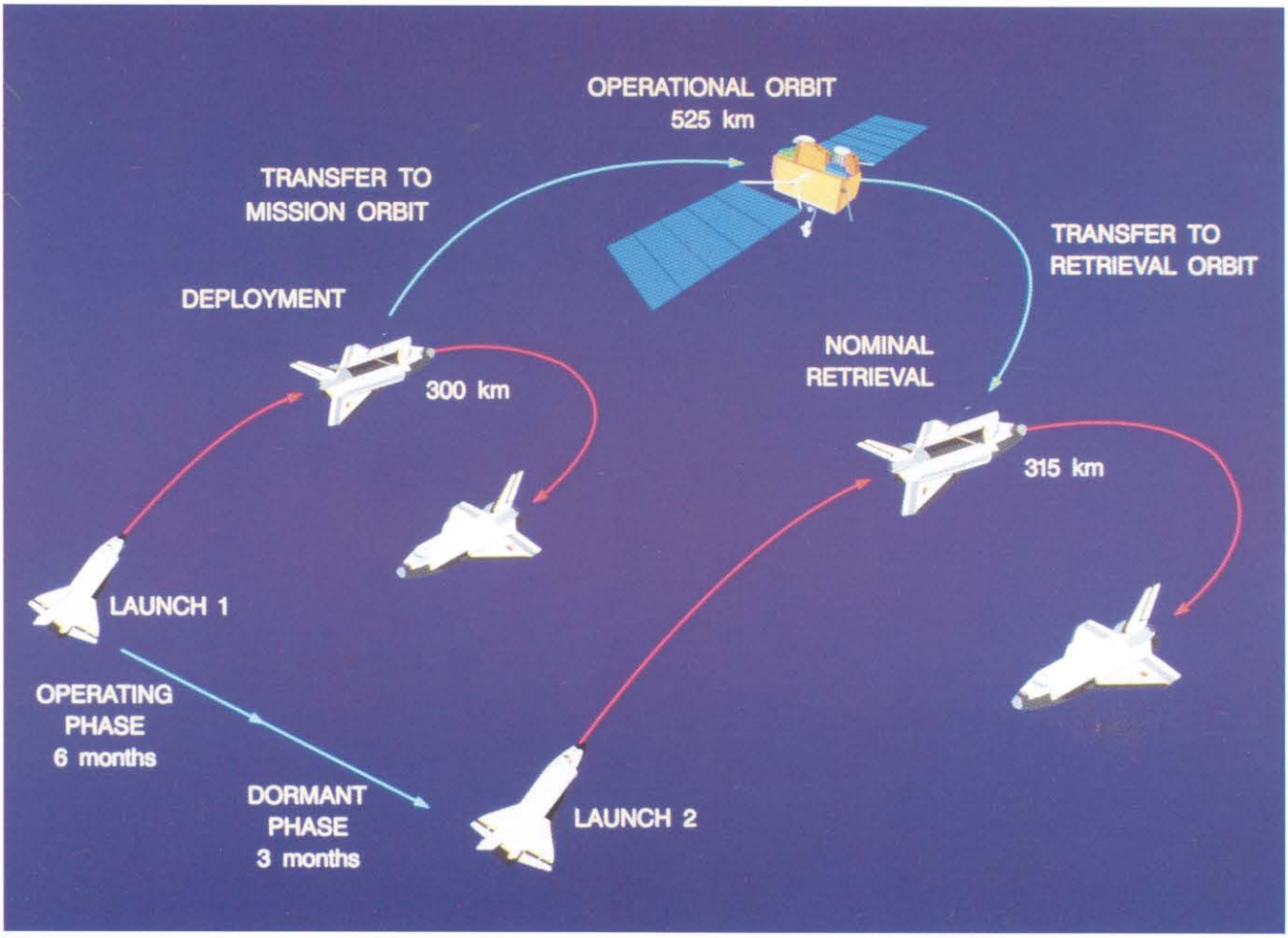


Eureca mission scenario

# ESA TELECOMMUNICATIONS PROGRAMME

| SATELLITES LAUNCHED | LAUNCH DATE | MISSION |
|---|---|---|
| OTS | 11.05.1978 | Fixed Services In-orbit Demonstration |
| MARECS-A | 20.12.1981 | Maritime Telecommunications (Voice and Data) |
| ECS-1 | 16.06.1983 | Fixed Services (Voice, Data and TV distribution) |
| ECS-2 | 04.08.1984 | Fixed Services (Voice, Data and TV distribution) |
| MARECS-B2 | 10.11.1984 | Maritime Telecommunications (Voice and Data) |
| ECS-4 | 15.09.1987 | Fixed Services (Voice, Data and TV distribution) |
| ECS-5 | 21.07.1988 | Fixed Services (Voice, Data and TV distribution) |
| OLYMPUS | 12.07.1989 | Fixed Services (Voice, Data, TV distribution and direct TV Broadcasting) |

*INMARSAT OPERATES THE MARECS SATELLITES*
*EUTELSAT OPERATES THE ECS SATELLITES*

D/TEL 24. 07.1989

esa

1990s aimed at making a substantial contribution to the scientific study and monitoring of the environment. Its full potential can only be realized if the long-term continuity of its unique data can be assured. Therefore, a programme to construct, launch and exploit a second flight model of ERS-1 was started in mid-1990. ERS-2 which is due for launch in 1994 will be a copy of ERS-1 but will also include the capability of a Global Ozone Monitoring Experiment (GOME).

This is also why part of the Agency's programme is to carry out a polar mission to further expand observation from space and to investigate such phenomena as climate change, ozone depletion, deforestation and desertification. This polar mission which is part of the Earth observing System, with missions to be flown by the United States and Japan, will considerably enhance Europe's capability for Earth observation from space. Following the decision by the ministerial council in Munich in November 1991, development of the first polar Earth observation mission has been started in 1992.

Here I should like to say a few words about international collaboration, since this will become an increasingly important aspect of future space activities, particularly in support of such missions as global change and environmental monitoring.

On a larger scale beyond Europe, we are increasingly faced with issues such as climate change, ozone depletion, deforestation, and desertification, where a broad international initiative is needed. Considering the global dimensions of environmental change, international cooperation is a key factor in the realization of the initiatives undertaken by the space nations.

The European polar platform missions scheduled for launch at the turn of the century should be seen in this international context alongside the Earth Observing System of the United States and the Japanese platforms. The objective of each of these missions will be to provide complementary data sets as a contribution to the study and assessment of the Earth's total system that makes up the environment.

## Microgravity

Space research also covers the study of materials and organisms in orbit under conditions where gravity is nearly absent. This discipline, which is still in its infancy includes a large variety of activities. The focus of the keenest scientific interest at present are areas such as material sciences, chemistry, fluid dynamics, pharmacy and life sciences.

It was against this background that ESA developed Spacelab, the first space laboratory, consisting of a laboratory module and pallets. Spacelab made its first flight in late 1983 on board the US Shuttle and has since been flown on several other occasions.

The most recent major milestone was the International Microgravity Laboratory mission IML-1 launched by the Discovery on 22 January,

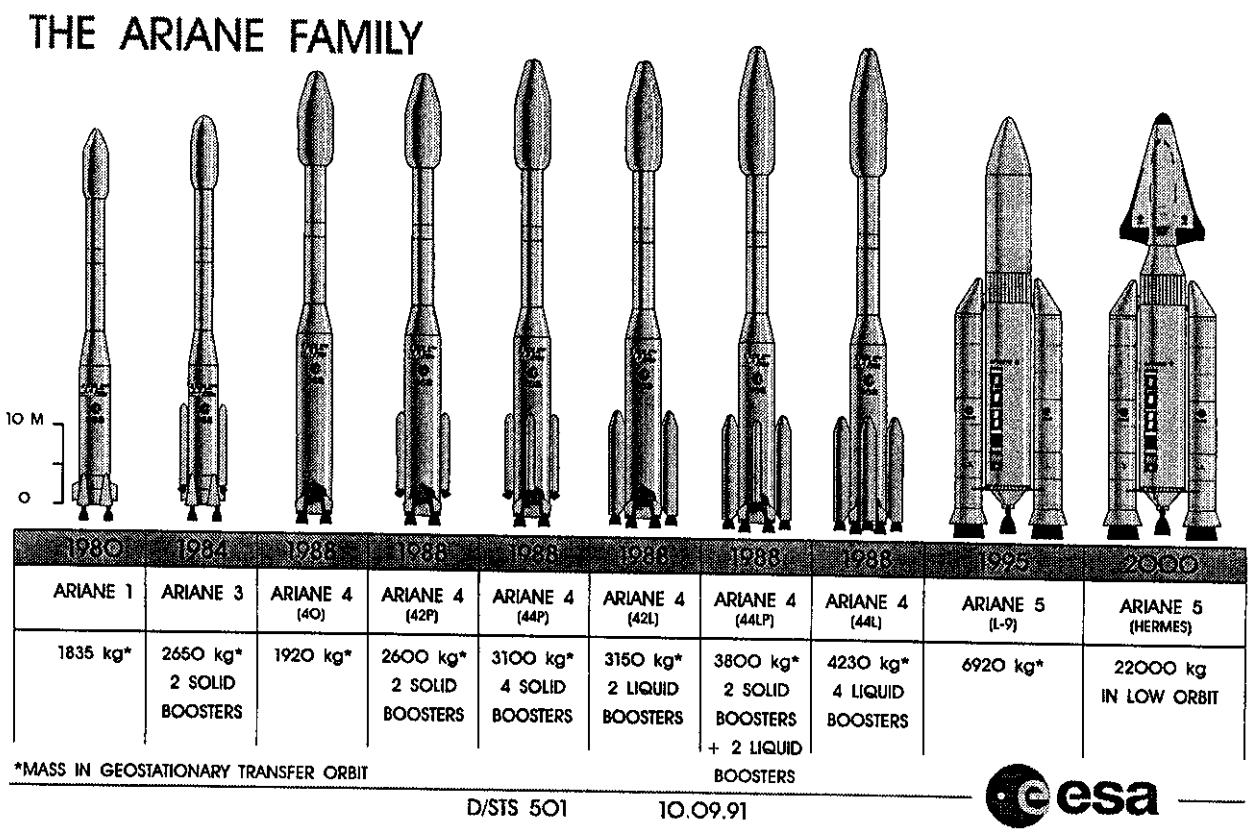

# ARIANE LAUNCH RECORD

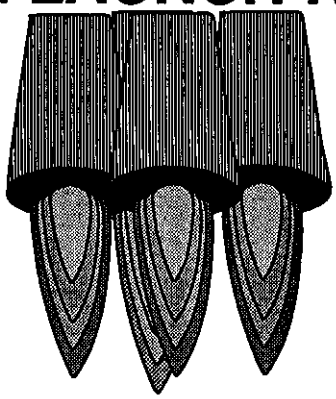

**48 LAUNCHES, of which**
**43 SUCCESSFUL placing**
**80 SATELLITES IN ORBIT**

10.02.1992

## ARIANE 5
*FUTURE HEAVY LAUNCHER FOR 1995, AND BEYOND*

### OBJECTIVES OF THE ARIANE-5 PROGRAMME

**Maintain competence, competitiveness and independence of Europe in the field of heavy launchers,**

**by developing an optimum European launching system for GTO missions which at the same time opens access to the low Earth orbit ( space stations and manned missions)**

**The Ariane-5 launch system will be called upon to carry three types of missions :**

- **launch commercial geostationary and sun-synchronous satellites, scientific satellites and experimental application satellites**
- **launch of the Hermes spaceplane**
- **launch elements of the Columbus programme**

D/STS 1.10.1991

and which was dedicated to fundamental life sciences and materials science experiments to which the Agency was providing the Biorack and the Critical Point Facilities and an astronaut.

There is also the first launch of the European Retrievable Carrier, Eureca. This satellite is a reusable unmanned platform mainly dedicated to research in the microgravity environment which will be launched by the Shuttle, remain in orbit for several months, and than be retrieved and brought back to Earth on a later Shuttle mission. This satellite weighs about 4.5 tonnes and is the largest satellite so far "made in Europe". It is also a first in so far as it is the first time that the Agency will fly a retrievable carrier. Eureca is due for July this year.

Additional flights of Spacelab and Eureca are planned in the period between 1995 and 1997 with the aim to prepare the user community for the utilization of the Columbus elements.

**Telecommunications**

In less than three decades the use of satellites for communications has revolutionized global communications and mobile communications systems hold a similar promise for the future.

Building on the basis of the Orbital Test Satellite (OTS), ESA has developed two series of operational satellites: the European Communications Satellites (ECS) which have been leased to the European Telecommunications Satellite Organization Eutelsat, and the Maritime Communications Satellites (Marecs), which have been leased to Inmarsat, the International Maritime Satellite Organization.

In July 1989, the Agency launched the large advanced experimental communication satellite Olympus. Through its experimental programmes which involve a large number of research institutes and development organizations, this satellite is demonstrating new applications in communications and broadcasting and will assist

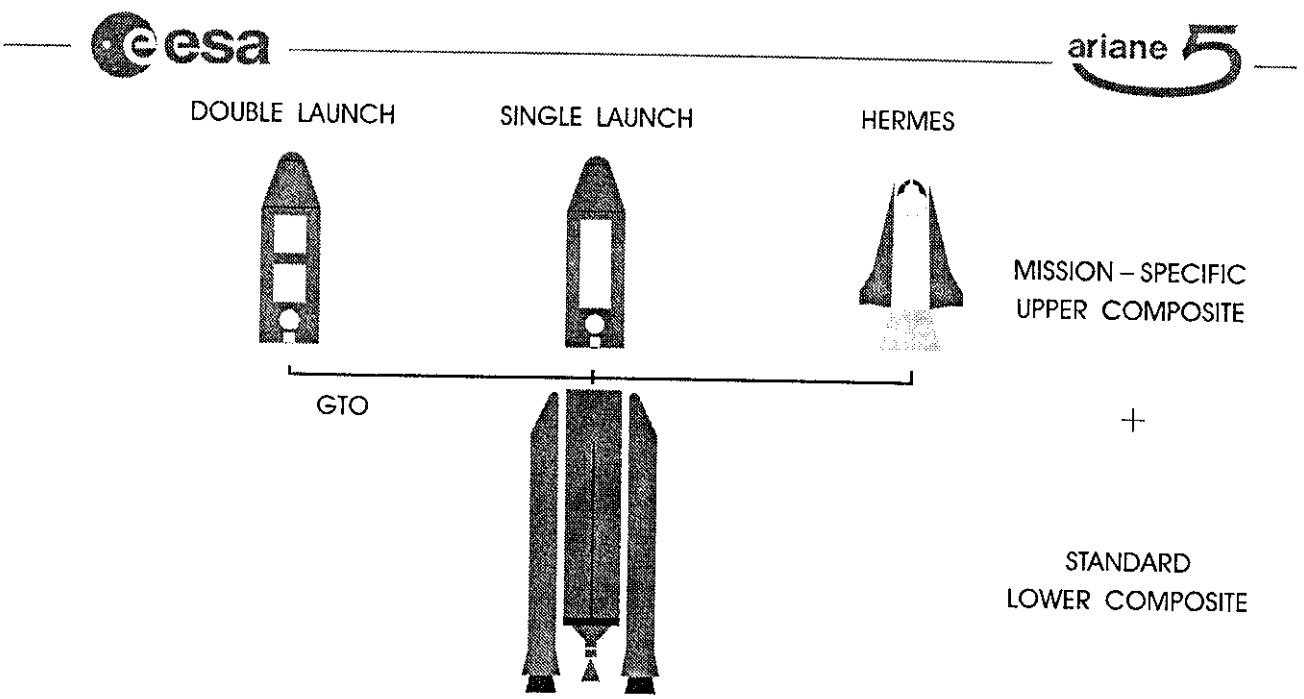

in the development of the use of new frequency bands.

The future ESA telecommunications programme includes the Artemis and the Advanced Orbital Test Satellite projects, whose aim is to develop and demonstrate new, advanced technologies such as communications to land-mobile terminals, Ka-band and optical inter-satellite data links.

As a continuation to the development of a European In-orbit infrastructure which will become available in the late 1990s to provide support to such programmes as Columbus, Hermes, and the polar Earth observation mission, the Agency plans to develop a Data Relay Satellite System.

Europe has had considerable success in the field of space telecommunications. However, the implementation of the Single European Act and the creation of a single market will certainly bring about a fundamental change in the market conditions for the producers, suppliers and operators of communication satellite systems.

Europe must be prepared for this new challenge and work actively to come forward in the world market as a competitive supplier of services. In this respect, ESA has a leading role to play, coordinating European initiatives and efforts.

**Space Transportation**

The exciting scientific and technical possibilities which space offers cannot be realized without a reliable and efficient launcher system, which is the key to all space activities. Without independent access to space Europe would be unable to compete in the world satellite market.

The development of the first version of the European launcher Ariane 1 was decided in 1973 in order to give Europe an independent launch capability. ESA delegated responsibility for the technical and financial management to the French national space agency CNES. After a first development launch in December 1979 and three further development launches, Ariane 1 became operational in January 1982. In 1984 responsibility for production, commercialization

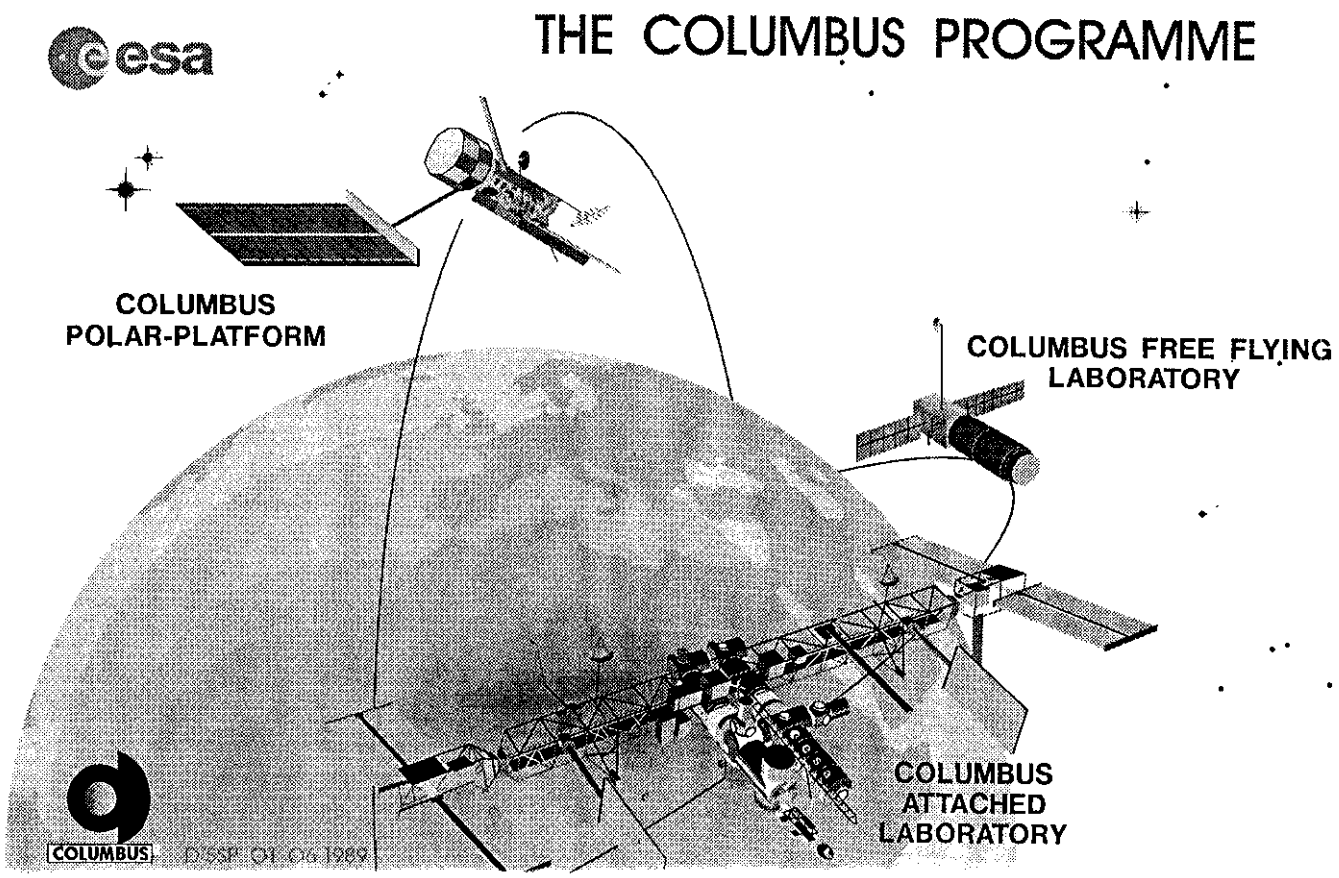

and operational launching was handed over to Arianespace, a private law company created in March 1980 by the 36 main European manufacturers in the aerospace and electronic industries, 13 major European banks and CNES.

An Ariane follow-on development programme was initiated in 1980 to develop an upgraded version of the launcher (Ariane 2 and 3) allowing it to launch heavy satellites and to perform dual launches, a major contribution to cost-effectiveness. Together with Ariane 1, this launcher was used 28 times. Its last launch took place in July 1989.

In the meantime, a second launch facility, ELA 2 was build in Kourou, French Guiana and used from March 1986 onwards. In January 1982, the development of Ariane 4 was initiated. Its first launch took place on 15 June 1988. Ariane 4 has six versions to give it a technical and operational flexibility. This version has been used 21 times, a further 49 launchers being under production and planned to be launched before the end of the century. Ariane has so far performed 48 launches putting 80 satellites in the desired orbit. Arianespace has a backlog of 35 satellites to be launched, worth approximately US $ 2.7 billion.

With its launcher Ariane, Europe has one of the world's most reliable and versatile space transportation systems and is able to compete successfully in the commercial launcher market. However, new expendable launch vehicles are under development in the United States. Japan also plans to produce a competitive launcher. Hence the decision of the ESA member states to undertake the development of a more powerful launcher, Ariane 5, in order to meet both its launcher needs and those of other users in the 90s.
Figure 21 here
In order to meet the further market requirements, detailed investigations were carried out to define an optimum European launching system for Geostationary Transfer Orbit missions while at the same time opening up access for Europe to manned missions.

In January 1985 the Ministers of the ESA member states meeting in Rome endorsed the proposal to develop the Ariane 5 heavy lift launcher, a decision which was confirmed at the ministers meeting in The Hague in November 1987. The first development launch is scheduled for 1995 and operational status for automatic missions is foreseen a year later.

In addition to the development of the launcher, the programme includes the development of the ELA 3 launch site together with certain production facilities in French Guiana.

Ariane 5 will be capable of placing payloads of up to 6.800 kg into geostationary transfer orbit and up to 18.000 kg in low Earth orbit. It will also serve as the transportation system for the Hermes manned spaceplane.

The launch cost will be 90% of that of the most powerful version of Ariane 4, which in view of the higher performance, represents a reduction of 45% in the cost per kg in orbit for the GTO missions.

All manufacturing and test facilities have been built and are in operation. Design is well advanced and manufacturing is well under way. Major systems such as the cryogenic engine Vulcain, the solid propellant booster, have started, or will soon start their tests at system level.

### In-orbit Infrastructure Programmes

In addition to the expansion of its launcher capacity, Europe's future space activities are centered around two major in-orbit infrastructure


**Hermes spaceplane**

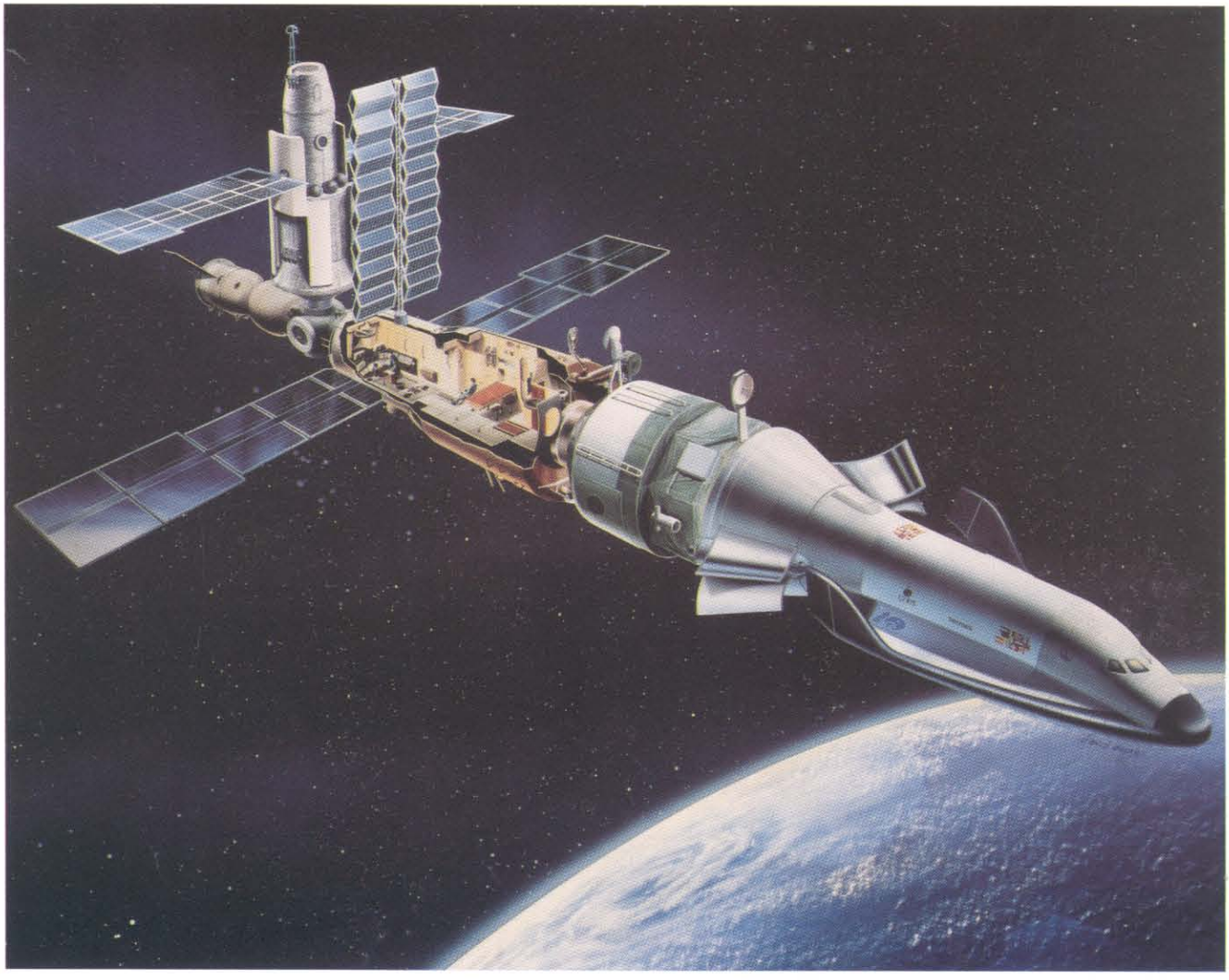

**Hermes docked to MIR**

programmes: Columbus and Hermes. The development phase of these programmes has been initiated in 1987. A final approval of the second phase is expected at the next ESA Council at ministerial level at the end of 1992 in Spain.

**Columbus**

Europe is also participating in the development of the International Space Station "Freedom" proposed by President Reagan in January 1984 together with Canada and Japan with an independent contribution called the Columbus programme.
The ministers at the Rome Council meeting in January 1985 accepted in principle the US invitation and welcomed the Agency's proposal to undertake the Columbus Programme, based on preliminary studies by Germany and Italy, as a European contribution to the International Space Station programme and as a first step towards a European autonomous capability in manned orbital operations.

Europe had already cooperated with the US in the Spacelab programme. However, cooperation in the space station was very different in character from any that had been undertaken before.

In November 1987 a new ministerial council in The Hague approved the first phase of the Columbus Development Programme to which 10 European countries participate. Less than one year later, on 29 September 1988, the multilateral Intergovernmental Agreement (IGA) and the ESA/NASA Memorandum of Understanding (MOU) were signed in Washington.

Columbus consists of three flight elements: the Attached Laboratory, which will be launched by the Shuttle and permanently assembled to the International Space Station Freedom; the Free-Flying Laboratory, launched by Ariane 5 and man-tended through regular servicing missions by the

## TOTAL SPACE PERSONNEL IN EUROPE

| | |
|---|---|
| • **INSTITUTIONS**<br>**(CNES, DLR, DARA, EUTELSAT, EUMETSAT, INMARSAT, ESA, ASI...)** | **7300** |
| • **UNIVERSITIES** | **2305** |
| • **INDUSTRY** | **38700** |
| **TOTAL :** | **48305** |

spaceplane Hermes; and the Polar Platform also launched by Ariane 5 but into a higher sun-synchronous orbit and carrying Earth observation instruments.

**Hermes**

Through the Ariane launcher programme, Europe has achieved the capability to launch satellites into space. With the Hermes programme, Europe intends to acquire the additional capability for manned operations in space.

The Hermes space vehicle will be launched atop Ariane 5. It consists of the Hermes spaceplane and a resource module. The spaceplane, after a mission of typically twelve days in space, returns to Earth in aerodynamic flight and lands horizontally on a conventional runway of 3 km length. The resource module, located at the rear end of the spaceplane, offers place for additional payload and equipment and allows to adapt the Hermes space vehicle to missions of various types. It is separated from the spaceplane in the early return phase.

Hermes can transport 3 crew members and 3 tonnes of cargo. The spaceplane brings the crew and 1.5 tonnes of cargo back to Earth.

Hermes and Ariane 5 constitute a coherent and complementary space transportation system. Whenever the mission objectives allow, space transportation tasks will be performed by Ariane 5 in the automatic, unmanned version. Hermes will only be used for missions which require the presence of a crew on board not for the mere transportation task, but for manned intervention in space.

Its main mission will be the servicing of the Columbus Free-Flying Laboratory. Other

# INT. SPACE OPERATORS / BUSINESS CORPORATIONS

EUTELSAT
European Telecommunications Satellite Organisation
Created provisionally in 1977, established in1982
and based in Paris. 26 members.

EUMETSAT
European organisation for the exploitation
of Meteorological Satellites.
Founded by 16 countries in 1983 and based in Darmstadt.

INMARSAT
International Maritime Satellite Organisation
Created in 1976 and based in London. 54 members.

ARIANESPACE
Established in 1980 for commercializing the
Ariane launchers. Based in Evry. 50 shareholders
(CNES, leading European aerospace firms, banks).

missions, such as the servicing of the Columbus Attached Laboratory, visits of the Russian space station Mir or autonomous Hermes missions are also under consideration.

With the exception of the United Kingdom all the Agency's member states are participating in the Hermes programme.Its first unmanned launch into space is currently planned for 2002 followed by the first manned spaceflight with a crew onboard in 2003.

Hermes represents a major technological challenge as well as a major management challenge to Europe. Its design and construction present engineers with the task of developing new technologies in fields such as aerodynamics, high temperature materials, power supply systems, automation and robotics. Hermes is not only a spacecraft but also a hypersonic aircraft. It is the first programme in Europe that brings together specialists from space technology and aeronautical engineering. Hermes thus constitutes the stepping stone for Europe towards any further advanced space transportation system of the more remote future.

## Conclusion

In carrying out these and many more complex missions, the European Space Agency (ESA) has shown and continues to show that scientists, engineers, industry and governments can overcome national interests and ambitions to join in a cooperative venture that has secured Europe a prominent position in space research. As a result of the increased maturity and level of Europe's space capability, our industry is a valued partner when conducting joint space activities with other nations.

However, despite some spectacular achievements in the past three decades, we are still very much at the beginning of the space age and much needs to be done to benefit from the exceptional opportunities in science and technology that are beckoning from space.

Europe is one of the world's highly industrialized regions and the continued success of its industries depends on their ability to remain in the forefront of technological and scientific developments. Space research and the technically challenging space projects undertaken jointly by European states within the framework of ESA can be seen as being an essential element in Europe's technological success.

Our principal partners and competitors, the USA and Japan have recognised the significance of vigorous initiatives in space as a focus for national will and technological development for their economies.

I am convinced that international collaboration will become an increasingly important aspect of future space activities, particularly in support of such missions as global change and environmental monitoring. Only by uniting the efforts and resources of the world's space agencies we will be able to stand up to one of the greatest challenges the world faces at the end of this century.


32
"הסימפוזיון
לשימושים
אזרחיים ב
"The 2
1992

# GAME THEORETIC SYNTHESIS FOR ROBUST AEROSPACE CONTROLLERS

**Jason L. Speyer**
**Mechanical, Aerospace and Nuclear Engineering Department**
**University of California, Los Angeles**

**Abstract**

A synthesis method is described and illustrated for the design of feedback controllers for linear time-invariant systems in the presence of plant and measurement disturbances, and parameter uncertainty. The synthesis method involves a state space description where the system disturbances and uncertainties are embedded in the system model. Furthermore, the cost criterion is a disturbance attenuation function composed of the ratio of the quadratic norm of certain outputs to the input disturbances. The outputs are chosen so that both desirable performance and stability robustness is obtained. The problem of finding the controller which minimizes the attenuation function in the presence of the worst disturbances is equivalent to a linear-quadratic game problem. The result is a linear controller whose gains are determined from two algebraic Riccati equations. This compensator is illustrated by three examples. The first, representing the control of a two-mass spring system, is used to motivate the approach to controller design. However, when viewed as a simple model of a flexible structure, the problem is interesting and challenging leading to a nonminimal phase conpensator. The second example which illustrates an important control problem with full state feedback, is that of controlling attitude or attitude rate as well as momentum of the space station. Finally, a VSTOL aircraft at a transition velocity illustrates the partial information case.

## 1. Introduction

A disturbance attenuation problem is solved by a game theoretic approach [1,2] where the control, restricted to a function of the measurement history, plays against adversaries composed of the process and measurement disturbances, and the initial state. The resulting differential game theoretic compensator for multivariable linear systems is derived by a state space approach using a quadratic performance criterion. However, compensator design is based upon many specifications such as transient response; stability and performance robustness with respect to process and measurement disturbances, parameter uncertainty, and unmodeled dynamics; and zero steady-state tracking error. Compensator design based upon linear-quadratic theory depends upon a proper state space that insures not only that the system is controllable but that the resulting compensator produces zero steady-state tracking error. Transient performance and stability robustness depends upon the choice of outputs and their weights in the quadratic performance index. These ideas are first illustrated by a spring-mass problem in the next section. In section 3 the general game problem is formulated to produce the worst case compensator. The resulting algorithm is presented and some interesting characterizations are given. In the following sections the mass-spring compensator is developed along with two other aerospace problems. The problem of momentum management and attitude control is one of full state feedback whereas the string-mass controller and the VSTOL aircraft controller involves only partial information where the controller is restricted to be only a function of the measurement sequence.

## 2. Two-Mass Spring System

Consider a two-mass spring system, shown in Figure 1, which approximates the dynamics of a flexible structure. The system is described by

$$\ddot{x}_1 + k(x_1 - x_2) = u + w \tag{1}$$

$$\ddot{x}_2 + k(x_2 - x_1) = w_c + w \tag{2}$$

with a noncolocated measurement

$$z = x_2 + v \tag{3}$$

where $x_1$ and $x_2$ are the positions of mass 1 and mass 2, respectively, k is an unknown spring constant, the masses are assumed to be 1 , u is the actuator input, w is a plant disturbance, v is a measurement disturbance, and $w_c$ is a cyclic disturbance described by

$$w_c(t) = A_w \sin(.5t + \varphi) \tag{4}$$

where $A_w$ and $\varphi$ are constant but unknown.

The design objective is to regulate $x_2$ in the presence of disturbances v and w and to reject the external cyclic disturbance in $x_2$ for all k with .5<k<2.

To include the cyclic disturbance within the state space representation, (1) and (2) are differentiated until $w_c$ disappears in the resulting system

$$x_1^{(IV)} = k(\ddot{x}_1 + .25\,x_1 - \ddot{x}_2 - .25\,x_2) - .25\,\ddot{x}_1 + \ddot{\tilde{u}} + \ddot{w} \tag{5}$$

$$x_2^{(IV)} = k(\ddot{x}_2 + .25\,x_2 - \ddot{x}_1 - .25\,x_1) - .25\,\ddot{x}_2 + \ddot{w} \tag{6}$$

where the parenthetical superscripts represent the time derivative order and $\tilde{u}$ is a new control variable defined as

$$\tilde{u} = \ddot{u} + .25u \tag{7}$$

Similarly, $\tilde{w}$ is considered a new disturbance defined as $\tilde{w} = \ddot{w} + .25w$. The new system (5) and (6) contains uncontrollable modes at $s = \pm .5j$ with respect to u. To remove the uncontrollable poles from (5) and (6), a new state, $\xi$, is introduced as $\xi = \ddot{x}_1 + .25\,x_1$ to compensate for the required oscillation in $x_1$ and u to regulate $x_2$. Replacing $\xi = \ddot{x}_1 + .25\,x_1$ and $\ddot{\xi} = x_1^{(IV)} + .25\,\ddot{x}_1$ in (5) and (6), reduces the system to sixth order with a state space representation

$$x = [\xi, \dot{\xi}, x_2, \dot{x}_2, \ddot{x}_2, x_2^{(III)}]^T \tag{8}$$

with dynamic equation

$$\dot{x} = Ax + B\tilde{u} + \Gamma\tilde{w},\quad z = Hx + v \tag{9}$$

where

$$A = \begin{bmatrix} 0 & 1 & 0 & 0 & 0 & 0 \\ -k & 0 & .25k & 0 & k & 0 \\ 0 & 0 & 0 & 1 & 0 & 0 \\ 0 & 0 & 0 & 0 & 1 & 0 \\ 0 & 0 & 0 & 0 & 0 & 1 \\ k & 0 & -25k & 0 & -k-.25 & 0 \end{bmatrix} \tag{10}$$

$$B = [0\ 1\ 0\ 0\ 0\ 0]^T \tag{11}$$

$$\Gamma = [0\ 1\ 0\ 0\ 0\ 1]^T \tag{12}$$

$$H = [0\ 0\ 1\ 0\ 0\ 0]^T \tag{13}$$

This state space is controllable with respect to $\tilde{u}$ and observable with respect to z. Note that the harmonic disturbance is embedded in this state description explicitly.

So far only the additive process disturbances have been addressed. The system matrix due to the uncertainty of k about a nominal value of k, $k_o$, is

$$A(k) = A(k_o) + \Delta A(\Delta k) \tag{14}$$

where $\Delta k = k - k_o$. The variation of the system matrix $\Delta A$ can be decomposed to form an input-output system which forms an internal feedback loop with an unknown gain $\Delta k$ as

$$\Delta A = D \Delta k E \tag{15}$$

where

$$D = [0 \ 1 \ 0 \ 0 \ 0 \ -1]^T \tag{16}$$

$$E = [-1 \ 0 \ .25 \ 0 \ 1 \ 0] \tag{17}$$

The matrix D is an input matrix and E is an output matrix where the internal output is

$$y_1 = Ex \tag{18}$$

A disturbance input associated with the parameter variation is defined as

$$w_1 = \Delta k \, y_1 \tag{19}$$

This puts parameter uncertainty into the same framework as other disturbance inputs. In the next section these ideas are generalized and embedded in the game theoretic formulation.

### 3. A Game Theoretic Approach to the Disturbance Attenuation Problem

The dynamic system of the last section is generalized to the linear system

$$\dot{x} = A x + B u + \Gamma w \tag{20}$$

$$z = H x + \Gamma_1 v \tag{21}$$

where from the last section identify $\Gamma = [\tilde{\Gamma}, D]$, $w = [\tilde{w}, w_1]^T$. Here , x, u, w, and z are of arbitrary finite dimension and the matricies A, B, $\Gamma$, H, and $\Gamma_1$ conform to these dimensions. Although the system is assumed above to be time-invariant, the following results apply to time-varying systems as well [1,2].

The synthesis problem is characterized by a vector of outputs whose quadratic norm is to be kept small by the controller in the presence of the worst disturbance inputs. These outputs are chosen in the design process to insure both performance and stability robustness and are of the form

$$y = \begin{bmatrix} C \\ 0 \end{bmatrix} x + \begin{bmatrix} 0 \\ C_1 \end{bmatrix} u \tag{22}$$

where the performance index is the quadratic norm

$$J' = \lim_{T\to\infty} \int_0^T y^T y dt = \lim_{T\to\infty} \int_0^T (x^T C^T C x + u^T C_1^T C_1 u) dt \tag{23}$$

where $C_1^T C_1 > 0$. Note that y can be partly composed of the output from the fictious loop given by (18). The control u is to be chosen so as to produce good transient response, limits in the control input excursions, and parameter insensitivity by the choice of C, $C_1$ and the inclusion of E of (18) in C. This choice of controllers is to be made under the assumption that the system disturbances attempt to maximize J' with quadratic constraints on their energy.

The above disturbance attentuation problem requires the determination of a linear controller restricted to the measurement history such that the disturbance attenuation function is bounded by the constant $\gamma^2$ as

$$\lim_{T\to\infty} \frac{\int_0^T y^T y dt}{\int_0^T (w^T W^{-1} w + v^T V^{-1} v) dt} < \gamma^2 \tag{24}$$

for all w and v where $(w(t), v(t)) \neq 0$. If $T_{wy}(s)$ is the closed-loop transfer matrix between disturbances and outputs using the linear controller that satisfies (24), then (24) can be shown [1,2 ] to be equivalent to a bound on the so-called $H_\infty$ norm

$$\| T_{wy} \|_\infty < \gamma \tag{25}$$

where $\| T_{wy} \|_\infty$ is the inifinity norm defined as the $\sup_\omega \bar{\sigma} (T_{wy}(\omega))$ where $\bar{\sigma}$ is the square root of the largest eigenvalue of the Hermetian matrix $T_{wy}^T(-\omega) \, T_{wy}(\omega)$ and $\omega$ is frequency. In other words, the peak amplitude is bounded from above. The motivation is to pass as little disturbance efforts through the transfer function to the design outputs in the above sense (25) as possible.

To solve the disturbance attenuation problem, a related linear-quadratic game problem is formulated and solved where the solution gives the desired linear controller to satisfy (24). The linear-quadratic game is to find a saddle point control $u^*(Z_t)$ where the measurement history $Z_t$ is defined as

$$Z_t = \{z(s), 0 \le s \le t\} \tag{26}$$

and the adversary strategies $v^*$, $w^*$ satisfying the saddle point condition †

$$J(u^*, v, w) \le J(u^*, v^*, w^*) \le J(u, v^*, w^*) \tag{27}$$

where ††

$$J(u, v, w) = \lim_{T\to\infty} \frac{1}{2} \int_0^T [y^T y - \gamma^2 (w^T W^{-1} w + v^T V^{-1} v)] \tag{28}$$

and is subject to the system of (20) and (21)

The game problem where J of (28) is minimized with respect to u and minimized with respect to v and w exists if $\gamma_2$ is large enough and certain conditions of detectability, stability and controllability are met [1,2 ]. Note that with W and V positive definite, the disturbance are penalized in the maximization process.

---

† The controls u, v, w are assumed to belong to the class whose integral square norm exists called $L_2$ functions

†† The limit of $T\to\infty$ is used to note that the game derivation was first solved in finite time and the infinite-time limit produced the desired controller [1, 2].

### 3.1 Game theoretic Compensator

In [1,2 ] it is shown that the order of the minimization and maximation operations is important in the consturction of the compensator. A controller strategy is sought which satisfies the saddle point condition (27), not just the value of the control sequence on the saddle trajectory. By maximizing first with respect to w the process disturbance, an estimation type algorithm results. This estimated state replaces the state variable in the remaining problem.

Effectively, the process of maximation in this game problem has an effect similar to the smoothing process of conditional expection in the stochastic control problem. The remaining min-max problem with respect to u and v reduces to a standard linear-quadratic differential game. The solution to this standard min-max problem produced a linear compensator [3].

By making a particular linear transformation [1,2], the final structure of the game theoretic time-variant compensator results as

$$\dot{x}_c = A x_c + Bu^* + \Gamma w^* + B_c (z - Hx_c) \tag{29}$$

$$u^* = -R^{-1} B^T \Pi x_c \tag{30}$$

$$w^* = \gamma^{-2} \Gamma W \Gamma^T x_c \tag{31}$$

$$B_c = \bar{M} H^T \bar{V}^{-1} \tag{32}$$

where $\bar{V} = \Gamma_1^T V \Gamma_1$, $R = C_1^T C_1$, and

$$\bar{M} = (I - \gamma^{-2} \bar{P} \bar{\Pi})^{-1} \bar{P} > 0 \tag{33}$$

$$0 = A^T \bar{\Pi} + \bar{\Pi} A - \bar{\Pi} (BR^{-1} B - \gamma^{-2} \Gamma W \Gamma^T) \bar{\Pi} + C^T C \tag{34}$$

$$0 = A \bar{P} + \bar{P} A - \bar{P} (H^T \bar{V}^{-1} H - \gamma^{-2} C^T C) \bar{P} + \Gamma W \Gamma^T \tag{35}$$

Note that as $\gamma^{-2}$ goes to zero the algorithm associated witht the linear-quadratic-Gaussian (LQG) compensator is recovered. The game theoretic compensator is a generalization of the LQG compensator. The estimator given by (29) is biased by the term $\Gamma w^*$. The strategy for the worst case process disturbance $w^*$ is assumed in the estimator rather than assuming the mean of the process as given by the Kalman filter. Furthermore, the existance of a $\bar{P} > 0$ and $\bar{\Pi} \geq 0$ from the two algebraic Riccati equations (ARE) and condition $\bar{M} > 0$ in (33) depends upon the value of $\gamma$. As $\gamma^{-2}$ increases from zero, the solution to (34) and (35) may take on more than one positive definite solution. The smallest solution [1,2 ] is chosen since the bandwidth is the smallest. However, as $\gamma^{-2}$ continues to increase one of two pathelogical solutions occur. First, the most usual (generic) case is that $\bar{M}$ becomes infinite. This means that the gain is infinite producing a closed-loop pole at infinity. To avoid unrealistic designs, the choice of $\gamma^{-2}$ becomes a design parameter. The second condition is that the solution to an ARE becomes complex. When either case occurs, then the smallest $\gamma$ is obtained and the smallest bound on the disturbance attentuation function (24).

### 3.2 System Parameter Uncertainty Modeled as an Internal Feedback Loop

By adopting an input-output decomposition of the parameter uncertainty, the uncertain system is represented as an internal feedback loop (IFL) in which the parameter uncertainty is embedded in the system as a fictitious disturbance. This process illustrated in section 2 for uncertainty in the A matrix is generalized to include all the system matricies. This notion applied to the LQG problem produced a general approach to loop transfer recovery [4].

Consider a time-invariant system with uncertainties in the system, input, and output matricies described by

$$\dot{x} = (A+\Delta A) x + (B+\Delta B) u \tag{36}$$

$$z = (H+\Delta H) x \tag{37}$$

where other disturbances as given by (20) and (21) are surpressed here. By using the input-output decomposition modeling of the perturbation, $\Delta A$, $\Delta B$, and $\Delta H$ are represented as

$$\Delta A = D L_a(\varepsilon) E, \quad \Delta B = F L_b(\varepsilon) G, \quad \Delta H = Y L_h(\varepsilon) Z \tag{38}$$

where $\varepsilon$ denotes the parameter variation vector which is constant but unknown.

As in section 2, an output $y_f$ is defined from the decomposition (38) as

$$y_f = \begin{bmatrix} E \\ 0 \\ Z \end{bmatrix} x + \begin{bmatrix} 0 \\ G \\ 0 \end{bmatrix} u \tag{39}$$

The process and measurement disturbances associated with the parameter decomposition is

$$\begin{bmatrix} w_1 \\ w_2 \\ v_f \end{bmatrix} = \begin{bmatrix} L_a(\varepsilon) & 0 & 0 \\ 0 & L_b(\varepsilon) & 0 \\ 0 & 0 & L_n(\varepsilon) \end{bmatrix} y_f \tag{40}$$

The dynamic system using the uncertainty modeling now becomes

$$\dot{x} = A x + B u + \Gamma_f w_f \tag{41}$$

$$z = H x + Y v_f \tag{42}$$

where $\Gamma_f = [D \; F]$ and $w_f = [w_1^T \; w_2^T]^T$.

The compensator given by (29) to (35) can include this modeling by augmenting y with $y_f$, w with $w_f$, and v with $v_f$. Note that the relative weightings between y and $y_f$ produces tradeoffs between performance robustness and stability robustness, respectively.

### 4. Spring-Mass system: Compensator Design and Results

Given the state space model constructed in section 2, the performance measure is now developed for control synthesis. Since the state is to be tracked, C = H where H is given in (13). Furthermore, $W^{1/2} = .07$, $\Gamma_1 = .033$, V = 1, $C_1 = .08$, $\gamma = .043$, and the n of $C^TC + n^2 E^TE$ is 10. The value of $n^2$ might be thought of as a weighting between transient performance and robust performance. All the above parameters where chosen by trial and error including n, $\Gamma$, $C_1$, and $\gamma$. Substitution of these values into the compensator algorithm of section 3 produces a compensator transfer function

$$K(s) \triangleq \frac{u(s)}{z(s)} = \frac{-4430(s+.08)(s-.44)(s-2.83)}{(s^2+.25)(s^2+1.78s+9.67)} \cdot \frac{s^2-.1s+.24}{(s^2+6.56s+13.51)(s^2+15.68s+124.99)} \tag{43}$$

Note that the difference between ũ and u is the transfer function $1/s^2$ +.25. The implementation of K(s) is shown in Figure 2. The compensator poles are at ±.5j, -3.28±1.66j, -.89±2.98j, -7.84±7.97j. Simulation have shown that eliminating the compensator poles -7.84±7.97j does not seem to effect either performance or robustness. The compensator has four nonminimal phase zeros; the complex zeros are at .05±.49j.

Figure 3 shows the root locus of 1-α G(s) K(s) with respect to α. Note the negative sign is embedded in K(S). The square boxes in the figure indicate the closed-loop poles located at -2.14, -.33, -.13±.56j, -.19±.25j, -.77±2.5j, -1.83±1.45j, and 7.84±7.97j. Note that the root locus eminating from the oscillatory plant pole at $\sqrt{2}$ j moves on to the real negative axis. Also, the compensator pole at -7.84 ±7.97j has not moved for the range of values of α. For the controller K(s), the gain margin is 3.23dB at the frequency .67 rad/sec and the phase margin is 25 degrees at the frequency .20 rad/sec. The root locus with respect to changes in the spring constant k, shown in Figure 4, shows that the compensator stabilizes the system over .5<k<2.

In the simulation, the measurement is assumed corrupted by zero white Guassian noise with a power spectral density of .33. Time responses, shown in Figure 5, for the nominal system and the perturbed system with k=.5 are simulated. For both simulations, $A_\omega$ =.5, φ=0, and all initial conditions are zero. Figure 5 shows that for the nominal case, the controlled variable $x_2$ has settled down and the cyclic disturbances is rejected in $x_2$ in about 20 seconds, and for the perturbed system with k=.5, the settling time has been slightly delayed. Furthermore, note that the control amplitude is not excessive for the given input noise indicating little amplification.

## 5. A Robust Momentum Management and Attitude Control System for the Space Station

A game theoretic controller developed in section 3 and in [1,2 ] is applied to the attitude/momentum control for the space station [6,7] which uses control moment gyros (CMGs ) as the primary actuating devices and gravity gradient torque to manage momentum stored in the CMGs. The moments of inertia of the space station are assumed constant but uncertain. Full state information is assumed since the attitude and attitude rates are assumed to be very accurately measured. Disturbance rejection filters are constructed to handle the external cyclic disturbance torques in much the same way as the harmonic disturbance was embedded into the state space as shown in section2.

Although the linear-quadratic regulator has guaranteed gain and phase margin, many systems remain sensitive to parameter variations. The application of the game theoretic approach combined with the internal feedback loop (IFL) decomposition for describing parameter uncertainty as presented in section 3 allows very large variations in the inertia of the space station with little deterioration in performance. This control problem is particularly interesting in that the variation in the moments of inertia are bounded by physical constraint. The IFL decomposition allows selective changes in the moments of inertia to be included in the design process. In the pitch channel, there are two independent parameter uncertainties, one associated with the system matrix and the other associated with the input matrix. The quadratic norm of the fictitious output from the IFL decomposition of the system matrix auguments the quadratic cost criterion and the augmented term represents a measure of system robustness. The effect of the fictitious inputs by the decomposition of the input matrix is to increase the gain. However, in the roll-yaw axis where there are three independent parameters, stab.lity robustness in directions associated with inertia variations that can be made large before reaching physical constraint is achieved without increased bandwidth. The essential design task is choosing the weighting for combining the parameter uncertainty directions which improve stability robustness subject to the physical constraints on the inertias.

### 5.1 Space Station Dynamics

The space station is expected to maintain a local vertical/local horizontal (LVLH) orientation during normal operation. Suppose that the space station control (body) axes are aligned with the principal axes. (For the phase-1 configuration of space station, this is a good assumption.) For the small deviation from LVLH frame, the linearized space station dynamics are described as

$$\ddot{\phi} + 4\omega_0^2 k_x \phi - \omega_o(1-k_x)\dot{\psi} = -\frac{1}{I_x}(T_x - w_x) \tag{44}$$

$$\ddot{\theta} - 3\omega_o^2 k_y \theta = -\frac{1}{I_y}(T_y - w_y) \tag{45}$$

$$\ddot{\psi} - \omega_o^2 k_z \psi + \omega_o(1+k_z)\dot{\phi} = -\frac{1}{I_z}(T_z - w_z) \tag{46}$$

where the body fixed axes (x,y,z) denote the roll, pitch, and yaw control axes with the roll axis in flight direction, the pitch axis normal to the orbit plane, and the yaw axis toward the Earth; φ, θ, and ψ denote the roll, pitch, and yaw Euler angles with respect to the LVLH frame; $(T_x,T_y,T_z)$ is the control torque vector produced by the CMGs with respect to the control axes; $(w_x, w_y, w_z)$ is an external disturbance torque vector with respect to the control axes; $\omega_o$ is the orbital rate of 0.0011 rad/sec; and $k_x$, $k_y$, and $k_z$ are the parameters defined from the moments of inertia, $I_x$, $I_y$, and $I_z$ as

$$k_x = \frac{I_y - I_z}{I_x},\ k_y = \frac{I_z - I_x}{I_y},\ k_z = \frac{I_x - I_y}{I_z}. \tag{47}$$

Terms involving $\omega_o^2$ in (44) to (46) represent the combined gravity gradient and gyroscopic torque in each axis. The CMG momentum dynamics are

$$\dot{h}_x - \omega_o h_z = T_x \tag{48}$$

$$\dot{h}_y = T_y \tag{49}$$

$$\dot{h}_z + \omega_o h_x = T_z \tag{50}$$

where $(h_x, h_y, h_z)$ are the CMG momentum vector with respect to the control axes. It is assumed that the Euler angle, the Euler angle rate, and the CMG momemtum are perfectly measured. The roll and yaw dynamics are coupled while the pitch axis is uncoupled.

The physical constraints for the parameters $k_x$, $k_y$, and $k_z$, due to the triangular inequality of moment of inertia [8] are

$$|k_i| < 1,\ i = x,y,z \tag{51}$$

The moments of inertia, $I_x$, $I_y$, and $I_z$, are assumed constant but uncertain and described by

$$I_i = I_{in} + \Delta I_i,\ \ i = x,y,z \tag{52}$$

where the subscript n and $\Delta I_i$ denote the nominal value and the variation of each moment of inertia, respectively. Then, the parameters, $k_x$, $k_y$, and $k_z$ can be represented as

$$k_i = k_{in} + \Delta k_i,\ \ i = x,y,z, \tag{53}$$

where $k_{in}$ denotes the value of $k_i$ with nominal values of the moments of inertia and $\Delta k_i$ denotes the variation due to the variation of the moments of inertia. The nominal values of the moments of inertia for the Phase-I configuration are

$$I_{xn} = 50.28E6,\ I_{yn} = 10.80E6,\ I_{zn} = 58.57E6$$

in unit of slug-ft$^2$. In order to check a stability margin for inertia variation, ten types of variations of the moments of inertia listed in Table 1 are considered. Each variation is limited by the physical constraint (51). Table 1 also shows the physical limit of each type of variation.

The external disturbances ($w_x$, $w_y$, $w_z$) are modeled as [9]

$$w_i = A_{1i}^d \sin(\omega_o t+\varphi_{1i}) + A_{2i}^d \sin(2\omega_o t+\varphi_{2i}) + B_i^d, \quad (54)$$

$i = x,y,z$ where $A_{1i}^d$, $A_{2i}^d$, and $B_i^d$ are assumed constant but unknown. The cyclic aerodynamic disturbance at orbital rate and twice the orbital rate are due to the diurnal bulge and the rotating solar panels, respectively.

### 5.2 Pitch Control

The pitch channel is described by (45) and (49). It can be shown by use of the Routh-Hurwitz criterion that if $k_y$ changes sign from its nominal value, then the system cannot be stabilized. The objective is to determine a controllable (or at least stabilizable) state space. Again, since $w_y$ is a sum of harmonics, a state space is constructed such that $w_i$ is embedded as was done in section 2. Even so, it is seen that the monentum can not be regulated about zero although oscillatory while regulating $\theta$. Instead, only $\dot\theta$ is regulated to be zero.

In the pitch channel the uncertain parameter appear linear in the system coefficients. These appear in (45) as $k_y$ and $I_{yn}/I_y$ where $1/I_y = (1/I_{yn})(I_{yn}/I_y)$ where $I_{y\,n}$ is the nominal value of $I_y$. The controller design process is completely described in [6,7]. Improved performance over the linear-quadratic regulator is shown in Figure 6. However, some of this improvement can be attributed to an increase in system gain. The closed-loop eigenvalues are -4.77, -1.52, -.55±.42j, -.13±1.00j, -.59±1.99j where these poles are normalized with respect to the orbital frequency.

Figure 7 shows the time responses for the nominal system and a perturbed system with $\delta = 60\%$ in $\Delta_1$ variation denoted by solid line and dotted line, respectively. As expected, the attitude approaches TEA attitude, -7.6 degree for nominal system, and about -5.degrees for the perturbed system while the CMG momentum oscillates with zero mean value at steady state.

### 5.3 Roll-Yaw Control

The controller for the roll-yaw axes can be developed in similar way to the pitch axis.

Define

$$e_x = \phi - \phi_c,\quad e_z = \psi - \psi_c \quad (55)$$

where $\phi_c$ and $\psi_c$ are the command roll and yaw attiitude, respectively, and are assumed constant. Representing (44) and (46) in terms of $e_x$ and $e_z$, and differentiating the resulting equations along with (48) and (50) yield a set of dynamics where the harmonic external disturbances ($w_x$, $w_z$) are embedded. This system containes uncontrollable modes at $s = 0$ (double pole), $s = \pm j\omega_o$ (double pole), and $s = \pm 2\,j\omega_o$ (double pole) which arise from the external disturbance torque. This means that the external constant disturbance torque and cyclic disturbance torque can be rejected in only two of the four states $e_x$, $e_z$, $h_x$, and $h_z$. In a similar way to the pitch control, these uncontrollable modes can be removed by changing the regulated variables. Tables 2 and 3 show the combination of two states in which the constant disturbance and the cyclic disturbance are rejected, respectively. As shown in Tables 2 and 3, an uncontrollable mode still exists in some of the outputs $e_x$, $e_z$, $h_x$, and $h_z$. Note that it is always $e_x$ that does not reject the cyclic disturbance. However, contrary to the pitch channel where bias in pitch angle can not be regultated, the bias in both yaw and roll angle can be rejected, leaving only an oscillation in the roll angle. In this paper only case 1 for constant disturbance rejection and case 6 for cyclic disturbance rejection are considered.

In order to reject the constant disturbance torque in the attitude channels, the uncontrollable double poles at $s = 0$ are embedded in the CMG-momentum channels by regulating $\dot h_x$ and $\dot h_z$ instead of $h_x$ and $h_z$. Similarly, the uncontrollable double poles at $s = \pm j\omega_o$ and $s = \pm 2j\omega_o$ are embedded in the roll-attitude and yaw CMG-momentum channels to reject the cyclic disturbance torque in yaw-attitude and roll CMG-momentun channels. That is,states representing oscillatory motion as represented by $\xi$ in section 2 are defined.

The dynamic system includes four system parameters, $k_x$, $k_z$, $f_x = I_{xn}/I_x$, and $f_z = I_{zn}/I_z$. However, one of them are represented in terms of others. $f_z$ are represented in terms of $k_x$ $k_z$ and $f_x$ as

$$f_z = \frac{I_{zn}}{I_{xn}} \frac{1+k_z}{1-k_x} f_x. \quad (56)$$

For small variations of $k_x$, $k_y$, and $f_x$, the variation of $f_z$, $\Delta f_z$, is approximated as

$$\Delta f_z \approx k_1 \Delta k_x + k_2 \Delta k_z + k_3 \Delta f_x \quad (57)$$

where

$$k_1 = \frac{I_{zn}}{I_{xn}} \frac{(1+k_{zn})}{(1-k_{xn})^2},\ k_2 = \frac{I_{zn}}{I_{xn}} \frac{1}{1-k_{xn}},\ k_3 = \frac{I_{zn}}{I_{xn}} \frac{1+k_{zn}}{1-k_{xn}} \quad (58)$$

The IFL decomposition is structured with respect to the three parameters $k_x$, $k_y$, and $f_x$.

The controller design design process is described in [6,7]. The closed-loop eigenvalues are

| | |
|---|---|
| -262, -1.75, | -1.05 ± 0.06j |
| -0.10 ± 0.98j | -028 ± 1.09j |
| -0.21 ± 0.06j | -0.23 ± 0.90j |
| -0.10 ± 1.97j | -0.38 ± 2.05j |

where these poles are normalized with respect to the orbital frequency. The largest closed-loop eigenvalues are seen to remain close to the orbital frequency. The stability margins in some specific variations are listed in Table 4. For all type of variations listed in Table 4 except $\Delta_1$, $\Delta_3$, and $\Delta_6$, the designed controller stabilizes the system far beyond the physical limit which means that good performance robustness is achieved for these directional variations. For $\Delta_1$, $\Delta_3$, and $\Delta_6$, 62% stability margin is achieved. Figure 8 shows the time responses for the nominal system and a perturbed system with $\delta = 60\%$ in $\Delta_1$ variation denoted by solid line and dotted line, respectively. With no noticable performance degration, the system appears to have good performance robustness. The constant disturbance torques are rejected in roll-yaw attitude channels while the cyclic disturbance torques are rejected in roll-CMG and yaw attitude channels. The CMG momentum in the roll channel approaches a constant value while the CMG

momentum in the yaw channel oscillates around a constant value. The biased CMG momentum in steady-state can be changed by changing the command attitudes, $\phi_c$ and $\psi_c$. The CMG momentum in roll-yaw channel is unbiased when the command attitudes are set to the torque equilibrium attitude (TEA).

## 6. Robust Hover Control for a Short Take-off/Vertical Landing Aircraft

A robust command tracker is developed for the transition-to-hover mode of a short take/off vertical landing aircraft designated the E7 [10]. The general configuration of the aircraft is shown in figure 1 from [11]. The control design focuses on the longitudinal dynamics alone, which have been shown to be well decoupled from the lateral dynamics. An analysis of the open-loop dynamics using singular vectors shows that the aerodynamic control effectors have sufficient authority at the given flight condition, such that the reaction control system thrusters are not needed.

Handling quality studies have shown that the desired control objective should be to command forward acceleration and flight path angle. Good compensator performance is indicated by good command tracking and decoupling under nominal design conditions and in the face of design uncertainties due to modelling error, dynamic unknowns, and external disturbances. At the very least, the compensator should stabilize the aircraft through all anticipated uncertainty regimes.

For this objective, the game theoretic controller is used. Good robustness with respect to the unmodeled actuator dynamics and for significant uncertainty in the flight conditions, specifically in the Nozzle Pressure Ratio (NPR) is demonstrated. Step command responses for the game theoretic controller show that tracking performance is minimally degraded by variations in the NPR.

### 6.1 System Model

The E7 is a Short Takeoff/Vertical Landing (STOVL) fighter/attack aircraft currently under development at General Dynamics. The conventional aerodynamic control effectors include elevons, ailerons and a rudder. The propulsive control effectors needed at low speeds where there is insufficient aerodynamics control authority include a Reaction Control System (RCS), an Augmented Deflector Exhaust Nozzle (ADEN), a fixed aft nozzle, and an ejector system. The general arrangement of the controls in shown in Figure 9 .

The RCS system consists of a forward thruster for noseup pitch control, a thruster on each wing also for pitch control as well as roll control and two rear thrusters for yaw control. The ADEN nozzle deflects the engine core air from 0 degrees (straight back) to 110 degrees (forward and down). The ejector system splits the engine fan air between the ejectors positioned under each wing root and the fixed aft nozzle. The distribution of the fan air is parameterized by the Mass Split Fraction which is zero when there is no aft nozzle thrust and one when there in no ejector thrust. See [10] for more details.

### 6.2 System Dynamics

The E7 linearized dynamics have been provided as a 16 state combined longitudinal and lateral model. A standard procedure is to decouple these modes by truncation. With conventionally configured aircraft this is usually a good approximation. Four linear, coupled first order differential equations describe the aircraft state dynamics, equations (59) to (67). The associated state derivatives are for now assumed to be known. Six more equations (62)-(67), describe the first-order actuator dyamics.

The longitudinal dynamics of the aircraft model including actuators are completely described by ten coupled linear differential equations. The longitudinal dynamics consist of the state u, w, q and θ which are respectively the perturbed forward body axis velocity, downward body axis velocity, pitch rate and pitch angle. Actuator states are also included as $\delta_e$, pla, k, theta, tpr and tp which are respectively the perturbed elevon angle, pilot lever angle (throttle), mass split fraction, aden nozzle angle, symmetric right and left wing thrusters and nose pitch thruster. The equations coefficients unfortunately have not yet been publicly released but the actuator dynamics and the open loop poles are given in Tables 1 and 2.

$$\dot{u} = U_u u + U_w w + U_q q + U_\theta \theta + U_\delta \delta_e + U_{pla}\, pla + U_k k + U_\theta \theta_n + U_{tpr}\, tpr + U_{tp} tp \quad (59)$$

$$\dot{w} = W_u u + W_w w + W_q q + W_\theta \theta + W_\delta \delta_e + W_{pla}\, pla + W_k k + W_{\theta n} \theta_n + W_{tpr}\, tpr + W_{tp}\, tp$$

$$\dot{q} = Q_u u + Q_w w + Q_q q + Q_\theta \theta + Q_{\delta e} \delta_e + Q_{pla}\, pla + Q_k k + Q_k k + Q_{\theta n} \theta_n + Q_{tpr} tpr + Q_{tp}\, tp \quad (60)$$

$$\dot{\theta} = q \quad (61)$$

$$\dot{\delta}_e = -\omega_{\delta_e} \delta_e + \omega_{\delta e} u_{\delta e} \quad (62)$$

$$\dot{pla} = \omega_{pla}\, pla + \omega_{pla}\, u_{pla} \quad (63)$$

$$\dot{k} = \omega_k k + \omega_k u_k \quad (64)$$

$$\dot{\theta}_n = \omega_{\theta n} \theta_n + \omega_{\theta n} u_{\theta n} \quad (65)$$

$$\dot{tpr} = \omega_{tpr}\, tpr + \omega_{tpr}\, u_{tpr} \quad (66)$$

$$\dot{tp} = \omega_{tp}\, tp + \omega_{tp}\, u_{tp} \quad (67)$$

### 6.3 System Observations

The measured quantities are the forward body axis acceleration $A_x$ and the flight path angle γ. Other inertial measurements such as normal acceleration $A_n$, pitch rate q and pitch angle θ are also available as well as the usual airmass measurements, airspeed V and angle of attack α. An inspection of the observability grammian shows that measureing only the tracked variables $A_x$ and γ is not enough to make a completely observable system.

Experiments with several combinations of measurements showed that the observability grammian is always singular when at least some of the actuator positions are not measured. This is because there are five actuators with identical dynamics (the pilot lever angle has a slower actuator) controlling three airframe states u, w, and q. Unlike many conventional aircraft, most control effectors in the E7 have position sensors so, for a good cause, it may be reasonable to take advantage of them. However, although the system is not completely observable with actuator measurements, it is detectable and it will be shown later that with careful regulator design, actuator measurements are not needed for performance or for stability enhancement.

An expression relating the forward acceleration and the flight path angle to the aircraft states is needed to form the tracking errors. The forward acceleration measured by the accelerometer is given as the sum of the acceleration at

the center of mass of the aircraft and the acceleration relative to the center of mass caused by rotation.

$$A_x = \dot{V}\cos\alpha + V(q - \dot{\alpha})\sin\alpha + \Delta z_{acc}\dot{q} - \Delta x_{acc}q^2 \quad (68)$$

All units are feet, seconds and radians. Since angle-of-attack $\alpha$ is given by the ratio of body axis downward velocity to body axis forward velocity

$$\tan\alpha = W/U, \quad (69)$$

the forward acceleration may be related to the current state variables as

$$A_x = Wq + \dot{u} \quad (70)$$

An expression for forward acceleration is found by combining (13) with the state equation (1) for $\dot{u}$ as

$$A_x = U_u u + U_w W + (W + U_q) q + U_\theta \theta + U_\delta \delta_e + U_{pla}\, pla + U_k\, k + U_{\theta n}\, \theta_n + U_{tpr}\, tpr + U_{tp} tp \quad (71)$$

The assumptions made to get from (68) and (69) to (70) are that pitch rate perturbations q are small so that the $\Delta x_{acc}q^2$ term may be neglected. Also the accelerometer is assumed to be colocated with the center of mass of the aircraft so that the term $\Delta z_{acc}\dot{q}$ is zero.

The flight path angle $\gamma$ is defined as the angle made by the velocity of the aircraft center of mass and the local earth fixed horizontal axis. Thus

$$\gamma = \theta - \alpha \quad (72)$$

If (69) is linearized, a perturbed angle-of-attack is related to the states by

$$\alpha = -(W/V^2)u + (U/V^2)w \quad (73)$$

so that a measurement equation for the flight path angle is

$$\gamma = (W/V^2)u + (U/V^2)w + \theta \quad (74)$$

### 6.4 Regulator Design

Proper formulation of the linear quadratic regulator requires that all states and controls go to zero in steady state. Since the command variables are forward acceleration $A_x$ and flight path angle $\gamma$, a reasonable choice for the design state space would include the commanded forward acceleration error and the commanded flight path angle error, $E_{Ax}$ and $E_\gamma$. First, a transformation from the state space (u, w, q, $\theta$, act) to the state space ($A_x$, $\gamma$, q, $\theta$, act) is a straight-forward but tedious application of (71) to the state equations (59) through (67). Here, the notation act denotes the set of actuators states ($\delta_e$, pla, k, $\theta_n$) where the RCS wings and nose thrusters tpr and tp have been eliminated. Unfortunately, the further transformation from a ($A_x$ $\gamma$, q, $\theta$, act) state space to one involving the tracking errors ($E_{Ax}$, $E_\gamma$, q, $\theta$, act) includes nonzero forcing terms on the error state equations. By differentiating all equations once, constant forcing terms are eliminated. The resulting set of system equations is augmented with the tracking errors $E_{Ax}$ and $E\gamma$ as integrals of the their first derivatives. The effect of the differentiation is to force the regulator to provide integral plus proportional compensation.

Application of the game-theoretic controller to the above equation of motion yields a singular Riccati equation for any choice of state weightings. This is because the system ($E_{Ax}$, $E_\gamma$, $E_{Ax1}$, $q_1$, $\theta_1$, $act_1$) (where the notation subscript 1 denotes the first derivative) is not completely controllable with respect to the controls ($u_{\delta e1}$, $u_{pla1}$, $u_{k1}$, $u_{\theta n1}$). To see this go back to the forward acceleration equation (20) and take the first derivative,

$$A_{x1} = Wq_1 + \dot{u}_1 \quad (75)$$

Taking the first derivative of the state equation for u (59) and substituting for $\dot{u}_1$ in (75) gives

$$A_x = U_u u_1 + U_w w_1 + (W + U_q) q_1 + U_\theta \theta_1 + \sum_{act} U_{act} act_1 \quad (76)$$

But, (59) provides an expression for $u_1$ in terms of $A_x$,

$$u_1 \equiv \dot{u} = A_x - Wq \quad (77)$$

which clearly shows that forward acceleration is linearly dependent on its first integral and the other states as

$$A_{x1} = U_u A_x + U_w w_1 + (W + U_q) q_1 + (U_\theta - U_u W)\theta_1 + \sum_{act} U_{act} act_1 \quad (78)$$

after the state $w_1$ is eliminated in favor of $\gamma_1$. When (78) is rewritten in terms of the error states $E_{Ax}$ and $E_\gamma$ the tracking command reenters the state equations. This cannot be so for proper application of the game-theoretic controller since the states and controls cannot all go to zero for a nonzero tracking command. Therefore, the state equation are differentiated once more, this time with the $E_{Ax1}$ state eliminated through (78). The state space for the game-theoretic controller becomes $\bar{X} = (E_{Ax}, E\gamma, E_{Ax1}, q_2, \theta_2, \delta e_2, pla_2, k_2, \theta n_2)$. The system controls for the game-theoretic controller are $\bar{U} = (u_{\delta e2}, u_{pla2}, u_{k2}, u_{\theta n2})$.

Instead of requiring the system to respond directly to a step command, the use of command prefilters was found to greatly improve the transient response. The first-order prefilters are implemented as

$$\dot{A}_{xc} = -\omega_{Ax}Ax_c + \omega_{Ax}u_{Ax} \quad (79)$$

$$\dot{\gamma} = -\omega_\gamma \gamma_c + \omega_\gamma u_\gamma \quad (80)$$

with $\omega_{Ax} = -2$ and $\omega_\gamma = -2$. The game-theoretic controller design state space $\bar{X}$ is augmented by the second derivative of the prefilter states to produce the final fourteenth-order stabilizable state space.

$$X = (E_{Ax}, E_\gamma, E_{Ax1}, E_{\gamma 1}, \gamma_2, q_2, \theta_2, Ax_{c2}, \gamma_{c2}, \delta e_2, pla_2, k_2, \theta n_2) = (\bar{X}, Ax_{c2}, \gamma_{c2}) \quad (81)$$

### 6.2 Performance of the Game Theoretic Controller to the E-7 Aircraft

In [10] the design procedure and design parameters are given. The closed-loop poles associated with the nominal game-theoretic compensator are given in Table 7. The tracking performance for both nominal and off-nominal flight conditions are evaluated in terms of two unit command inputs: one (1.0) foot per second$^2$ of forward acceleration with no flight path angle change, and one (1.0) degree of flight path angle with no change in forward

acceleration. The response of the commanded states to the acceleration change at the nominal flight condition is plotted in Figure 10. The flight path angle never deviates more than 0.1 degrees from its trim condition, and it settles within four (4) seconds after the command. The forward acceleration response is excellent, exhibiting no overshoot and a settling time of 2-3 seconds. Also note that the integral of the coupling response is quite small, such that the effect of the flight path errors on the aircraft position wil be negligible.

For this game theoretic compensator, the nominal response of the commanded states to the unit flight path step is shown in Figure 11. The peak overshoot is about 15%. The foward acceleration peak coupling is from about -±0.40 feet/second$^2$. The settling times for both the coupling and the commanded flight path angle are between 2 and 3 seconds.

By simulating each command time response at all five values of the nozzle pressure ratio (0.2, 0.225, 0.25, 0.275, 0.3), both stability and performance robustness are analyzed for the game-theoretic compensator. The responses at each flight condition to the forward acceleration command are displayed together in Figure 12, and the responses to the flight path angle are shown in Figure 13. Stability of the closed-loop system is verifed for the entire range of uncertainty in the nozzle pressure ratio. Additionally, the performance of the nominal tracker is almost duplicated for the four off-nominal responses to the forward acceleration command. This result indicates that the closed-loop modes which dominate the acceleration response have been desensitized to the dynamic parameters which vary with the nozzle pressure uncertainty. The settling times remain essentially constant across the NPR range. In Figure 13, some degradation of the overshoot of flight path angle may be seen for decreased values of NPR. As much as 25% overshoot is evident in one off-nominal response. However, the coupling into forward acceleration actually improves in some of the off-nominal simulations, and the settling times of both the decoupling and the tracking are not degraded with respect to the parameter uncertainty. These characteristics seem to occur in the game-theoretic compensator, which explicitly includes the expected uncertainties in the gain calculations.

## 7. Conclusions

The game theoretic controller and the IFL decomposition have been described and illustrated. Complex examples have been used to illustrate the robustness of this system. These examples include the two-mass spring system with a harmonic disturbance. The spring constant was assumed unknown. The momentum management and attitude control system for the space with harmonic inputs. Here, the moments of inertia were uncertain. Finally, the VSTOL aircraft controller was designed using this methodology where the nozzle pressure ratio was uncertain. In each of these cases, a state space that was stabilizable had to be determined. This is critical in obtaining a rational compensator design. This process usually meant inserting integrations so the the effective multivariable controller was essential a PI compensator.

## References


1. I. Rhee and J.L. Speyer, "A Game Theoretic Controller and Its Relationship to H-infinity and Linear-Exponential -Gaussian Synthesis", Proc. of 28th IEEE Conference on Decision and Control, Dec. 1989.

2. I. Rhee and J.L. Speyer, "A Game Theoretic Approach to a Finite-Time Disturbance Attenuation Problem", to be published in the IEEE Transaction on Automatic Control.

3. A.E. Bryson and Y. -C. Ho, *Applied Optimal Control*, Hemisphere Publishing Corporation, 1975

4. I. Rhee and J.L. Speyer, "Application of a Game Theoretic Controller to a Benchmark Problem", Proceedings of the 1990 American Controls Conference.

5. M. Tahk and J.L. Speyer, "Modeling of Parameter Variations and Asymptotic LQG Synthesis, "IEEE Trans. on Automatic Control, Vol. AC-32, No. 9, Sept. 1987.

6. I. Rhee and J.L. Speyer, "A Game Theoretic Controller for a Linear Time-Invariant System with Parameter Uncertainty and Its Application to the Space Station", Proceedings of the 1990 Guidance and Control Conference, August 1990.

7. I. Rhee and J.L. Speyer, "A Robust Momentum Management and Attitude Control System for the Space Station", to be published in the AIAA Journal of Guidance, Control and Dynamics.

8. P.C. Hughes, *Spacecraft Attitude Dynamics*, John Wiley and Sons, 1986.

9. B. Wie, K.W. Byun, V.W. Warren, D. Geller, D. Lang and J. Sumkel, "New Approach to Attitude/Momentum Control of the Space Station", AIAA Journal of Guidance, Control, and Dynamics, Vol. 12, No. 5, Sept-Oct 1989.

10. R.K. Douglas, S.A. Mackler, J.L. Speyer, "Robust Hover Control for a Short Take-off/Vertical Landing Aircraft", Proceeding of the 1990 AIAA Guidance and Control Conference, August 1990.



## Acknowledgement

This research was partly supported by the Air Force Office of Scientific Research under Grant No. AFOSR 91-0077 and NASA Johnson Space Flight Center.


Table 1: Variation type and physical limit of variation due to the triangular inequality

| Variation Type $(\Delta_i = [\Delta I_x \ \Delta I_y \ \Delta I_z])$ | Physical Bound of $\delta$ |
|---|---|
| $\Delta_1 = \delta[\ I_{xn}\ I_{yn}\ I_{zn}\ ]$ | $-100.0\% < \delta < \infty$ |
| $\Delta_2 = \delta[\ -I_{xn}\ I_{yn}\ I_{zn}\ ]$ | $-15.9\% \leq \delta \leq 2.6\%$ |
| $\Delta_3 = \delta[\ I_{xn}\ -I_{yn}\ I_{zn}\ ]$ | $-81.9\% \leq \delta \leq 13.1\%$ |
| $\Delta_4 = \delta[\ I_{xn}\ I_{yn}\ -I_{zn}\ ]$ | $-2.1\% \leq \delta \leq 19.5\%$ |
| $\Delta_5 = \delta[\ 0\ I_{yn}\ I_{zn}\ ]$ | $-27.5\% \leq \delta \leq 5.3\%$ |
| $\Delta_6 = \delta[\ I_{xn}\ 0\ I_{zn}\ ]$ | $-90.0\% \leq \delta \leq 30.3\%$ |
| $\Delta_7 = \delta[\ I_{xn}\ I_{yn}\ 0\ ]$ | $-4.1\% \leq \delta \leq 48.4\%$ |
| $\Delta_8 = \delta[\ 0\ -I_{yn}\ I_{zn}\ ]$ | $-40.0\% \leq \delta \leq 3.6\%$ |
| $\Delta_9 = \delta[\ -I_{xn}\ 0\ I_{zn}\ ]$ | $-17.5\% \leq \delta \leq 2.3\%$ |
| $\Delta_{10} = \delta[\ -I_{xn}\ I_{yn}\ 0\ ]$ | $-31.3\% \leq \delta \leq 6.4\%$ |

Table 2: Rejection of the constant disturbance torque for roll-yaw axes

| Case | States | Uncontrollable mode in resulting system |
|---|---|---|
| 1 | $e_x$, $e_z$ | none |
| 2 | $h_x$, $h_z$ | none |
| 3 | $e_x$, $h_x$ | none |
| 4 | $e_z$, $h_z$ | none |
| 5 | $e_x$, $h_z$ | $s = 0$ |
| 6 | $h_x$, $e_z$ | $s = 0$ |

Table 3: Rejection of the cyclic disturbance torque for roll-yaw axes

| Case | States | Uncontrollable mode in resulting system |
|---|---|---|
| 1 | $e_x$, $e_z$ | $s = \pm j\omega_o$ |
| 2 | $h_x$, $h_z$ | none |
| 3 | $e_x$, $h_x$ | $s = \pm j\omega_o$ |
| 4 | $e_z$, $h_z$ | $s = \pm 2j\omega_o$ |
| 5 | $e_x$, $h_z$ | $s = \pm j\omega_o$ |
| 6 | $h_x$, $e_z$ | none |

Table 4: Stability margin for variations in δ.

| Variation Type | Lower & upper margin of $\delta$ | |
|---|---|---|
| | Pitch | Roll-Yaw |
| $\Delta_1$ | $-99\% \leq \delta \leq 82\%$ | $-90\% \leq \delta \leq 75\%$ |
| $\Delta_2$ | $-7\%^a \leq \delta \leq 19\%$ | $-90\% \leq \delta \leq 99\%$ |
| $\Delta_3$ | $-99\% \leq \delta \leq 99\%$ | $-62\% \leq \delta \leq 56\%$ |
| $\Delta_4$ | $-22\% \leq \delta \leq 7\%^a$ | $-73\% \leq \delta \leq 63\%$ |
| $\Delta_5$ | $-14\%^a \leq \delta \leq 33\%$ | $-99\% \leq \delta \leq 99\%$ |
| $\Delta_6$ | $-99\% \leq \delta \leq 99\%$ | $-73\% \leq \delta \leq 66\%$ |
| $\Delta_7$ | $-51\% \leq \delta \leq 16\%^a$ | $-99\% \leq \delta \leq 99\%$ |
| $\Delta_8$ | $-14\%^a \leq \delta \leq 43\%$ | $-62\% \leq \delta \leq 66\%$ |
| $\Delta_9$ | $-7\%^a \leq \delta \leq 20\%$ | $-74\% \leq \delta \leq 89\%$ |
| $\Delta_{10}$ | $-16\%^a \leq \delta \leq 37\%$ | $-99\% \leq \delta \leq 99\%$ |

Table 5: E7 First-order Actuator Data

| (all units are radians/sec) | | | | | |
|---|---|---|---|---|---|
| $\omega_{\delta_a}$ | = | 20.0 | $\omega_{pla}$ | = | 1.0 |
| $\omega_k$ | = | 20.0 | $\omega_{\theta_n}$ | = | 20.0 |
| $\omega_{tpr}$ | = | 20.0 | $\omega_{tp}$ | = | 20.0 |

Table 6: E7 Open-Loop Poles

| Mach = 0.1, Altitude = 100 feet, NPR = 0.25 (radians/sec) | | |
|---|---|---|
| $s_1$ | = | 0.4599 |
| $s_2$ | = | -0.4686 |
| $s_{3,4}$ | = | -0.4299 ± i0.3840 |
| $s_5$ | = | -1.000 |
| $s_{6-10}$ | = | -20.00 |

Table 7: Game-Theoretic Closed-Loop Poles

| | | |
|---|---|---|
| $s_1$ | = | -0.0 |
| $s_2$ | = | -0.1660 |
| $s_3$ | = | -0.9834 |
| $s_4$ | = | -1.0170 |
| $s_5$ | = | -1.0954 |
| $s_6$ | = | -1.7413 |
| $s_7$ | = | -1.8997 |
| $s_{8,9}$ | = | -2.00 |
| $s_{10}$ | = | -2.0497 |
| $s_{11}$ | = | -2.4363 |
| $s_{12}$ | = | -5.9921 |
| $s_{13}$ | = | -6.2625 |
| $s_{14,15}$ | = | -3.3261 ± i5.4482 |
| $s_{16,17}$ | = | -5.1934 ± i4.9756 |
| $s_{18,19}$ | = | -20.00 |
| $s_{20}$ | = | -20.1969 |
| $s_{21,22}$ | = | -18.2501 ± i12.3112 |
| $s_{23,24}$ | = | -14.8304 ± i16.3966 |
| $s_{25}$ | = | -25.5644 |
| $s_{26,27}$ | = | -21.8026 ± i17.3338 |

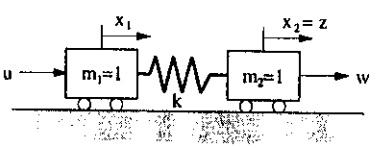


Figure 1: Mass-spring system

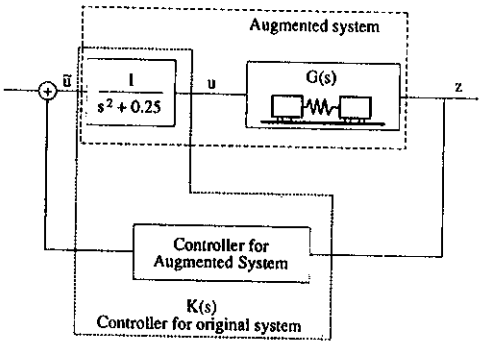


Figure 2: Block diagram of closed loop system

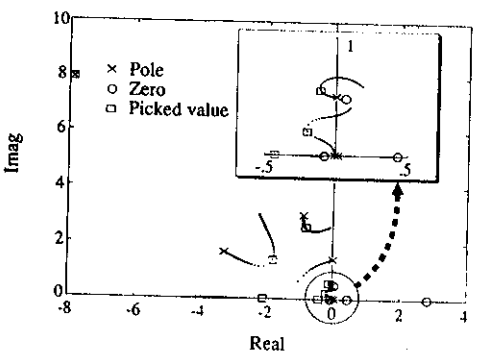


Figure 3: Root locus of 1 - αG(s)K(s) with respect to α

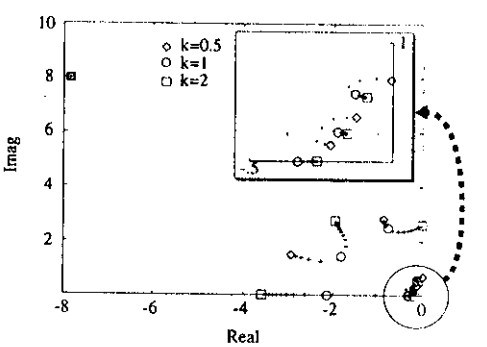


Figure 4: Root locus of closed loop system with respect to k

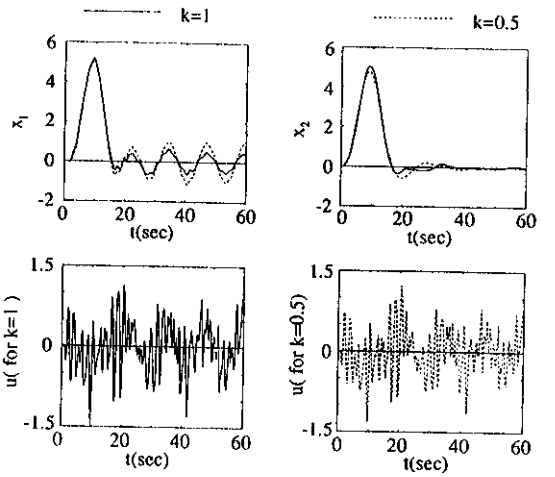


Figure 5: Time response

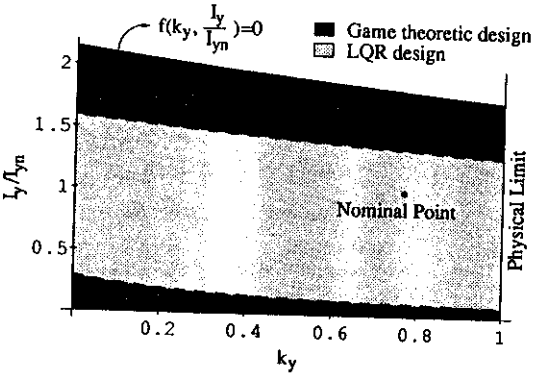


Figure 6: Comparison of stable region for pitch control

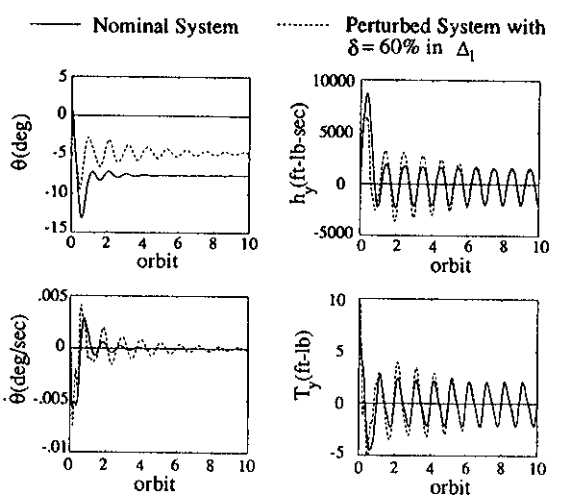


Figure 7: Time response for pitch axis

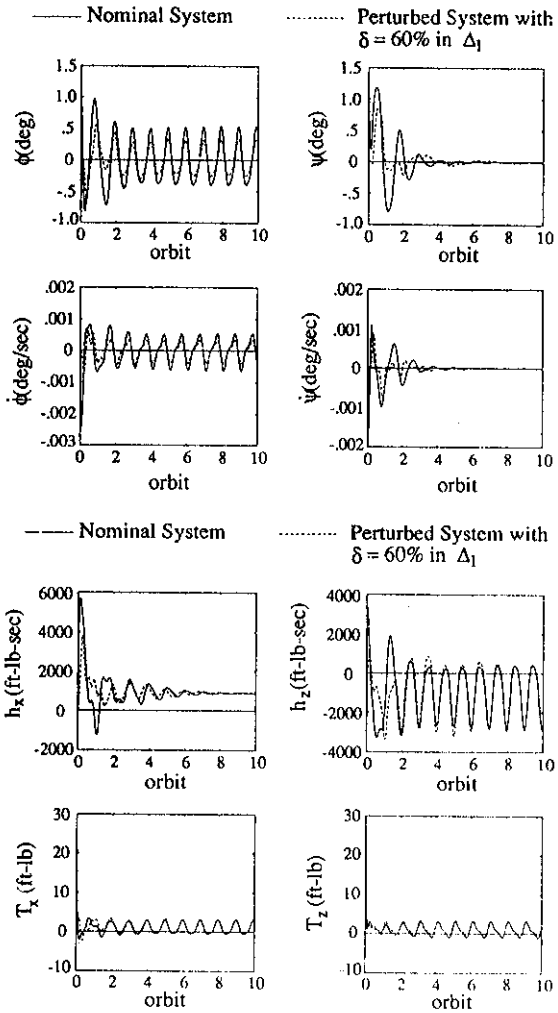


Figure 8: Time response for roll-yaw axis

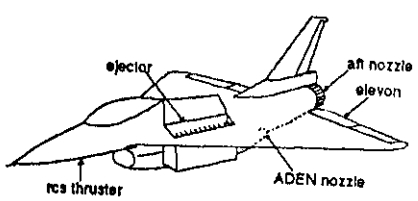


Figure 9: E7 Geometry

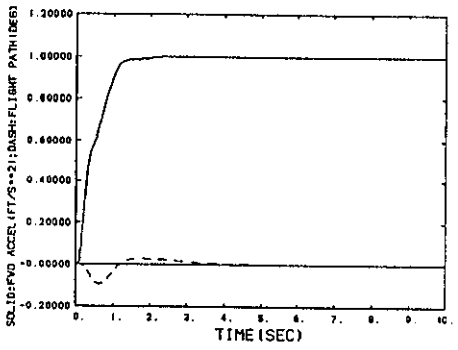


Figure 10: E7 Step Forward Acceleration Response

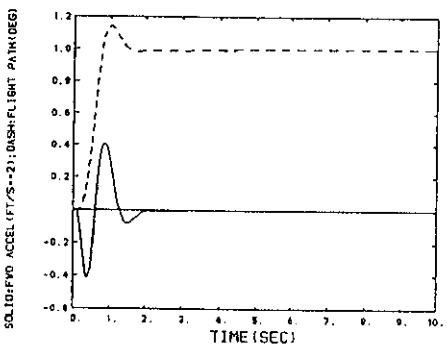


Figure 11: E7 Step Flight Path Angle Response

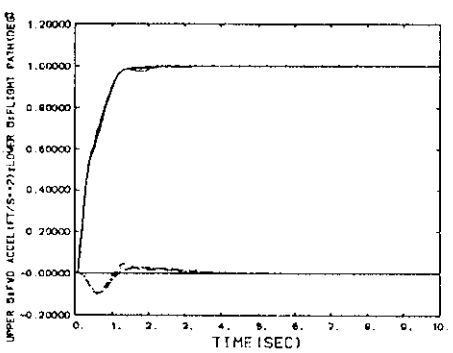


Figure 12: E7 Step Forward Acceleration Responses, all NPR

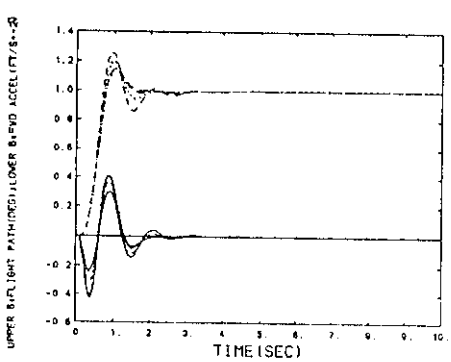


Figure 13: E7 Step Flight Path Angle Response, all NPR

# An Efficient Solution Procedure for the Thermoelastic Analysis of Truss Space Structures

D. Givoli and O. Rand
Faculty of Aerospace Engineering
Technion-Israel Institute of Technology
Haifa 32000, Israel

## Abstract

A solution procedure is proposed for the thermal and thermoelastic analysis of truss space structures in periodic motion. In this method, the spatial domain is first discretized using a consistent finite element formulation. Then the resulting semi-discrete equations in time are solved analytically by using Fourier decomposition. Geometrical symmetry is taken advantage of completely. An algorithm is presented for the calculation of heat flux distribution. The method is demonstrated via a numerical example of a cylindrically shaped space structure.

## Introduction

The thermal and structural design and analysis of large space structures have caught much attention in the last few years. Space structures are typically three dimensional truss-type structures which are exposed to thermal loading in the form of solar radiation, infra-red planetary radiation and planetary albedo (solar radiation reflected from planets). Finding the spatial and temporal variation of the temperature field in the structure resulting from this radiation is important for the thermal design. In addition, the dynamic temperature field may also give rise to the dynamic deformation of the structure. This deformation is of interest due to the limitations on the allowed magnitude of the deflection of instruments and antennas, and due to the necessity to avoid a resonance.

Works that have dealt with this subject may be divided roughly into two categories: those which are concerned with general concepts and preliminary design issues, and those which involve an accurate analysis of a specific type of model. The former type of works include Refs. 1-10. Foldes and Dienemann [1] and Archer [2] discuss the performance requirements for large multibeam antenna systems, and the considerations involved in the design of the reflectors used with these systems. Based on these considerations, Clark and Allen [3] describe the evolution of the Hughes HS 376 reflector thermal design. Mikulas et al. [4] describe some design concepts for the space station truss station, and consider several approaches regarding the construction of the structure in space. Nash and Lardner [5] discuss the relative importance of the various factors influencing the mechanical response of large space structures. They consider both truss structures and thin membranes. Anderson and Nimmo [6] propose to use statically determinate trusses for large platforms, and compare the frequencies of such trusses with those of redundant ones. Ard [7] and Hedgepeth and Miller [8] discuss structural concepts of large parabolic antenna reflectors or solar concentrators, and especially design concepts for deployable reflectors. Peskett and Gethin [9] consider various aspects of the thermal design and analysis of a spacecraft, including the derivation of the thermal loading. They also perform a case study analysis of an orbiting structure. Ory et al. [10] consider in detail some preliminary design aspects for large orbiting platforms, and propose two alternative structural configurations.

References 11-16 belong to the second type of works, which involve accurate computer analysis. Thornton et al. [11] describe an integrated thermal-structural finite element formulation with solar radiation, and use a three member module of an orbiting truss as a testing model. Thornton and Paul [12] review the subject of computerized thermal- structural analysis of large space structures, and use for illustration a tetrahedral truss structure as a model for a microwave radiometer system. Mahaney and Thornton [13] investigate the effects of self-shadowing on the thermal-structural behavior of space structures. Their numerical experiments indicate that such effects are significant, and must be included in the calculations. Ko [14] describes in detail the thermal and elastic analyses performed for the space shuttle orbiter, including internal convection and radiation effects. Thermal stresses are found to be very sensitive to variation in temperature distribution.

Lutz et al. [15] propose to use different finite element models for the thermal and structural analyses of a frame-type structure. The temperature field is first determined at selected cross sections of some of the beam members, via a two-dimensional

finite element analysis. The forces and moments due to this temperature distribution are then calculated, and the global structural response of the structure is obtained from the finite element model of the three dimensional frame.

## The Proposed Method

Rand and Givoli [16] propose a numerical method for thermal and elastic problems with periodic loading, which combines finite element spatial decomposition and spectral treatment in time. The method is proposed as a basis for the analysis of large space structures, although an actual space structure model was not considered. The solution procedure is shown to be superior in many cases to standard time-integration techniques.

Here the method developed in Rand and Givoli [16] is extended. The extensions have to do with the exploitation of geometrical symmetry, and with the development of a general algorithm for computing "view factors". These two aspects will be discussed in more detail in Givoli and Rand [17].

Consider a three-dimensional truss structure exposed to a time-periodic incoming heat flux, with a period of $2\pi/\omega$. This periodicity may originate, for example, from the fact that the structure orbits around the earth or that it rotates around a certain axis. Each truss member emits radiation to space. The incident heat flux gives rise to a time-dependent temperature field, which in turn induces the dynamic deformation of the structure. In each truss member, the temperature field $\tau$ is governed by the nonlinear equation,

$$\rho c \frac{\partial \tau}{\partial t} = \frac{\partial}{\partial s}\left(k \frac{\partial \tau}{\partial s}\right) - C_R \tau^4 + q \ , \qquad (1)$$

whereas the displacement field u is governed by the linear equation,

$$\rho A \frac{\partial^2 u}{\partial t^2} = \frac{\partial}{\partial s}\left\{EA\left[\frac{\partial u}{\partial s} - \alpha(\tau - T_{ref})\right]\right\} . \qquad (2)$$

In the case where the structure spins, the axial component of the centrifugal force $\rho A\omega^2 r$ (where r is the distance from the axis of spin) is added to the right hand side of Eq. (2).

The consistent finite element discretization of Eqs. (1) and (2), leads to the two following systems of ordinary differential equations in time:

$$\text{Thermal:} \qquad \mathbf{G}\dot{\mathbf{T}}(t) + \mathbf{P}\mathbf{T}(t) + \mathbf{R}(\mathbf{T}(t)) = \mathbf{Q}(t) \qquad (3)$$

$$\text{Elastic:} \qquad \mathbf{M}\ddot{\mathbf{d}}(t) + \mathbf{K}\mathbf{d}(t) = \mathbf{F}(t) \ . \qquad (4)$$

In Eq. (4) the vector $\mathbf{T}$ contains the unknown temperatures at the nodes, and the vector $\mathbf{R}$ depends nonlinearly on it. In Eq. (5) $\mathbf{d}$ contains the unknown displacements at the nodes in the directions x, y and z. A dot indicates differentiation with respect to time. In both Eqs. (3) and (4) periodic solutions with period $2\pi/\omega$ are sought.

The system (3) has to be solved first for the temperature vector $\mathbf{T}(t)$. Then $\mathbf{T}(t)$ is substituted in the right hand side of Eq. (4), which is solved to yield the displacement vector $\mathbf{d}(t)$. The number of equations in (3) and the number of equations in (4) depend on the finite element models chosen for the thermal and elastic problems, and on the number and type of boundary conditions imposed. For later reference, let $M_T$ and $M_d$ be the number of equations in (3) and (4), respectively.

The method of solution of Eqs. (3) and (4) is based on the discrete Fourier decomposition of each time-dependent function in Eqs. (3) and (4) into a finite number of harmonics, N. In other words, if $\mathbf{f}(t)$ is any vector variable appearing in Eqs. (3) or (4), then it is approximately represented by the finite Fourier expansion,

$$\mathbf{f}(t) \simeq \mathbf{f}_0 + \sum_{n=1}^{N} (\mathbf{f}_{cn} \cos n\varphi + \mathbf{f}_{sn} \sin n\varphi). \qquad (5)$$

Here $\mathbf{f}_0$, $\mathbf{f}_{cn}$ and $\mathbf{f}_{sn}$ (n=1,..,N) are real constant vectors, and $\varphi$ is nondimensional time or azimuth angle, $\varphi=\omega t$. Expressions such as Eq. (5) are used for all the variables in Eqs. (3) and (4). The coefficients $\mathbf{Q}_0$, $\mathbf{Q}_{cn}$ and $\mathbf{Q}_{sn}$, as well as $\mathbf{F}_0$, $\mathbf{F}_{cn}$ and $\mathbf{F}_{sn}$, associated with the thermal and elastic load vectors $\mathbf{Q}$ and $\mathbf{F}$, are found using a Fast Fourier Transform (FFT) scheme. Then, from Eqs. (3) and (4) one obtains a system of algebraic equations for the unknown coefficient vectors $\mathbf{T}_0$, $\mathbf{T}_{cn}$, $\mathbf{T}_{sn}$, $\mathbf{d}_0$, $\mathbf{d}_{cn}$, $\mathbf{d}_{sn}$. All the calculations involving arithmetic manipulation of the Fourier series representations (5) are performed *symbolically* by the computer code itself, in the manner explained in Rand and Givoli [16] and Givoli and Rand [17]. Equation (3) yields a

nonlinear algebraic system of $M_T(2N+1)$ equations and unknowns, which is solved via a Newton-Raphson type iterative procedure, whereas Eq. (4) yields a linear algebraic system of $M_d(2N+1)$ equations and unknowns, which is solved by standard Gauss elimination.

The comparison of this method to the standard time-integration of Eqs. (3) and (4) using finite differences in time is discussed in detail in Rand and Givoli [16]. The proposed method is shown to be superior in many cases. Another advantage that the present method has is the ability to incorporate and exploit structural symmetry in a very simple and natural manner, as shown next.

Concentrating first on the thermal analysis, we note that many geometrical configurations of space structures possess a certain kind of symmetry, which will be defined as follows. Suppose that the total set of finite element nodes may be divided into a number of subsets, each subset having what may be termed "delayed equivalence" among its members. This means that any two nodes i and j belonging to the same subset have the same temperature with a constant time delay between them. In other words, if $T_i(t)$ and $T_j(t)$ are the temperatures of nodes i and j respectively, then $T_i(t)=T_j(t-\tau_{ij})$, where $\tau_{ij}$ is a constant time delay depending on i and j. In terms of the azimuth angle $\varphi$, there is a constant phase shift between the two nodes: $T_i(\varphi)=T_j(\varphi-\Delta\varphi_{ij})$, where $\Delta\varphi_{ij}$ is the constant difference in phase between nodes i and j.

It is easy to see that this type of symmetry may be exploited in the present method, since phase shift constants are simply translated into multiplying factors in the final system of equations (e.g. $\sin(\varphi+\Delta\varphi_{ij})=(\cos\Delta\varphi_{ij})\sin\varphi+(\sin\Delta\varphi_{ij})\cos\varphi)$). All the unknowns associated with a certain node can be expressed in terms of the corresponding unknowns associated with the representative node of the same group. Doing this may lead to a significant reduction in computational cost and in required storage.

A similar technique can be applied in the elastic analysis. One should note, however, that in the elastic case the degrees of freedom, not the nodes, have the phase shift relations between them. These relations involve vector transformation between the displacements in the fixed global coordinate system and the displacements expressed in a local coordinate system rotating with the structure.

Whether the space structure rotates around a certain axis or orbits around the earth, the orientation of each truss member changes in time with respect to the direction of the incoming solar heat flux vector, $\mathbf{q}_{sun}$. Other external sources of heat flux are earth-emitted and earth-reflected radiation, but for simplicity only solar radiation will be considered here. Let $\mathbf{q}_{sun}=q_{sun}\mathbf{b}$, where $q_{sun}$ is the magnitude of the solar radiation and $\mathbf{b}$ is a fixed unit vector indicating its direction. If $q_i$ denotes the external normal heat flux that member i absorbs, then generally

$$q_i(t) = \alpha_s \frac{p}{A} \beta_i(t) q_{sun} , \qquad (6)$$

where $\alpha_s$ is the surface absorptivity, p/A is the circumference-area ratio of the cross-section, and $\beta_i$ is the so-called *view factor* associated with member i (and with the sun).

Typically, there are four types of truss members: members which are parallel to the axis of rotation z, members which are vertical to z, diagonal members and internal members which are never exposed to solar radiation. The graph of $\beta_i$ for a "vertical member" is that of a truncated sine, the one for a "parallel member" has a step-function character, while the graph for a diagonal member lies between the former two. There is, of course, a phase-angle shift between the view factors of two truss members of the same type.

For a large and complicated space structure, the calculation of the view factor $\beta_i(t)$ for each truss member is best done automatically as a preprocess before the analysis. The following algorithm performs this calculation for a general rotating space structure. It is assumed that the coordinates of the joints are given in a fixed reference Cartesian system (X,Y,Z), where Z is the axis of rotation, and that there are a total number of $N_{tm}$ members in the truss.

**Algorithm for computing view factors for a general rotating space structure:**

(1) Given: the solar radiation vector $\mathbf{q}_{sun}=q_{sun}\mathbf{b}$, the angular velocity $\omega$, the reference coordinates of all the joints. Set i=0.

(2) Advance the member number, i←i+1. If $i>N_{tm}$ stop.

(3) Determine the reference coordinates of the two joints of member i: $(X_1, Y_1, Z_1)$ and $(X_2, Y_2, Z_2)$. Determine also whether member i belongs to an opaque part or to a transparent part of the structure and whether it is external or internal.

(4) If member i belongs to an opaque part of the structure and it is internal, set $\beta_i=0$, and go back to step 2.

(5) For j=1,2 calculate:

$$R_j = \sqrt{X_j^2+Y_j^2} \quad ; \quad \Phi_i = \arctan Y_j/X_j$$

$$x_j(t)=R_j\cos(\omega t+\Phi_j) \; ; \; y_j(t)=R_j\sin(\omega t+\Phi_j) \; ; \; z_j=Z_j$$

(6) Calculate:

$$\mathbf{r}(t) = (x_1(t) + x_2(t), \quad y_1(t) + y_2(t), \quad 0)$$

$$\mathbf{s}(t) = (x_2(t) - x_1(t), \quad y_2(t) - y_1(t), \quad z_2 - z_1)$$

$$A(t) = s_2(t)b_3 - s_3b_2$$

$$B(t) = s_3b_1 - s_1(t)b_3$$

$$C(t) = s_1(t)b_2 - s_2(t)b_1$$

$$\mathbf{n}(t) = (-C(t)s_2(t) + B(t)s_3,$$

$$-A(t)s_3 + C(t)s_1(t), \; -B(t)s_1(t) + A(t)s_2(t))$$

$$\mathbf{e}(t) = \mathbf{n}(t)/|\mathbf{n}(t)|\,\mathrm{sign}[\mathbf{r}(t)\cdot\mathbf{n}(t)]$$

$$\lambda(t) = \mathbf{b}\cdot\mathbf{e}(t)$$

(7) If member i belongs to a transparent part of the structure, then

$$\beta_i(t) = |\lambda(t)| \; .$$

Otherwise,

$$\beta_i(t) = \begin{cases} |\lambda(t) & ; \text{ if } \lambda(t)<0 \\ 0 & ; \text{ if } \lambda(t)\geq 0 \end{cases}$$

(8) Next i (go back to step 2).

The algorithm given above together with Eq. (6) determines the function $q_i(t)$, i.e. the external thermal loading on each truss member. This function is incorporated in an FFT routine for the calculation of the Fourier coefficients $Q_0$, $Q_{cn}$ and $Q_{sn}$, for n=1,...,N, as mentioned before.

For a more detailed analysis, see Givoli and Rand [17].

## Numerical Example

One model used to demonstrate the performance of the numerical method is that of a cylindrically shaped space structure made of a composite graphite-epoxy material and spinning around its axis. The structure is shown in Fig. 1. The two ends of the cylinder are assumed to be fixed to rigid bases, so that they are constrained to rotate without deformation. The thermal and mechanical properties of graphite-epoxy are: $\rho c=1.76\cdot10^6$ J/m$^3$ $^\circ$K, k=10.1 W/m $^\circ$K, $C_R=9.1\cdot10^{-7}$ W/m$^3$ $^\circ$K$^4$, $\alpha_s=0.92$, $\rho A=51.3$ kg/m, $EA=1.41\cdot10^6$ N, $\alpha=7.3\cdot10^{-7}$ 1/$^\circ$K. Other parameters are $q_{sun}=1300$ W/m$^2$, $T_{ref}=299^\circ$K, and $p/A=20$ m$^{-1}$. The cylinder is of length 6m and radius 1.4m. Each truss member is represented by one finite element with linear shape functions.

The thermal analysis is considered first. Although the structure contains 50 joints, the temperatures at only three of them are independent unknowns, since the rest of the nodes are equivalent to one of these three in the sense of a "delayed equivalence". In the present model, nodes 1, 2 and 3 in Fig. 1 were chosen as representative nodes.

The structure is assumed to be covered with an opaque material, so self-shadowing effects are present. The angular speed is set to $\omega=10^{-5}$ rad/sec, namely the structure rotates very slowly. In Fig. 2

the solution at the three representative nodes is shown. The temperature in the unshaded region is $400^{\circ}K$, whereas it reaches a minimum value of about $100^{\circ}K$ in the shaded region. Thus, with an angular velocity of $\omega=10^{-5}$ rad/sec the temperature is undergoing large variations in time and in the spatial circumferential direction. On the other hand, it is clear that the variation of temperature along the axial direction z (which manifests itself in the difference between the temperatures at nodes 1, 2 and 3) is small.

The thermal analysis is now repeated with higher and lower values of $\omega$. It turns out that the temperature distribution of Fig. 2 remains unchanged when $\omega$ is decreased, and in fact the same solution is practically obtained for the quasi-steady state $\omega=0$. On the other hand, increasing $\omega$ above the value of $10^{-3}$ rad/sec makes the variations in the temperature field smaller. This can be seen in Fig. 3 where the solutions corresponding to angular speeds of $\omega=10^{-5}$ rad/sec, $\omega=10^{-4}$ rad/sec and $\omega=10^{-3}$ rad/sec are shown. For the case $\omega=10^{-3}$ the temperature is almost constant ($330^{\circ}K$). This can be regarded as the "fully-dynamic" state; the structure spins so fast that no significant temperature differences develop between the shaded and unshaded regions.

Now we turn to the thermoelastic analysis of the structure, based on the temperature field just found. The delayed-equivalence symmetry is exploited here as well. In fact there are only 225 unknowns out of the 2250 unknowns that one would have if symmetry was not taken advantage of. This obviously leads to great saving in computational effort and storage requirements.

We consider the case where the structure is opaque, and rotating with $\omega=10^{-5}$ rad/sec. Figure 4 shows the deformed mesh at time $t=0$ (which is identical to the deformation at times $t=2\pi/\omega$, $t=4\pi/\omega$, etc., due to the periodicity of motion). The displacements are magnified by a factor of 200. The self-shadowing effect is apparent in the figure: the part of the structure exposed to solar radiation at time $t=0$ expands much more than the shaded part of the structure, which gives rise to the unsymmetrical deformation observed.

For additional numerical examples see Givoli and Rand [17].


### Acknowledgements

This work was supported in part by the L. Kraus Research V.P.R. Fund.


### References


1. Foldes, P. and Dienemann, M.W., "Large Multibeam Antennas for Space", *J. Spacecraft and Rockets*, **17**, 1980, pp. 363-371.

2. Archer, J.S., "High Performance Parabolic Antenna Reflectors", *J. Spacecraft and Rockets*, **17**, 1980, pp. 20-26.

3. Clark, S.C. and Allen, G.E., "Thermo-Mechanical Design and Analysis System for the Hughes 76-in. Parabolic Antenna Reflector", *Spacecraft Thermal Control, Design and Operation*, H.E. Collicott and P.E. Bauer, eds., AIAA publication, N.Y., 1983.

4. Mikulas, M.M., Croomes, S.D., Schneider, W., Bush, H.G., Nagy, K., Pelischek, T., Lake, M.S. and Wesselski, C., "Space Station Truss Structures and Construction Considerations", NASA Technical Report 86338, NASA Langley Research Center, Hampton, 1985.

5. Nash, W.A. and Lardner, T.J., "Parametric Investigation of Factors Influencing the Mechanical Behavior of Large Space Structures", AFOSR Report No. TR-86-0858, 1985.

6. Anderson, M.S. and Nimmo, N.A., "Determinate Space-Truss Platforms", 26th Structures, Structural Dynamics and Materials Conf., Part 2, AIAA Publication, N.Y., 1985, pp. 723-728.

7. Ard, K.E., "Design and Technology Study for Extreme Precision Antenna Structures", NASA Contractor Report CR-174861, NASA Lewis Res. Center, Cleveland, 1985.

8. Hedgepeth, J.M. and Miller, R.K., "Structural Concepts for Large Solar Concentrators", *Acta Astro.*, **17**, 1988, pp. 79-89.

9. Peskett, S.C. and Gethin, D.T., "Thermal Analysis of Spacecraft", *Numerical Methods in Thermal Problems*, eds. R.W. Lewis & K. Morgan, Vol. VI, Part 1, Pineridge Press, 1989, pp. 713-729.

10. Ory, H., Menking, M., Hornung, E. and Erben, E., "Development of Large Orbital Structure Systems", 40th Congress of the IAF, Paper No. IAF-89-340, Beijing, China, 1989.

11. Thornton, E.A., Dechaumphai, P. and Wieting, A.R., "Integrated Finite Element Thermal-Structural Analysis with Radiation Heat Transfer", 23rd Structures, Structural Dynamics and Materials Conf., Part 1, AIAA Publication, 1982, pp. 188-196.

12. Thornton, E.A. and Paul, D.B., "Thermal-Structural Analysis of Large Space Structures: An Assessment of Recent Advances", *J. Spacecraft and Rockets*, **22**, 1985, pp. 385-393.

13. Mahaney, J. and Thornton, E.A., "Self-Shadowing Effects on the Thermal-Structural Response of Orbiting Trusses", *J. Spacecraft and Rockets*, **24**, 1987, pp. 342-348.

14. Ko, W.L., "Solution Accuracies of Finite Element Reentry Heat Transfer and Thermal Stress Analysis of Space Shuttle Orbiter", *Int. J. Num. Meth. Engrg.*, **25**, 1988, pp. 517-543.

15. Lutz, J.D., Allen, D.H. and Haisler, W.E., "Finite-Element Model for the Thermoelastic Analysis of Large Composite Space Structures", *J. Spacecraft*, **24**, 1987, pp. 430-436.

16. Rand, O. and Givoli, D., "A Finite Element Spectral Method With Application to the Thermo-elastic Analysis of Space Structures", *Int. J. Num. Meth. Engrg.*, **30**, pp. 291-306, 1990.

17. Givoli, D. and Rand, O., "Thermoelastic Analysis of Space Structures in Periodic Motion", to appear in *AIAA J. Spacecraft and Rockets*.


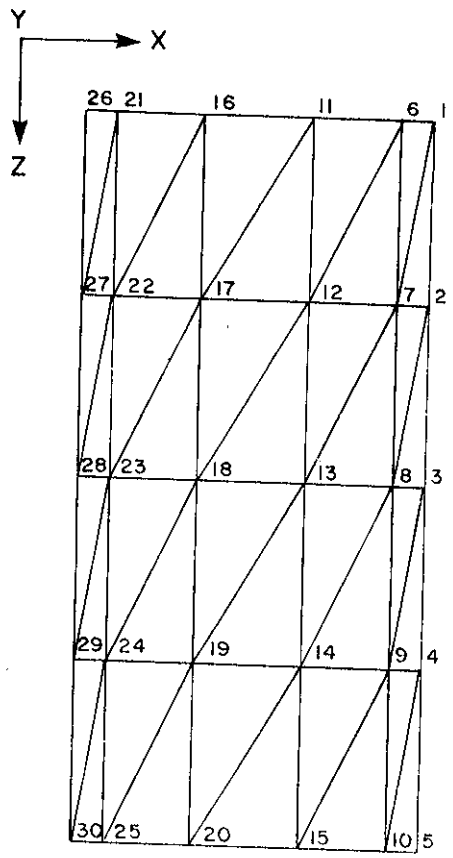


Fig. 1. The cylindrically shaped truss model. Each truss member is represented by a single finite element.

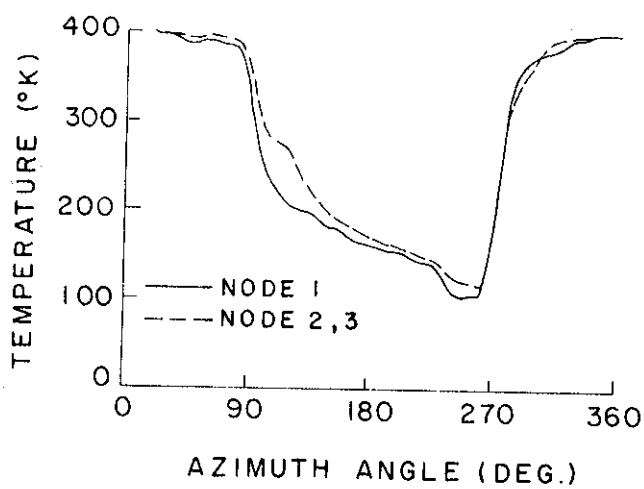


Fig. 2. The temperature variation at the three representative nodes of the cylindrical structure, with $\omega=10^{-5}$ rad/sec.

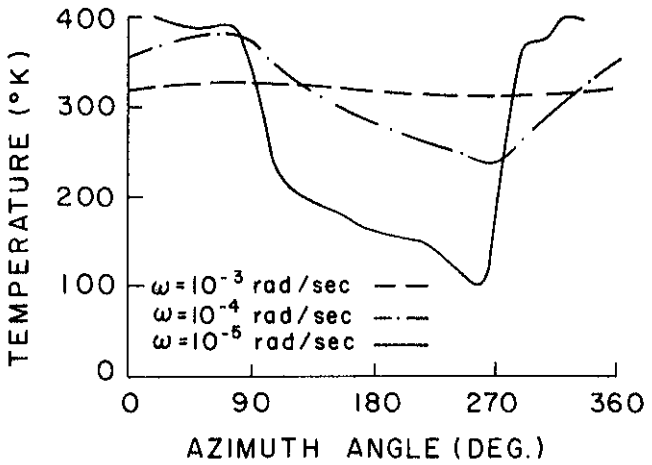


Fig. 3. The temperature variation with $\omega=10^{-3}$ rad/sec, $\omega=10^{-4}$ rad/sec and $\omega=10^{-5}$ rad/sec.

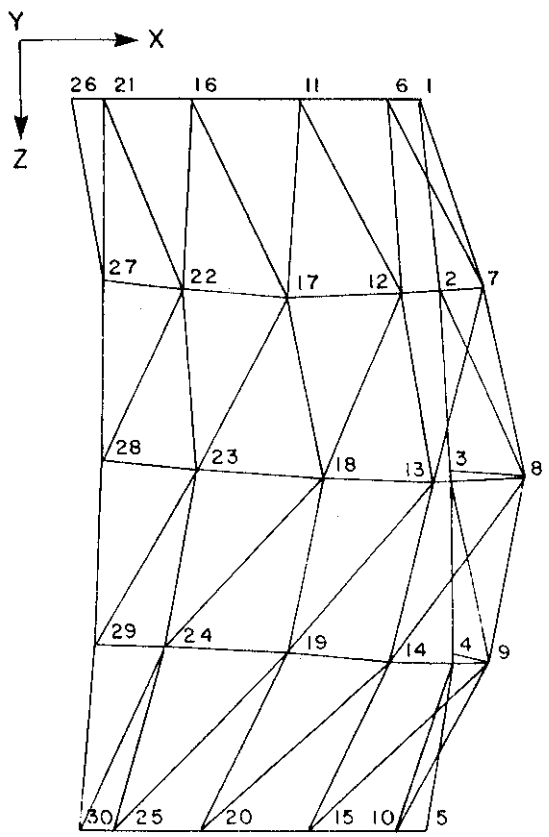


Fig. 4. The deformed cylindrical structure at time t=0, with the displacements magnified by a factor of 200.

# PASSIVE DAMPING AUGMENTATION OF FLEXIBLE BEAM-LIKE LATTICE TRUSSES FOR LARGE SPACE STRUCTURES

K.Cohen and Assoc. Prof. T.Weller
Faculty of Aerospace Engineering
Technion - Israel Institute of Technology
Haifa 32000, Israel

**Abstract**

A Timoshenko beam continuum model is developed to determine the transient response of a beam-like latticed large space structure, subjected to a unit impulse. It is demonstrated that an increase in diagonal stiffness, on account of the stiffness of the vertical girder, leads to a rise in the transverse shear rigidity. This results in higher natural frequencies and reduction in peak displacement. In addition, in an asymmetrical truss configuration coupling between the extensional and shear modes raises the maximum peak displacement compared to that obtained for a symmetric truss. The model is modified to investigate the introduction of passive damping in the form of several dynamic vibration absorbers. For simple, yet efficient analysis, a unique absorber parameter optimization procedure, based on the classical steady-state criteria, is used to tune the absorbers, having a total allocated mass budget of 10%, to the first two frequencies of the latticed structure. It is found that inclusion of transverse shear rigidity, as a design parameter in damping augmentation studies, reduces settling time for predetermined maximum peak displacements.

## 1. Introduction

Future ventures into outer space include concepts like large space stations, high resolution radars and communication antennas, astronomical observatories, solar power stations and space defence platforms. Qualifying as large space structures, L.S.S., these facilities, besides, having a large number of high density, low frequency structural modes, also require design for a very low gravitational environment. L.S.S. are in general comprised of repetitive latticed trusses, span large areas with few intermediate supports, are light weighted and flexible. Since dynamic testing of these structures in a 1-g environment is very complicated and dubious to a certain extent, sound analytical modeling of the structural dynamics problem, though being a tedious task, is of crucial importance.

L.S.S. need to meet target tracking, slewing, stringent line-of-sight and jitter control, pointing accuracies and microgravity acceleration requirements. However, on being disturbed, the structure is likely to remain excited for some time because of its high structural modal density at low frequency modes and possibly small damping. It is vital, therefore, to introduce means for passive energy dissipating, active counteracting or their combination to restrain the response of a given structure within an "inmission displacement-time allowables envelope" using vibration control methods.

In passive control, vibrational energy may be dissipated by employing

passive methods using viscoelastic materials that cause material damping at joints, or as additive layers. Tuned mass dampers and impact/friction forces manifesting at structural joints are other efficient sources of passive energy dissipation. These methods prove to be relatively cheap, simple, reliable and inherently stable. Active vibration suppression techniques for damping augmentation comprise of sensors and actuators that counteract the effects of the applied loads and disturbances, using external power sources. Experience has proved that the application of passive damping technology to a finite bandwidth actively controlled structure provides essential stabilization and enhances performance by reducing the burden on the active systems.

L.S.S., like those intended for the Space Station are asymmetric and therefore the effects of bending, shear, torsion and longitudinal motion are coupled. At present, there is little information on the advantages, trade-offs and limitations of these couplings in the vibration suppression of large space structures.

Following the detailed literature survey conducted in [1], the problem of undesirable vibrational energy, in large, flexible, beam-like repetitive lattices of non-symmetric geometry space structures, is minimized by augmenting dissipation, using passive means in the form of dynamic vibration absorbers. Whereas recent efforts concentrated on using tuned mass dampers for vibration suppression of L.S.S. with models possessing a number of discrete (non-continuous) degrees-of-freedom [2], or in systems having symmetric configurations [3], the present study treats a continuous, 20-bay, latticed beam-like structure and examines the effects of asymmetry and resident transverse-shear on the structural dynamic problem. Later, a unique procedure, for obtaining optimal tuning and damping parameters of several absorbers, is applied to a cantilevered truss in order to minimize the settling time of the transient, transverse-displacement response.

## 2. Equations of Motion

A two-dimensional version of the orthogonal tetrahedral configuration (non-symmetric) is considered (Fig.1). These trusses are primary candidates for the Space Station [4]. For a lattice shown in Fig. 1, the smallest possible repeating cell, which may be isolated from the grid, extends over one bay of the original structure (Fig. 2). The equivalent continuum beam properties, stiffness coefficients and density parameters, for the plane-strain case, are computed by performing the static tests described in [5].This results in the following relations:

$$\begin{bmatrix} N \\ M \\ Q \end{bmatrix} = \begin{bmatrix} C_{11} & 0 & C_{13} \\ 0 & C_{22} & 0 \\ C_{13} & 0 & C_{33} \end{bmatrix} \begin{bmatrix} \epsilon^{\circ}x \\ k^{\circ}y \\ 2\epsilon^{\circ}xy \end{bmatrix} \qquad (1)$$

where N, M, and Q are the extensional force, the bending moment and the transverse shear force respectively (Fig.3) and:

$[C_{ij}]$ - stiffness matrix of the continuum beam element (Fig. 3).
$\epsilon^{\circ}x$ - extensional strain.
$k^{\circ}y$ - curvature change of the beam.
$\epsilon^{\circ}xy$ - transverse shear strain.
$C_{13}$ - coupling between the extensional and transverse shear stiffnesses.

whereas, the matrix of material densities is given as:

$$[m] = \begin{bmatrix} m_{xx} & 0 & 0 \\ 0 & m_{zz} & 0 \\ 0 & 0 & m_{\theta\theta} \end{bmatrix} \qquad (2)$$

During this study, the lattice geometry, structural mass [mij] and transverse bending rigidity are fixed, i.e. the Euler-Bernouli model remains identical!! The stiffness properties $C_{11}$, $C_{13}$, and $C_{33}$ are varied using the following non-dimensional geometric coefficient:

$$\beta = \frac{2*Ad}{Ag} \qquad (3)$$

where Ad and Ag are the cross-sectional areas of the diagonal and vertical members of the truss depicted in Fig. 2.

The static tests described in [5] assume small displacements to obtain the values of the matrix [Cij*] (where $[Cij]^{-1}=[Cij^*]$). The validity of this assumption for a wide range of the coefficient β should not be taken for granted. For this purpose, the equivalent beam properties, $C_{13}^*$ and $C_{33}^*$, corresponding to the plain-strain case are computed, using the COSMOS/M finite element program [6], for both non-linear (large displacements) and linear (small displacements) responses induced by a static shear force. Since the present study restricts itself to linear analysis only, it is imperative to be aware of the range of β wherein beam behavior is linear.

The effect of the coupling factor, $C_{13}$, is evaluated for the repeating cell depicted in Fig. 4 for which :

$$Ad1 + Ad2 = Ad \qquad (4)$$

where Ad1 and Ad2 are the cross-sectional areas of the diagonal members of the truss (Fig. 4). For simplicity , the following non-dimensional geometric coefficient is defined:

$$\beta^* = \frac{Ad1}{Ad2} \qquad (5)$$

By varying values of Ad1 and Ad2 in Eqn. 4, i.e. β*, the structural dynamics problem of the symmetrical L.S.S. (β*=1) is compared to that of the asymmetric configuration (where in the extreme case β*=0).

Assuming a Timoshenko beam, the equations of motion, representing an anisotropic continuum model of a two-dimensional latticed structure, are developed. This results in a set of three coupled partial differential equations with the displacement variables u(x,t), w(x,t), Θ(x,t).

$$C_{22}\frac{\partial^2\Theta}{\partial x^2} + C_{13}\frac{\partial u}{\partial x} + C_{33}\frac{\partial w}{\partial x} - m_{\theta\theta}\frac{\partial^2\Theta}{\partial t^2} = C_{33}\Theta \qquad (6)$$

$$C_{11}\frac{\partial^2 u}{\partial x^2} + C_{13}\frac{\partial^2 w}{\partial x^2} - C_{13}\frac{\partial\Theta}{\partial x} - m_{xx}\frac{\partial^2\Theta}{\partial t^2} = 0 \qquad (7)$$

$$C_{13}\frac{\partial^2 u}{\partial x^2} + C_{33}\frac{\partial^2 w}{\partial x^2} - C_{33}\frac{\partial\Theta}{\partial x} - m_{zz}\frac{\partial^2 w}{\partial t^2} = 0 \qquad (8)$$

The natural frequencies and mode shapes of the vibrating anisotropic beam are obtained numerically, for

various values of $\beta$ and $\beta^{*}$, using a spreadsheet, by solving the eigenvalue problem which is comprised of a 6*6 determinantal frequency equation. The above procedure was verified in [1] by comparing values obtained using LOTUS 1-2-3, to those computed using the COSMOS/M finite element program [6], as well as, to those displayed in [5].

Transient disturbances, modeled as initial conditions and correspond to a unit impulse, may simulate shuttle docking or crew motion [2]. A linear dynamic analysis of the truss, based on the normal mode method, evaluates the response at time "t" by integrating the uncoupled equations of motion from time "zero" to time "t". The size of the time-step increment which is a key factor in the accuracy of the results, and the total number of modes included in the analysis obviously affect the accuracy . However, this improvement is at the cost of complexity and solution time. Therefore, the value of time-step and number of modes required need to be selected in compliance with the adequecy of the solution.

Finally, "i" dynamic vibration absorbers are attached to the beam-like structure at a distance $a_i$ from the origin (Fig.5). The addition of the absorbers affect Eqn. (8) in the following manner:

$$C_{1s}\frac{\partial^2 u}{\partial x^2} + C_{ss}\frac{\partial^2 w}{\partial x^2} - C_{ss}\frac{\partial \theta}{\partial x} - \sum_{i=1}^{n}\left[c_i\left(\frac{dq_i}{dt} - \frac{\partial w(a_i,t)}{\partial t}\right) + k_i\{q_i - w(a_i,t)\}\right]\delta(x-a_i) - m_{ss}\frac{\partial^2 w}{\partial t^2} = 0 \qquad (9)$$

where $\delta(x-a_i)$ is the Dirac delta function for i =1,..n whereas $k_i$ and $c_i$ are the stiffness and damping constants of the ith absorber respectively. Furthermore, the displacement of the ith absorber in the z direction is denoted by the variable $q_i$. Then, the equation of motion of any absorber is given as:

$$m_i\frac{d^2 q_i(t)}{dt^2} + c_i\left[\frac{dq_i(t)}{dt} - \frac{\partial w(a_i,t)}{\partial t}\right] + k_i\left[q_i(t) - w(a_i,t)\right] = 0 \qquad (10)$$

Following the results of [2], the total mass of the absorbers are kept at 10% of the structural mass of the beam. In addition, for a 2-DOF system, the optimal tuning ratio, is identical to that of the steady-state, S.S., minimized solution [7]. The ratio of the frequency of the ith tuned mass damper to the ith natural frequency, $To_i$, is obtained by equating the first two peaks of the S.S. response as follows:

$$To_i = \frac{1}{1 + \mu_i w_i^2(1)} \qquad (11)$$

where $To_i$ is referred to as the "tuning ratio" and $\mu_i$ is the ratio of absorber mass to the structural mass of the latticed beam-like structure. The value of $w_i(1)$ is obtained from the characteristic function representing the respective mode of an Euler-Bernouli cantilever beam [7]. The application of Eqn. 11 to tune an absorber attached to a truss, was found to be simple, time-saving and efficient [1].

Damping is introduced into the system in the form of concentrated dampers, placed at a point of maximum modal displacement of the truss and the absorber masses. The dampers are modeled, using the COSMOS/M finite

element program [6], in such a manner that their inclusion does not affect the frequency solution of the lattice with undamped absorbers. The effect of the dampers (irrespective of the fact that damping may be non-proportional) are considered in the modal analysis by applying assumed external forces on the combined 'beam'-undamped absorbers configuration. The product of the relative nodal velocities, between the point of absorber attachment and the mass of the undamped absorber, with the defined damping coefficient of the absorber, c, is equated to the above assumed external force. This numerical process is continued by performing iterations at each time step of the solution until convergence is reached. This occurs when the assumed force yields nearly the same damper force obtained from the response of the system.

The method of obtaining the optimal tuning and damping parameters of several absorbers, attached to a vibrating truss, is presented in Fig. 6. The criteria for selecting the above parameters is the requirement for the minimal settling time reached for a predetermined value of the maximum absolute peak displacement.

## 3. Results

The repeating cell of the lattice, which is a 2-D version of the orthogonal tetrahedral lattice, Fig. 2, is defined by the following parameters:

Lc = 7.5m
Lg = 5m
Ac = 80 X $10^{-4}m^2$
Ad = 40 X $10^{-4}m^2$
Ag = 60 X $10^{-4}m^2$
$\sigma$ = 2768 $kg/m^3$ (density of all truss members)
E = 71.7 X $10^9 N/m^2$ (Young's modulus of all truss members)

In order to arrive at the values of the matrix [Cij*], the assumption of linearity in truss deflection is to be justified. The equivalent continuum beam properties, $C_{13}^*$ and $C_{33}^*$, corresponding to the plane-strain case, were computed using the COSMOS/M finite element program [6]. To evaluate the non-linear effects, the ratios of the coefficients $C_{13}^*$ over $C_{33}^*$ yielded for the linear and non-linear analysis are compared in Table 1. As $\beta$ increases, the ratio, $C_{k3}^*$(linear)/$C_{k3}^*$(non-linear), for k=1,3, obtains a maximum for $\beta$=3.00. Since, the present work restricts itself to linear analysis only, the values of $\beta$ in the following discussions are varied within an "envelope" wherein the above ratio, presented in Table 1, is approximately equal to unity, i.e. for $1.33 < \beta < 3.00$. This property of non-linearity is attributed to unaccounted transverse shear deformation and extensional-shear coupling which restrict continuum modeling presented in [5], to geometrically linear truss structures.

In Table 2 the eigenfrequencies are compared with those of [5], who uses a higher order Timoshenko beam finite element analysis which takes into account coupling among the three basic deformations u, w and $\Theta$. The first four modes yielded by an equivalent Euler-Bernouli beam were also included and it is apparent that the discrepancy between them and the ones corresponding to the Timoshenko beam justifies the efforts to use the Timoshenko beam model. For comparison, the original truss structure was modeled and computed by the COSMOS/M finite element program [6]. It should be noted that mode 5 is a longitudinal mode. Comparisons in Table 2 verify the continuum type model used for the analysis of anisotropic beam-like lattice trusses.

| No. | β | $C_{13}^*$(LIN)/$C_{13}^*$(NON-LIN) | $C_{33}^*$(LIN)/$C_{33}^*$(NON-LIN) |
|---|---|---|---|
| 1. | 0.04 | 0.0151 | 0.8371 |
| 2. | 0.41 | 0.7277 | 0.9785 |
| 3. | 1.33 | 0.8955 | 0.9859 |
| 4. | 1.78 | 0.9085 | 0.9858 |
| 5. | 3.00 | 0.9183 | 0.9842 |
| 6. | 23.30 | 0.7718 | 0.9475 |

Table 1: $C_{k3}^*$(LINEAR)/$C_{k3}^*$(NON-LINEAR) for various values of β; k=1,3.

| MODE | SUN'S FEM [5] | SUN'S TIM-OSHENKO[5] | COSMOS/M [6] | CONTINUUM MODEL LOTUS 1-2-3[1] | EULER-BERNOULI |
|---|---|---|---|---|---|
| 1 | 1.5626 | 1.576 | 1.5626 | 1.572 | 1.593 |
| 2 | 9.1179 | 9.206 | 9.1179 | 9.173 | 9.982 |
| 3 | 23.222 | 23.460 | 23.2222 | 23.340 | 27.954 |
| 4 | 40.289 | 40.767 | 40.2888 | 40.472 | 54.779 |
| 5 | 43.357 | 43.740 | 43.3573 | 43.541 | --- |

Table 2: Natural frequencies of asymmetric truss [rad/sec]

| β | Ag[$10^{-6}$m$^2$] | Ad[$10^{-6}$m$^2$] | $C_{11}$[$10^6$N] | $C_{13}$[$10^6$N] | $C_{33}$[$10^6$N] |
|---|---|---|---|---|---|
| 1.33 | 60.0 | 40.0 | 12.955 | 0.989 | 0.659 |
| 1.61 | 53.8 | 43.4 | 13.047 | 1.050 | 0.700 |
| 1.78 | 50.8 | 45.1 | 13.090 | 1.078 | 0.718 |
| 2.09 | 45.8 | 47.8 | 13.148 | 1.117 | 0.745 |
| 2.40 | 41.8 | 50.1 | 13.190 | 1.145 | 0.763 |
| 3.00 | 35.6 | 53.4 | 13.228 | 1.171 | 0.780 |

Table 3: The effect of β on matrix [Cij]

| Symmetric ($\beta^*$=1.0) | | | Non-symmetric ($\beta^*$=0.67) | | |
|---|---|---|---|---|---|
| Time(s) | w(m) | u(m) | Time(s) | w(m) | u(m) |
| 0.85 | 0.0844 | 0.0028 | 0.85 | 0.0844 | 0.0028 |
| 3.13 | -0.0830 | -0.0031 | 3.12 | -0.0830 | -0.0029 |
| 4.86 | 0.0837 | 0.0030 | 4.85 | 0.0835 | 0.0030 |
| 7.33 | -0.0798 | -0.0032 | 7.32 | -0.0808 | -0.0032 |
| 9.05 | 0.0888 | 0.0034 | 9.03 | 0.0892 | 0.0034 |
| 10.77 | -0.0819 | -0.0034 | 10.75 | -0.0818 | -0.0032 |
| 13.04 | 0.0838 | 0.0024 | 13.06 | 0.0852 | 0.0029 |
| 14.95 | -0.0743 | -0.0019 | 14.92 | -0.0783 | -0.0026 |

Table 4: Peak impulse longitudinal and transverse response

The matrix [Cij], computed for different values of β, is presented in Table 3. It should be noted that the bending stiffness, $C_{22}$, is constant (and therefore not given in the Table 3), while the variations in the axial stiffness, $C_{11}$, are slight when compared to those in $C_{13}$ and $C_{33}$. It is apparent from Table 3 that the values of $C_{13}$ and $C_{33}$ increase with increasing β values, resulting in a stiffer structure. Consequently, the resulting natural frequencies, increase with β (which in fact represents an increase in diagonal stiffness ,on account of the stiffness of the vertical girder) for a constant structural mass. As a result of this phenomenon the fundamental frequency for β=3.0 is 1.5708 rad/sec as compared with 1.5626 rad/sec for β=1.33. Thus, an increase in diagonal stiffness, on account of the stiffness of the vertical girder, leads to a rise in the shear coefficients, $C_{13}$ and $C_{33}$.

In an asymmetrical truss, coupling between the extensional and shear modes lowers the value of equivalent shear rigidity as compared to a symmetric truss, thus lowering the natural frequencies. It is evident from Fig. 7 that coupling between the longitudinal and shear modes is at its highest for the asymmetric truss where $\beta^*=0$. On the other hand in the symmetric case all the $C_{ij}$ matrix coefficients of the 2-D structure are uncoupled. In addition the shear coefficient, $C_{33}$, is higher for $\beta^*=1$ than those corresponding to non-symmetric configurations, $\beta^*<1$.

Following [1], it was verified that for the linear dynamic analysis of the 20-bay truss structure, depicted in Fig. 1, the selection of an appropriate time-step (used in the integration of the uncoupled equations of motion), 0.1 sec, and the number of modes required before truncation, 5, is adequate.

Transient responses for the symmetric and asymmetric configuration of β=1.33 are given in Fig. 8 and a comparison is made with the asymmetric truss having β=3.0. The peak displacement response, measured at the free end of the cantilever, for the asymmetric truss, β=3.0, is found to be the lowest of the three. Calculations show that for β=1.33 the area under the displacement-time curve of the symmetric lattice is slightly smaller than that of the asymmetric one.

For β=1.33, a unit impulse applied on a symmetric truss, $\beta^*=1.0$, as well as a non-symmetric truss, $\beta^*=0.67$, leads to extensional deflections, u(t), of an order of 5% of the transverse deflections, w(t), i.e. $u(t)/w(t) < 0.05$. It can be seen from Table 4 that the inclusion of coupling between the transverse shear and the longitudinal extension, reflected by the coefficient $C_{13}$, does not contribute additional damping of any kind to the structure.

**One Absorber Only**

Classical steady-state criteria [7], is used to tune the absorber (having an allocated mass budget of 10%) to the fundamental frequency of the Euler-Bernouli beam. The normalized impulse response envelopes for various damping ratios for β=1.33 and 3.0 are given in Figs. 8 and 9 , respectively. In both cases the damper value which minimizes settling time is reached for $\delta o=0.5$. The settling time for achieving 5% of the maximum peak displacement, for the asymmetric truss (of [5]), β=1.33, was 21 sec, whereas for β=3.00, the settling time was a mere 13 sec.It is

worthwhile noting in Figs. 8 and 9 that a considerable change in the value of $\delta$ in the neighborhood of $\delta_o$ almost does not affect the response of the system. As the value of $\delta$ is increased, a reduction in absorber performance takes place as a result of a high damper force which restrains relative movement of the absorber mass.

**Two Absorbers**

The most efficient way to apply absorbers is by tuning them only to the modes that make a significant contribution to the transient response. For $\beta$=3.0, Table 5 depicts the effects of the respective modes, on the absolute peak displacement response curve. For clarity, these effects are presented in non-dimensional form, $R_k$, where $R_k$ is the ratio of the area, under the absolute peak displacement-time curve, using the first k modes to the area obtained using the first 15 modes. From Table 5, the main contributors are found to be the first two modes. Therefore, two absorbers, with a total mass equalling 10% of the mass of the truss, attached at the free end of the cantilevered truss, will be tuned to the first two modes.

| No. of modes | $R_k$ |
|---|---|
| One | 0.890 |
| Two | 0.985 |
| Three | 0.999 |
| Four | 1.003 |
| Six | 1.001 |
| Seven | 0.987 |
| Eight | 0.998 |
| Nine | 0.999 |
| Fifteen | 1.000 |

Table 5: Contribution of modes to Transient response.

Using the method outlined in Fig. 6 with values of 0.1, 0.09, 0.08, 0.07 and 0.055 for mass ratios of the absorber tuned to the fundamental frequency, $\mu_1$, the minimum settling time to reach 0.6% of the maximum undamped absolute peak displacement is reached. From Fig. 11, it can be seen that the above minimal settling time ,19 sec., is obtained for $\mu_1$=0.07 and $\mu_2$=0.03. The curves in Fig. 11, being magnified, commence after the first 10 seconds and they (the curves) also justify the additional absorber tuned to the second frequency. As the value of $\mu_2$ exceeds approximately 0.03, the efficiency of the dual absorber system falls.

As an example , Sesak et al. [2], apply two absorbers to suppress the vibration of the pitch rotation (payload pointing response example). The Uncoupled Dynamic Optimization (U.D.O.) method, which yielded the best results, computes the spring and damper constants for each absorber, using the tuning laws of a 2-DOF system, assuming no spatial coupling (coupling, whereby the location of an absorber at the maxima of one mode also affects the other mode).

The U.D.O. is applied to a 20-bay truss ($\beta$=3.0, $\mu_1$=0.07 and $\mu_2$ =0.03) and the response thus obtained is compared with that reached using the solution presented in Fig. 6, Coupled Dynamic Optimization (C.D.O.) method. Table 6 highlights the differences and the similarities of the two methods described above.

| Parameters | U.D.O | C.D.O. |
|---|---|---|
| $T_1$ | 0.7813 | 0.7813 |
| $T_2$ | 0.8929 | 0.8929 |
| $K_1$ [N/m] | 10.797 | 9.721 |
| $K_2$ [N/m] | 211.66 | 211.66 |
| $\delta_1$ | 0.50 | 0.38 |
| $\delta_2$ | 0.75 | 0.75 |

Table 6: absorber parameters.

| Freq. No. of Truss | Natural Frequency Truss only | Absorber 1 only $\mu_1$=0.07 | Absorber 2 only $\mu_2$=0.03 | U.D.O. method | C.D.O. method |
|---|---|---|---|---|---|
| Abs. 1 | - | 1.0651 | - | 1.0539 | 1.0202 |
| 1 | 1.5708 | 1.7952 | 1.4826 | 1.7133 | 1.6799 |
| Abs.2 | - | - | 7.6798 | 7.6825 | 7.6823 |
| 2 | 9.2466 | 9.2672 | 10.4226 | 10.4397 | 10.4380 |
| 3 | 23.7929 | 23.7999 | 23.9546 | 23.9620 | 23.9613 |
| 4 | 41.3662 | 41.3687 | 41.4161 | 41.4185 | 41.4183 |
| 5 | 43.8344 | 43.8356 | 43.8594 | 43.8606 | 43.8606 |

Table 7: Natural frequencies (rad/sec) obtained during the comparison of absorber optimization methods.

From Fig. 12, it can be seen that the method provided in Fig. 6 offers a quicker settling time, 19 seconds, when compared to that obtained using the U.D.O method, 30 seconds. The cause of this difference lies in the calculation of the stiffness of absorber 1, tuned to the fundamental frequency, k1. Whereas k1 is given by:

$$k1 = T_1^2 m_1 \Omega_1^2 \qquad (12)$$

the tuning ratios are basically a function of the absorber mass ratio alone. Using Fig. 6, the value of $\Omega_1$, used in Eqn.12, is the fundamental frequency of the combined system consisting of the truss and absorber 2, tuned to the second natural frequency of the truss. From Table 7, it is evident that the introduction of absorber 2 alone, to the truss, affects the value of the first natural frequency significantly whereas the addition of absorber 1 alone has hardly any affect on the values of the higher frequencies. Therefore, tuning of absorber 1 to 1.4826 rad/sec gives better results due to the appreciable amount of spatial coupling, caused by the location of both absorbers at the maxima of the first two modes (free end of the absorber).

**Conclusions and Recommendations**

An analytical Timoshenko beam-like model of a 2-D truss was developed to determine the transient response of a beam-like latticed structure to a unit impulse excitation. The shearing coefficients of the continuum model, $C_{13}$ and $C_{33}$, were found to be useful design parameters that affect the damping augmentation of the L.S.S.
The model was modified to investigate the addition of passive damping in the form of dynamic vibration absorbers. For a given mass distribution, the C.D.O. method presented in Fig.6, utilizes the effects of spatial coupling to provide a simple, time-saving and efficient means of determining the stiffness and damping constants of the absorbers.

The analytical model presented could be further developed to analyze 3-D beam-like and plate-like latticed structures, which include coupling between the bending, transverse shear, twisting and extensional modes. Design procedures concerning the geometric configurations of flexible large space structures, reflected by the parameter $\beta$, could be investigated in a non-linear

analysis to provide internal damping mechanisms that would lower the burden on specialized means of damping augmentation. The passive damping mechanisms, discussed in this work, may be introduced into a finite bandwidth, actively controlled structure using a multi-disciplinary approach.

## References


1. K.Cohen and T.Weller, "Passive damping augmentation of flexible beam-like lattice trusses for large space structures", Technion, Israel Institute of Technology, TAE 655, August 1990.

2. J.R.Sesak, M.J.Gronet and G.M.Marinos, "Passive stabilization of large space systems", NASA contractor report 4067, NAS1-17660, 1987.

3. J.N.Juang, "Optimal design of a passive vibration absorber for a truss beam", J.Guidance, Vol. 7, No. 6, pp. 733-739, Nov-Dec 1984.

4. A.K.Noor and M.M.Mikulas, "Continuum modeling of large lattice structures: Status and projections", Large space structures: Dynamics and Control ed. S.N.Atluri and A.K.Amos, Springer-Verlag Berlin Heidelberg, pp. 1-34, 1988.

5. B.Necib and C.T.Sun, "Analysis of Truss Beams using a high order Timoshenko beam finite element", J. of Sound and Vibration, Vol. 130, No. 1, pp. 149-159, 1989.

6. M.Lashkari, "COSMOS/M user guide: stress, vibration, buckling, dynamics, and heat transfer analysis", Structural Research and Analysis Corporation, Release Ver. 1.5, 1987.

7. R.G.Jacquot, "Optimal dynamic vibration absorbers for general beam systems", J.Sound and Vibration, Vol. 60,No. 4, pp. 535-542, 1978.


## Figures

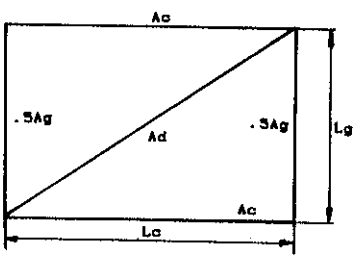


Fig. 1: 2-D Version of the orthogonal tetrahedral lattice.

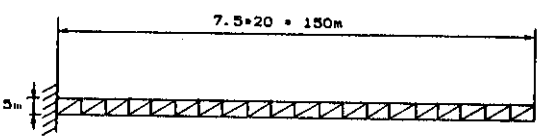


Fig. 2: Repeating cell of asymmetric lattice.

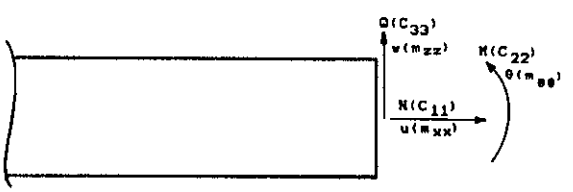


Fig. 3: Simplified beam element and sign convention.

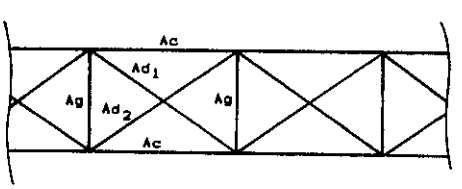


Fig. 4: Repeating cell of truss for examining effects ofsymmetry.

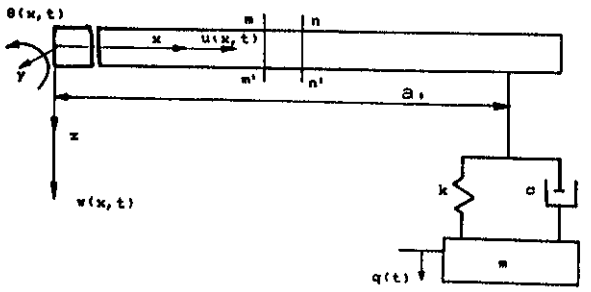


Fig. 5: Cantilever beam with "ith" dynamic absorber attached.

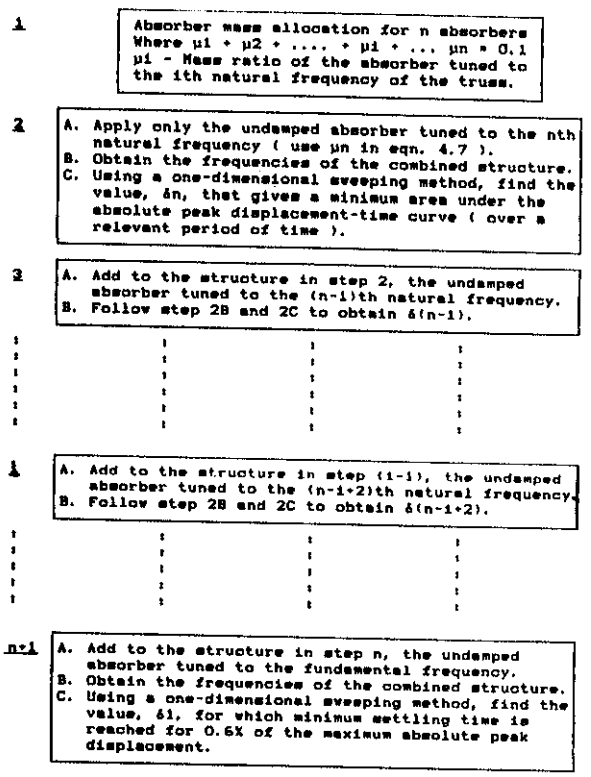


Fig. 6: The Coupled Dynamic Optimization (C.D.O.) method.

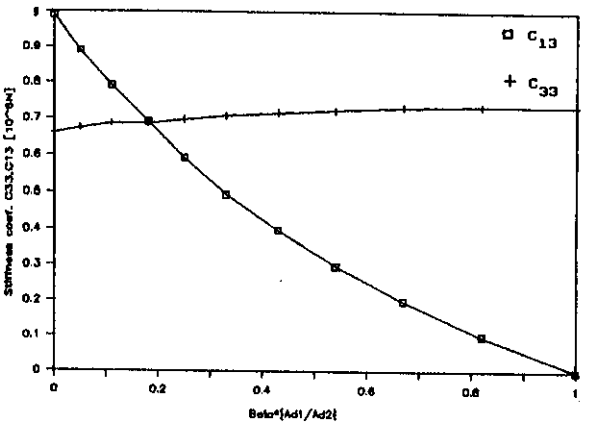


Fig. 7: Effects of asymmetry: shear coefficients vs. $\beta^*$.

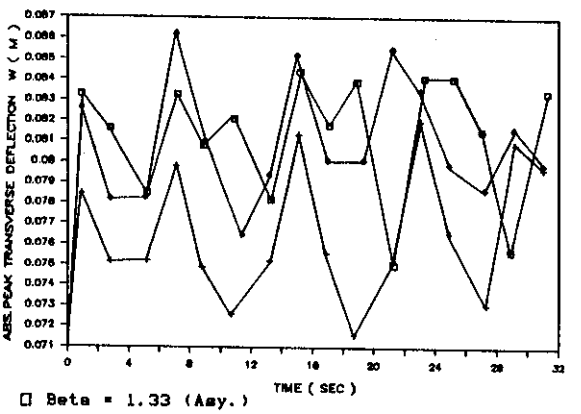


Fig. 8: Impulse response envelopes of undamped truss for various geometric configurations.

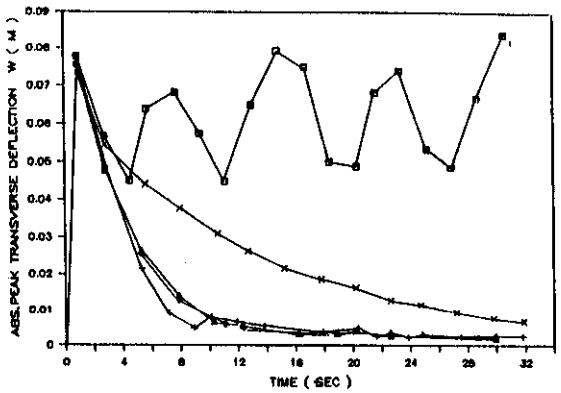


□ δ = 0.00

+ δ = 0.37

◇ δ = 0.47

△ δ = 0.50

× δ = 1.50

Fig. 9: Impulse response envelopes for various damping ratios (β=1.33).

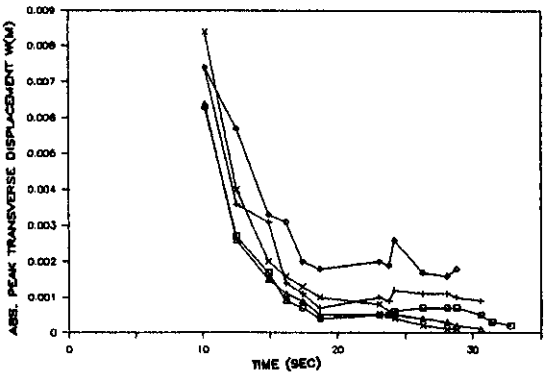


◇ μi = 0.1

+ μi = 0.09

□ μi = 0.08

△ μi = 0.07

X μi = 0.055

Fig. 11: Impulse response envelopes for various mass distributions.

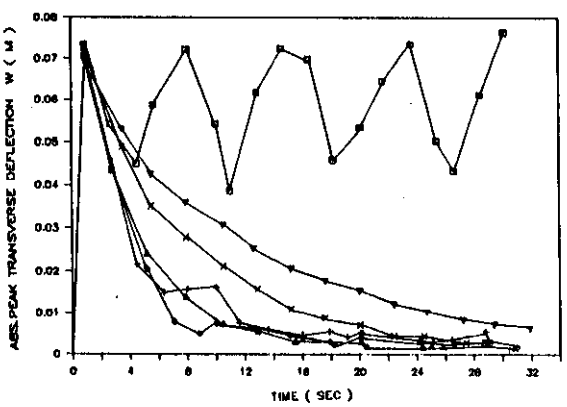


□ δ = 0.00

+ δ = 0.25

◇ δ = 0.37

△ δ = 0.50

× δ = 0.95

▽ δ = 1.50

Fig. 10: Impulse response envelopes for various damping ratios (β=3.00).

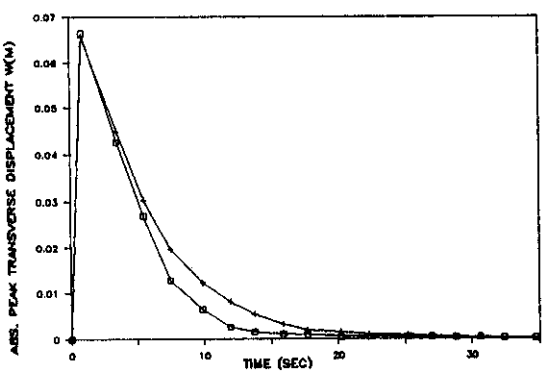


+ UNCOUPLED METHOD

□ COUPLED METHOD

Fig. 12: Impulse response envelopes using C.D.O. and U.D.O. methods.

# PREDICTION OF PROPELLANT BEHAVIOR IN SPINNING FLOW OF A SPACE MOTOR

A. Gany, Y. Levy and Y.M. Timnat
Faculty of Aerospace Engineering and Space Research Institute
Technion - Israel Institute of Technology
Haifa 32000, Israel.

## Extended Abstract

A model for the two phase flow dynamics in spinning spherical motors was developed in connection with the Ofeq program. The model is based on the sectional approach to solve the two-phase flow equations[1]. The distribution and trajectories of aluminum/alumina particles resulting from the combustion within high energy solid propellant space motors have significant impact on the motor characteristics, since particles remaining inside the combustor degrade the overall performance. In order to examine the model predictions, an experimental simulation was built. Measurements are based on laser Doppler anemometry (incorporating the pedestal amplitude technique) yielding data on the velocity and size distribution of paraffin droplets injected. These include small size droplets (below 5 micrometers), that move with the gas velocity, and larger size droplets (20 micrometers average), injected by a rotational spray system which simulate the aluminum oxide particles.

The test chamber is formed by two cylindrical pyrex tubes with a sudden contraction in diameter, which is rotated at various speeds by a frequency controllable motor. The optical system is mounted on a moving X-Z table allowing sectional measurements of the three velocity components and the size-velocity correlations. An illustration of the test system is shown in Fig. 1. The signal is recorded by a photomultiplier, connected to an electronic system, which allows to perform simultaneous measurements of velocity and size. The results are obtained by means of a specially developed data acquisition code. The optical system is based on a 5W argon ion laser, uses a beam-splitter and a frequency-shifter and focuses the scattered light resulting from the measuring volume onto the aperture of a photomultiplier. The electronics include a validation criterion, which ensures that the pedestal amplitude associated with a measured Doppler frequency belongs to the same particle.

The data obtained till now are preliminary in nature; they comprise the axial velocity of the gas (both its distribution on the axis of symmetry and the behavior in a radial cross-section above the sudden contraction - Figs. 2,3) as well as a two-phase flow test case, which presents the relation between the axial velocity and the size of the droplets. These results were obtained without rotation of the apparatus. Measurements performed when the simulated combustor rotated, show that the effect on the axial velocity is negligible, while the tangential velocity approximately corresponds to solid body rotation (Fig. 4).

## Reference

1. G. Avital, J.B. Greenberg, T. Tambour and Y.M. Timnat, "Spray Dynamics and Fuel Vapor Distribution in a Spinning Combustion Chamber," Progress in Astr. and Aeron. 132, 187-204, 1991.

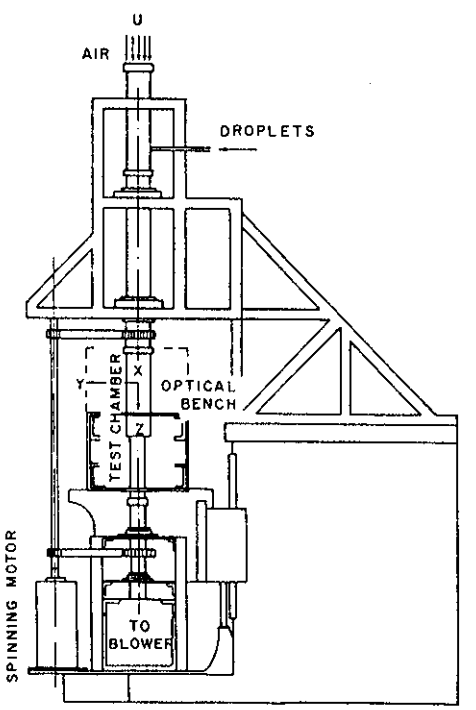


Fig. 1. Illustration of the test system.

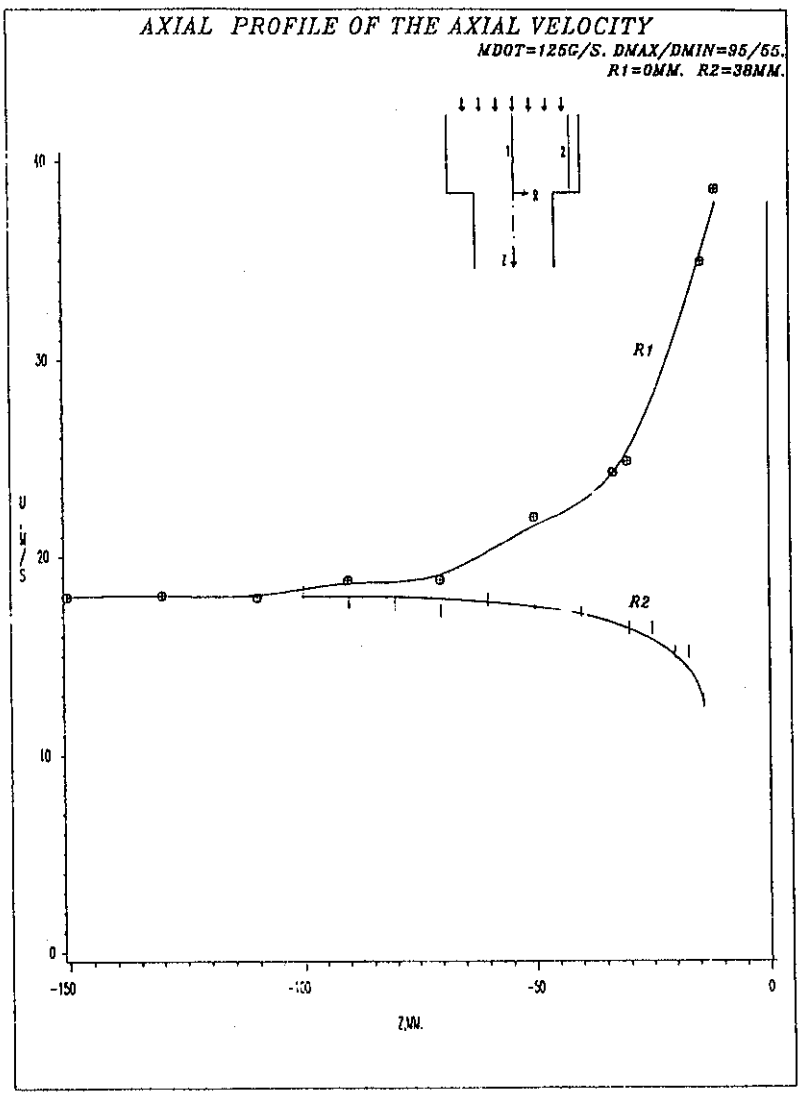


Fig. 2. Axial gas velocity vs axial location.

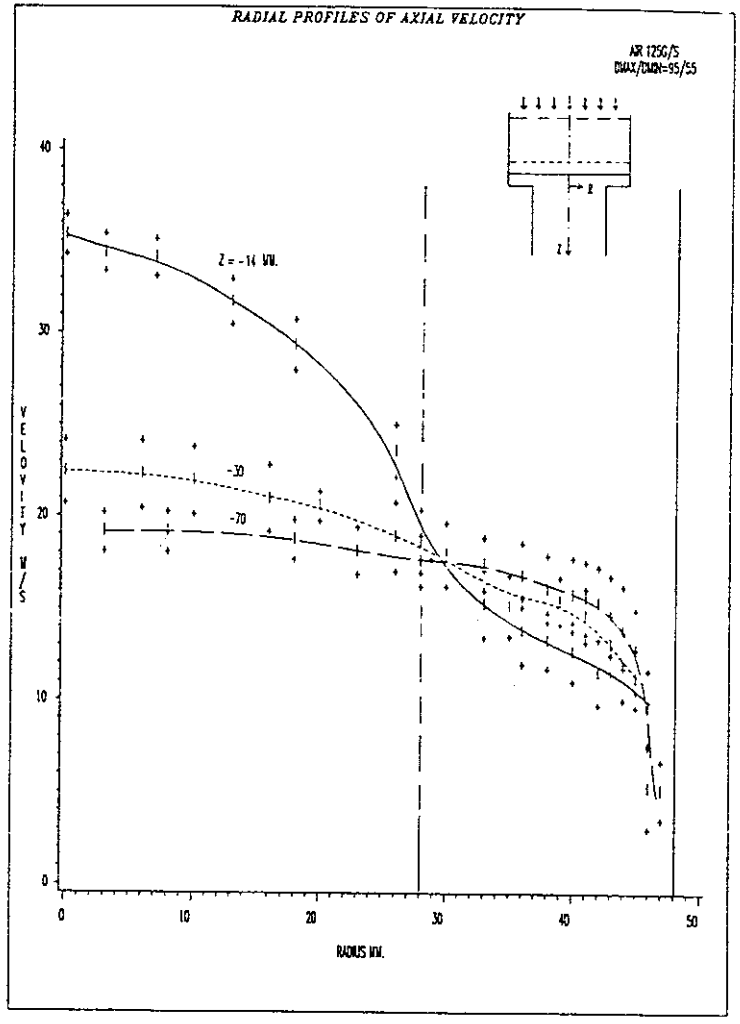


Fig. 3. Radial distributions of the axial gas velocity at different cross-sections.

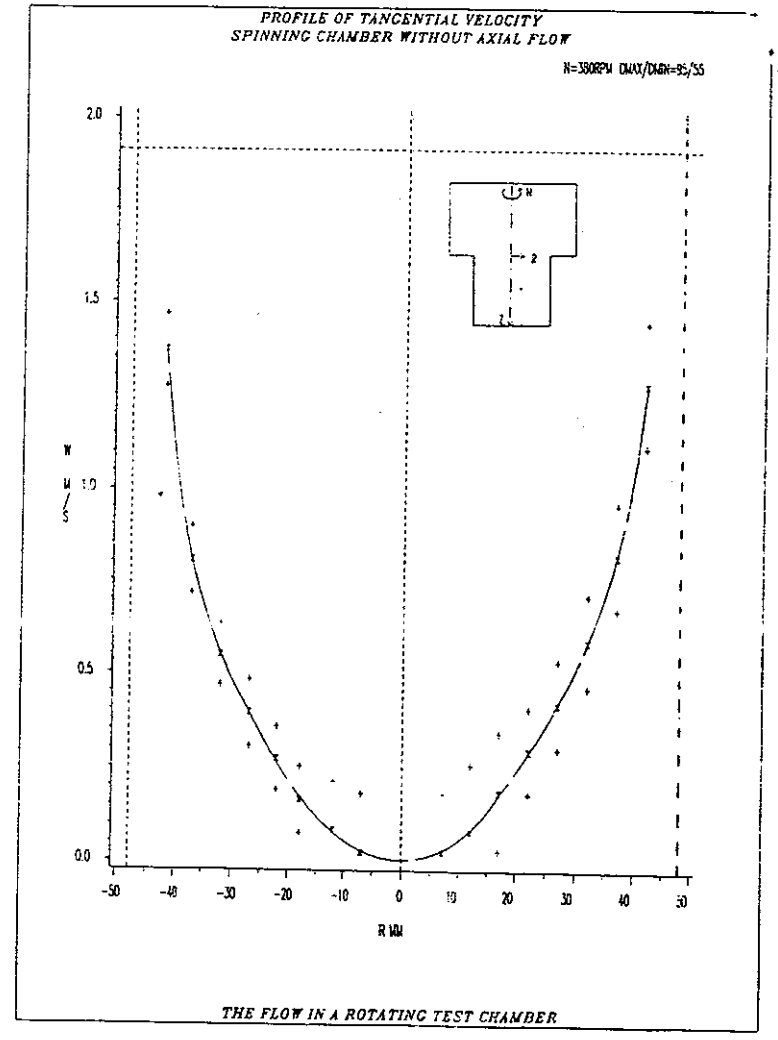


Fig. 4. Tangential velocity distribution as a function of radial location for spinning rate of 380 rpm.

# ENHANCED ORBITAL GYROCOMPASSING BY THE OPTICAL FLOW SENSED BY AN EARTH-POINTING CAMERA

Leora Topaz and Arthur J. Grunwald
Faculty of Aerospace Engineering
Technion, Haifa 32000, ISRAEL

## Abstract

A novel method for improving the orbital gyrocompassing process involving the attitude angle estimation of an earth pointing satellite in low-earth orbit is described. This estimation process usually employs a discrete, variable-gain Kalman Filter scheme, processing the measurements of roll, pitch and yaw rate gyros, a horizon sensor and sometimes a sun sensor. The improved method uses an electro-optical sensor for enhancing the process by direct measurement of the satellite azimuth angle. Simulations have shown that this additional measurement drastically reduces the estimator convergence time, in prticular when the sun-sensor is ineffective, i.e. at high sun elevation angles. The azimuth sensing method is based on estimating the image shift between successive picture frames of an on board CCD full-matrix camera, pointing towards the earth. The shift estimation algorithm, is based on minimizing a cost function, expressing mean-squared differences in brightness patterns of certain areas of the two frames. An extensive experimental evaluation program has been carried out, using a computer-controlled two-axis light table with actual satellite images, a CCD camera and a digital computer for the on-line implementation of the algorithm. The robustness and accuracy characteristics of the method were investi- gated with regard to relevant parameters such as: image texture content, camera focal length, sampling rate and the number of pixels processed. The results demonstrate high robustness for a wide range of parameter variations, and show that for an adequately chosen set of parameters it is possible to estimate the azimuth angle with an accuracy of 0.1- 0.2 degrees.

## 1. Introduction

Accuracy requirements in satellite attitude control are strongly mission-dependent and vary from several degrees, as in directing solar panels, to less than 0.1 deg, as in pointing a telescope or a high resolution aerial surveillance camera. During the past three decades, a variety of attitude determination methods have been employed, [1-5]. These methods are largely based on measurements of a number of reference directions, such as the direction to stars, planets or the sun. The common denominator between these methods is the use of a Kalman Filter to estimate the attitude from a set of noise corrupted measurements, Leffets et al. [5], (1982).

Satellites in low-altitude geocentric orbits, frequently utilize a horizon sensor, a sun sensor or a star tracking sensor, Wertz [6], (1988). The gyro-compassing method is based on measuring angular body rates and using the notion that the vector of rotation rate of the local-level plane is perpendicular to the orbital plane. However, these methods require considerable time for the azimuth estimates to converge to the required accuracy. The use of high precision level sensors can speed up the process, but these sensors are typically heavy and costly, Wertz [6].

This research deals with the orbital gyro-compassing method, first addressed by Bryson [2], (1971), using three rate gyros, measuring the body axis components of the satellite angular rotation rate with respect to inertial space, and a horizon sensor. Bryson used a fixed-gain Kalman filter for estimating the angular orientation. Although the system is fully observable, the final alignment with this sensor package might take as long as 300 seconds. The incorporation of a sun sensor, which requires information of the position of the satellite in orbit, can drastically reduce the convergence time if the sun elevation angle is small. However, for high sun elevation angles, the azimuth measurement becomes inaccurate and the sun sensor is essentially ineffective.

The enhanced method presented in this paper is a relatively low-cost solution for these cases. It utilizes the optical flow of an earth-pointing camera. Since, as it will be explained in the next section, the direction of the flow includes azimuth information with respect to the orbital plane, convergence times can again be reduced to several seconds. The optical flow is estimated by computing the magnitude and direction of the shift between two successive image frames. Although the use of optical flow techniques is not new and has been widely used in computer vision and robotics [7-9], its particular use for accurate satellite attitude determination, has not been attempted earlier, to the best of our knowledge.

This paper consists of two parts: in the first part the need for the direct sensing of the azimuth angle in orbital gyrocompassing is pointed out, the principle of operation of the novel azimuth sensing method is described and requirements for acceptable sensor noise are determined. The second part describes the development and experimental evaluation of the algorithm for the optical flow estimation process and describes the efforts for obtaining robust and accurate performance over a wide range of viewing conditions and image characteristics.

## 2. Description of the Method

### 2.1 Attitude determination by orbital gyrocompassing

The coordinate systems, used in the attitude determination process, are defined in Fig. 1. The orbital axis system **o**, for a circular orbit, has its $x_o$-axis in the direction of the orbital flight vector, its $y_o$-axis perpendicular to the orbital plane and its $z_o$-axis pointing towards the center of earth. Thus, $x_o$-o-$y_o$ constitutes the local level plane and $x_o$-o-$z_o$ the orbital plane. The alignment system **a**, defines the desired final attitude of the satellite. System **a** is rotated with respect to system **o** about the $z_o$ axis, by the azimuth angle $\Psi_o$, to ensure solar energy reception by solar panels. The ground system **g**, has its $x_g$-o-$z_g$ plane locally level and the $x_g$-axis pointing towards the true north. The angle $\Psi_g$ is the azimuth of the ground track with respect to the north, and varies with the position of the satellite in orbit. Finally, the body system **b**, fixed with respect to the satellite body. The input axes of the various sensors, such as the horizon sensor, sun sensor and camera, are aligned with the body system **b**.

The orientation of system **b** with respect to system **a** is defined by 3 sequential rotations, yaw, pitch and roll, $\psi$, $\theta$ and $\phi$, about the $z$, $y$ and $x$ axes, respectively, see Fig 1. The orbital gyrocompassing method in this research is aimed at estimating the angles $\psi$, $\theta$ and $\phi$, to an accuracy 1 milliradian. Bryson's basic orbital gyrocompassing method [2], included the following sensors: (1) an orthogonal triad of rate gyros, measuring the rate components of the vector of rotation of the satellite with respect to inertial space in $x_b$, $y_b$ and $z_b$ direction, being the roll rate $p$, the pitch rate $q$ and the yaw rate $r$, respectively; (2) a horizon sensor or gravity gradient sensor, providing direct measurements of $\theta$ and $\phi$. In addition to these sensors, some applicationsalso include: (3) a sun sensor, which provides a combination of all three angles $\psi$, $\theta$ and $\phi$. The method, presented here, also adds (4) an optical sensor, which derives the azimuth $\psi$, from the optical flow of an earth-pointing camera. The basic principle of operation of this optical sensor, is outlined in the next section.

For a satellite in the final stages of its alignment, $\psi$, $\theta$ and $\phi$ are usually less than 4 degrees. The relation between the rates of $\psi$, $\theta$ and $\phi$ and p, q, r is derived from the Euler differential equations. On the assumption of small angles, this relation becomes:

$$\begin{bmatrix} \dot{\phi} \\ \dot{\theta} \\ \dot{\psi} \end{bmatrix} = \begin{bmatrix} 0 & 0 & \omega_o \cos\Psi_o \\ 0 & 0 & -\omega_o \sin\Psi_o \\ -\omega_o \cos\Psi_o & \omega_o \sin\Psi_o & 0 \end{bmatrix} \begin{bmatrix} \phi \\ \theta \\ \psi \end{bmatrix} + \begin{bmatrix} p+\omega_o \sin\Psi_o \\ q+\omega_o \cos\Psi_o \\ r \end{bmatrix} \quad (1)$$

where $\omega_o$ is the angular velocity of orbital motion. The rate gyro measurements, $p_{rg}$, $q_{rg}$ *and* $r_{rg}$ include measurment noises $w_p$, $w_q$, $w_r$ which represent the roll, pitch and yaw rate gyros (drifts). Replacing p, q, and r with the rate gyro measurements, the system of Eq. (1) can be written as:

$$\dot{\underline{x}} = A\underline{x} + B\underline{u} + \underline{w} \quad (2)$$

where the angles $\psi$, $\theta$ and $\phi$ constitute the state vector to be estimated, the rate gyro measurements with the $\omega_o$ terms the input vector, and the rate gyro noises the disturbance vector. It is clear from Eq. (1) that rate gyro measurements by itself, are not sufficient to compute the required angles, since the system includes very slow and undamped poles. Therefore, a Kalman scheme has been employed, in which Eq. (1) constitutes the "system model" and with the measurement equation given by:

$$\begin{bmatrix} z_{\phi hs} \\ z_{\theta hs} \\ z_{\alpha} \\ z_{\beta} \\ z_{\psi as} \end{bmatrix} = \begin{bmatrix} 1 & 0 & 0 \\ 0 & 1 & 0 \\ H_{31} & H_{32} & H_{33} \\ H_{41} & H_{42} & H_{43} \\ 0 & 0 & 1 \end{bmatrix} \begin{bmatrix} \phi \\ \theta \\ \psi \end{bmatrix} + \begin{bmatrix} v_{\phi hs} \\ v_{\theta hs} \\ v_{\alpha} \\ v_{\beta} \\ v_{\psi as} \end{bmatrix} \quad (3)$$

or, written as:

$$\underline{z} = H\underline{x} + \underline{v} \quad (4)$$

where $\underline{z}$ is the vector of measurements, composed of horizon sensor outputs $z_{\phi hs}$ and $z_{\theta hs}$, of sun sensor outputs $z_{\alpha}$ and $z_{\beta}$, and the optical azimuth sensor output $z_{\psi as}$. $H$ is the measurement matrix and $\underline{v}$ the vector of measurement noises.

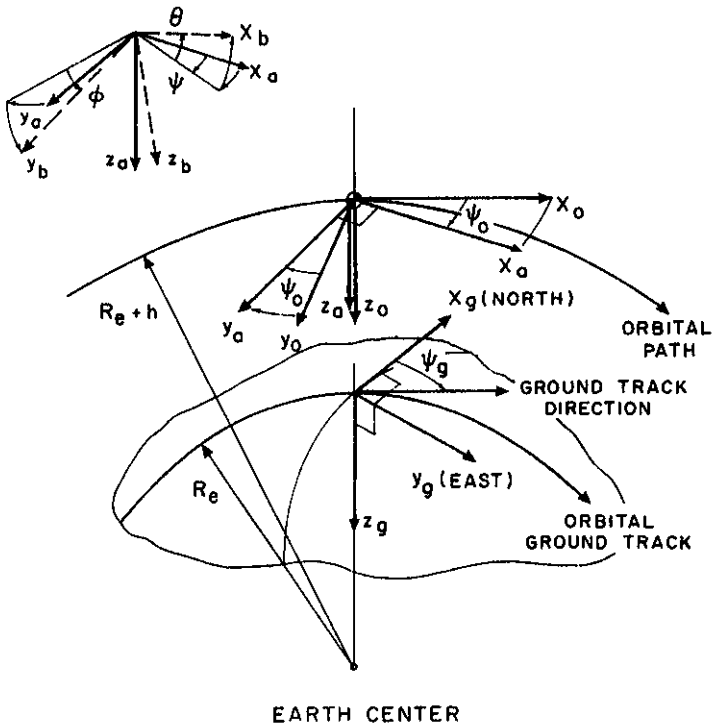


**Fig. 1.** Satellite attitude angle determination; definition of coordinate systems.

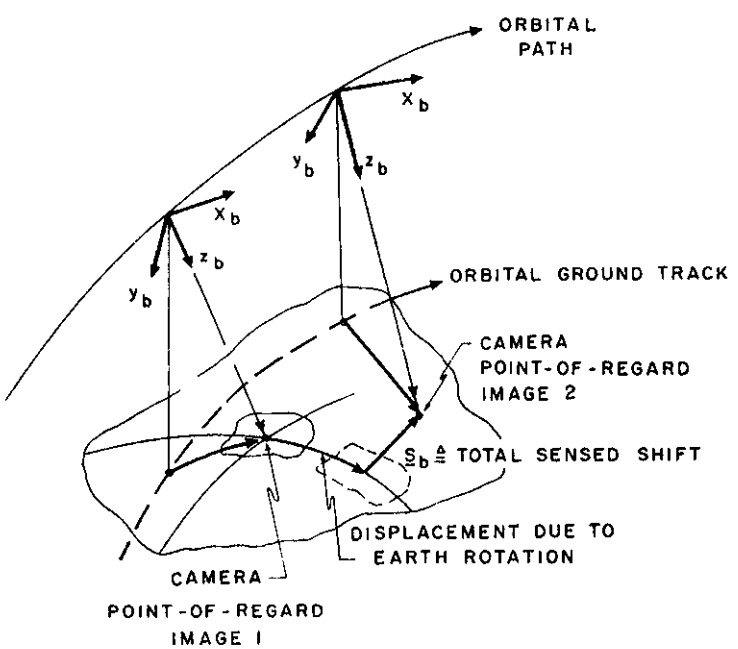


**Fig. 2.** Shifting of the camera point-of-regard as a result of the translational and rotational motion of the satellite with respect to the ground plane.

Based on Eqs.(1) and (3) a discrete, variable gain, Kalman filter has been formulated, according to Gelb [10]. Note that in this formulation the rate gyro drifts are considered as the "system noise", and the noise of all other sensors as "measurement noise". System and measure- ment noise components are assumed to be uncorrelated and modeled by zero-mean Gaussian White Noise processes.

Eq. (3) shows, that the sun sensor measurements are linear combination of all three angles, $\psi$, $\theta$ and $\phi$. The principle of operation of the sun sensor is described in Appendix. It is shown there that the elements of matrix $H$, which linearly combine the angles, are trigonometric functions of the sun azimuth angle $\lambda$ and elevation angle $\delta$. For $\delta$=90 deg the terms $H_{33}$ and $H_{34}$ are zero, and the sun sensor no longer provides information about $\psi$.

### 2.2. Azimuth measurement from image shifts

An earth-looking camera is able to provide direct information about the azimuth angle of the satellite with respect to the velocity vector direction, by considering the interframe image shift vector. The basic principle, underlying this method is shown in Fig. 2. The camera point-of-regard is the point at which the $z_b$-axis (or camera viewing axis) intersects the ground plane, and which also corresponds to the center of the image. After a small interval of time, $\Delta t$, due to both the translatory and the rotational motion of the satellite, the camera point-of-regard will have shifted to a different location on the ground plane. The shift vector $\underline{S}_b$ denotes the displacement of the camera point-of-regard in meters on the ground plane, expressed in the **b**-system. For a given focal length of the camera lens and given viewing geometry, the ground displacement can be translated into pixels in the image plane. By comparing the two successive frames, the displacement of the second image with respect to the first one, in pixels in the image plane, can be found.

The relation between the shift vector $\underline{S}_b$ on one hand, and the satellite motions on the other hand, are drived by considering only instantaneous motion:

$$\underline{S}_b = -(\underline{V}_b + \underline{\omega}_b \times \underline{\rho}_b)\,\Delta t \qquad (5)$$

where $\underline{V}_b$,$\underline{\omega}_b$ are the translatory and rotational velocities of the satellite with respect to the ground plane, respectively; $\underline{\rho}_b$ is the position vector of the camera point-of-regard, at the time the first image was taken.

The translatory velocity of the satellite with respect to the ground plane originates both from the orbital velocity vector and from the rotational motion of the earth. The $x,y$ components of the velocity vector $\underline{V}_o$ of the satellite with respect to the ground plane, expressed in the orbital axis system, are given by:

$$\begin{aligned} V_{ox} &= -\Omega R_e \cos\lambda \sin\Psi_g + \omega_0 (R_e + h) \\ V_{oy} &= \Omega R_e \cos\lambda \cos\Psi_g \end{aligned} \qquad (6)$$

where $R_e$=6378 km is the equatorial earth radius, $\Omega$=15 deg/sec is the earth angular velocity, $\lambda$ is the geographical latitude at the time the first image frame was taken, $\Psi_g$ is the azimuth of the satellite ground track direction with respect to the north at the same time, and $h$ the altitude of the orbit.

The rotational velocity of the satellite with respect to the ground plane is the rotational velocity with respect to the local level plane, given by Eq. (1). Finally, the position vector of the camera point-of-regard, expressed in the **b**-system, is given by:

$$\underline{\rho}_b = \begin{bmatrix} 0 \\ 0 \\ h/(\cos\theta\cos\phi) \end{bmatrix} \qquad (7)$$

By combining the effects of translational and rotational motion of the satellite with respect to the ground plane, the shift vector $\underline{S}_b$ can be found. After rearrangement this yields the following explicit expression for the desired azimuth angle $\psi$ :

$$\psi = \tan^{-1}\left(-\frac{V_{oy}}{V_{ox}}\right) - \Psi_0 + \tan^{-1}\left(-\frac{S_{by} - ph\Delta t}{S_{bx} + qh\Delta t}\right) \qquad (8)$$

Eq. (8) shows that the computation of $\psi$ on the basis of the components $S_{bx}$,$S_{by}$ of the image shift vector, also requires the angular rates $p$ and $q$ obtained from rate gyro measurements, and knowledge of the position of the satellite in orbit, i.e. $\Psi_g$ and $\lambda$ for computing $V_{ox}$,$V_{oy}$ in Eq.(6).

The error in the computation of $\psi$, depends both on the errors $\Delta S_{bx}$,$\Delta S_{by}$ in computing the shift vector and on the measurement errors $\Delta p$, $\Delta q$ of the rate gyros. The errors in $\psi$ as caused by each one of these

components are obtained by deriviation of Eq. (8), and can be shown to be:

$$\Delta\psi_{sx} = -\frac{A}{C}\frac{1}{\Delta t}\Delta S_{bx}; \qquad \Delta\psi_{sy} = \frac{B}{C}\frac{1}{\Delta t}\Delta S_{by};$$
$$\Delta\psi_{p} = -\frac{B}{C}\frac{1}{\Delta t}\Delta p \; ; \qquad \Delta\psi_{q} = -\frac{A}{C}\frac{1}{\Delta t}\Delta q \tag{9}$$

where:

$$A \equiv V_{ox}\sin(\Psi_0+\psi) + V_{oy}\cos(\Psi_0+\psi)$$
$$B \equiv -V_{ox}\cos(\Psi_0+\psi) + V_{oy}\sin(\Psi_0+\psi) \tag{10}$$
$$C \equiv (V_{ox}^2 + V_{oy}^2)$$

It is clear from Eqs. (8) that the effect of the shift errors and rate gyro errors on $\Delta\psi$ varies with the position in orbit. For example, for an orbit with inclination of 28.5 deg, and an altitude of 300 km, a time interval between frames of $\Delta t$=0.5 sec and shift errors of $\Delta S_{bx}=\Delta S_{by}$=20 m on the ground plane, the error in $\psi$ will vary between 0.02-0.3 deg. Similarly, rate gyros drifts of $\Delta p=\Delta q$=1.0 deg/hour will cause an error in $\psi$, varying between 0.0008-0.015 deg. Since rate gyros used in satellites are well within this accuracy range, the success of this method largely depends on the accuracy at which the image shift can be determined.

### 2.3. Simulation results

In order to investigate the effect of the various parameters and noise levels on the estimator performance, the variable gain discrete Kalman filter, formulated for Eqs. (1) and (3), has been subjected to a covariance analysis. Since the measurement matrix $H$ governs the dynamics of the filter gain matrix, and since $H$ may vary substantially with the sun elevation angle $\delta$, it was of particular interest to investigate the effect of $\delta$ on the filter convergence time and on the estimation errors in the steady state. Furthermore, it was of interest to determine whether and under what conditions the addition of the proposed direct azimuth measurement method is effective. The filter convergence time is defined here as the time in which the standard deviations of the errors in the estimates of $\psi$, $\theta$ and $\phi$ converge below a 1 milliradian threshold.

The effect of rate gyro noise on the convergence time and estimation accuracy, was found to be several orders of magnitude smaller than the effect of the noise of horizon, sun and azimuth sensors. The effect of the latter ones are discussed hereafter.

Fig. 3 shows the dependence of the convergence time on the sun elevation angle $\delta$, for the basic system and the system enhanced with the optical azimuth measurement. The standard deviation of the measurement noise of horizon sensor $\sigma_{hs}$, sun sensor $\sigma_{ss}$, and azimuth sensor $\sigma_{as}$, was set to 0.1 deg. Fig. 3 clearly shows that the convergence time for the basic system increases almost exponentially with $\delta$. For angles of $\delta$ close to 90 deg the sun sensor is no longer effective and the process might take as long as several minutes. In contrast, for the larger sun elevation angles, i.e. for $\delta$>45 deg, the convergence time of the system enhanced with the azimuth measurement, no longer depends on $\delta$, and remains constant at 3 sec.

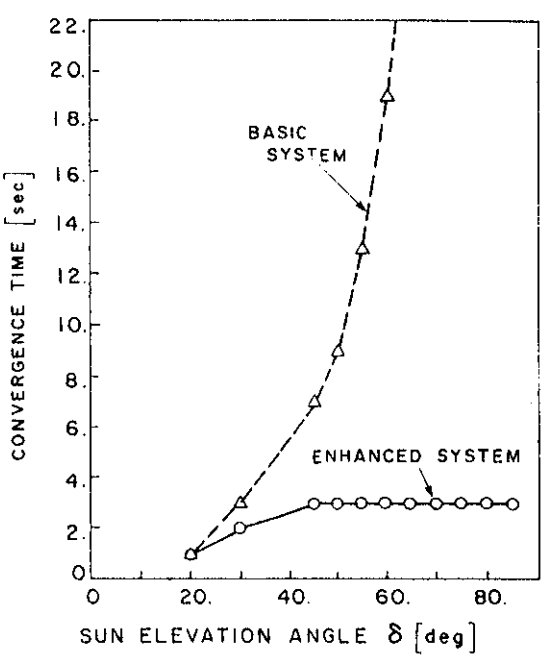


**Fig. 3.** Convergence time as a function of the sun elevation angle $\delta$; basic system and enhanced system.

Fig. 4 shows how the noise of the azimuth sensor in the enhanced system affects the convergence time. For low sun elevation angles, i.e. $\delta$=30 deg, the azimuth sensor noise hardly affects the convergence time, which remains within 1-3 sec. However, for higher sun elevation angles, i.e. $\delta$=60 deg, the estimates increase markedly with an increase in azimuth sensor noise. This was expected, since for higher $\delta$, azimuth information from the sun sensor deteriorates and the estimator places a larger weight on the azimuth sensor.

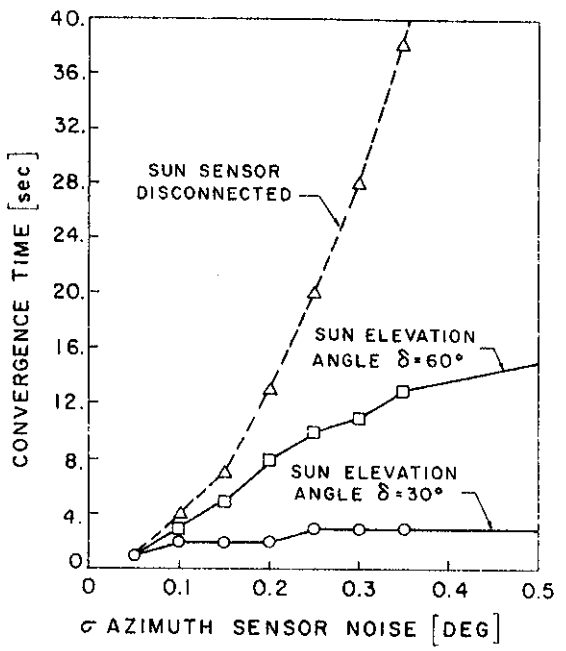


**Fig. 4.** Convergence time as a function of azimuth sensor noise for different sun elevation angles.

Fig. 4 also shows the curve for a disconnected sun sensor; this is equivalent with $\delta$=90 deg. In this case the convergence time increases almost exponentially with $\sigma_{as}$.

In Table I convergence times for various sun elevation angles and different combinations of sensor noise, for the basic and the enhanced system, are compared. Table I confirms that the azimuth measurement enhancement drastically reduces the sensitivity of the convergence time to the sun elevation angle. For $\delta$=85 deg, the addition of an azimuth sensor with a measurement noise of $\sigma_{as}$=0.1 deg, reduces the convergence time from 4 minutes to 3 seconds. Table I also shows that even a noisier azimuth sensor, i.e. $\sigma_{as}$=0.3 deg, still markedly contributes for high sun elevation angles and has no negative effect for low angles.

## 3. The Image Shift Estimation Algorithm

### 3.1. Theoretical background

A robust and accurate real-time algorithm has been developed for estimating the interframe shift vector in the image plane. The algorithm has been tailored specifically to operate on widely varying low earth- orbit satellite images, and is classified as a variant of sum-of-square difference (SSD) methods, Matthies et al. [11], (1989) and Heel [12], (1990) and Merhav and Bresler [13-15], (1986,1987) These methods are slightly more computationally demanding, but are more accurate than alternative gray level gradient methods, Fennema et al. [8], (1979), Nagel [9], (1983) . On the other hand, the SSD methods are significantly less computationally demanding than methods which require the computation

| Sun Elevation Angle $\delta$ [deg] | Estimator Convergence Time [sec] | | | |
|---|---|---|---|---|
| | Basic System (Without Azimuth Sensor) | | Azimuth Sensor Enhanced System Sun Sensor Noise $\sigma_{ss}=0.1^{\circ}$ | |
| | Sun Sensor Noise $\sigma_{ss}=0.1^{\circ}$ | Sun Sensor Noise $\sigma_{ss}=0.3^{\circ}$ | Azimuth Sensor Noise $\sigma_{as}=0.1^{\circ}$ | Azimuth Sensor Noise $\sigma_{as}=0.3^{\circ}$ |
| 20 | 2 | 5 | 2 | 2 |
| 60 | 19 | 88 | 3 | 11 |
| 85 | 218 | 288 | 3 | 26 |

**Table I.** Convergence times for various sun elevation angles and different combinations of sensor noise; basic and enhanced system.

of spatial autocorrelation functions of the entire image, Barnea et al. [16], (1972), Mustafavi et al. [17], (1978).

The basic algorithm, developed in our laboratory in earlier work for estimating the ground speed vector of low-flying aircraft, attempts to find the interframe shift vector $\underline{S}$ in the image plane. This is achieved by locating an area in the second image, which best resembles a test area, defined in the first image, see Fig. 5. For simplicity the test area is chosen as a rectangular window at the center, but in principle, it might take any continuous shape or position in the first image, provided it will appear within the boundaries of the second image. Although the shift is the dominant factor in the difference between successive image frames of an earth-looking camera, additional differences might originate from: (1) additive image noise, typical in video systems; this effect is modeled by adding a spatially and temporally uncorrelated Zero-Mean Gaussian White Noise component to the gray level of each pixel. (2) Optical distortions, resulting from irregularities in the atmosphere and the lens. (3) Geometrical distortions, resulting from changes in camera slant angle. (4) Image rotation about the viewing axis. For sufficiently high sampling rates, i.e. larger than 1 Hz, for a nominally down looking camera, and for relatively slow camera rotations about the viewing axis, effects (2), (3) and (4) can be neglected. Furthermore, for an approximately known camera orientation, effects (3) and (4) can be compensated for by appropriate geometrical transformations.

Let $Fk(x,y)$ be the true gray level of the pixel at screen coordinates $x,y$ and of the $k$-th frame, $Nk$ the noise additive to the gray level of this pixel, $Ik(x,y)$ the measured gray level, and $\underline{S}=(s_x,s_y)$ the unknown shift vector between two successive frames $k=1$ and $k=2$, then it follows by definition that:

$$F_2(x-s_x,y-s_y) \equiv F_1(x,y) \tag{11}$$

and:

$$I_2(x-s_x,y-s_y) = I_1(x,y) + N_{12}(x,y) \tag{12}$$

where:

$$N_{12}(x,y) = N_2(x-s_x,y-s_y) - N_1(x,y) \tag{13}$$

Since $N1$ and $N2$ are uncorrelated Gaussian White Noise processes, also $N12$ is an uncorrelated Gaussian White Noise process. The unknown shift vector $\underline{S}$ is estimated by minimizing the following cost function:

$$J(\hat{s}_x,\hat{s}_y) = \frac{1}{n^2} \sum_{i=1}^{n} \sum_{j=1}^{n} [I_2(x-\hat{s}_x,y-\hat{s}_y) - I_1(x,y)]^2 \tag{14}$$

expressing the mean square difference in gray level between the pixels of the first and the second frame, within the test window ($n \times n$ pixels). In the presence of uncorrelated Gaussian White image noise, the best estimate of $\underline{S}$ is obtained when $J$ reaches an absolute minimum. Since the image constitutes a field of random gray levels, $J$ is a random function.

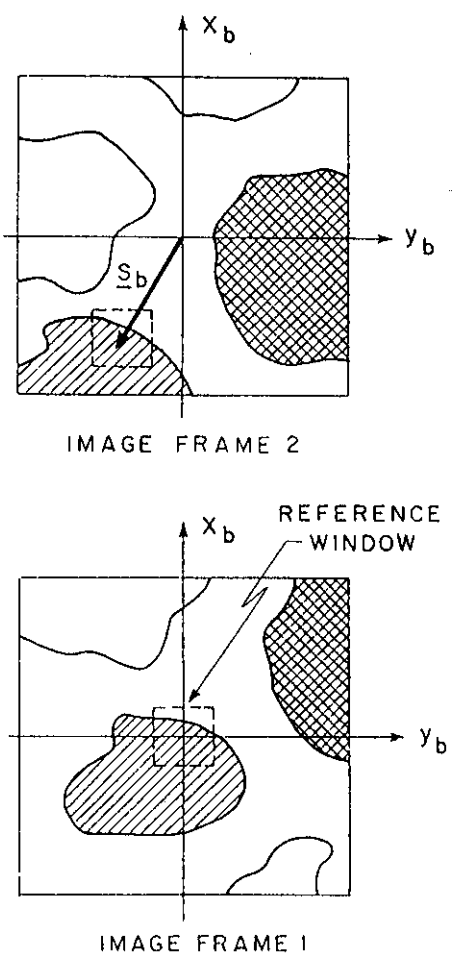


**Fig. 5.** Determining the in-plane shift vector between two successive image frames, by locating an an area in the second frame which matches with a reference window in the first frame.

Fig. 6 shows a one-dimensional representation of a typical cost function shape, and the corresponding gradient of $J$. Since $J$ is a random function, also the gradient vector will be random. The range about the true shift, in which the gradient has a positive slope, is referred to as the "similarity zone". For texture-rich images this range is generally smaller than for texture-poor images.

For each pair of successive image frames, the shift vector $\underline{S}$, which brings the components of the gradient vector to zero, is found as follows: (1) An initial guess for $\underline{S}$ is made, based on linear prediction, using the computed position in orbit and the measured angular rates of the spacecraft. (2) A global search is performed, untill the computed value of the cost function for a window centered about $\underline{S}$, is minimal with respect to the values computed for a 3×3 pixel neighborhood of $\underline{S}$. (3) A parabolic surface is fitted through the nine values and the minimum for this surface is computed analytically, using a Newton-Raphson scheme. This scheme has been chosen, since it was found that for a sufficiently large reference window (larger than 8 by 8 pixels), the shape of the mean square difference cost function is near parabolic about the minimum. For a reasonably good initial guess the process converges within 2-3 steps.

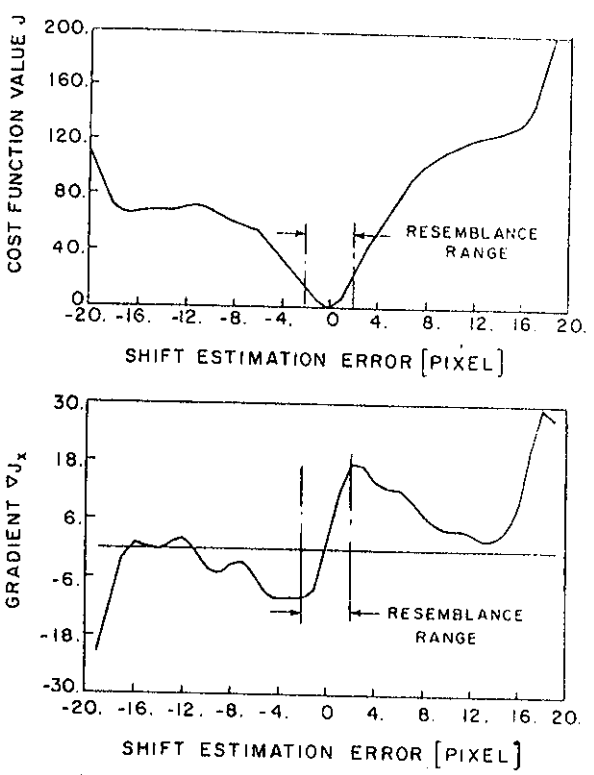


**Fig. 6.** Cost and gradient functions for a 8x8 pixel reference window, for image type A.

It is clear that for the algorithm to operate correctly, the initial guess of $\underline{S}$ for each frame should be within the resemblance range. This condition is referred to as "continuous tracking". The degree at which the condition of continuous tracking can be guaranteed under a wide range of conditions, is hereafter referred to as the robustness properties of the algorithm. However, if the initial guess is outside the resemblance range, two undesired phenomena might occur,Mostafavi [17] : (1) "false locking", in which the algorithm converges to a local minimum of $J$. This phenomenon can never be prevented completely, but its chance of appearing can be drastically reduced by either choosing a larger reference window, which improves the confidence level of the computed cost function, or by improving the initial guess by reducing the time between frames. Both these solutions will demand larger computational resources. (2) "loss of locking", which might occur when the reference window is outside the boundaries of the shifted image. Both these phenomena can be identified, by checking the consistency of the cost $J$ and the estimated displacement between successive frames.

### 3.2. Experimental program

An extensive experimental program has been carried out for evaluating the method under laboratory conditions whichclosely resembe the actual situation, using real satellite photographs representing a wide range of different conditions and image textures. The experimental setup included a two-axis (x-y) high-precision computer-controlled servo-driven light table, fitted with Linear Optical Encoders for measuring its position with a resolution of 2 ηm, a Javelin CCD camera, an FG100 Image Digitizing Card, and a Motorola 1131 system, based on the MC68020/MC68881 processors, and operating at 16 Mz. The camera had a 573 by 573 pixel grid with a width-to-height ratio of 4:3 and a measured signal-to-noise ratio of 40 db. The Image Digitizing Card did sample 512 by 512 pixels at a maximum rate of 25 frames/sec. By changing the height of the camera above the table, its focal length or its angular orientation, a variety of different viewing geometries could be simulated.

The tests involved moving the table in small steps along a pattern of straight parallel lines at a given azimuth angle with respect to the north, thus covering most of the image, without passing the same area twice. At each step the image was sampled, together with an accurate reading of the table's position by means of linear optical encoders. The encoder signals were used for computing the actual image shift vector and its azimuth angle. This angle

was compared with the one estimated by the algorithm, and the error was recorded. Each run included 100 image frame samples.

Experimental parameters were: (1) reference window size $n$; (2) size of shift between frames $\underline{S}$; (3) azimuth of the orbital direction of motion $\psi_g$; and (4) camera focal length, expressed in terms of the pixel ground plane footprint. In addition, the effect of image texture contents was investigated for four typical images: type A: an urban area; type B: a hilly area with canyon; type C: wave-like sand dunes; and type D: a mixed area of small settlements, cultivated fields and uncultivated mountain area.

### 3.3. Results

#### 3.3.1. Shape of cost function

As mentioned earlier, the success of the algorithm can be largely attributed to the near parabolic shape of the cost function near the absolute minimum. Thus, the gradient in the vicinity of the minimum is almost linear. A one-dimensional example of a cost function and its gradient, computed for image type A and for a 8X8 pixel reference window, is shown in Fig. 6. Fig. 6 clearly shows the parabolic shape of the cost function, and the steep and linear characteristic of the gradient in the vicinity of the minimum. Note also that the similarity zone (resemblance range) can be clearly identified.

#### 3.3.2. Robustness Tests

For all image types and for a reference window size of 16x16 pixels, the algorithm was always found to converge to the absolute minimum, provided the initial guess for the shift vector $\underline{S}$ was within 5 pixels of its true value. For a larger error in the initial guess, convergence could no longer be guaranteed under all conditions. This robustness was achieved by an efficient limited area global search.

#### 3.3.3. Accuracy tests

No consistent effect of the direction of motion azimuth $\psi_g$ on the errors in estimated shift in $x$ and $y$ direction, was found. Therefore, the estimates were dominated by specific image features such as the direction of the canyon or the wave pattern in types B and C or the lack of homogeneity of image D, rather than the absolute direction, per se. Hence, following Eq. (9), the estimated azimuth was not affected by $\psi_g$, and only the results for $\psi_g$=45 deg. are presented here. Table II shows standard deviations of the errors in the estimated shifts in $x$ and $y$-directions and azimuth angle, $\sigma_{\varepsilon sx}$, $\sigma_{\varepsilon sy}$ and $\sigma_{\varepsilon\psi}$, respectively, of runs of 100 image frames, for various image types, reference window sizes and shifts between frames. The large variability in the results can be attributed to the fact that during each run, different areas of the image were scanned. Nevertheless, the results clearly show that increasing the reference window size yields improved accuracies, e.g. the average values of $\sigma_{\varepsilon sx}$ for image type A are 0.20, 0.16 and 0.12 pixels, for window sizes of 16x16, 32x32 and 48x48 pixels, respectively. In Fig. 7 averaged values of $\sigma_{\varepsilon sx}$ are plotted against the square-root of the number of pixels in the reference window. The curves show an almost linear dependency, both for a shift of 50 and 100 pixels per frame.

For a given pixel ground plane footprint of 50 m/pixel and a ground speed of 7200 m/sec (speed of radial-to-earth-surface intersection point) shifts between frames of 20, 50 and 100 pixels, correspond to sampling rates of 7.2, 2.88 and 1.44 frames per second. The results in Table II show, that the size of the shift between frames has no effect on the shift estimation error. This was expected, since the size of the shift affects the quality of the initial guess, rather than the final accuracy. Since for the largest shift of 100 pixels the initial guess was still within the resemblance range, all estimates converged to absolute minima. However, following Eqs. (9) and (10), the error in the estimated azimuth angle is expected to increase linearly with the inverse of the time between frames $\Delta t$, or for a given footprint, with the inverse of the shift between frames. Fig. 8 indeed confirms this linear dependency for the four image types. Although extending the shift between frames beyond 100 pixels might result in even more accurate azimuth estimates, the resulting lower sampling rates might adversely affect the quality of the initial guess and hence the robustness of the algorithm. Furthermore, sampling rates might be below the minimum set by system requirements.

Fig. 8 also clearly shows the effect of the image texture contents. The urban area A with its rich texture contents, allowed a two times better azimuth estimation accuracy than the relatively texture poor wave-like sand dunes C. In general, the accuracy improves with texture contents, i.e. when the resemblance range is relatively narrow, the mean-square difference gradient is steep and the cost function surface is near-parabolic. Consequently, texture rich images will require a better initial guess.

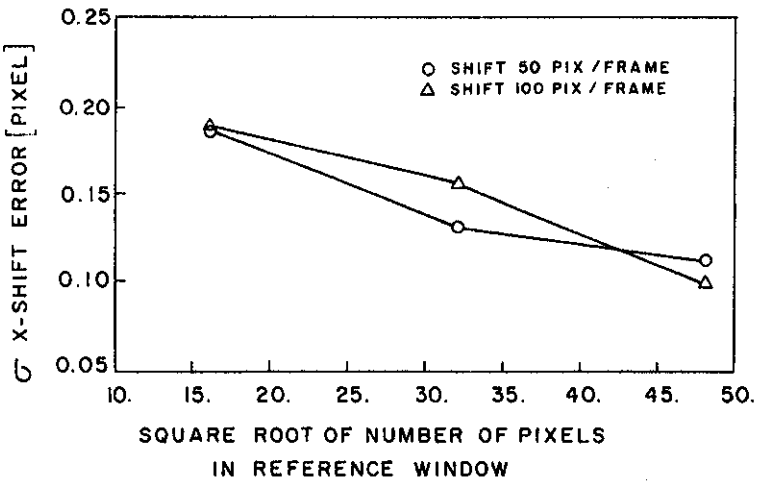


**Fig. 7.** Error in estimated shift in $x$-direction as a function of square root of number of pixels in reference window.

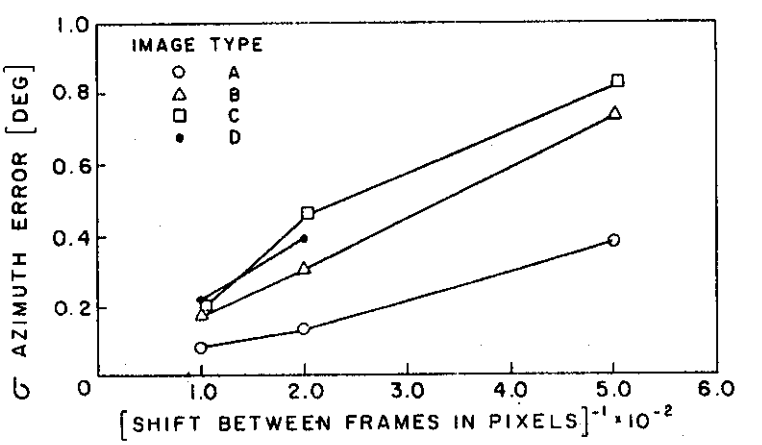


**Fig. 8.** Error in estimated azimuth angle as a function of the inverse of shift between frames, for various image types.

| Image Type | Reference Window Size $[pixel]^2$ | Shift Between Frames [pixel] | Shift Estimation Error | | Azimuth Estimation Error $\sigma_{\varepsilon\psi}$ [deg] |
|---|---|---|---|---|---|
| | | | $x$-direction $\sigma_{\varepsilon sx}$[pixel] | $y$-direction $\sigma_{\varepsilon sy}$[pixel] | |
| A | 16x16 | 20 | 0.216 | 0.278 | 0.8077 |
| | | 50 | 0.186 | 0.173 | 0.1948 |
| | | 100 | 0.189 | 0.305 | 0.1337 |
| | 32x32 | 20 | 0.181 | 0.117 | 0.3833 |
| | | 50 | 0.130 | 0.096 | 0.1287 |
| | | 100 | 0.155 | 0.164 | 0.0811 |
| | 48x48 | 20 | 0.161 | 0.096 | 0.3694 |
| | | 50 | 0.111 | 0.084 | 0.1017 |
| | | 100 | 0.098 | 0.076 | 0.0509 |
| B | 32x32 | 20 | 0.224 | 0.248 | 0.7291 |
| | | 50 | 0.200 | 0.320 | 0.3060 |
| | | 100 | 0.227 | 0.345 | 0.1709 |
| C | | 20 | 0.347 | 0.623 | 1.4044 |
| | | 50 | 0.246 | 0.422 | 0.3932 |
| | | 100 | 0.228 | 0.486 | 0.2176 |
| D | | 20 | 0.243 | 0.315 | 0.8151 |
| | | 50 | 0.274 | 0.447 | 0.4511 |
| | | 100 | 0.277 | 0.295 | 0.1873 |

**Table II.** Shift and azimuth angle estimation errors for various reference window sizes, shifts between frames and image types.

The effect of increasing the camera focal length, or, alternatively, decreasing the pixel ground plane footprint by a factor of two, is shown in Table III. The data refer to a reference window size if 32x32 pixels and a shift between frames of 100 pixels. For the texture rich image types A, B and D, the footprint does not affect the accuracy. However, for the texture poor wave-like sand dunes C, the reduced footprint yields an improvement in texture contents and, consequently, an improvement in estimates. Although, for a given image shift in pixels, the effect of reducing the footprint on the quality of the azimuth estimate is minor, its largest benefit is the increased sampling rate. This facilitates a better initial guess, and thus improves the robustness.

| Image Type | Azimuth Estimation Error $\sigma_{\varepsilon\psi}$ [deg] | |
|---|---|---|
| | Footprint 25 [m/pixel] | Footprint 50 [m/pixel] |
| A | 0.0805 | 0.0811 |
| B | 0.1648 | 0.1709 |
| C | 0.1616 | 0.2176 |
| D | 0.1719 | 0.1873 |

**Table III.** The effect of the pixel ground plane footprint on the azimuth angle estimation error, for various image types.

| Reference Window Size [pixel]$^2$ | 16x16 | 24x24 | 32x32 | 48x48 |
|---|---|---|---|---|
| Computation time per iteration [msec] | 1.64 | 3.61 | 6.36 | 14.19 |

**Table IV.** Single iteration computation time for various reference window sizes.

### 3.3.4. Computational requirements

Table IV lists the computation times needed for one iteration of the algorithm, for various reference window sizes. The algorithm has been implemented in assembly language on the 16 Mz Motorola 1131 system, based on the MC68020/MC68881 processors. Table IV shows that for a 32x32 pixel reference window and an average of 3 iterations, the algorithm requires about 20 msec per frame, which is well within the 40 msec time span between the frames of a standard television camera.

## 4. Discussion

The proposed azimuth angle sensing method constitutes a low-cost improvement of the orbital gyrocompassing process. The image shift algorithm demonstrates a high degree of robustness over a wide range of varying situations and allows the estimation of the azimuth angle to within 1 milliradian. For high sun elevation angles, this measurement reduces the estimator convergence time from 4-5 minutes to several seconds.

The success of the azimuth sensing method depends on the degree at which the condition of "continuous tracking" can be maintained. It has been shown that for a wide range of image textures and viewing conditions continuous tracking can be guaranteed, provided the initial guess of the shift vector remains within the resemblance range, or generally less than ±5 pixels. Since the initial guess is based on linear prediction, its quality deteriorates with an increase in sampling interval and likewise its probability to be outside the resemblance range. Hence the probability of occurrence of loss of lock or false lock increases with the sampling interval. However, since the satellite motions are near-deterministic, for the sampling interval of 1 second considered, the initial guess is well within the resemblance range. Although the quality of the initial guess affects the robustness, the accuracy is not affected, provided the algorithm converges to the absolute minimum. However, more iterations and thus more computational resources might be needed to reach the minimum.

The pixel ground plane footprint for a given image shift in pixels, improves the azimuth estimates for texture poor images and has no meaningful effect for texture rich images. However, for the given shift, a reduction in footprint increases the sampling rate. Since a smaller footprint requires a heavier lens, the largest footprint should be chosen, which still meets the demands of accuracy, robustness and sampling rate, i.e. a footprint of 50 m/pixel with a 2.88 frames/sec sampling rate seems appropriate for the problem concerned.

Reference window size is proved to improve robustness and accuracy, by smoothing the cost function as well as the slope of the gradient near the optimum. However, computational efficiency requires to keep the window as small as possible. Texture rich images are shown to have a narrow resemblance range and steep gradient slope, whereas for texture poor images the opposite is the case. Thus, in order to improve accuracy, robustness and computational efficiency, the size of the reference window should be matched to the image. This matching could be performed automatically on-line, in which the slope of the gradient could be used for selecting the optimal window size.

Accuracy and robustness might be further improved by employing a number of reference windows, located at different areas of the image. The shift vector estimate would be based on the weighted average of the estimates for each window individually, where the weighting factors would be determined by the gradient slopes.

A certain shortcoming of the method is its need for orbital position data and rate gyro measurements. Thus the sensor cannot operate in a stand-alone mode and needs to be interfaced with existing satellite systems. On the other hand, when digitized image sequences from an existing camera are available, the method does not require additional hardware, except for a slight increase in on-board computational resources. When camera images are not available or can not be used, the installation of a miniature, light-weight CCD camera might be a suitable solution.

## 5. Acknowledgement

The subject of this research was proposed by Professor S. Merhav, Head of the Flight Control Laboratory of the Faculty of Aerospace Engineering of the Technion, Haifa, Israel, and was subsequently funded by the Electronics Division of the Israel Aircraft Industries.

## 6. References

1. Potter, J.E. and van der Velde, W.E., "Optimum Mixing of Gyroscope and Star Track Data," Journal of Spacecraft, Vol. 5, No. 5, May 1968, pp. 536-540.

2. Bryson, A.E. and Kortum, W., "Estimation of the Local Attitude of Orbiting Spacecraft," Automatica, Vol. 7, Pergamon Press, 1971, pp. 163-180.

3. Gai, E., Daly, K., Harrison, J. and Lemos, L., "Star-Sensor Based Satellite Attitude /Attitude Rate Estimator," AIAA Journal of Guidance, Control and Dynamics, Vol. 8, No. 5., Sept-Oct. 1985, pp. 560-565.

4. Psiaki, M.L., Martel, F. and Pal, P.K., "Three-Axis Attitude Determination via Kalman Filtering of Magnetometer Data," AIAA Journal of Guidance, Control and Dynamics, Vol. 13, No. 3, May-June 1990, pp. 506-514.

5. Leffets, E.J., Markley, F.L. and Shuster, M.D., "Kalman Filtering for Spacecraft Attitude Estimation." AIAA Journal of Guidance, Control and Dynamics, Vol.5, No.5, Sept-Oct. 1982, pp. 417-429.

6. Wertz, J.R., "Spacecraft Attitude Determination and Control," Reidel Publishing Company, Dordrecht, Holland, 1988.

7. Verri, A. and Poggio, T., "Motion Field and Optical Flow: Qualitative Properties," IEEE Trans. on Pattern Analysis and Machine Intelligence," Vol. 11, No. 5, May 1989, pp. 490-498.

8. Fennema, C.L. and Thompson, W.B., "Velocity Determination in Scenes Containing Several Moving Objects," Computer Vision, Graphics, and Image Processing, Vol. 9, 1979, pp. 301-315.

9. Nagel, H.H., "Displacement Vectors Derived from Second-Order Intensity Variations in Image Sequences," Computer Vision, Graphics, and Image Processing, Vol. 21, 1983, pp. 85-117.

10. Gelb, A., "Applied Optimal Estimation," MIT Press, Mass., USA, 1980.

11. Matthies, L., Kanade, T. and Szeliski, R., "Kalman Filter Algorithms for Estimating Depth from Image Sequences," Int. Journal of Computer Vision Vol. 3, 1989, pp. 209-236.

12. Heel, J., "Dynamic Motion Vision," North-Holland Robotic and Autonomous Systems, Vol. 6, 1990, pp. 297-314.

13. Merhav, S.J. and Bresler, Y., "On-Line Vehicle Motion Estimation from Visual Terrain Information; Part I: Recursive Image Registration," IEEE Trans. on Aerospace and Electronics Systems, Vol. AES-22, No. 5, Sept. 1986, pp. 583-587.

14. Bresler, Y. and Merhav, S.J., "On-Line Vehicle Motion Estimation from Visual Terrain Information; Part II: Ground Velocity and Position Estimation," Trans. on Aerospace and Electronics Systems, Vol. AES-22, No. 5, Sept. 1986, pp. 588-603.

15. Bresler, Y. and Merhav, S.J., "Recursive Image Registration with Application to Motion Estimation," IEEE Transactions on Acoustics, Speech, and Signal Processing, Vol. ASSP-35, No. 1, Jan. 1987, pp. 70-85.

16. Barnea, D.I. and Silverman, H.F., "A Class of Algorithms for Fast Digital Image Registration," IEEE Trans. on Computers, Vol. C-21, No. 2, Feb. 1972, pp. 179-186.

17. Mostafavi, H. and Smith, F.W., "Image Correlation with Geometric Distortion; Part I: Acquisition Performance," IEEE Trans. on Aerospace and Electronic Systems, Vol. AES-14, No. 3, May 1978, pp. 487-493.

## 7. Appendix

Fig. 9 shows the sun sensor geometry. The sun azimuth angle is $\lambda$ and the sun elevation angle is $\delta$. The angles between the $z_b$-axis and the projections of the sun vector on the $y_b$-$o$-$z_b$ and $x_b$-$o$-$z_b$ planes, are $\alpha$ and $\beta$, respectively. The output signals of the sun sensor are the tangents of $\alpha$ and $\beta$. Based on the known position of the satellite in orbit and the position of the sun, the tangents of $\alpha$ and $\beta$ in the alignment system $a$, can be computed. The difference between the measured tangents of the angles $\alpha$ and $\beta$ and the computed ones, constitute the measurements $z_\alpha$ and $z_\beta$, and express the angular difference between the actual orientation $b$ and the desired orientation $a$. The complex relation between the sun sensor measurements $z_\alpha$ and $z_\beta$ on one hand, and the angles $\psi$, $\theta$ and $\phi$ on the other hand, is developed in Ref. [ 6]. As shown in Eq. (3) $z_\alpha$ and $z_\beta$ can be expressed as a linear combination of the angles. The coefficients of $H$ are given by:

$$H_{31} = \frac{\sin\lambda\cos\lambda}{\tan^2\delta}\ ;\ H_{32} = -\left(1 + \frac{\cos^2\lambda}{\tan^2\delta}\right);\ H_{33} = \frac{\sin\lambda}{\tan\delta}$$

$$H_{41} = \left(1 + \frac{\sin^2\lambda}{\tan^2\delta}\right);\ H_{42} = \frac{-\sin\lambda\cos\lambda}{\tan^2\delta}\ ;\ H_{43} = \frac{-\cos\lambda}{\tan\delta}$$

where $\lambda$ and $\delta$ are computed analytically and are the sun azimuth and elevation angles with with respect to the alignment system $a$.

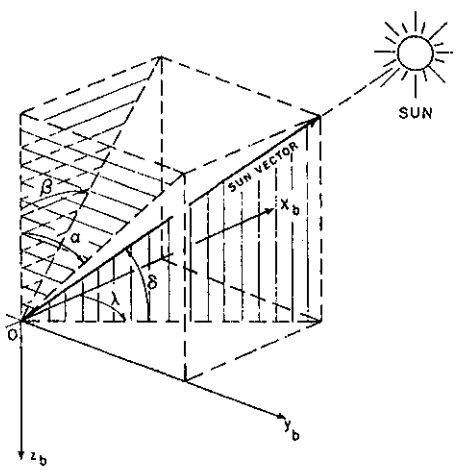


Fig. 9. Sun sensor geometry.

# Attitude Stabilization of Bias Momentum Satellites.

Dr. Marcel Sidi

Israel Aircraft Industries Ltd

M B T ,Yahud,56000

Abstract.

In earth pointing satellites the use of momentum bias is a common practice for stabilizing against external disturbances.This approach is of great utility specially in systems in which the measurment of the yaw angle is not available.The momentum bias provides a natural gyroscopic stability,however, harmonic external disturbances or energy dissipation in the rotor of the momentum wheel might cause instability effects of the nutation or orbital dynamics. An active control is necessary to prevent this possibility.Whatever the control moments should be, magnetic,solar or hydrazine thrusters, the design of the control law is,in general, based on approximate techniques because of the impossibility to separate the x from the z axis dynamics.

In the present paper,a way is suggested to design a controller that meets exactly the stability and disturbance attenuation specifications.

Nomenclature

| | |
|---|---|
| ø,θ,Ψ | -Euler angles in reference frame |
| hw | -bias momentum of the wheel on the y-body axis |
| Ix,Iy,Iz | -principal moments of inertia |
| Ixy,Iyz | -products of inertia |
| Txc | -torque command on the x axis |
| Tzc | -torque command on the z axis |
| Tyc | -torque command on the y axis |
| Kx,Kxd,a | -controller parameters |
| wo | -orbital frequency |
| wnut | -nutation frequency |
| wn1,wn2 | -modal frequencies of the closed loop controlled system |
| z1,z2 | -damping coefficients of the second order modal poles |
| Nex,Nez | -external disturbances |
| s | -Laplace variable |
| woh | - =wo*h |
| Ψss | -steady state error in yaw (Ψ) |
| øss | -steady state error in roll(ø) |
| HS | -Horizon (Earth) Sensor |
| RG | -Rate Gyro |
| Nø | -RMS noise level of the roll (ø) and pitch (θ) sensor (HS) |
| NRG | -RMS noise level of the Rate Gyro |

## Introduction.

Most of the recent earth- pointing three-axes- stabilized communication or other satellites use a momentum wheel that provides a natural inertial attitude stabilization against external disturbances such as solar disturbances,for high orbit geostationary satellites,or solar and aerodynamic disturbances for low-orbit satellites.

Unfortunately,use of the momentum wheel providing the momentum bias is not sufficient for stabilizing when disturbances exist :harmonic disturbances of the orbital or nutation frequencies may lead to destabilization .

A different kind of destabilization was observed on the OTS/MARECS family of communication satellites .On-orbit experiments showed that energy dissipation in the rotor part of the momentum wheel caused instability of the nutation mode which was not adequetly damped with the active solar sail control system (See Ref.1).

An important feature in using momentum bias in a three-axes earth-pointing satellite is that measuring the yaw angle Ψ becomes unnecessary, since yaw ( Ψ ) and roll ( ø ) errors interchange every quarter of the orbit period.(Estimation of the yaw angle requires complicated and expensive instrumentation , specially when sun measurments are not available during an eclipse.For low orbit satellites the eclipse duration equals almost half the orbit period).

The control moments used in active control during the sailing mode of momentum biased satellites are usually based on the magnetic control moments such as in the RCA Series 3000 family (See Ref.2);gas thrusters,INTELSAT V family (See Ref.3),or with solar pressure moments achieved through differential positioning of the solar pannels,as in the OTS,MARECS family, (See Ref.4 ).

In all these alternatives,the design technique for computing the linear feedback control law should be the same.However, design problems may arise because of different saturation moment levels ,and sensor noise.

Under certain rough approximations there are design techniques to achieve

desired immunity to disturbances,with "satisfactory" damping coefficients which are only approximately achieved (see Ref.5).

In the following,we shall show a way to design the linear control law such that the desired specifications are exactly achieved.In the following stage of the design ,the moment saturation and the attitude and rate measurments noise effects are considered, and the linear control law is changed accordingly.

## 2.Design of the Active Control.

In this section we assume that there exists only principle axes of inertia ,and the momentum axis of the momentum wheel is antiparallel to the y axis of the satellite.

### 2.1 Linearized Attitude Equations.

With no product of inertia, the pitch axis dynamics ( y ) can be separated from the lateral dynamics ( x and z axes ) .

$$Ix.\ddot{\phi} - wo.hw.\dot{\phi} - \dot{\psi}.hw = Nex + Txc \qquad (1)$$

$$Iz.\ddot{\psi} - wo.hw.\dot{\psi} + \dot{\phi}.hw = Nez + Tzc \qquad (2)$$

It is easily shown that if :
hw >>wo*√(Ix*Iz),then the determinant of the above equations is :

$$\delta(s)=(s^2 + wo^2).(s^2 + wnut^2)$$

with $wnut=\sqrt{hw^2/(Ix*Iz)}$

An external harmonic disturbance with a frequency wo, leads to a linearly growing harmonic output of $\psi$ and $\phi$.

### 2.2 The Linear Control Law:Exact Approach.

In case $\psi$ and $\phi$ can both be measured,the straightforward control law should be :

$$Txc = -kx.\phi - kxd.\dot{\phi} \qquad (3)$$

$$Tzc = -kz.\psi - kzd.\dot{\psi} \qquad (4)$$

Since we are interested in the practical case in which measurment of the yaw angle is not practically possible, Tzc becomes :

$$Tzc=-a.Txc \qquad (5)$$

See Fig.1.

Equations (1) and (2) become:

$$Ix.\ddot{\phi} - wo.hw.\phi - \dot{\psi}.hw + kx.\phi + kxd.\dot{\phi} = Nex \qquad (6)$$

$$Iz.\ddot{\psi} + \dot{\phi}.hw - \psi.wo.hw + a.kx.\phi + a.kxd.\dot{\phi} = Nez \qquad (7)$$

With hw=-h and woh=wo*h ,the determinant of eqs. (6) and (7) becomes :

$$\delta(s)=s^4.Ix.Iz + s^3.Iz.kxd + s^2.(Ix.woh+Iz.woh+Iz.kx+h^2+a.h.kxd) + s.(kxd.woh+h.a.kx) + woh^2 + kx.woh \qquad (8)$$

Solving for $\phi$ and $\psi$ from (6) and (7) in terms of Nex and Nez,we get:

$$\psi ss=Nez/woh+a.Nex.kx/[woh.(kx+woh)] \qquad (9)$$

With kx>>woh and a<1 which usually hold and, given the permitted $\psi ss$,Nex,Nez, and wo,we easily find the minimum necessary hw=-h.

$$\phi ss/\ Nex = 1/(woh+kx) \qquad (10)$$

hw (=-h) has been computed from eq.(9), knowing the maximum external disturbances and the permitted $\psi ss$.Knowing the maximum permitted $\phi ss$ and hw,we compute kx from eq.(10).The next step shall be to find kxd and a.

The determinant of the closed loop system ,Eq.(8), is of the forth order,which means that we expect two complex roots,(wn1,z1) and (wn2,z2). Hence,δ(s) of the closed loop system can be equated to:

$$[s^2+2.z1.wn1+wn1^2][s^2+2.z2.wn2+wn2^2]=$$

$$s^4+s^3.(z1.wn1+z2.wn2).2 + s^2.[(wn1)^2+(wn2)^2+4.z1.z2.wn1.wn2] + s.(z1.wn2+z2.wn1).2.wn1.wn2 + (wn1)^2.(wn2)^2 \qquad (11)$$

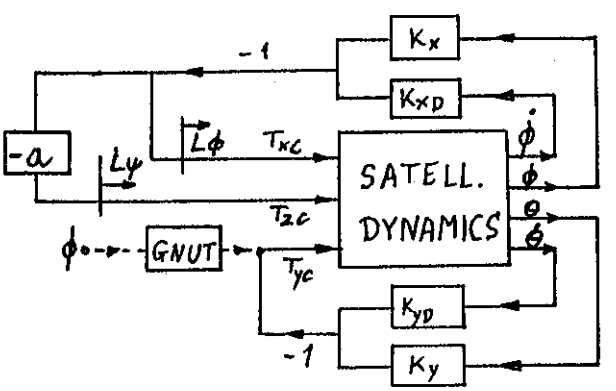


FIG. 1

Untill now,we have computed hw and kx from specifications on acceptable steady state errors in $\Psi_{ss}$ and $\phi_{ss}$,the maximum disturbances Nex and Nez being known.What is left is to find kxd and a.

After equating coefficients of both polynomials in eqs.(8) and (11) we have the following four equations:

$$(wn1)^2.(wn2)^2=woh.(woh+kx)/(Ix.Iz) \quad 12)$$

$$2.wn1.wn2.(z1.wn2+z2.wn1)=(kxd.woh+a.h.kx)/(Ix.Iz) \quad (13)$$

$$(wn1)^2+(wn2)^2+4.z1.z2.wn1.wn2=[(Ix+Iz).woh+Iz.kx+h^2+a.h.kxd]/(Ix.Iz) \quad (14)$$

$$2.(z1.wn1+z2.wn2)=kxd/Ix \quad (15)$$

In these four equations,kx,woh,Ix, Iz ,z1 and z2 are known.We are left with four unknowns which are kxd,a,wn1 and wn2. The first two unknowns are control gains we are looking for.The last two,wn1, and wn2, are byproduct results.

The solution of these equations is straightforward if we put z1=z2.Eq.(10) shows that kx may become negative.There is nothing wrong with that possibility. However,stability considerations,as per eq.(8) show that kxd must always be positive.

For illustartion purposes,we shall deal with the following two examples :

Example 1 (geosynchronous orbit) :

Nex=Nez=5.exp(-6) Nm.
$\Psi_{ss}$=0.4 deg.; $\phi_{ss}$=0.05 deg
Ix=800; Iz=1000 Kg.m$^2$
z1=z2=0.7

From eq.(9) we compute h=10 Nms. From eq.(10) we find kx=0.005 . By solving the simultaneous equations (12) to (15) we find :

kxd=18.; a=0.559
wn1=0.0159 ; wn2=1.43* exp(-4) rad/sec

Example 2 (a circular orbit,R=7378 kms)

For the same data and specifications as in Example 1,we find that:

kx=-0.00423 ; kxd= 20.2; a=0.723

wn1=0.0175; wn2=4.82 exp(-4) rad/sec

Simulation in the frequency domain shows that the roots of the closed loop systems achieved the desired damping coefficients (z1=z2=0.7) with exactly the same modal frequencies wn1 and wn2.

It is important to show the open loop gains $L\phi$ and $L\Psi$ of the Txc and Tzc feedback loops as shown on Figs.2 & 3,on the Nichols chart,for Example 1. The Gain and Phase margins (GM and PM) obtained are clearly satisfactory.

The above results are the first stage of the design process.We must then consider the problem of sensor noises which are amplified and mixed with the torque commands Txc and Tzc.

( Most of the numeric results will be given for Example 1,if not otherwise stated).

## 3. Sensor Noise Amplification.

The most common way to measure the roll angle $\phi$ is by using an Earth Horizon Sensor (HS).These sensors are naturally noisy.A good instrument has a noise level of about 0.03 deg RMS.

It is easily shown by solving eqs.(3),(5),(6) and (7) that the sensor noise amplification is infinite if adequate filters are not added to kx and kxd.Moreover,if no rate gyro (an expensive device) is used to measure

the rate $\dot{\phi}$ , $\phi$ must be differentiated,adding to the noise amplification.

In the following,both cases will be treated individually.

### 3.1. No Rate Gyro for Measuring $\dot{\phi}$ .

With no rate gyro in the loop,the final controller becomes:

$$G(s)=(kx+s.kxd)/(1+s/\alpha1)(1+s/\alpha2) \quad 16)$$

$\alpha1$ and $\alpha2$ are to be chosen such that the RMS noise amplification Txc/N$\phi$ is minimized with no appreciable deterioration of the stability margins (hence also of z1 and z2 )

For the present Example 1 ,with $\alpha1$=0.1 and $\alpha2$=0.2 rad/sec ,we find : Txc/N$\phi$=0.484;Tzc/N$\phi$=0.0993 .

The gain and phase margins of L$\phi$1 and L$\Psi$1 are practically the same ,see Figs.2 and 3.

The closed loop modal roots changed to :wn1=1.436* exp(-4) ,z1=0.6699
wn2=1.968* exp(-2) ,z2=0.6648
which are acceptable results.

For a good Infra-red Earth Sensor, the noise level is of the order of 0.03 degs RMS (3$\sigma$).With the noise amplification of the present solution, the noise level at the moment controllers will be of the order of :

TxcN$\phi$ = 0.03*0.484/57.321=253 $\mu$Nm. RMS

In geostationary orbits,it is quite difficult to obtain torque commands of similar magnitudes.

The maximum achievable torques with solar pannels are of the order of 5 to 15 μNm ,which is much below the torque noise level of the present solution.The logical way to circumvent the moment saturation problem is to increase its level.However,this approach is generally not practically possible from an engineering point of view.For instance,for a solar sail controlled satellite,increasing the moment saturation level by a factor of two is accompanied by increase of the solar pannels surfaces by approximately the same factor.

With magnetic torquers providing 350 A.m²(as used in the satellite SATCOM/KU),torques in the range of 35 μNm are achievable.

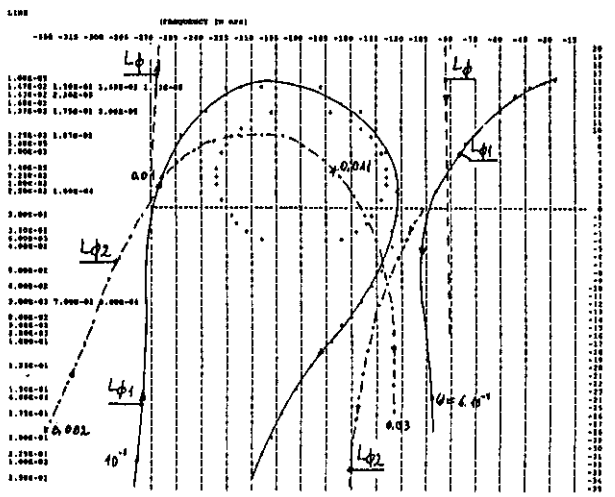

FIG. 2

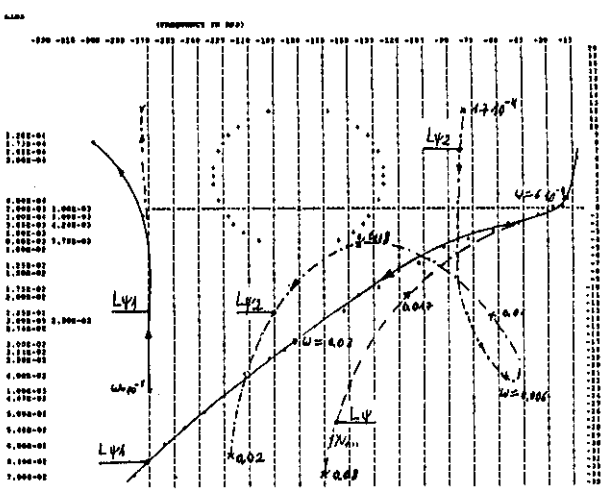

FIG. 3

Hence,in both cases,the torque controllers shall be saturated by the amplified noise of the Earth sensor (unless the torque capabilities are drastically increased).

In Example 2,with the low orbit satellite,the noise amplification is about 0.45 ,which leads to a noise torque of about 0.25 mNm RMS.

With the same magnetic torquers,in a low orbit satellite (about 1000 Kms height),torques in the range of 5-7 mNm can be easily achieved ,(depending on the orbit inclination),so that the noise amplification problems is much easier to handle. See Figs.4,and 5 for a 6D of freedom simulation.

In these figures,with a ø measurment noise of 0.03 deg. RMS,the torque command noise levels and the magnetic torquers levels are as follows:

Txcn= 0.2 mNm RMS;Tzxn=0.15 mNm RMS. Mxn =8.9 A.m² RMS;Mzn=12.4 A.m² RMS, which are well below the saturation levels.

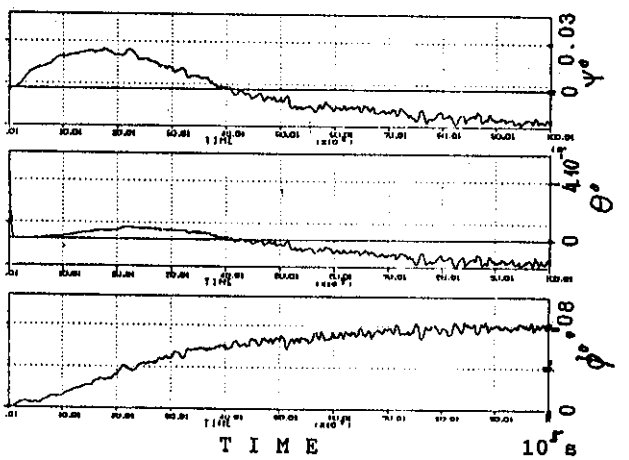


FIG. 4

In case that the torque noise level stays beyond the torque capabilities of the controller,as in Example 1 ,it is imperative to decrease the torque noise level if the control system is to work at all.We shall mention two possible methods to decrease the amplified noise:

1. Decrease of the noise amplification by simultaneously decreasing the damping coefficient factor of the nutation mode,without decreasing appreciably the damping of the orbit mode, which is at a much lower frequency range than the nutation mode.

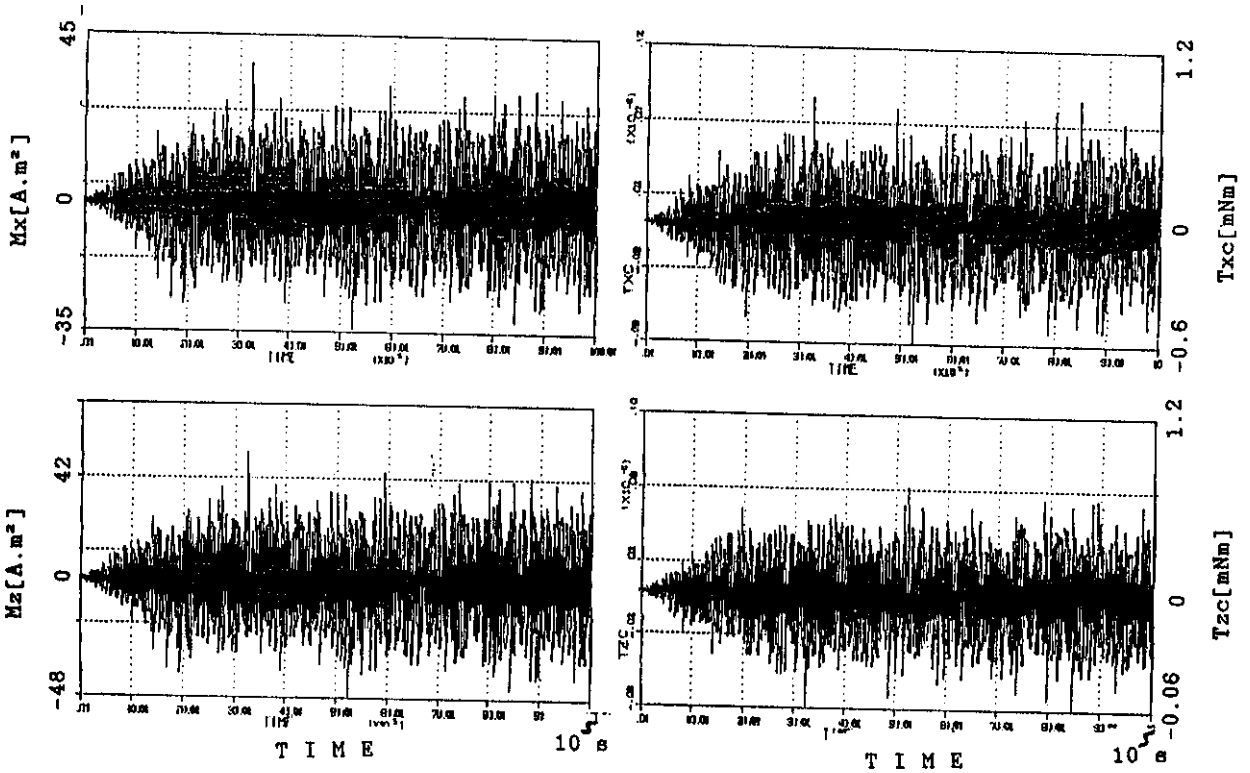


FIG. 5

This effect is easily achieved by decreasing the gain coefficient kxd in Eq.(3). Some results follow in Table 1:

| kxd | z1 -orb | z2 -nut | Txc/Nø | Tzx/Nø |
|---|---|---|---|---|
| 18. | 0.699 | 0.6648 | 0.4484 | 0.0983 |
| 9. | 0.675 | 0.34 | 0.237 | 0.0460 |
| 4.5 | 0.67 | 0.137 | 0.117 | 0.0225 |
| 1. | 0.664 | 0.0296 | 0.0234 | 0.0049 |
| 0.39 | 0.664 | 0.0028 | 0.0091 | 0.0019 |

The above table clearly shows that in order to satisfy the torque capabilities of the satellite in Example 1,a drastic decrease of the nutation damping factor is necessary,with all the drawbacks involved as in Ref. 1.
With the nutation damping approaching zero,any initial nutation is almost undamped.Should it stay undamped ,but with a non-diverging acceptable amplitude,this could be a solution.Unfortunately,as we have already mentioned, unpredictable physical effects may cause nutational instability of the system (Ref.1).

To emphasize the meaning of Table1 suppose we agree to decrease the damping factor of the nutation mode to z2 = 0.0296 ;this is accomplished by decreasing kxd to kxd=1. The results of a 6D simulation are shown in Figs.6 and 7 . In Fig.7,the levels of Txc, Tzc,Mx and Mz are prohibitively high,and unacceptable.With the same level of measurment noise of the Earth sensor of 0.03 deg. RMS,the following noise levels were seen:
Txcn=9.7 μNm RMS ;Tzcn=5.45 μNm RMS
Mxn =53 A.m² RMS ;Mzn =95 A.m² RMS

These values are still high for a practical engineering solution.

2.There is a possibility to keep a much lower level of noise amplification, by a greater decrease of kxd,but, with the use of the product of inertia, to reincrease adequately the damping factor of the nutation mode.

Although not in the scope of the present paper,this approach will be briefly discussed in Section 5.

### 3.2. A Rate Gyro Exists for Measuring ø

In this case ,use is made of the Earth sensor for measuring ø only;the rate $\dot{ø}$ is measured with the rate gyro. In this case the Earth sensor output is not differentiated.

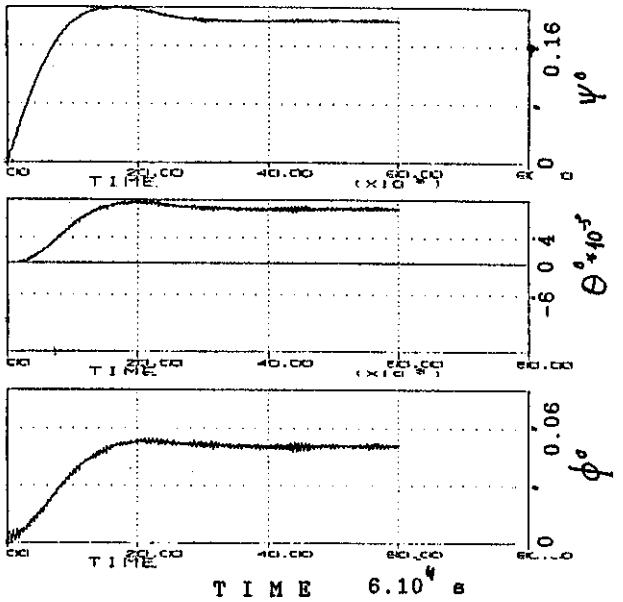


FIG. 6

The noise PSD of a good rate gyro is about 0.02(degr/hr)²/hz (as in the Ferranti gyroscope used in the Telecommunication Satellite Olympus) .

The bandwidth of the control loops are less than 0.2 rad/sec=0.0477 hz/sec.

Hence,the torque command due to the rate gyro will be less than 1 μNm. RMS,which is an acceptable level.

## 4.The Controller Saturation Problem.

The controller saturation problem is to be carefully investigated. It is evident that the controller moment saturation level must be higher than the disturbance moment level in both x and z axes,by at least a factor of two to three.Even with this moment saturation margin,care must be taken to prevent moment saturation by decreasing accordingly kx and kxd during initial transients.

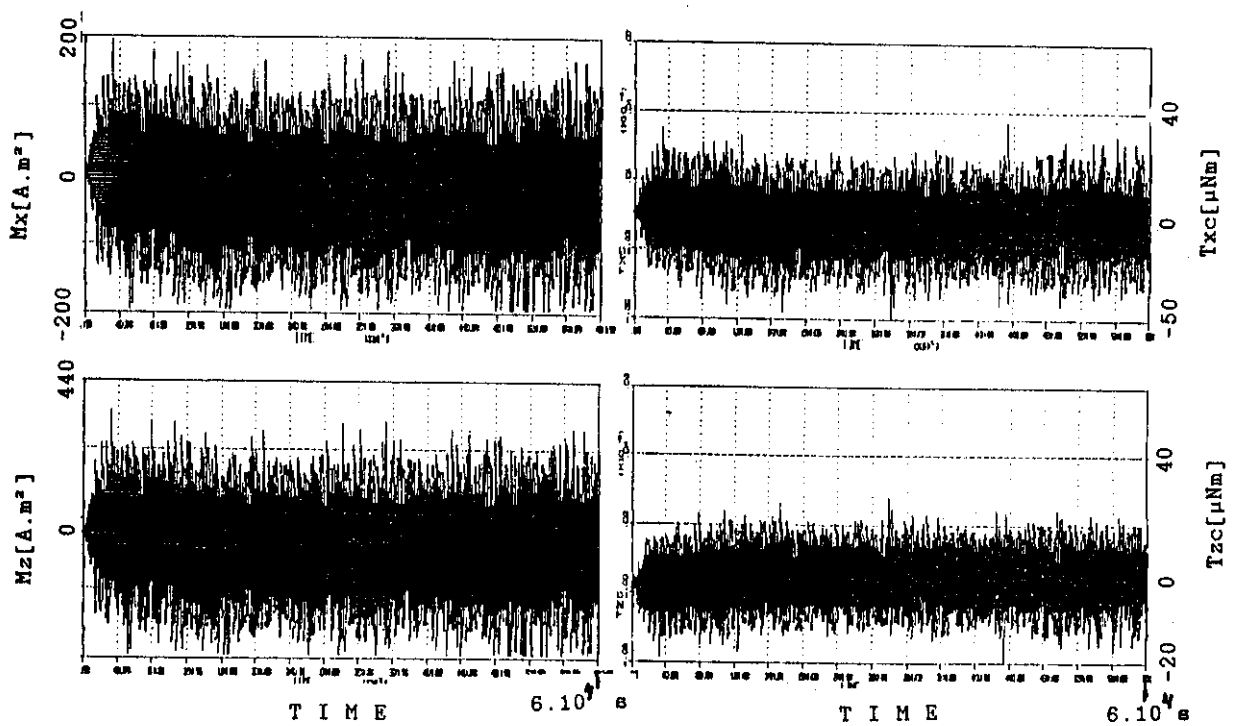


FIG. 7

In Example 1,the noise amplification of both horizon sensor and rate gyro noises were computed and are respectively :

Txc/NRG =3.49;Txc/Nø=8.66*exp(-4)

(The torque command level due to the ø noise is insignificant).

## 5. Active Denutation via Iyz or Ixy

An original way to stabilize the nutation mode by using products of inertia was first mentioned in Ref.6. A complete analysis of the proposed approach follows in Ref.7. The results obtained by using this approach are very good,so that ,although not in the scope of the present paper,a short review of the results is worthwhile.

The basic idea is to damp the nutation mode of the x-z axes dynamics via the torque capabilities of the momentum wheel.A normal momentum wheel has torque capabilities in the range of at least 50 to 100 mNm,which is several orders higher than the torque capabilities achievable in geosynchronous satellites with solar pannels,and even with magnetic torquers ,as explained in the previous sections.

If products of moment do exist,for instance, Iyz or Ixy ,(it is immaterial which one ) the nutation mode can be damped via the y axis dynamics whose control torques are achieved with the momentum wheel. Use is then made of the control network GNUT(s) in Fig.1.

A complete analysis and design procedure are given in Ref.7.

For the special Example 1 of this paper:

$$GNUT(s)= 2000.s./(wnut=0.03,znut=1). \quad (17)$$

kxd has been drastically decreased to the value of kxd=0.05,which,with GNUT(s) =0 ,leaves the system practically undamped,(see Fig.8),but with a very low amplification of the HS noise.

In Fig.1,the y-axis attitude loop for controlling the pitch angle $\theta$ is achieved with the aid of the gains ky and kyd. The closed-loop bandwidth is $wn\theta$ =0.1 rad/sec.

Use of GNUT(s) as per Eq.(17) and a product of inertia of Iyz=20 $Kg.m^2$ helps to damp the nutation mode to a very satisfactory level,see Fig.9.; for this case kxd=0.05.

Fig.10 shows the torque command magnetic torquers levels,which have been drastically diminished,compare with Fig.7. The RMS values are also very low:

Txcn=0.6 μNm RMS ;Tzcn= 0.33 μNm RMS
Mxn =3.3 $A.m^2$ RMS ;Mzn = 5.9 $A.m^2$ RMS.

With the aid of this approach,the difficulty of damping the nutation mode in Solar Sailing (See Ref.1 ), using solar pannels for achieving control moments,is virtually solved.

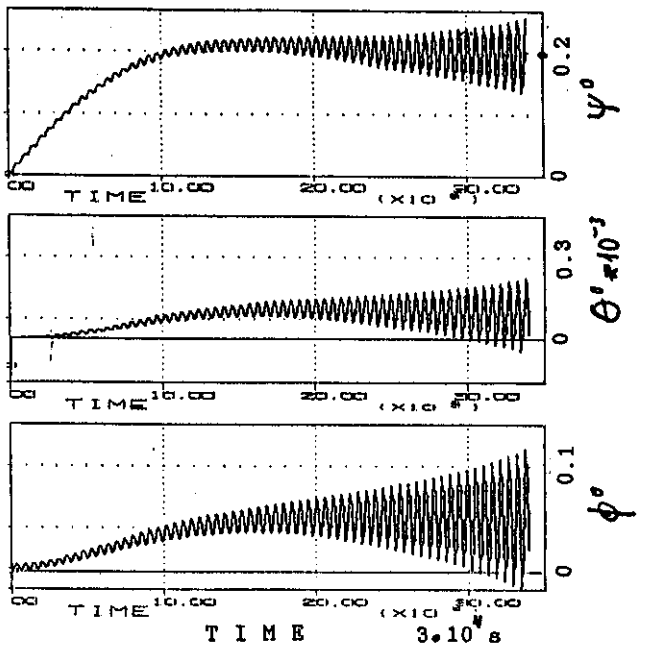


FIG. 8

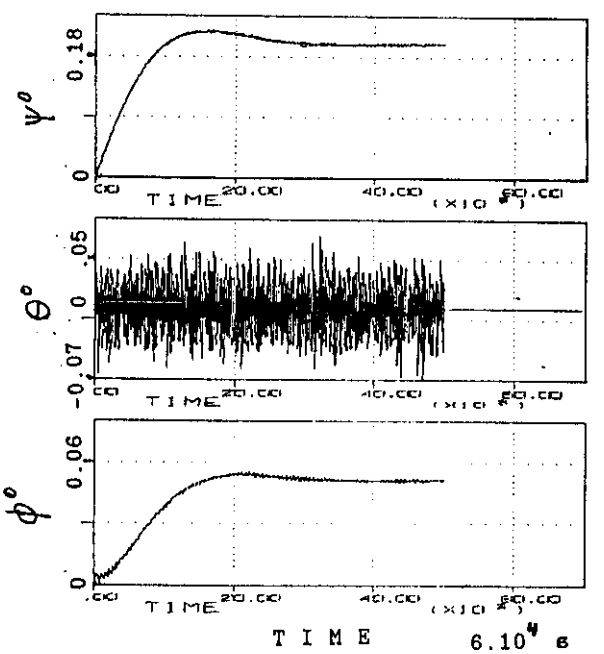


FIG. 9

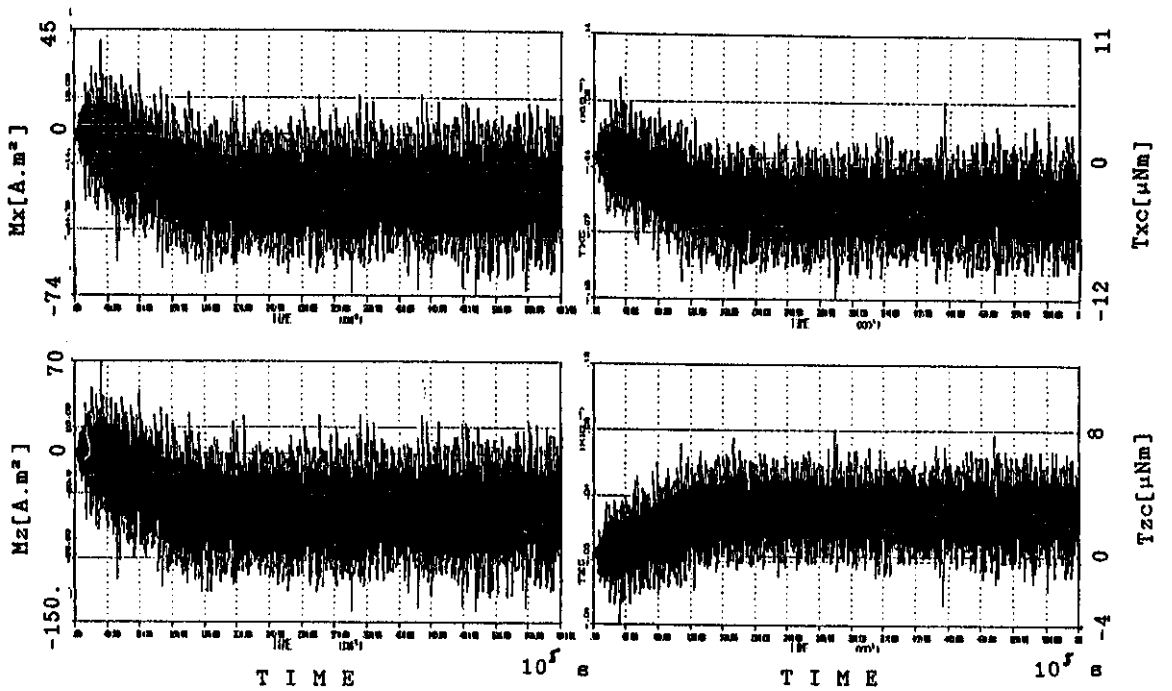


FIG. 10

## 6. Summary and conclusions.

In the present paper, a simple procedure has been shown to exactly compute the gains of the controller of a momentum biased satellite so that desired damping factors of both the orbit and the nutation modes shall be achieved at will.

It has been shown that attitude sensor noise leads, specially for high orbit satellites, to unacceptable levels of command torques, which cannot be achieved by common torque controllers. In these cases, in order to decrease the need of very high torque capabilities, the damping coefficients of the nutation mode should be drastically decreased in the conventional control systems, with no products of inertia. In these cases, uncontrolled instability of nutation may occur because of unpredictable causes.

Use of products of inertia, with a compatible control network, via the pitch (y axis) dynamics and the momentum wheel, helps to satisfactory damp the nutation mode with no problem of excessive amplification of the noise at the level of the x and z axes torque commands.

## REFERENCES


1. Benoit A., Bailly M. "In-Orbt Experience Gained with the European OTS/ECS/TELECOM 1 Series of Spacecraft", AAS 87-054, Proceedings of the Annual Rocky Mountain Guidance and Control Conference, 1987, Keystone, Colorado.
2. Fox S., "Attitude Control Subsystem Performance of the RCA Series 3000 Satellite." Paper 86-0614, AIAA 11 th Communication Satellite Systems Conference, 1986, San Diego, California
3. Bittner H., Bruderl E., Roche c., Schmidts W., "The Attitude Determination and Control Subsystem of INTELSAT V Spacecraft". Proceedings of AOCS Conference, Noordwicjk, 3-6 October 1977.
4. Lievre J., "Solar Sailing Attitude Control of Large Geostationary Satellite", IFAC, Automatic Control in Space, Toulouse, France, 1985.
5. Dougherty H., Lebbock K., Rodden J., "Attitude Stabilization of Synchronous Communications Sattelites Employing Narrow-Beam Antennas", J. Spacecraft, Vol. 8, No 1, August 1971.
6. Muhlfelder L., "Attitude Control System Evolution of Body-Stabilized Communication Spacecraft", AIAA Guidance and Control Conference, 1984, Seattle, Washington.
7. Sidi M., "Hydrazine Sail with Active Denutation via Product of Inertia and Momentum Wheel", 1(3799.1)889-PR, 1990.

Appendix A

Magnetic Control Law.

In this Appendix we assume the existence of magnetic torquers and a momentum wheel for the attitude control of the momentum biased satellite.

In any feedback control configuration, the control commands are some linear or nonlinear function of the measured states.

In the attitude control of satellites ,the states are usually the Euler angles $\phi$, $\theta$ and $\psi$ ,and their derivatives,the quaternion errors ,the directional cosine errors ,etc.

Once the moment control commands around the three body axes have been computed according to the prefered control law,they have to be translated to commands on the magnetic torquers, and the momentum wheel.

The computed control commands are Txc,Tyc and Tzc.

$$\overline{Tc} = \overline{M} \times \overline{B} \qquad (A1)$$

where Mx,My,Mz are the components of the magnetic dipole $\overline{M}$ produced by the magnetic torquers located on the satellite principle axes. Bx,By,Bz are the components of the earth magnetic field $\overline{B}$ in body axes. They are measured by the body fixed magnetometer.

Since $\overline{Tc}$ and $\overline{B}$ are known,we have to find $\overline{M}$.

The matrix form of Eq.(A1) is:

$$\begin{vmatrix} Txc \\ Tyc \\ Tzc \end{vmatrix} = \begin{vmatrix} 0 & Bz & -By \\ -Bz & 0 & Bx \\ By & -Bx & 0 \end{vmatrix} \cdot \begin{vmatrix} Mx \\ My \\ Mz \end{vmatrix} \qquad (A2)$$

Inversion of Eq.(A2) in this nominal form is not possible because the determinant of the matrix is null.

Tc is the result of a vector multiplication.Hence, not all the three axes can be controlled with the three magnetic torquers.In our case,instead of My, we shall use the momentum wheel to control the y axis attitude;the moment achieved by the wheel will be hw=hwd .

Eq.(A2) becomes:

$$\begin{vmatrix} Txc \\ Tyc \\ Tzc \end{vmatrix} = \begin{vmatrix} 0 & 0 & -By \\ -Bz & 1 & Bx \\ By & 0 & 0 \end{vmatrix} \cdot \begin{vmatrix} Mx \\ hwd \\ Mz \end{vmatrix} \qquad (A3)$$

The determinant of the matrix is now finite and equal to $By^2$.Inversion of Eq.(A3) shows that:

$$Mx = Tzc/By \qquad (A4)$$

$$Mz = -Txc/By \qquad (A5)$$

and the torquer on the y axis is superfluous.

The magnetic control of the examples in Section 2 is based on Eqs.(A4) and (A5).

# DYNAMICS AND CONTROL OF A FREE FLYING TWO ARMED ROBOT IN SPACE

Liron Emwald
Technion - Israel Institute of Technology
Haifa 32000, Israel

M. Guelman
RAFAEL, M.O.D.
P.O.Box 2250, Haifa, Israel

P.Th.L.M. van Woerkom
National Aerospace Laboratory, NLR
Postbox 90502
1006 BM Amsterdam, The Netherlands

## Extended Abstract

For the control of manipulator arms two basic approaches exist: the "joint space" approach and the "operational" or "cartesian" approach. In the joint space control approach [1], the control scheme has two levels. On the first level of control transformation is made from a Cartesian description of the end effector path into joint trajectories. This is the problem of inverse kinematics. On the second level the joint control is actually implemented. In the operational space approach the end effector is directly controlled through the joint torques. When using the operational space approach [2] there is no need to compute the joint angles, since they are the result of commanded joint torques. The end effector path generation task is embedded in the control itself.

For a free flying robot in space the problem of controlling the robot manipulator end effector and actually achieve its desired position and orientation, acquires an additional complexity. When using the usual joint controls method the manipulator inverse kinematic equations are applied to compute the required joint angles to achieve the prescribed and effector trajectory. When these joint angle trajectories are implemented, the commanded arm motions produce reaction forces and moments on the robot base that in turn induce both a translation of its center of mass and a rotation about its center of mass. The manipulator joint angles that would normally be commanded in the case of a fixed base will fail to achieve the required task.

In Ref. 3 the control of a manipulator mounted on a free flying satellite was considered and solutions obtained for the inverse kinematics problem. This solution was obtained under very strong assumptions namely:

1. The space base attitude control system will null the effects of the manipulator induced rotational disturbances.

2. The center of mass of the composite system remain inertially fixed.

3. No external forces or torques are applied by and on the manipulator.

In Ref. 4 a control method was proposed based on the operational space approach capable of achieving the desired end effector position and orientation, or their respective desired rate, for a spacecraft mounted manipulator **without constraints** in spacecraft motion or in manipulator exerted forces or torques.

In the operational space approach a joint control torque is defined using the **computed** values of the system generalized matrix of inertia, Coriolis centripetal torque/force vector and the Jacobian matrix generalized inverse and derivative, based on the assumed **known** values of the mass and geometric properties of the manipulator, the payload itself being assumed part of the last manipulator link.

In this work the operational space approach for control is generalized for the case of a free flying robot in space with two manipulator arms. A system model was developed based on the recursive Newton Euler algorithm [5]. By adequately partitioning the system matrices and vectors the control system structure is defined and control algorithms are developed. It is shown that both the robot base and end effectors are free to behave independently and

achieve their required inertial position and attitude as required.

One of the major tasks of the free flying robot is to deal with different classes of payloads, and it should be able to grasp and release payloads with geometric and mass characteristics that in general will be unknown to the robot manipulator control system. It is shown by use of the system digital simulation that when the payload varies in only a few percent with respect to its assumed value the system becomes oscillatory and for larger variations it becomes even **unstable.**

In Ref. 6 was considered the problem of synthesizing the robust algorithms for local joint control with the aim of obtaining an algorithm which is robust with respect to generalized modelling errors and an algorithm based on the use of an observer together with feedforward and feedback loops was proposed there. In this work is shown that in the limit this observer behaves as if the joint **angular acceleration** is directly available to the system.

This basic idea is generalized for the free flying robot by assuming that angular accelerations are measured at each joint. This additional information enables to perform, after an initialization period, an exact on line computation of the components of the generalized matrix of inertia and the Coriolis/centripetal vector. This exact computation enables to assure robust control with the operational space approach. Both the robot base and end effectors are free to behave independently and achieve their required inertial position and attitude as required, while very large variations are allowed for the payload mass/inertia characteristics.

Numerical results are shown indicating that the free flying robot is able to deal with payloads that vary by orders of magnitude without degradation in its performance.

**References**


1. Paul, R.P., "*Robot Manipulators: Mathematics Programming and Control*", Cambridge, Massachusetts, the MIT Press, 1981.

2. Khatib, O., "The Operational Space Formulation in Manipulator Control", Proceedings 15th International Symposium on Industrial Robots, Tokyo, September 1985.

3. Longman, R.W., Lindberg, R.E. and Zedd, M.F., "Satellite Mounted Robot Manipulators-New Kinematics and Reaction Moment Compensation", Paper 85-185, AIAA Guidance, Navigation and Control Conference, New York, N.Y., August 1985.

4. Guelman, M., "Dynamics and Control of a Spacecraft Based Manipulator", National Aerospace Laboratory NLR, The Netherlands, Report TR 87047, February 1987.

5. Wang, L.T. and Ravani, B., "Recursive Computations of Kinematic and Dynamic Equations for Mechanical Manipulators", *IEEE J. of Robotics and Automation*, Vol. RA-1, No. 3, September 1985.

6. van Woerkom, P.Th.L.M. and Steenman, G.J.J., "Synthesis of Local Control for a Robotic Manipulator Joint", National Aerospace Laboratory NLR, The Netherlands, Report TR 88142, August 1988.

# TECHSAT ATTITUDE CONTROL

M. Shachar and R. Vansover

Faculty of Aerospace Engineering
Technion - Israel Institute of Technology
Haifa 32000, Israel

## Abstract

TechSAT is an academic program, of the Technion - Israel Institute of Technology. Emphasizing new engineering solutions, it will be a low cost, 50 kg microsat, sun synchronized, 3-axes stabilized, nadir pointing and launched by Arianne as a piggyback.
Actually it is a gyrostat, based on a momentum wheel, a static horizon sensor, three magnetotorquers and a 3-axes magnetometer, all specially designed for TechSAT with total power consumption < 3W.
The satellite is designed to be released with unknown attitude and with zero stored momentum. The wheel is accelerated to its biased momentum and the body is slowly controlled to become stabilized, using algorithms that utilize magnetometer data only, to an accuracy of $5^o$, which is considered as "coarse cruise".
Next, "fine cruise" uses the static horizon sensor and a final accuracy of $0.1^o$ is reached.

## Nomenclature

XT,YT,ZT = Trajectory Frame, see fig 1.
$\psi,\theta,\phi$ = Euler angles - yaw, roll, pitch defined from Trajectory frame. $\psi$ is the first rotation and $\theta$ is the third.
$\beta$ = The angle between total angular momentum vector and orbit normal
$= \sqrt{(\psi^2+\phi^2)}$
$x,y,z$ = Body Frame. If $\psi = \phi = \theta = 0$ then $(x,y,z)$ = (XT,YT,ZT)
$\hat{i},\hat{j},\hat{k}$ = unit vectors along $x,y,z$
$\hat{i}_{XT},\hat{j}_{YT},\hat{k}_{ZT}$ = unit vectors along XT,YT,ZT
Bo = strength of magnetic field on the equator = $2.22*10^{-5}$ Tesla
$\vec{B}$ = Magnetic Field :
$= B_{XT}\cdot\hat{i}_{XT} + B_{YT}\cdot\hat{j}_{YT} + B_{ZT}\cdot\hat{k}_{ZT}$
$= B_x\cdot\hat{i} + B_y\cdot\hat{j} + B_z\cdot\hat{k}$
$\vec{M}$ = Magnetic Dipole resulting from body fixed magnetotorquers :
$= M_x\cdot\hat{i} + M_y\cdot\hat{j} + M_z\cdot\hat{k}$
$\vec{T}$ = External Torque on Body Frame :
$= T_x\cdot\hat{i} + T_y\cdot\hat{j} + T_z\cdot\hat{k}$
$h_w$ = Momentum of the wheel
$\omega_o$ = Orbital rate

## Introduction

This paper is a status report of the design of TechSAT's Attitute Control , updated to September 1991.
TechSAT will be launched by Arianne as a piggyback. Its height will be 700 Km, in a circular orbit and Sunsynchronous.
TechSAT is a microsat having a weight of 50 Kg, Dimensions of 45 X 45 X 45 cm and moments of inertia of Ixx = 0.7 Kg·m$^2$, Iyy = 0.8 Kg·m$^2$ and Izz = 0.5 Kg·m$^2$.
Designed to be a three axes stabilized platform , the momentum bias solution was chosen due to its simplicity.
The hardware includes a momentum wheel, a static horizon sensor, a three axes magnetometer, three body fixed magnetotorquers and an on-board computer.
Basic requirements and goals are :
1. Full autonomous. Updating once every few days from a ground station is acceptable.

2. Having body mounted solar pannels, the total average power will be 15 Watts. 8 Watts are allowed for total house keeping. That led to the need for small size and low power consuming hardware. The result is new hardware, specialy designed for TechSAT.
3. Accuracy of $0.5^o$
4. Reduced performance without the horizon sensor : 5 to 10 deg accuracy.

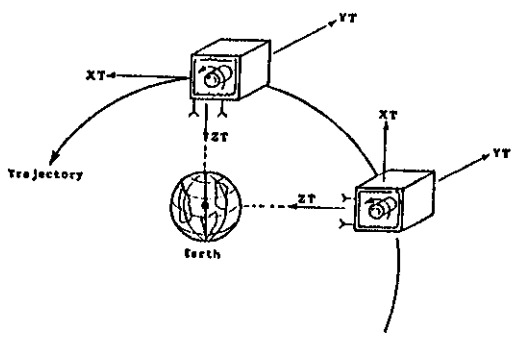


Fig 1 : Spacecraft and wheel's final orientaion

**TechSAT's attitude control missions:**

1. Nadir pointing, three axes stabilized.
2. Wheel and electronics start to operate after release from launcher. The initial attitude is unknown . The initial momentum is approximately zero.
3. Modes of operation defined in table 1.

table 1 : Modes of opration

| Name of Mode | Hardware Involved | | | | Accuracy |
|---|---|---|---|---|---|
| | Wheel | Magneto torquer | Magneto meter | Horizon sensor | |
| Aquisition-option 1 | + | + | + | + | $5^o \div 10^o$ |
| Aquisition-option 2 | + | + | + | | $5^o \div 10^o$ |
| Coarse cruise | + | + | + | | $5^o \div 10^o$ |
| Fine cruise | + | + | + | + | $< 0.5^o$ |

from table 1 it is seen that the spacecraft has the option to operate without a horizon sensor.

4. The total allowed power consumption of attitude control hardware is < 3 Watts.

**Sequence of Operation**

Step 1 : Immediately after release the bias momentum is built up.

$$\vec{h}_w = \hat{j} \cdot h_{w\_bias} \ , \ h_{w\_bias} = -0.6 \ Nt \cdot m \cdot sec$$

since the total initial momentum is nearly zero :

$$0 = \hat{j}(\omega_y \cdot I_y + h_w)$$

now the initial angular momentum for the next step can be calculated :

$$\omega_y(0) = -\frac{h_w}{I_y} = \frac{0.6}{0.8} \frac{[Nt \cdot m \cdot sec]}{[Kg \cdot m2]}$$

So, at the end of step 1 the spacecraft has a high angular momentum :

$$\omega_y(0) = -0.75 \frac{[Rad]}{[Sec]}$$

Step 2 : Aquisition Process, which includes :

1) Removal of body's initial angular momentum, $\omega_y(0)$.
2) Pitch axis of the spacecraft is oriented to be normal to orbit plane with accuracy of $\beta < 10^o$
3) Pitch angle $\theta$ will be less than $10^o$

Step 3 : Cruise :

Two option - Fine and Coarse - as stated in table 1.

**The Aquisition Process (Step 2) :**

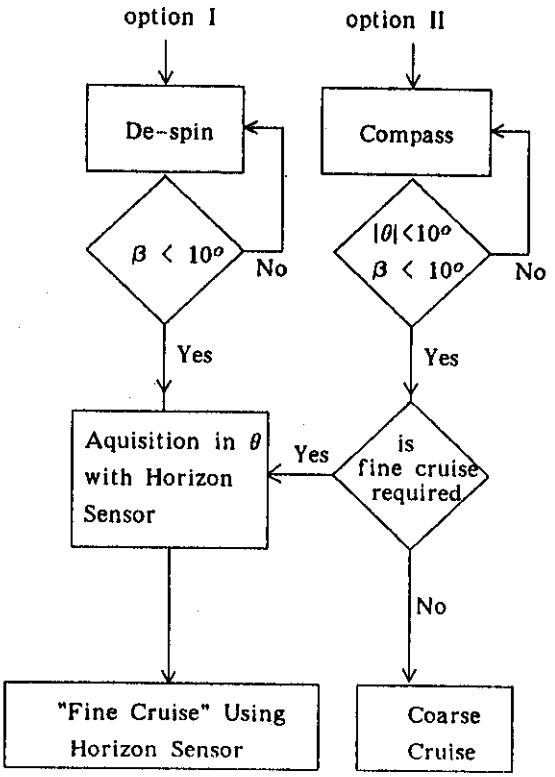


**Torques that take a role in the system :**

1. Magnetic Torque

$T = M \times B = [1\ A_m \cdot m^2][2.22 \cdot 10^{-5}\ \text{Tesla}]$
$= 2.22 \cdot 10^{-5}\ [\text{Nt} \cdot \text{m}]$

2. Reaction Torque (wheel)

$T_{wheel} = 0.02\ \text{Nt} \cdot \text{m}\ (\text{max})$

3. Solar Disturbance Torques

$T_{D\_solar} = (S_{panel}) \cdot (P_{solar}) \cdot (L_{unbalance})$

$= (0.45)^2 \cdot (4.5 \cdot 10^{-5}) \cdot (0.1)$

$T_s \simeq 10^{-7}\ \text{Nt} \cdot \text{m}$

4. Gravitational Torques

For small angles (Ref [6]):

$$\vec{T}_{G_b} \simeq 3\omega_o^2 \begin{bmatrix} \phi \cdot (I_z - I_y) \\ \theta \cdot (I_z - I_x) \\ 0 \end{bmatrix} < 10^{-7}\ \text{Nt} \cdot \text{m}$$

5. Disturbance due to Solar Pannel Currents

Due to parazitic dipoles of the solar pannel :

$T_{D\_p} = 10^{-7}\ \text{Nt} \cdot \text{m}$

6. Magnetotorquer Disturbances

Residual Dipole :

$M_{residual} = 0.25\%\ \text{of}\ M_{sat}$

$$T_d = \frac{0.25}{100} \cdot M_{sat} \cdot B_o =$$

$$= \frac{0.25}{100} \cdot [1\ A_m \cdot m^2]\ [\ 2.22 \cdot 10^{-5}\ \text{Tesla}]$$

$< 10^{-7}\ \text{Nt} \cdot \text{m}$

Careful attention should be given to the residual dipole. Otherwise it may become the largest disturbance torque in the system.

**"De-spin" Algorithm**

This algorithm is analyzed in Ref[2].

$$M_n = -K \cdot \dot{B}_{n\_measured} \qquad (n = x,y,z) \qquad (1)$$

The Bang-Bang form :

$$M_n = -\text{Sign}[\dot{B}_{n\_measured}] \qquad (n = x,y,z) \qquad (2)$$

This algorithm has three effects:
1) Removal of the body's angular momentum
2) Nutation Damping
3) Orientation of the pitch axis to become normal to the orbit plane.

About the first effect mentioned above Ref[2] states :

- The kinetic energy associated with the

component of $\vec{\omega}$ parallel to $\vec{B}$ cannot be reduced.
- But fortunately : the direction of $\vec{B}$ is not fixed along the orbit.

The net effect : the satellite is rotating once per orbit about the trajectory pitch axis. (see fig. 2)

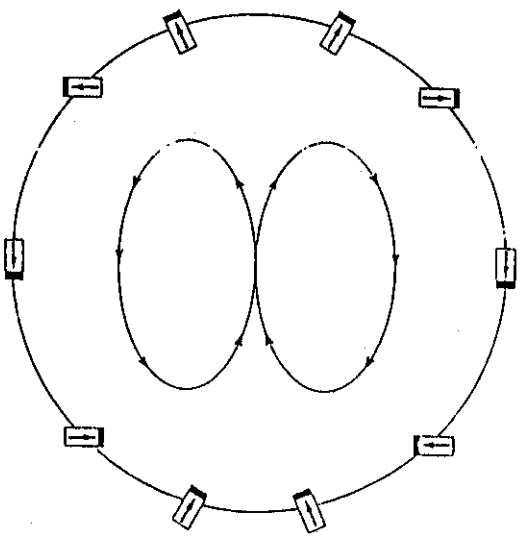

Fig. 2 : A possible final situation resulting from the De-spin algorithm.

For the De-spin algorithm the contribution of this paper is in two points :
1) An analytic proof that only one direction of the spin orientation is stable.
2) Simulation results with measurement noise.

For the analytic proof a great simplification of the magnetic field was done . It was assumed that the magnetic field instead of behaving as a dipole (which by itself is a simplification), rotates only once per orbit, having a component along XT only (fig 3).

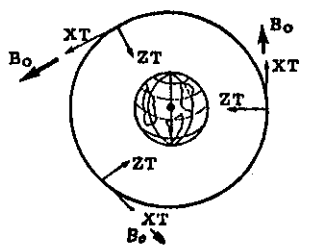


Fig 3 : Simplified Magnetic Field

$$\vec{B} = B_o \cdot \hat{i}_{XT} \qquad (3)$$

A further simplification was the small angle approximation of $\psi$ and $\phi$ :

$$B_y = -\psi \cdot B_{XT} + B_{YT} + \phi \cdot B_{ZT}$$

and by substituting (3)

$$B_y = -\psi \cdot B_o \qquad (4)$$

Applying the De-spin algorithm along the $y$ axis :

$$M_y = -K \cdot \dot{B}_y = -\dot{\psi} \cdot B_o \qquad (5)$$

substituting (4) and (5) into the physical law $\vec{T} = \vec{M} \times \vec{B}$

$$T_x = 0 \quad \text{and} \quad T_z = -K \cdot B_o^2 \cdot \dot{\psi} \qquad (6)$$

The small angle approximation enables to analyze roll/yaw effects and pitch effect independently. Small angle dynamics for $x$ and $z$ axes has the form :

$$\begin{bmatrix} T_x \\ T_z \end{bmatrix} = \begin{bmatrix} I_x \cdot \ddot{\phi} - \omega_o \cdot h_w \cdot \phi - h_w \cdot \dot{\psi} \\ I_z \cdot \ddot{\psi} - \omega_o \cdot h_w \cdot \psi + h_w \cdot \dot{\phi} \end{bmatrix} \qquad (7)$$

From (6) and (7) a characteristic equation for the roll/yaw axes (x and z) comes out :

$$S^4 \cdot I_x \cdot I_z +$$
$$S^3 \cdot I_x \cdot K \cdot B_o^2 -$$
$$S^2 \cdot \{I_x \cdot \omega_o \cdot h_w + I_z \cdot \omega_o \cdot h_w - h_w^2\} -$$
$$S \cdot K \cdot B_o^2 \cdot \omega_o \cdot h_w +$$
$$\omega_o^2 \cdot h_w^2 = 0$$

The Routh stability criteria requires :

$$K > 0 \qquad (8)$$
$$h_w < 0 \qquad (9)$$

Eq. (9) is actually the proof of the statement that only one direction of the spin orientation is stable. Stability is achieved when the spin of the wheel points towards the negative direction of YT.

One can argue about such simplifications of the magnetic field [eq.(3)] on which this proof is based, mainly because the classical dipole approach rotates twice per orbit and therefor $B_{XT}$ is positive in one half of the orbit and negative in the other. But according to the simplification of eq.(3) $B_{XT}$ is always positive.

The answer to this argument is that the basic phenomena of spin orientation results from a precession torque due to the De-spin law and the rotation of magnetic field. The direction of this rotation is not important because the characteristic equation includes $B_o$ in a square form only. It is also unimportant whether the field rotates once or twice per orbit.

Fig. 4a shows a simulation result of the system with an ideal magnetometer and 4b with a noisy magnetometer, both in the Bang-Bang case. The important point to note is the fact that convergence time is much longer in the presents of noise, in the Bang-Bang case.

## "Compass" Algorithm

The following is a simple and straight forward algorithm that enables to stabilize the spacecraft in all three axes by magnetometer data only.

eq.(11):

damping "compass"

$$M_B = -K(\dot{\vec{B}}_{B\_measured} - \dot{\vec{B}}_{B\_expected}) + C\vec{B}_{B\_expected}$$

magnetometer data — from a priori knowledge of magnetic field model

where:

$\vec{B}_{B\_expected}$ – represents the three components of the magnetic field that the spacecraft "expects to measure with an ideal sensor", by assuming that its Body Frame is exactly aligned with the Trajectory Frame. This information is further based on an a priori information of the magnetic field model and the orbital position of the spacecraft. This information has to be programmed in the on-board computer and updated from time to time.

$\dot{\vec{B}}_{B\_expected}$ – is the calculated derivative of the three components of $\vec{B}_{B\_expected}$ .

$\dot{\vec{B}}_{B\_measured}$ – represents the derivatives of the three Body Frame components, as measured or calculated from magnetometer's data.

In the practical Bang-Bang implementation of the compass algorithm the magnetotorquers are "fired" to +Msat, -Msat or zero. Only 26 directions of $\vec{M}_{B\_Bang}$ are possible. The one resulting with minimum angle difference relative to the "linear $\vec{M}_B$" [eq.(11)] is chosen.

Two interesting statements can be discussed about the compass algorithm :

First, it is apparently a strait forward three dimensional extension of the classical compass. But a question appears if such an extension is possible. No doubt that in a static magnetic field this is impossible because there will be ambiguity around the direction of the magnetic field. This ambiguity is resolved due to the fact that the magnetic field rotates.

Second, a significant fact appears that this algorithm is unstable, unless the momentum wheel is used, designed to point the spin to the negative direction of $y$. Other ways to stabilize the algorithm are a subjects to a follow-on research.

The technique to prove the above statement is similar to the one used in the De-spin algorithm.

Again, using small angle approximation together with (3) :

$$\begin{bmatrix} B_x \\ B_y \\ B_z \end{bmatrix} = \begin{bmatrix} 1 & \psi & -\theta \\ -\psi & 1 & \phi \\ \theta & -\phi & 1 \end{bmatrix} \begin{bmatrix} B_{XT} \\ B_{YT} \\ B_{ZT} \end{bmatrix} = B_o \begin{bmatrix} 1 \\ -\psi \\ \theta \end{bmatrix}$$

$$= B_o \cdot (\hat{i} - \hat{j}\cdot\psi + \hat{k}\cdot\theta) \qquad (12)$$

from (12) :

$$\dot{\vec{B}} = B_o \cdot (-\hat{j}\cdot\dot{\psi} + \hat{k}\cdot\dot{\theta}) \qquad (13)$$

from the definition of $\vec{B}_{B\_expected}$ and by the use of (3) :

$$\vec{B}_{B\_expected} = \hat{i}\cdot B_o \qquad (14)$$

$$\dot{\vec{B}}_{B\_expected} = 0 \qquad (15)$$

substituting (13), (14), and (15) into (11):

$$\vec{M} = -K\cdot[-\hat{j}\cdot\dot{\psi} + \hat{k}\cdot\dot{\theta}] + C\cdot[\hat{i}\cdot B_o] \qquad (16)$$

From (12) and (16)

$$\vec{T} = \vec{M} \times \vec{B} =$$

$$= B_o^2 \cdot [\hat{i}\cdot K\cdot(\dot{\psi}\cdot\theta - \dot{\theta}\cdot\psi) - \hat{j}\cdot(K\cdot\dot{\theta} - C\cdot\theta)$$

$$- \hat{k}\cdot(K\cdot\dot{\psi} - C\cdot\psi)]$$

$$\vec{T} \simeq B_o^2 \cdot [-\hat{j}\cdot(K\cdot\dot{\theta} - C\cdot\theta) - \hat{k}\cdot(K\cdot\dot{\psi} - C\cdot\psi)] \qquad (17)$$

combining (17) with (7) a characteristic equation comes out :

$$S^4\cdot I_x\cdot I_z +$$
$$S^3\cdot I_x\cdot K\cdot B_o^2 +$$
$$S^2\cdot[I_x\cdot C\cdot B_o^2 - \omega_o\cdot h_w\cdot(I_x + I_z) + h_w^2] +$$
$$S\cdot[-\omega_o\cdot h_w\cdot K\cdot B_o^2] +$$
$$\omega_o\cdot h_w\cdot(\omega_o\cdot h_w - C\cdot B_o^2) = 0$$

and from Routh criteria :

$$K > 0 \qquad (18)$$
$$h_w < 0 \qquad (19)$$

Eq.(19) is actually the proof that the compass algorithm needs the momentum wheel for stability, and that the momentum must be directed to the negative direction of YT.
Fig. 5a shows a simulation result of the system with an ideal magnetometer and 5b with a noisy magnetometer, both in the Bang-Bang case of the "Compass" algorithm.

**End of acquisition criteria**

At present this has not been completed. However, it is assumed that this is achievable from the magnetometer and horizon sensor data.

**Coarse Cruise**

Coarse Cruise is actually the same as compass algorithm. The only difference is the control cycle. During acquisition it was found that control torques have to be updated once per second. It is expected that at cruise update of once per 2 or 3 seconds will be enough.

**Fine Cruise**

Classical approaches for algorithms that where based on biased momentum, a horizon sensor and magnetotorquers included passive, mechanical, nutation dampers. Stickler (Ref.[2]) suggested the use of the magnetometer data for this purpose. The attempt in the TechSAT project is to design a complete roll/yaw loop by use of horizon sensor data only. This has not been completed yet.

## Technical Data of Hardware

Horizon sensor (Manuf. EL-OP)

Features :

- weight < 1Kg
- power consumption < 1 Watt
- Accuracy ± 0.05°
- F.O.V. ± 14°

Type : static sensor
Configuration : 4 sensor units at 90° intervals
Function : detect horizon radiation profile
Criterion : find angle to 50 Km tangent height
Spectral range : 14 -16 um

Momentum Wheel (Manuf. IAI/TAMAM)

- Torque range 0 to 0.02 Nm
- Torque resolution 5μNm (12 bit)
- Torque linearity < 2%
- Torque ripple 10% of applied Torque with fundamental freq. of 5760 Hz (1800 rpm)
- Tachometer pulses per resolution 192 pulses/resolution
- Nominal momentum 2 Nm (1800 rpm)
- Momentum range 0 to 4 Nm at 0 to 3600 rpm, respectively
- Torque transfer function T - Torque Nm
  α - angular acceleration in $\frac{Rad}{Sec^2}$
  $T = 0.01\ \alpha$
- Temperature range -10 to 60 dec.c
- Input voltage to electronics > 20 Vdc
- Power P - Watt
  ω - speed $\frac{Rad}{Sec}$
  T -Torque Nm
  $P = 0.5 + 0.002\omega + T\cdot\omega$
- Mass M < 2.3 Kg
- Outline dimensions Cylinder: 250 diameter 60 mm height

Magnetometer (Manuf. IAI/TAMAM)

- Dynamic range ± 0.6 Gauss
- Scale Factor 10 V/Gauss
- Zero field output at 25 ± 2 mGauss max.
- Uncertainty in axis alignment ± 0.1°
- Evolution of bias in temp ± 50 μGauss/°C
- Evolution of SF in temp ± 1% in temp range
- Bandwidth (-3dB) 20 ÷ 100 Hz
- Noise 0.1 mGauss
- Noise Bandwidth (0.01 ÷ 10)Hz
- Operating temp. range -40°C ÷ 80°C
- Power consumption (max) 1 Watt
- Mass 0.35 Kg
- Dimensions 110 x 35 x 35 mm

Magnetotorquer (Manuf. IAI/TAMAM)

| | | |
|---|---|---|
| - Dipole moment [Am²] linear range | 1 | 10 |
| - Dipole moment [Am²] saturation range | 1.5 | 14 |
| - Dipole moment [Am²] residual | 0.002 | 0.03 |
| - Length x Dia. [mm] | 175x5.3 | 300x9 |
| - Weight [gr.] core | 34 | 158 |
| wire | 10 | 110 |
| - Power [Watts] | 0.1 | 0.3 |

Note : The 1 [ Am² ] magnetotorquer is designed to be in use. The other one is optional.

## Summary

In this paper it was proved that there is a closed solution to a three axes stabilized spacecraft that operates autonomously, from release phase, with magnetometer data only. The main source of steady state errors of up to 5° in the "coarse cruise" will be the modeling error of the magnetic field. Adding the horizon sensor will improve the accuracy to less than 0.5° and eliminate the necessity for magnetic field updating. The simulations show that the convergence time is less than 70 hours in practical noise environment. A major breakthrough is the advanced control hardware that enables to operate the spacecraft with low power consumption. It is believed that TechSAT is probably the smallest three axes stabilized spacecraft with such performance.
Follow on topics will include :

- Roll/yaw and pitch loops during Fine Cruise
- Sensitivity and round off error analysis
- Disturbance torque analysis
- Magnetic field modeling error analysis
- Filters and optimal estimators
- End of aquisition algorithms
- Suitability for other orbits (lower heights, smaller inclination)

## References

1. Bar-Itzhack I Y & Shorshi G, *Near Earth Orbit Determination Using Magnetometers*, Faculty of Aerospace Engineering, Technion - Israel, 1991.
2. Stikler C & Alfriend K T . *Elementary Magnetic Attitude Control Systems*, J. Spacecraft, Vol. 13, No 5, May 1976, p.282
3. McElroy T T, *Attitude Determination and control of a Spinning satellite Using the Earth's Magnetic Field*, The University of Michigan Ph.D. thesis, 1973, Engineering, electrical.
4. Wertz J R (ed) 1978, *Spacecraft Attitude Determination and control*, D. Reidel Publ. Co., Boston. Publ. ISBN 0-87259-004-6
5. Agrawal B N, *Design of Geosynchronous Spacecraft*, Prentice-Hall Publ. ISBN 0-13-200114-4, 1986, p.130-135

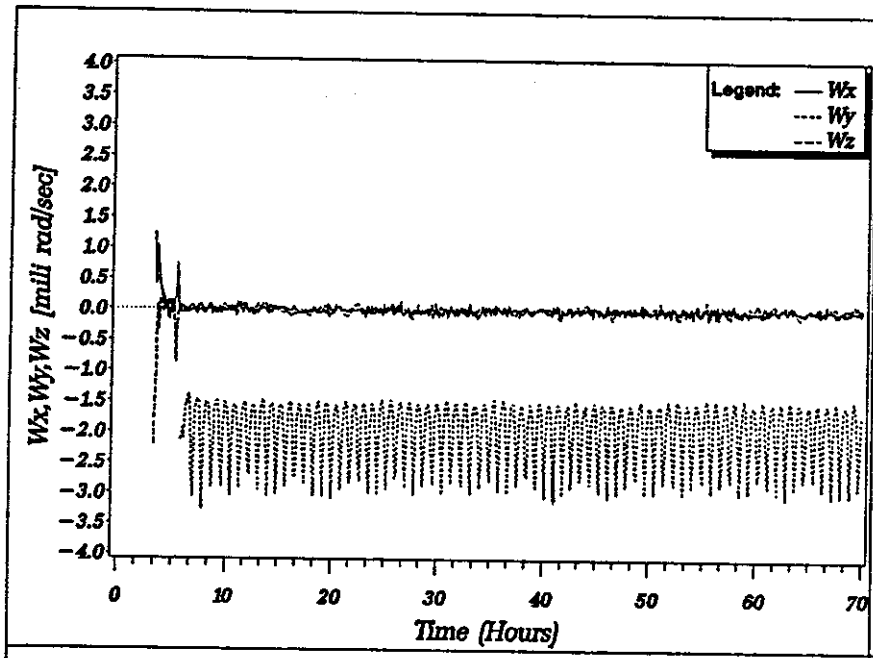


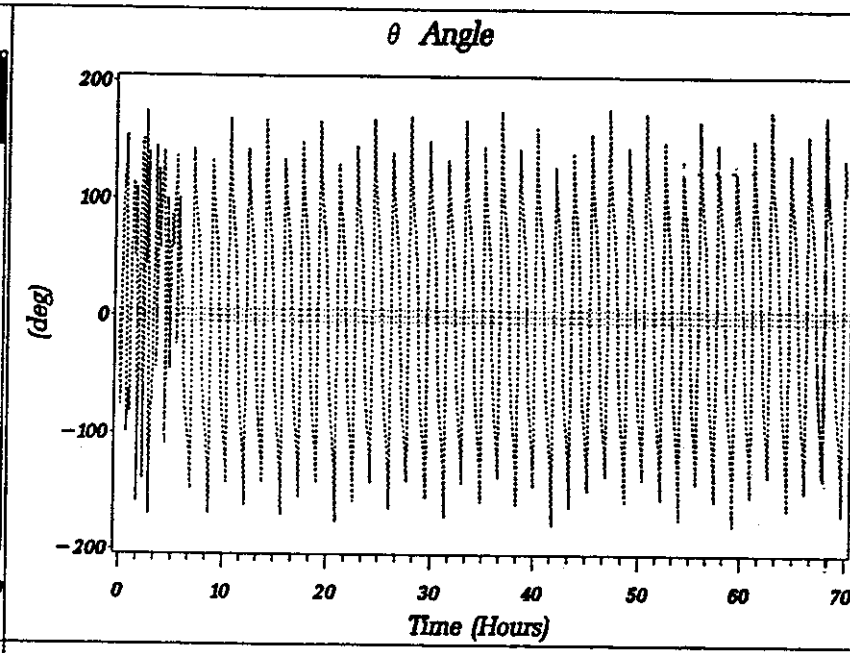


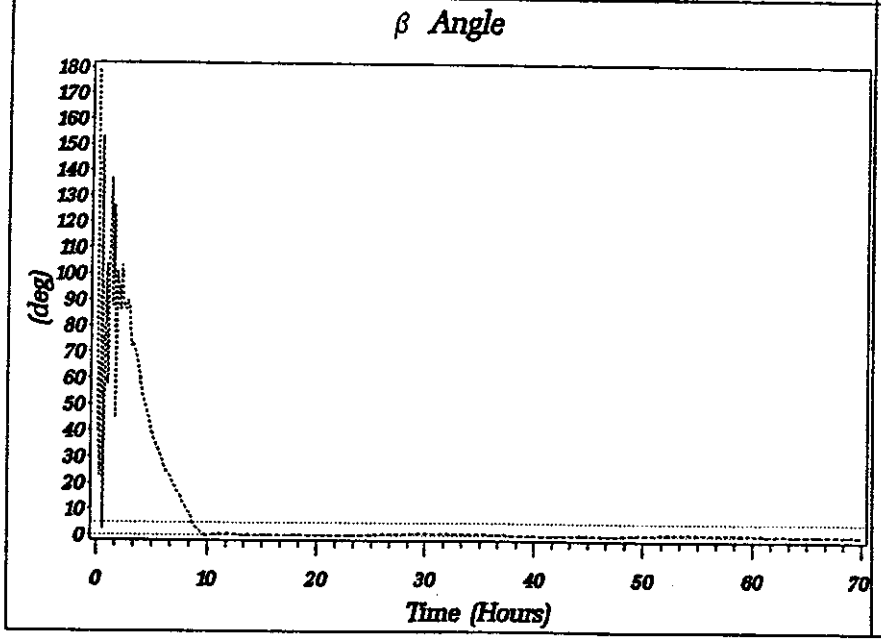


```
98.15     ;orbit_inclination.(98.15.or.90.0)[deg]
11.70     ;magnetic_dipol_deflection.....[deg]
5.00e+07  ;K_of_control_law
1.00e+04  ;C_of_control_law
1         ;c_law:_0=nothing,1=De-spin,2=improved,3=compass,4=horizon
3         ;0=no_limit,1=linear,2=vector_bang,3=signed_bang
0.0       ;delta_alfa_above_poles.....[deg]
1.0       ;Msat.....[Amp*m^2]
0.7       ;Ix.....[kg*m^2]
0.8       ;Iy.....[kg*m^2]
0.5       ;Iz.....[kg*m^2]
-0.60     ;H_wheel_final.....[N*m]
0.0       ;Wheel_start_time(0=no_start_process).[sec]
0.25      ;Wx_initial(1).OR.Phi_dot(2).....[rad/sec]
0.80      ;Wy_initial(1).OR.Teta_dot(2).....[rad/sec]
0.25      ;Wz_initial(1).OR.Psi_dot(2).....[rad/sec]
0.00      ;Phi_initial.....[deg]
0.00      ;Theta_initial.....[deg]
179.00    ;Psi_initial.....[deg]
0         ;0=no_gravity,1=gravity
0.10      ;dt_for_integration.....[sec]
2         ;1=circular,2=Model_B,3=Model_A
0.0       ;Sigma_of_magnetometer_noise.....[miliGauss]
1         ;0=open_loop,1=close_loop
10        ;control_interval
```

Fig 4a : Simulation results of De-spin with no noise.

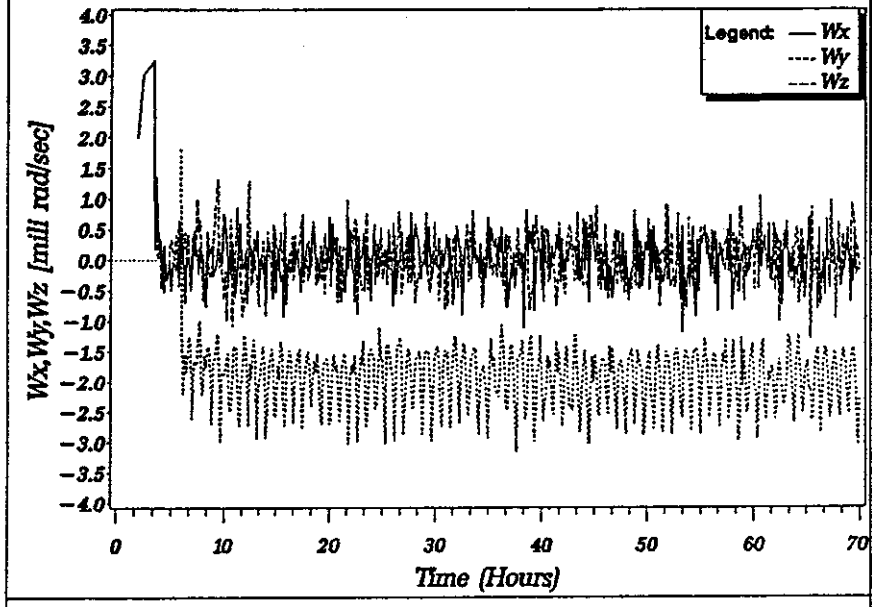


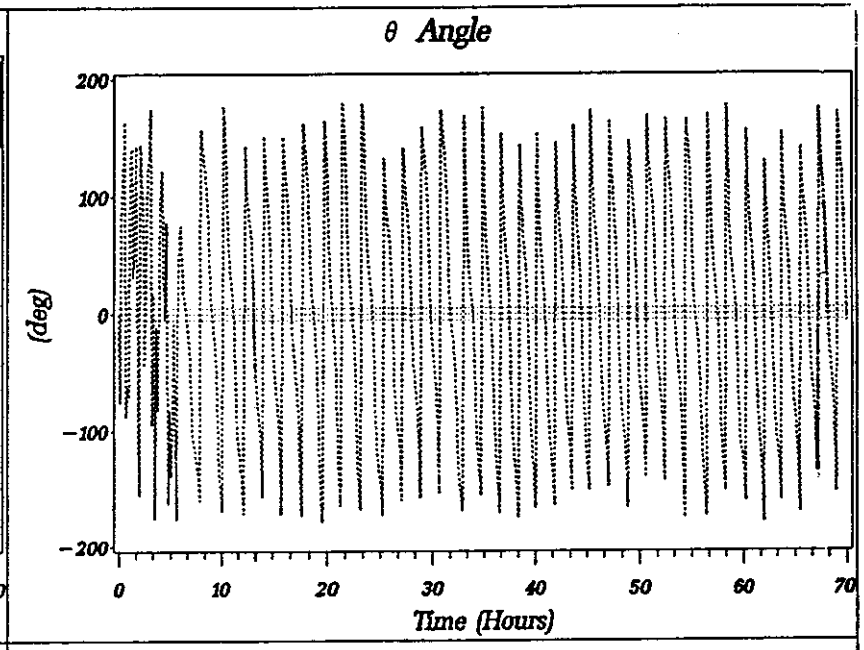


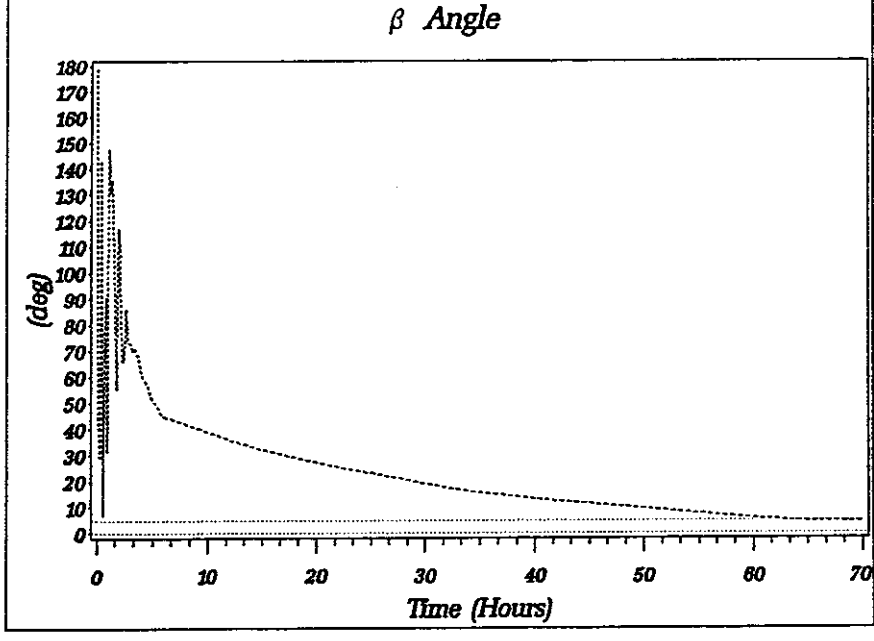


```
98.15     ;orbit_Inclination.(98.15 or 90.0)[deg]
11.70     ;magnetic_dipol_deflection.......[deg]
5.00e+07  ;K_of_control_law
1.00e+04  ;C_of_control_law
1         ;c_law:_0=nothing,1=De-spin,2=improved,3=compass,4=horizon
3         ;0=no_limit,1=linear,2=vector_bang,3=signed_bang
0.0       ;delta_alfa_above_poles..........[deg]
1.0       ;Msat............................[Amp*m^2]
0.7       ;Ix..............................[kg*m^2]
0.8       ;Iy..............................[kg*m^2]
0.5       ;Iz..............................[kg*m^2]
-0.60     ;H_whell_final...................[N*m]
0.0       ;Wheel_start_time(0=no_start_process).[sec]
0.25      ;Wx_initial(1).OR.Phi_dot(2).....[rad/sec]
0.80      ;Wy_initial(1).OR.Teta_dot(2)....[rad/sec]
0.25      ;Wz_initial(1).OR.Psi_dot(2).....[rad/sec]
0.00      ;Phi_initial.....................[deg]
0.00      ;Theta_initial...................[deg]
179.00    ;Psi_initial.....................[deg]
0         ;0=no_gravity,1=gravity
0.10      ;dt_for_integration..............[sec]
2         ;1=circular,2=Model_B,3=Model_A
1.0       ;Sigma_of_magnetometer_noise.....[miliGauss]
1         ;0=open_loop,1=close_loop
10        ;control_interval
```

Fig 4b : Simulation results of De-spin with noise.

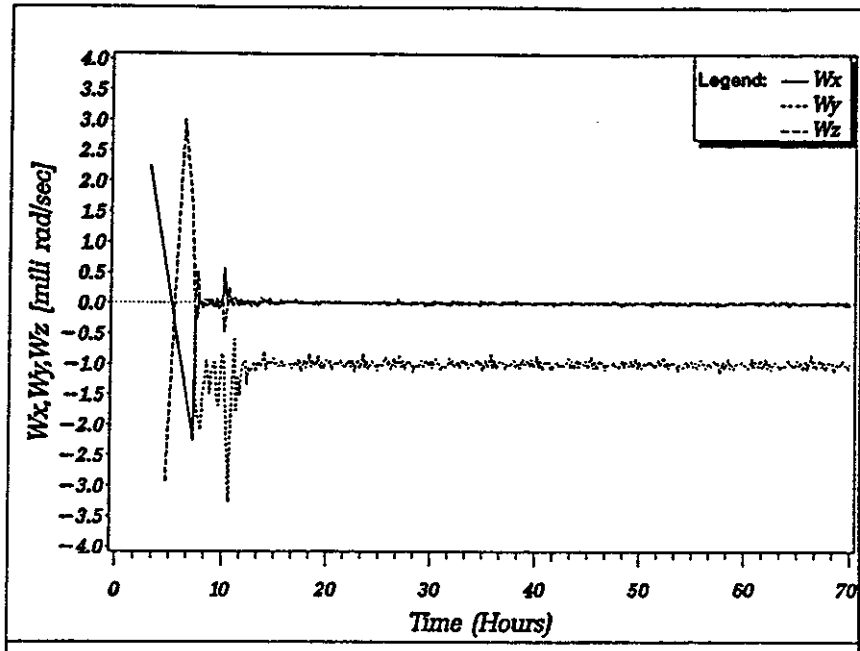


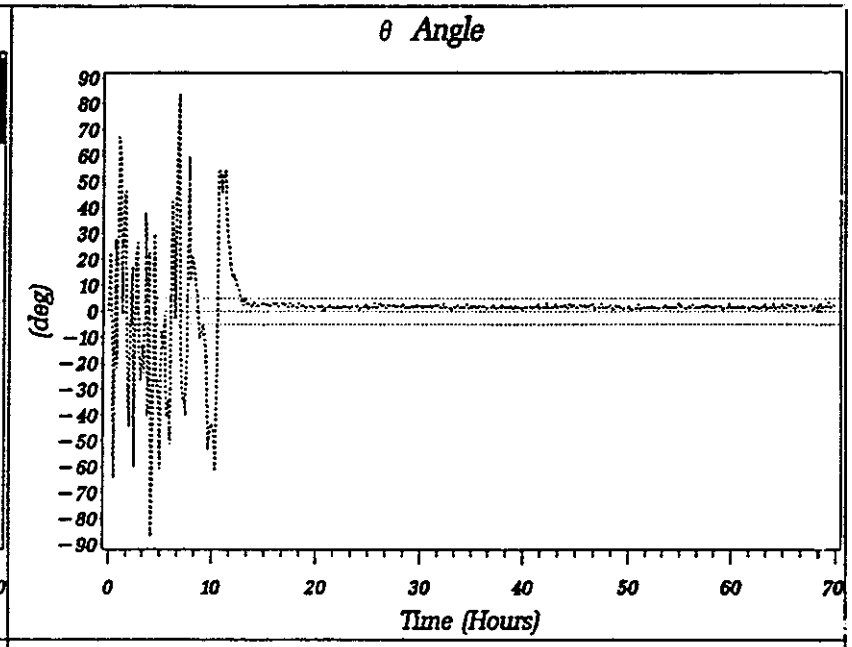


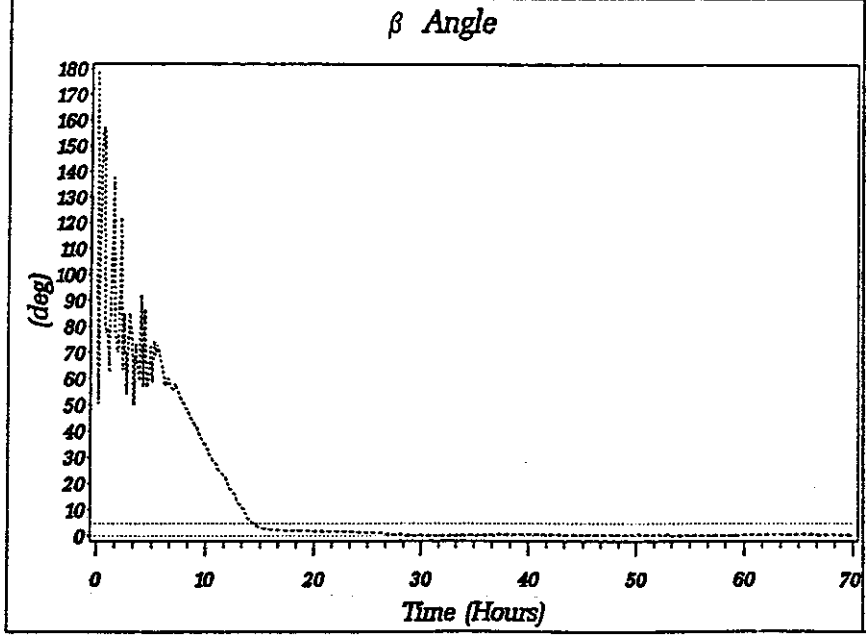


```
98.15     ;orbit_Inclination.(98.15.or.90.0)[deg]
11.70     ;magnetic_dipol_deflection.......[deg]
5.00e+07  ;K_of_control_law
1.00e+04  ;C_of_control_law
3         ;c_law:_0=nothing,1=De-spin,2=improved,3=compass,4=horizon
2         ;0=no_limit,1=linear,2=vector_bang,3=signed_bang
0.0       ;delta_alfa_above_poles..........[deg]
1.0       ;Msat............................[Amp*m^2]
0.7       ;Ix..............................[kg*m^2]
0.8       ;Iy..............................[kg*m^2]
0.5       ;Iz..............................[kg*m^2]
-0.60     ;H_wheel_final...................[N*m]
0.0       ;Wheel_start_time(0=no_start_process).[sec]
0.25      ;Wx_initial(1).OR.Phi_dot(2).....[rad/sec]
0.80      ;Wy_initial(1).OR.Teta_dot(2)....[rad/sec]
0.25      ;Wz_initial(1).OR.Psi_dot(2).....[rad/sec]
0.00      ;Phi_initial.....................[deg]
0.00      ;Theta_initial...................[deg]
179.00    ;Psi_initial.....................[deg]
0         ;0=no_gravity,1=gravity
0.10      ;dt_for_integration..............[sec]
2         ;1=circular,2=Model_B,3=Model_A
0.0       ;Sigma_of_magnetometer_noise.....[miliGauss]
1         ;0=open_loop,1=close_loop
10        ;control_interval
```

Fig 5a : Simulation results of "Compass" with no noise.

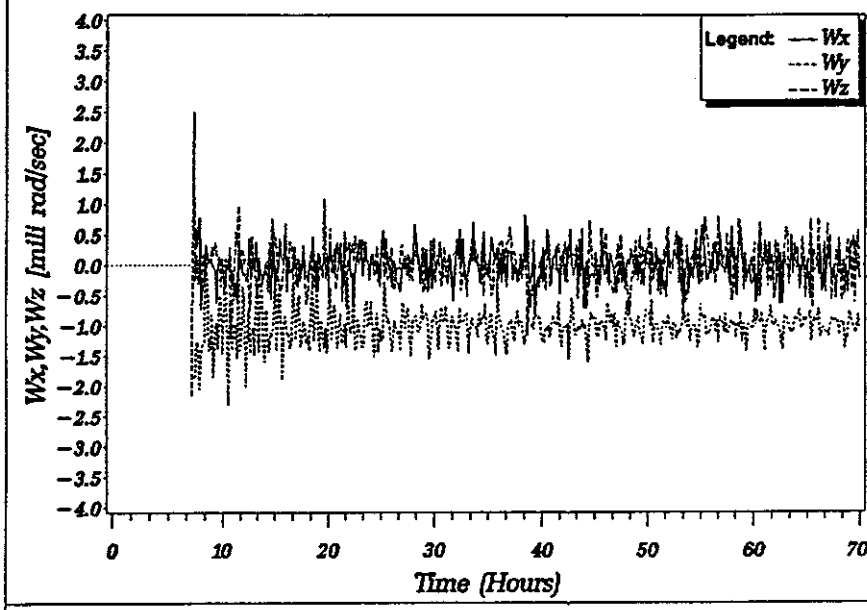


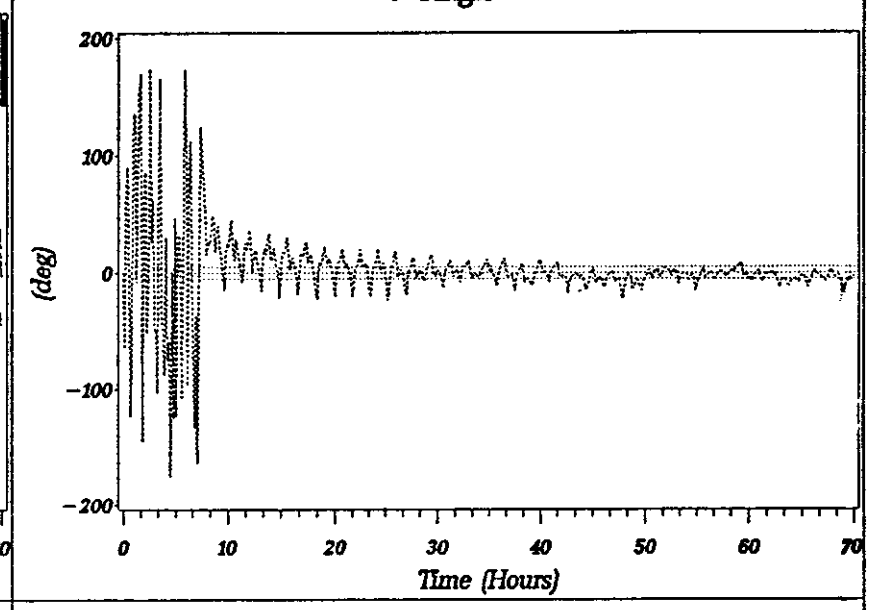


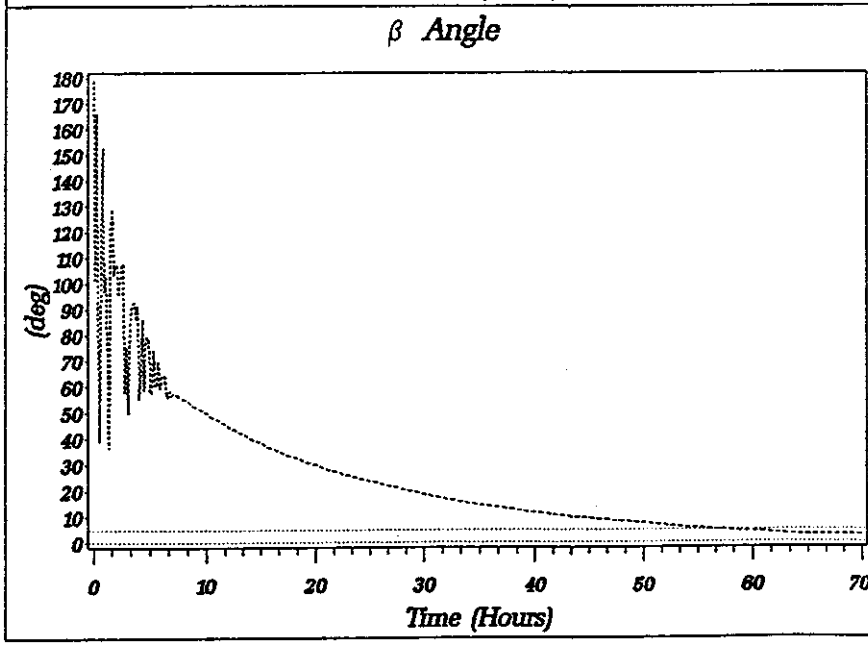


```
98.15      ;orbit_inclination.(98.15 or 90.0)[deg]
11.70      ;magnetic_dipol_deflection.......[deg]
5.00e+07   ;K_of_control_law
1.00e+04   ;C_of_control_law
3          ;c_law:_0=nothing,1=0e-spin,2=improved,3=compass,4=horizon
2          ;0=no_limit,1=linear,2=vector_bang,3=signed_bang
0.0        ;delta_alfa_above_poles.........[deg]
1.0        ;Msat...........................[Amp*m^2]
0.7        ;Ix.............................[kg*m^2]
0.8        ;Iy.............................[kg*m^2]
0.5        ;Iz.............................[kg*m^2]
-0.60      ;H_wheel_final..................[N*m]
0.0        ;Wheel_start_time(0=no_start_process).[sec]
0.25       ;Wx_initial(1).OR.Phi_dot(2).....[rad/sec]
0.80       ;Wy_initial(1).OR.Teta_dot(2)....[rad/sec]
0.25       ;Wz_initial(1).OR.Psi_dot(2).....[rad/sec]
0.00       ;Phi_initial....................[deg]
0.00       ;Theta_initial..................[deg]
179.00     ;Psi_initial....................[deg]
0          ;0=no_gravity,1=gravity
0.10       ;dt_for_integration.............[sec]
2          ;1=circular,2=Model_B,3=Model_A
1.0        ;Sigma_of_magnetometer_noise.....[milliGauss]
1          ;0=open_loop,1=close_loop
10         ;control_interval
```

Fig 5b : Simulation results of "Compass" with noise.

# OFEQ-2

# ORBIT, ATTITUDE AND FLIGHT EVALUATION

32nd ISRAEL ANNUAL CONFERENCE ON AVIATION AND ASTRONAUTICS

February 1992

Written by: Michael Grumer
Joseph Komem
Dr. Joseph Kronenfeld
Ophir Kubitski
Vitaly Lorber
Dr. Haim Shyldkrot

Space Technology Department, MBT Systems & Space Technology, Electronics Division, Israel Aircraft Industries, Ltd.

**ABSTRACT**

The most significant events and phenomena that occured during Ofeq-2 flight are evaluated in this work. Particular attention will be paid to the physical and technological factors which affected its orbital lifetime. Comparison of Ofeq-2 telemetry results with prelaunch estimations, and with Ofeq-1 flight data will be presented. The satellite, orbit and mission characteristics are first defined and a description of Ofeq-2 principal systems then follows. Topics addressed include the interaction between the spinner's attitude with respect to the sun and consequent electrical power generation. The coning angle development history, the role of the solar data evaluation, and the factors influencing drag are also analyzed. All of these affected the Ofeq-2 power outage-recovery event. The orbit determination and the coning angle evolution estimation methods used are discussed in some detail.A brief report on radiation effects on computer RAM is also given. An integrative systems engineering approach summary of the TLM data reconstruction and analysis concludes this paper.

## 1. INTRODUCTION

Ofeq-2, Israel's second R&D satellite, was inserted into an orbit of.214 km perigee altitude by 1570 km apogee altitude, on April 3, 1990. Ofeq-2, like its predecessor Ofeq-1, was designed as a flight test bed to further validate and demonstrate the satellites' design as well as ground station facilities and operations for future Israeli satellites.

The goals and objectives of the Ofeq-2 flight were to continue augmenting IAI space technology capabilities and in particular, to verify two-way communications. Specifically, the downlink channel (TLM) and the new uplink channel (TLC) for sending commands to the satellite. Another goal was to further test onboard systems operations during exposure to the space environment, especially the new logical functions for protecting the computer system against Single Event Upsets (SEU).

All goals were accomplished very well. However, the differences in the flight results of the two satellites were quite considerable. Remarkably, nearly all of the differences appear to be due to the growth, or rather the lack of growth, of the spinner's coning angle. This factor will be further reported in some detail.

## 2. DESCRIPTION OF OFEQ-2

### 2.1 Satellite Systems Description

The Ofeq-2 satellite consists of the following systems: Structure, Electrical Power System, Thermal Control System, Orientation Sensors System, Communication System and Computer System.

Ofeq-2 general characteristics are :

| | | |
|---|---|---|
| Dimensions | : Diameter of the Base | - 1.2 meters |
| | Height | - 2.3 meters |
| Weight | : 174 kg | |
| Telemetry | : S-Band, 2.5 KB/Sec | |
| Thermal Control | : Passive, except for the Battery Heater. | |

Orientation : Spin Stabilized, Passive control.

Orbital Data : 210 km Perigee Altitude
1600 km Apogee Altitude
143.2$^0$ Inclination

### 2.1.1 Structure

A general view of the satellite is shown in Figure 1. The basic structure is an octagonal truss of aluminum rods connected by aluminum fittings. The inner shelves support the satellite systems' equipment. The solar arrays are wrapped around the satellite and are attached to the truss without any load carrying paths. The antenna is at the lower base of the satellite.

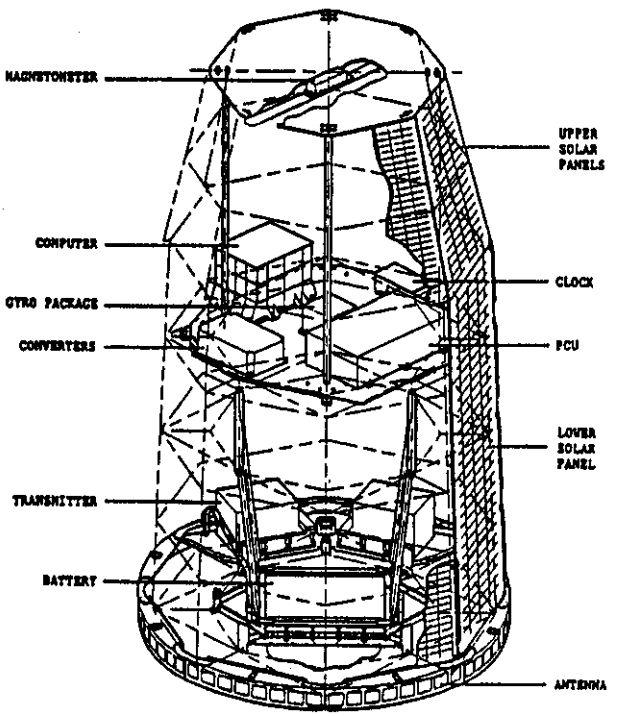


Figure 1. Ofeq-2 - General View

### 2.1.2 Electrical Power System (EPS)

The EPS consists of 16 solar panels that serve as the primary power source, a Ni-Cd battery, a relay unit, a power control unit (PCU) and a DC-DC converter (see Figure 2).

The mode of operation of the EPS is by charging the battery via shunt switches controlled by the PCU. The battery charge controller shorts out any excess power from the solar panels and then charges the battery directly through the main bus. The main bus provides unstabilized voltages to the DC-DC converter, which in turn provides stabilized voltages to the other systems. The main bus voltage varies in accordance with the battery state of charge.

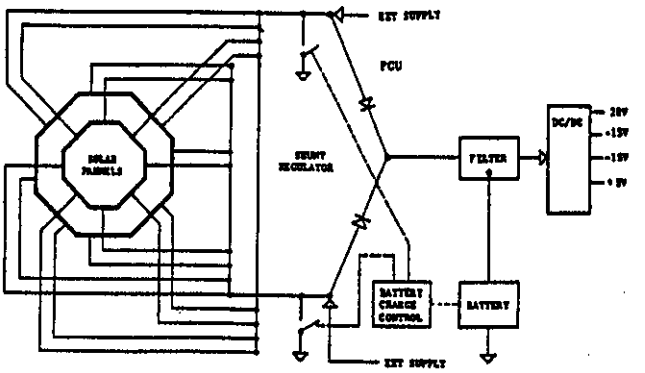


Figure 2. Electrical Power System - Principle of Operation

### 2.1.3 Thermal Control System

The thermal control system employs both active and passive means to maintain the proper thermal environment. The system consists of : multi-layer insulation (MLI) blankets, thermal paints and coatings, a radiator, insulators and conductors. It also contains battery active heaters, the activation of which is performed by the PCU.

A number of thermistors located in various places around the satellite provide temperature measurements to be TLM-transmitted for thermal analysis on ground.

### 2.1.4 Orientation Sensors System

These sensors provide the raw information used to evaluate satellite orientation. The pertinent sensors include : a rate gyro assembly, a magnetometer, and solar cells arranged to act as a sun sensor. Additionally, the thermistors provide data helpful in estimating satellite orientation. The rate gyro system is a three-axis package which provides angular body rates about the three satellite axes. This data is used to generate spin rate data as well as coning information. The three-axis magnetometer is located on the top of the satellite and provides data concerning its orientation with respect to the earth's magnetic field. It also enables reconstruction of the satellite's attitude with reference to the sun.

### 2.1.5 Communication System

The communication system consists of two redundant transmitters and two redundant receivers, an S-Band antenna, and a doubly-redundant clock (Figure 3).

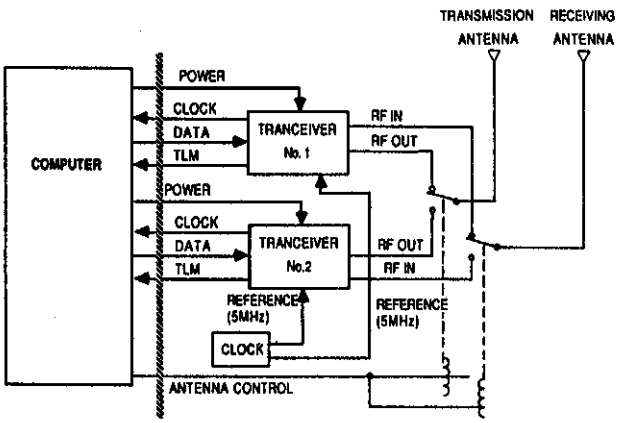


Figure 3. Communication System - Functional Block Diagram

### 2.1.6 The Computer System

The computer system consists of a doubly-redundant data processing computer, a doubly-redundant TLM data storage unit, power units and several auxiliary units. The functions are implemented on eight PCB cards. The functions are : The TLM memory storage switching logic, the computer switching logic, the switching on and off of the gyro and magnetometer logic, and the swapping logic of the two transmitters or receivers (Figure 4).

## 2.2 Orbital Data & Planning

An early orbit estimate is given below. Key orbital parameters are indicated :

| | | |
|---|---|---|
| Time of Vector | : | 4-April-1990 |
| Semi-major Axis | : | 7276.1 km |
| Eccentricity | : | .095682 |
| Inclination | : | $143.2^0$ |
| Argument of Perigee | : | $72.4^0$ |
| Apogee Altitude | : | 1600 km |
| Perigee Altitude | : | 210 km |
| Mean Anomaly | : | $50^0$ |

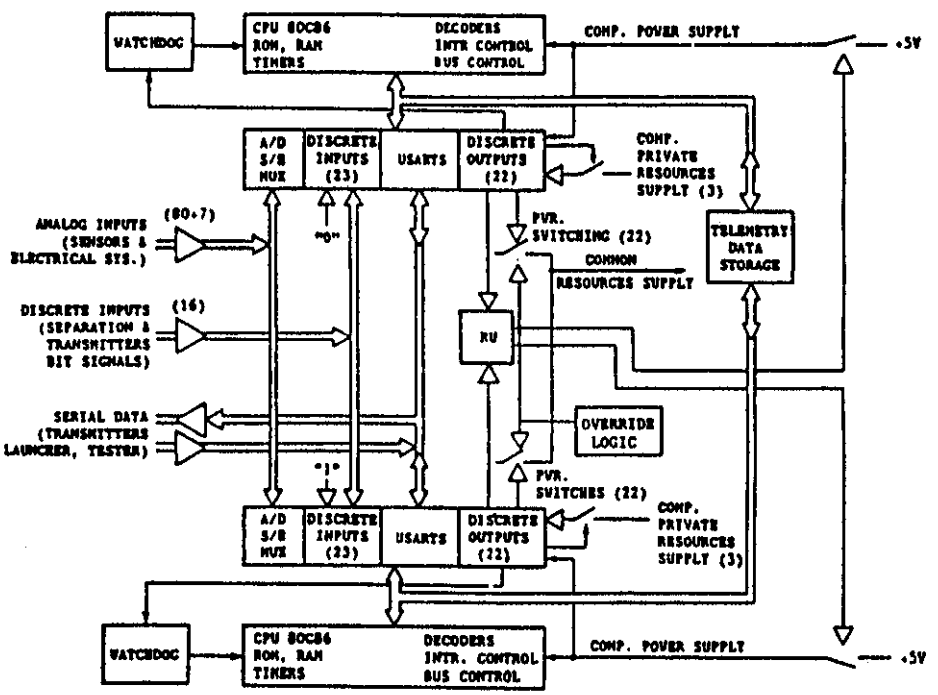


Figure 4. Computer System - General Block Diagram

The basic plan was to receive TLM for every communication opportunity and subsequently test the uplink system. This was done during communications with the ground station. State vector data was processed during tracking from the ground, and used to determine future communication passes. The same data was also used as a basis for providing orbital lifetime estimations, and to anchor our reconstruction efforts.

# 3. FLIGHT TEST RESULTS EVALUATION

## 3.1 Summary of Major Events

The insertion point of the actual orbit was slightly higher than planned. This caused longer AOS times and a slightly longer on-orbit lifetime.

The biggest differences between the Ofeq-1 and the Ofeq-2 launches were : the smaller initial coning angle, the slightly lower spin rate and the slower growth rate of the coning angle in the latter case. These factors had a general impact on the Ofeq-2 flight. Figures 11 and 12 show both the Ofeq-1 and Ofeq-2 coning histories. See Reference [1] for Ofeq-1 flight evaluation.

During Ofeq-1 flight we had expected to arrive at sun angles with respect to the solar panels which would result in a loss of power or a power outage after about 30 days. This did not occur. However, this power outage did eventually occur on about the 30th day (May the 2nd) on Ofeq-2. The reason was due to the low coning angle values during this period. On Ofeq-2, the coning angle at the time of the power outage was about $7.6^0$, whereas on Ofeq-1, after the same time on orbit, the value was approximately $70^0$. At this time, the angle between the angular momentum vector and the sun vector on Ofeq-2 approached zero, with the sun pointing at the tail. This was crucial to the electrical power outage and led to several phenomena, observed in the Ofeq-2 flight, that the large coning on the previous flight had prevented :

(i) Both satellites started spin-stabilized, but the transition from a spin-stabilized condition about the minor axis to a flat-spin tumble ocurred much later on Ofeq-2.

(ii) High temperatures at the rear of satellite and cold temperatures at the top.

(iii) Power outage and recovery.

Only the detection of the SEU's and one latch-up phenomenon were not related to the coning.

Until the outage, all systems operated as expected and all tests were accomplished satisfactorily. Special tests to detect single event upsets (SEU's) were successful, as were the TLC uplink tests. Analysis of the results from the magnetometer and rate gyros indicated performance conforming with specifications. It is this first part of the Ofeq-2 flight experience that may, in the authors' opinion, deserve the notice of the space community.

## 3.2 Orbit Determination Module

### 3.2.1 Trajectory Generation

Trajectory generation (position and velocity) is performed through integration of the orbital equations of motion. These equations are expressed in terms of the rectangular components of the perturbing acceleration vector acting on the satellite. The perturbation model includes the effects of a point-mass earth, the 6th order zonal harmonics in the gravitational potential, and drag. High-precision Gauss-Jackson type numerical integration was used for solution of the equations.

### 3.2.2 Observations Modeling

An orbit generator computes simulated observations of the satellite from any specified tracking site. The simulated data (radar range, azimuth, elevation and Doppler) are generated for specified observation intervals and sampling frequencies. The generator has the capability to simulate the effects of atmospheric refraction and modifies the observations according to these effects. Modeling of the observations also includes calculation of the observation matrix, which contains the partial derivatives of the computed observations with respect to satellite initial position and velocity vectors.

### 3.2.3 Estimator

The purpose of the estimator is to estimate the satellite orbit and associated parameters. Our estimation used the Differential Correction Algorithm. This algorithm minimizes the sum of the squares of the weighted residuals between actual and computed observations while simultaneously constraining the state to satisfy an a priori state to within a specified uncertainty. The iterative estimation process differentially corrects the estimated variables and ultimately determines the weighted least squares solution.

Then the mean and covariance matrices are determined for the estimated variables.

### 3.2.4 Results Estimation and Prediction

During the Ofeq-2 lifetime, the ground tracking station measured the satellite range, radial velocity (Doppler), azimuth and elevation. These data were used to estimate and then to predict its orbit. The results of the orbit prediction errors for one and eleven passes forward are summarized in Table 1.

Table 1. Results Estimation and Prediction

| Type of Error | Predicition Error [meters] | |
|---|---|---|
| | for 1 pass | for 11 passes |
| Radial | 50 - 400 | 150 - 650 |
| Along-track | 50 - 1600 | 2000 - 14000 |
| Cross-track | 10 - 500 | 150 - 650 |

## 3.3 Orbit and Orbital Lifetime

### 3.3.1 Summary

The kinematical lifetime of the satellite was calculated before the launch, immediately after injection data was obtained, occasionally during the stay in orbit and extensively towards the fall. Before the launch we forecast that for a nominal injection, the satellite would revolve for 54 days. Shortly after receipt of the injection data, the central value was changed to 57 days. The uncertainty due to the solar data was assesed as 10 days.

Actually, the satellite's lifetime in orbit was 98 days. The date of impact was evaluated, towards the end, as 9th of July 1990 02:45 UTC with an uncertainty of 45 minutes. The location of impact was correspondingly estimated as $10^0$N latitude and $160^0$E longitude. This is shown in Figure 5, where the ground track of the satellite for the last three revolutions is depicted. The uncertainty corridor of impact is also given in this figure.

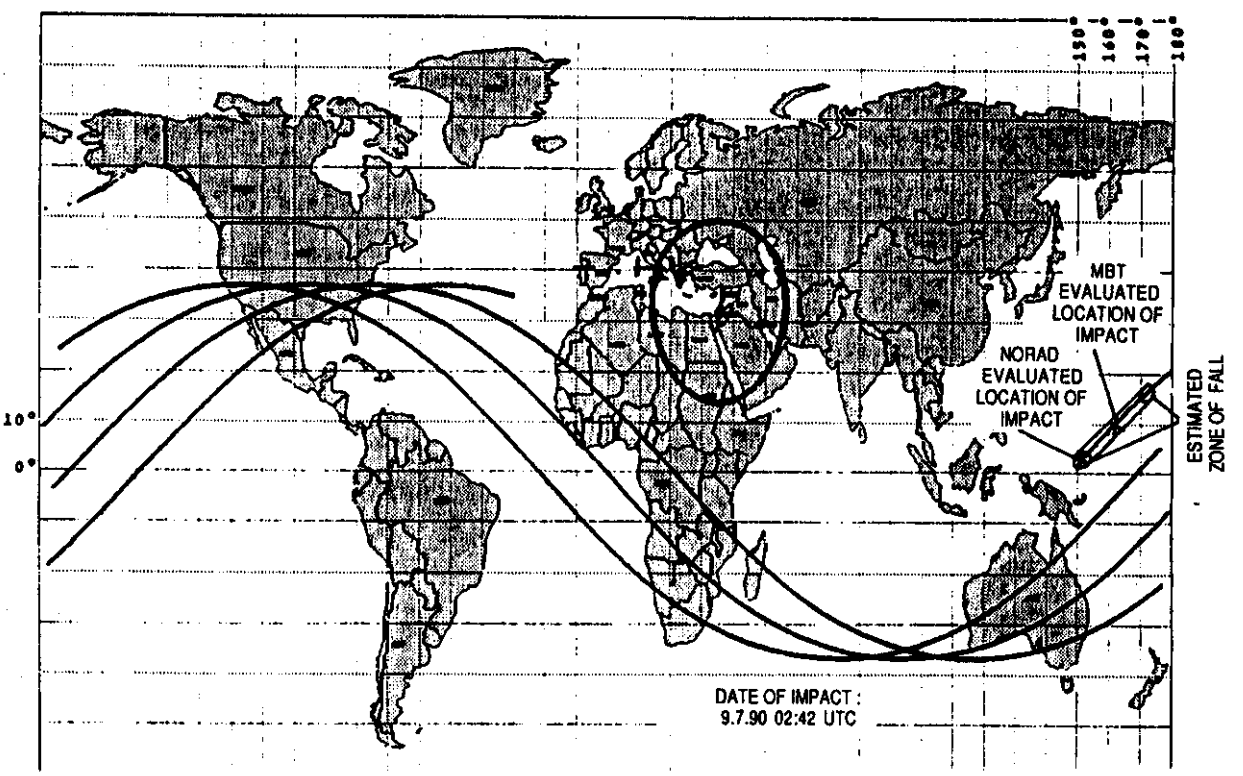


Figure 5. Ofeq-2 Ground Track for the Last Three Revolutions

Our re-entry forecast was confirmed by data recieved from NORAD. According to them, the location of impact was $2.8^0$N latitude and $151.1^0$E longitude. As for the date of impact, their last value was 9-JUL-1990 02:53 UTC with an uncertainty of 6 minutes.

### 3.3.2 Evaluation of Orbital Data and Reconstruction

Towards the end of life, and after the satellite fall, a reconstruction of the orbital history was done. In doing so, we assesed the reasons for the initial discrepancy of the lifetime calculations and give them here as follows :

(i) Deviation of Solar Data

The actual average solar flux during most of the satellite's lifetime was lower even than the -2σ line of confidence for the 22nd solar cycle. The solar flux (F10.7) statistics are shown in Figure 6, and the known monthly averages of the solar data as used in the reconstruction are given in Table 2. Note that for the started solar cycle, the statistics are calculated for the collected cycle data and this narrows the uncertainty band compared to, for instance, the global statistics. The uncertainty that we used initially was the narrower one. The conclusion therefore for short lifetimes, as in our case, is to use the global uncertainty limits.

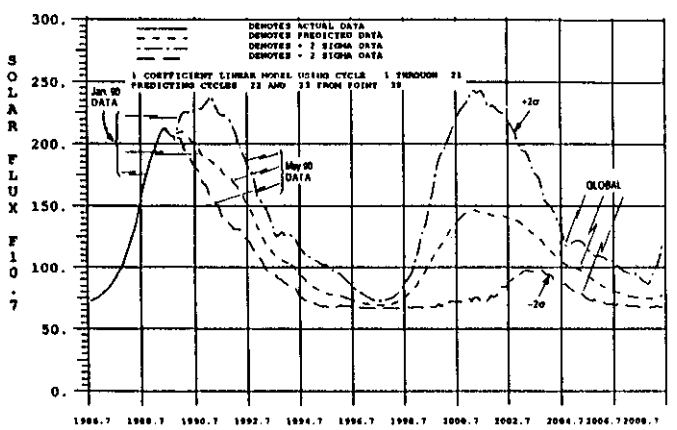


Figure 6. Long Range Estimates of Smooth 10.7 cm Solar Flux for Cycles 22 and 23

Table 2. Ofeq-2 Drag Reconstruction Data

| DATE D:M:Year | Drag Correction Factor | Average F10.7 Solar Flux | Daily F10.7 Solar Flux | Ap Magnetic Index |
|---|---|---|---|---|
| 01:4:1990 | 0.6 | 184.8 | 184.8 | 24.9 |
| 01:5:1990 | 0.6 | 186.8 | 186.8 | 17.6 |
| 16:5:1990 | 0.95 | 186.8 | 186.8 | 17.6 |
| 02:6:1990 | 0.945 | 168.8 | 168.8 | 16.0 |
| 19:6:1990 | 0.935 | 168.8 | 168.8 | 16.0 |
| 23:6:1990 | 0.865 | 168.8 | 168.8 | 16.0 |
| 26:6:1990 | 0.885 | 168.8 | 168.8 | 16.0 |
| 28:6:1990 | 0.86 | 168.8 | 168.8 | 16.0 |
| 01:7:1990 | 0.88 | 200.8 | 200.8 | 16.5 |
| 06:7:1990 | 0.925 | 200.8 | 200.8 | 16.5 |

(ii) Deviation of Cross Sectional Area

Due to the slow coning development, the satellite cross sectional area was not the random average that we had initially used (2.1 sqm). The area development, according to the dynamics reconstruction (section 3.4.2) is shown in Figure 7. As for the start of life, the average is lower than the value used, but no distinct conclusions should be drawn since a correlation with the perigee times of the orbit was not done. However, at the end of the life, the average and minimal areas are higher than the value used. This trend is consistent with the orbital reconstruction data given in Table 2. In this table, the correction factor for the drag is higher towards the end of life. Note that this factor also corrects the Cd coeficient.

(iii) Deviation of Cd

The dynamical reconstruction had shown that this coeficient should be nearly 1.7 instead of the initially used 2.3 value. The fit for Cd and CG is given in Figure 8.

Measured and reconstructed semi-major axis orbit parameters are given in Figure 9. The reconstruction was done by using the monthly average solar data (F10.7 and Ap indices). The global usage of cross-sectional area and Cd is corrected by a common factor. All the parameters are given in Table 2, and are used at time break points.

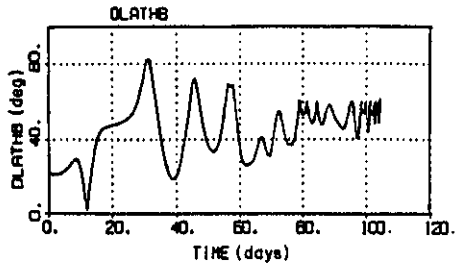


(a) Sun Angle to Base Plane

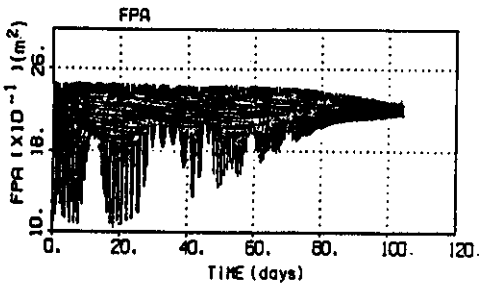


(b) Cross Sectional Area

Figure 7. Ofeq-2 Reconstructed Parameters

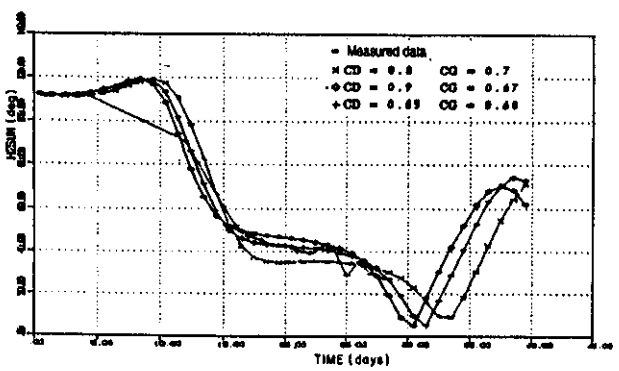


Figure 8. Angle Between Sun and Angular Momentum Vectors

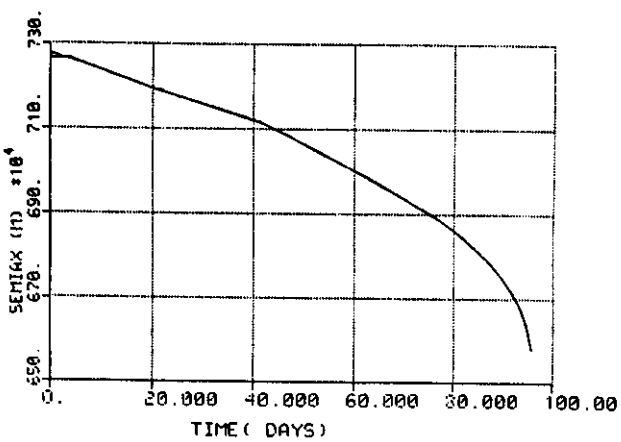


Figure 9. The Semi-Major Axis Parameter Variation

As was pointed out above, the deviations of the area and Cd as analysed dynamically are roughly consistent with the overall factor needed to reconstruct the actual orbital history.

## 3.4 Dynamic Behavior

### 3.4.1 The Dynamic Model

The torque-free attitude motion of a rigid axi-symmetrical body may be described as a superposition of spinning about the symmetry axis at a constant angular velocity, and precession of the symmetry axis about the inertially fixed angular momentum vector at a constant rate and a constant nutation (coning) angle (see Figure 10). This simple coning picture is basically valid for Ofeq-2 with a spin period of about 1 second, and a precession period of about 3 seconds. However, small environmental forces generate perturbing torques on the satellite that lead to a relatively slow variation in its angular momentum. For low earth-orbiting satellites the major perturbation is due to aerodynamic forces. For Ofeq-2 at the perigee altitude of about 200 km, the aerodynamic moment is of the order of magnitude of $10^{-4}$ Newton-meter. Since the angular momentum is about 200 Newton-meter-second, the direction of the angular momentum changes by less than a microradian per second. Thus, the dynamics of a spinning satellite like Ofeq-2 are characterized by two widely differing time scales : the short time scale of body rotations and the long time scale of angular momentum variation. Because of the fast rotations, the short period variations in the perturbing torques are averaged out, and the angular momentum is affected by the average torques only.

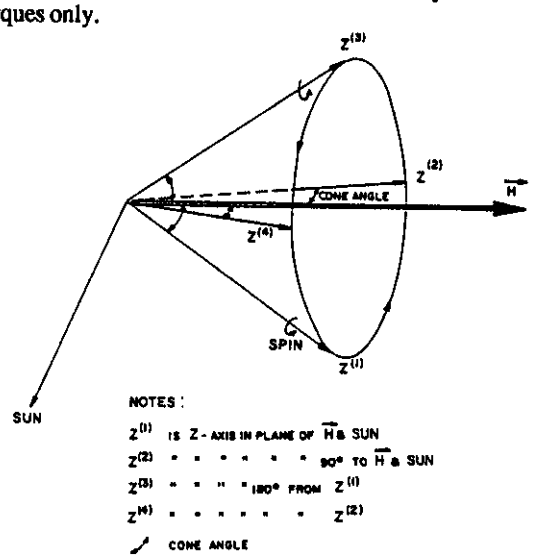


Figure 10. Geometry of Satellite Coning Angle

It can be shown that for an axi-symmetrical rigid body the average aerodynamic torques are perpendicular to the angular momentum. Therefore, they affect only the direction of the angular momentum but not its magnitude. Also, the angular momentum component along the spin axis remains constant due to the symmetry of the body. Hence, the nutation angle of a rigid body is not affected by the aerodynamic torques. However, the satellite is not a rigid body and since it is spinnig about a minor inertia axis, the nutation angle grows due to internal energy dissipation.

The above model provides our basis for the orbit and attitude dynamics simulation. First, the aerodynamic force and torque are integrated over one precession period for inertially fixed angular momentum and constant coning angle. Then, the motion of the angular momentum and the orbit decay are obtained by integrating the average force and torque. Finally, the coning angle is updated according to the time evolution curve that is obtained from the energy dissipation model.

### 3.4.2 Dynamics Reconstruction

In the process of dynamics reconstruction, first the energy dissipation model is adjusted on the basis of TLM data to fit the nutation angle growth. Then, the drag coefficient, Cd, and the distance of C.P. from C.G. are derived from the TLM and tracking data. The drag coefficient is set to fit the semi-major axis decay, then C.P. is set to fit the motion of the angular momentum vector.

This data is further used in the dynamic simulation of the satellite to predict the future attitude and orbital conditions. Figure 8 gives the result of a typical forecast, and how it compared to actual data. This simulation and the electrical power simulation provided the expected onset and duration of the power outage.

### 3.4.3 Measured Data from TLM Processing

Data was regularly received from the orientation sensors, and processed. This data is shown in Table 3, and consist of the coning angle, angle between the sun and the angular momentum vector, plus the location of the angular momentum vector in the inertial frame (X to vernal equinox, Z along the North pole) in terms of declination and right ascension.

Table 3. Mission Dynamical Parameters Reconstruction Using Magnetometer TLM Output

| TIMEDY | DATE | ORBIT NO. | LATHI | LONHI | SPIN RATE | TRAVEL RATE | CONANG GYRO | CONANG MGN | H2SUN | ANGMOM |
|---|---|---|---|---|---|---|---|---|---|---|
| 2 | 5.4 | 18 | -10.20 | 123.50 | 364.2 | 0.77 | 0.44 | 0.36 | 110.60 | 195.7 |
| 4 | 7.4 | 44 | -5.10 | 127.60 | 363.4 | 1.17 | 0.64 | 0.54 | 112.00 | 195.3 |
| 5 | 8.4 | 76 | -4.30 | 127.40 | 365.1 | 1.31 | 0.65 | 0.60 | 111.00 | 196.2 |
| 12 | 15.4 | 185 | 69.90 | 126.50 | 362.2 | 2.86 | 1.66 | 1.34 | 91.00 | 194.7 |
| 13 | 16.4 | 200 | 62.96 | 115.50 | 362.9 | 3.40 | 1.82 | 1.57 | 81.00 | 195.0 |
| 15 | 18.4 | 229 | 59.60 | 75.70 | 360.4 | 4.20 | 2.20 | 1.97 | 61.00 | 193.0 |
| 16 | 19.4 | 242 | 49.60 | 69.70 | 360.0 | 4.46 | 2.50 | 2.10 | 52.10 | 193.6 |
| 17 | 20.4 | 260 | 45.36 | 66.60 | 357.8 | 4.92 | 2.70 | 2.30 | 47.10 | 192.5 |
| 18 | 21.4 | 275 | 31.77 | 73.40 | 356.4 | 5.53 | 3.10 | 2.60 | 45.30 | 191.8 |
| 19 | 22.4 | 293 | 24.14 | 76.13 | 357.1 | 6.20 | 3.44 | 2.93 | 43.30 | 192.2 |
| 20 | 23.4 | 308 | 21.74 | 75.27 | 357.4 | 6.86 | 3.80 | 3.20 | 43.14 | 192.3 |
| 21 | 24.4 | 323 | 24.78 | 72.74 | 355.5 | 7.04 | 4.10 | 3.34 | 40.30 | 191.4 |
| 22 | 25.4 | 337 | 23.83 | 72.63 | 356.2 | 7.82 | 4.90 | 3.68 | 39.30 | 191.8 |
| 23 | 26.4 | 353 | 17.02 | 77.23 | 355.8 | 9.04 | 5.00 | 4.26 | 42.00 | 191.8 |
| 24 | 27.4 | 368 | 12.91 | 76.76 | 356.9 | 9.97 | 5.50 | 4.73 | 40.92 | 191.4 |
| 25 | 28.4 | 383 | 14.89 | 65.48 | 353.2 | 10.85 | 5.90 | 5.17 | 28.91 | 190.6 |
| 26 | 29.4 | 399 | 20.19 | 72.67 | 353.2 | 12.72 | 6.50 | 6.05 | 34.83 | 190.9 |
| 27 | 30.4 | 415 | 22.82 | 67.78 | 351.8 | 11.90 | 7.10 | 5.49 | 29.60 | 190.0 |
| 28 | 1.5 | 430 | 19.43 | 67.00 | 350.0 | 11.95 | 7.62 | 5.73 | 27.50 | 189.0 |

TIMEDY – Time [day]

LATHI – See 3.4.3 [deg]

LONHI – See 3.4.3 [deg]

SPIN RATE – Spin Rate in body axes [deg/sec]

TRAVEL RATE – (TRANAN) Transversal Angular Velocity in Body Axes [deg/sec]

CONANG – Nutation angle, $\theta_{nut}$ [deg]

MGN – Magnetometer

H2SUN – Angle between angular momentum and sun vectors [deg]

ANGMOM – Angular momentum [New-m-sec]

## 3.5 Estimated Coning Angle Evolution

Our only previous "hands on" experience with coning was from Ofeq-1. That, as was mentioned earlier, grew quite rapidly. However, we assumed that since the satellites were very similar, the coning characteristics of the two should also be quite similar.

In order to better understand the coning process that occurred on Ofeq-1, a dynamical model was developed to simulate the nutation growth in a simple spinner. The simulation includes the essential elements to account for the internal energy dissipation in Ofeq satellites.

The model developed simulates the increase in the transversal angular velocity up to flat-spin and the corresponding decay of the spin rate. It is expressed in the body axes of the satellite. The model simulates a simplified sloshing mechanism in one or multiple tanks (compare with Reference [2]).

The model uses the following equations of motion:

$$\dot{p} = -1/I_z\,[I_l\,(q\,\dot{e} - r\,\dot{a})] \qquad (1)$$

$$\dot{q} = -1/I_x\,[\,(I_z - I_y)\,r\,p + I_l\,(\ddot{a} - \dot{e}\,p)\,] \qquad (2)$$

$$\dot{r} = -1/I_y\,[\,(I_x - I_z)\,p\,q + I_l\,(\ddot{e} + \dot{a}\,p)\,] \qquad (3)$$

$$\ddot{a} = -1/I_l\,[2\,F_d\,\dot{a} + I_l\,p^2 a + 2\,M_s\,(R^2 + Z_c^2)\,\dot{q}] \qquad (4)$$

$$\ddot{e} = -1/I_l\,[2\,F_d\,\dot{e} + I_l\,p^2 e + 2\,M_s\,(R^2 + Z_c^2)\,\dot{r}] \qquad (5)$$

Where: $I_l = 2\,M_s\,R^2$

| | |
|---|---|
| p | – spin axis angular velocity |
| q, r | – satellite transversal angular velocities |
| a, e | – imaginary angular displacement coordinates of liquid movement in the XZ and YZ planes |
| $F_d$ | – linear coefficient of viscous friction |
| $M_s$ | – lumped liquid mass within a spherical tank |
| R | – gyration radius of $M_s$ |
| $I_x, I_y, I_z$ | – satellite's principal moments of inertia |
| $Z_c$ | – distance parameter. |

The simulation complied with the conservation of the satellite model's angular momentum to about 0.1% from the initial nutation angle up to flat-spin conditions. Also, for $Z_c = 0$, and throughout the range of nutation angle up to $90^0$ (flat-spin), the kinetic energy loss of satellite plus liquid in the model, was equal to the energy dissipated within the viscous dampers.

Up to nutation angles, $\theta_{nut} = 15^0$, the dynamical process fits nicely with the energy sink approach,

$$\theta_{nut2} / \theta_{nut1} = \mathrm{Exp}\,(\Delta t / \tau_{nut})$$

with $\tau_{nut}$, the time constant of the coning angle growth, increasing slowly.

$\tau_{nut}$ can be expressed in the following form:

$$\tau_{nut} = I_z\,[\,(I_z / I_x) - 1]\,p^2\,\theta^2_{nut} \,/\, \dot{E}_{dissipation} \qquad (6)$$

Where E is satellite's kinetic energy.

Equation (6), when applied to telemetry received from Ofeq-2, resulted in $142 < \tau_{nut}\ (\mathrm{Revs}) < 184$, with $\theta_{nut}$ increasing from $0.4^0$ to about $7.6^0$ at the end of the first month in orbit.

Adjusting the full model to the different initial conditions of Ofeq-1 and Ofeq-2, similar forecasts were made based on the TLM recorded conditions of both satellites. This is shown below in Figures 11 and 12, for Ofeq-1 and Ofeq-2 respectively.

## 3.6 Thermal and Power Correlations

### 3.6.1 Thermal Data

Temperatures were, as expected, mostly high in the aft section and low in the front section. Further increase and decrease in temperature as the sun pointed to the rear of the satellite did indeed occur, just as originally expected. Figures 13 and 14 show the front and aft cover temperatures of the satellite. The low temperatures to which the magnetometer was exposed could have caused problems, since they exceeded the recommended operating limits, as shown in Figure 15. Even so, perfomance did not really degrade. However, a significant drop in temperature did occur when the battery temperature dropped just prior to the power outage. This data gave us the clue that the battery state of charge had dropped to 70% or less. When fed into the EPS simulation, it gave good initial conditions for estimating the power balance situation, which in turn allowed us to make pretty accurate estimations on the power outage and return, especially in the reconstruction of the return to power.

### 3.6.2 Electrical Power Data

The above discussion describes the state of the battery charge and the overall balance prior to the power outage. However, up to the time of the drop in battery temperature, the orbit-by-orbit power balance was as expected, and performance was according to design specifications. The battery voltages and solar array currents (Figures 16 and 17) also indicate the drop in voltage due to the low charge currents.

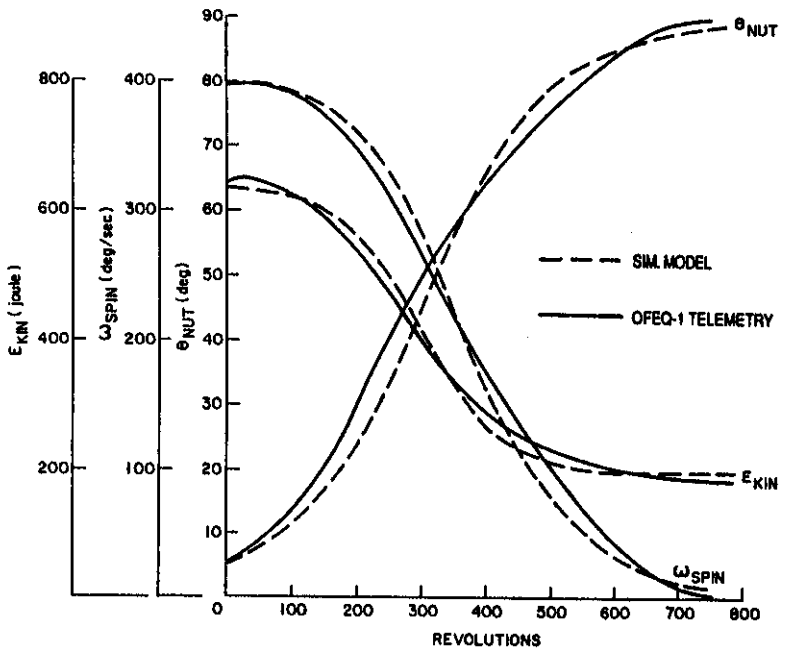


Figure 11. Ofeq-1 - Coning Evolution

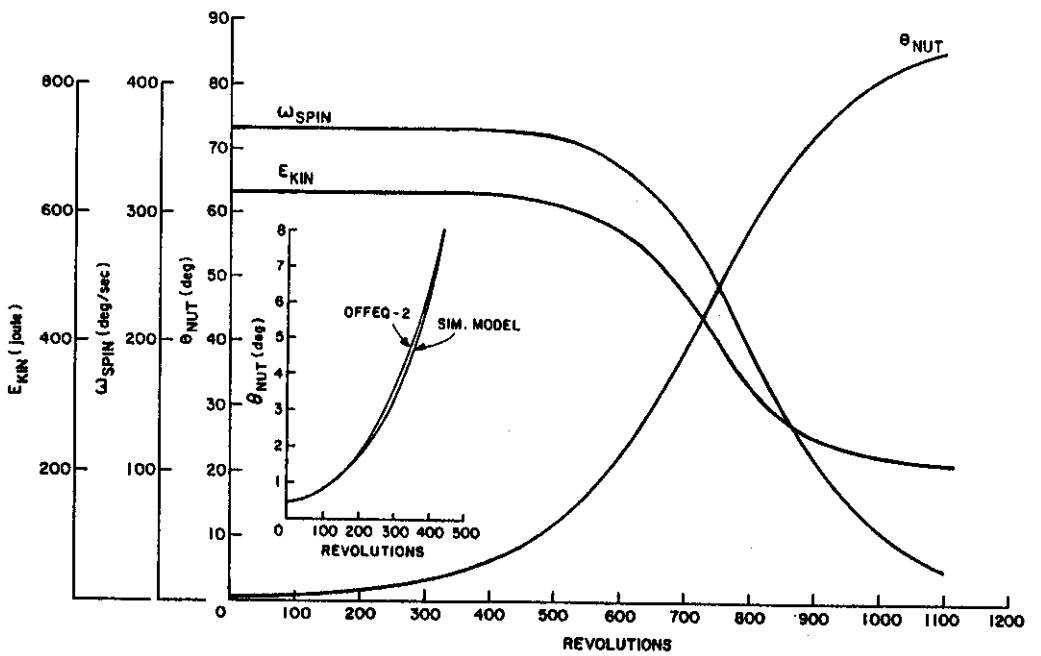


Figure 12. Ofeq-2 - Coning Evolution

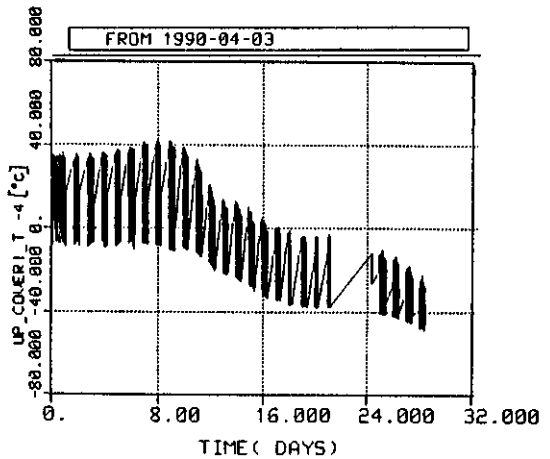


Figure 13. Upper Cover Temperature Telemetry

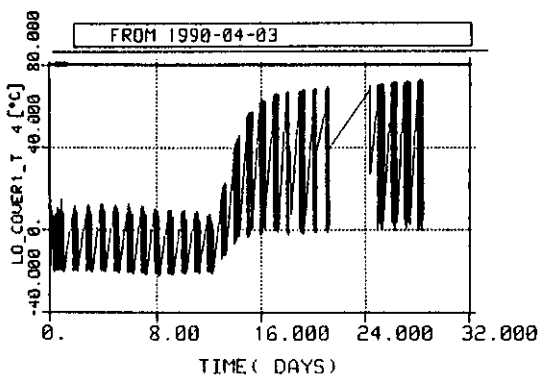


Figure 14. Lower Cover Temperature Telemetry

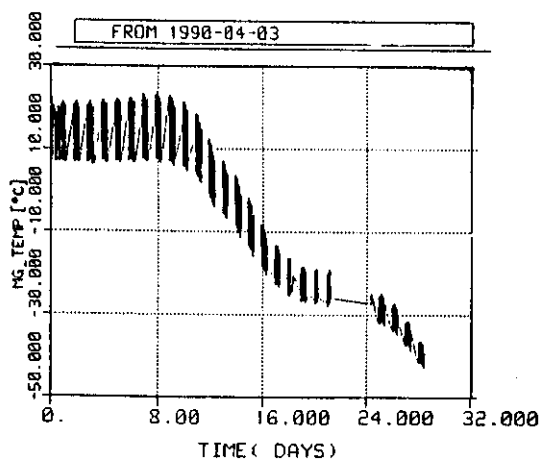


Figyre 15. Magnetometer Temperature Telemetry

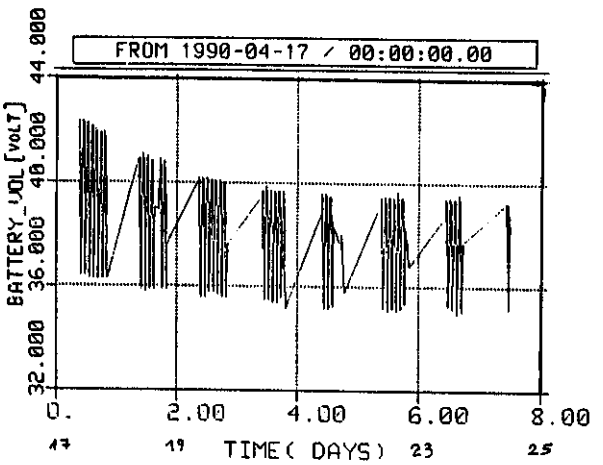


Figure 16. Battery Voltage Telemetry
17th of April to 25th of April 1990

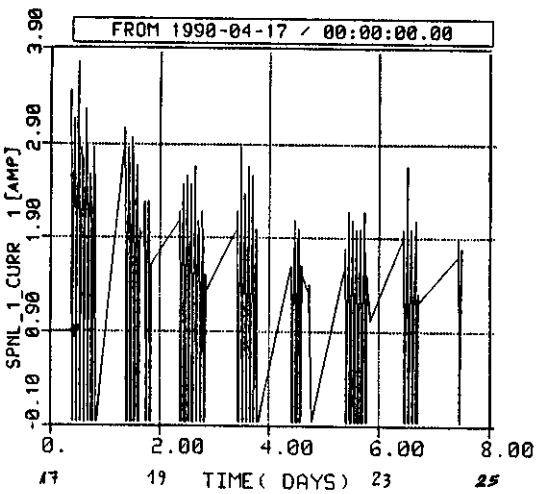


Figure 17. Solar Panel_1 Current Telemetry
17th of April to 25th of April 1990

The EPS balance for the power outage was reconstructed by simulation, using the forecasted attitude from the above- mentioned dynamics simulation, the expected satellite temperatures, and the sun angles as related to the solar panels. The measured voltages and state of charge at the times of the battery temperature drop were used as input for the EPS balance simulation. The simulation then estimated the times of the loss and return of power to an accuracy of a few hours.

The electrical power outage which occurred during the night of the 1st and 2nd of May 1990, was due to low sun angles relative to the solar panels. As the satellite slowly changed its orientation, the sun angle increased and the electrical power was finally resumed on the 8th of May 1990.

A computer simulation of the EPS was done for a period of two weeks, starting April 26th, in order to examine the event of power outage and recovery in real time while it was occuring in orbit.

### 3.6.3 EPS Simulation

The EPS simulation consists of three modules :

(i) Solar panels simulation:

This computes the work point on the I - V curves of the solar cells according to their characteristics, voltage, temperature and angle to the sun. The output of this module is the current (and power) generated by the solar panels as a function of time.

(ii) Battery simulation:

This consists of voltage profiles as a function of charge/discharge current, battery temperature and battery state of charge/discharge.

(iii) Electrical power consumption:

This consists of a table of power consumption by all pertinent satellite operating systems, as a function of time. The inputs to this simulation were : the angle of the sun, the coning angle, the length of satellite day, the length of eclipse, the battery temperature and the average temperature of the solar panels.

### 3.6.3. EPS Simulation Results

Figure 18 describes the simulated electrical balance for the period April 26 to May 10 1991. The upper part consists of two graphs: Power generated and power consumed. The power generated varies from 120 watts to 155 watts at time zero. The reason for the power variations is due to the sun angle variation with respect to the solar panels as a result of the satellite coning. The power generated drops to zero during the eclipse. The power consumed is given one constant value during the satellite day (51 watts) and a lower value during eclipse (48 watts).

The lower graph in Figure 18, describes the state of charge in the battery. The battery is discharged during eclipse and charged during the day. However, starting from zero time, the power generated is not sufficient to fully charge the battery during the day, thus causing a slow overall discharge. During actual satellite operation, the power generated changed slowly as the sun angle became lower and coning increased, until, finally, the battery was fully discharged on May 1, 1990 at 17:00 (see Figure 18). The battery's full discharge lasted until May 8 1990 after 12:00, even though adequate power had been available from the panels for the past two days.

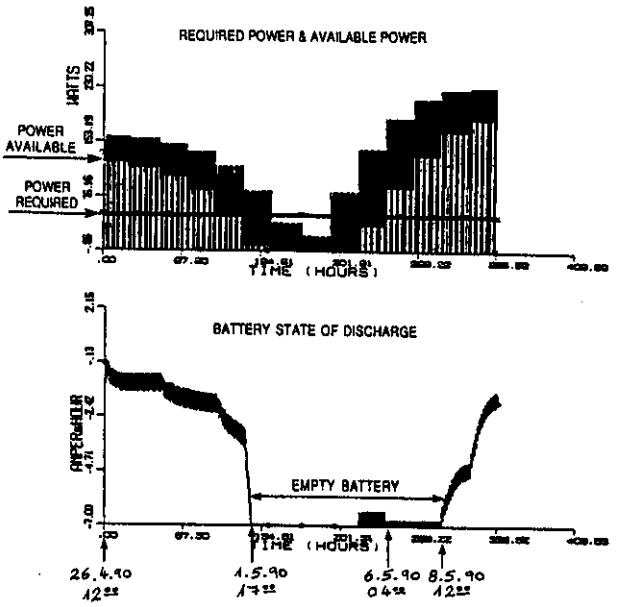


Figure 18. Electrical Power Reconstruction 26th of April to 10th of May 1990

The reason for the battery not being charged even though the solar panels generated an average of 100 watts on the 6th of May, had to do with the end-of-charge mechanism. The power control unit (PCU) controls the end-of-charge by reducing the charge current as the battery voltage increases due to increase of the state of charge. Since the battery temperature was much higher than planned, the PCU stopped battery charging much too early. Thus, the battery charge resumed only two days after sufficient power had been generate. The battery temperature drop indicated that the charge had been reduced to the 70% level.

## 3.7 Radiation Effects

Ofeq-2 was equipped with a detection mechanism capable of monitoring SEU and latch-up events affecting the computer's RAM. During the flight, twelve SEU events and one latch-up were detected. Most of the events ocurred during the satellite's passage in the South Atlantic Anomaly zone of the Van Allen radiation belts and a few occured at undefinable times and locations.

The recurrence of the SEU events is in agreement with the calculated predictions. Just one SEU event ocurred outside the South Atlantic Anomaly. It is presumed to have happened because an especially energetic particle of galactic radiation origin penetrated the satellite. Our predictions did not foresee such an event and the fact that it did occur may mean that such highly energetic particles are more prevalent than expected outside the belts region.

## 4. SYSTEMS RECONSTRUCTION APPROACH

### 4.1 Introductory Remarks

The approach described here and alluded to above is the classical or traditional one, used in space systems operation for years, not always with complete success. However, in the case of Ofeq-2 it worked well, as it usually does when the data is known. It simply integrates several disciplines to yield a more complete picture of what occurred. Figure 19 depicts the procedure and processes used.

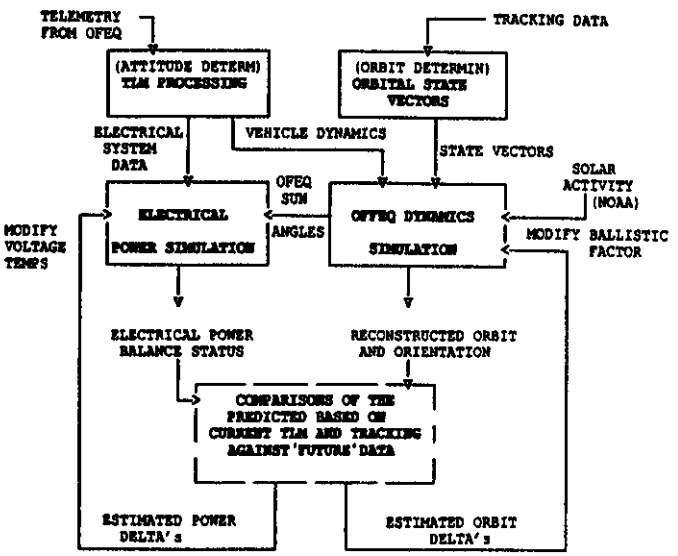


Figure 19. Orbit and Attitude Reconstruction Process

The major factor governing the behavior of Ofeq-2 was the slow growth of the coning angle compared to Ofeq-1. Given this condition, and the fairly predictable precession of the satellite in the orbit plane and the even better known position of the sun, the results are no less than expected. However, integration of disciplines was required, as described in previous sections.

### 4.2 Steps in the Procedure

TLM data was processed yielding satellite orientation data, temperatures, power system currents and voltages. These data also provided a preliminary check against redlines. Tracking data was concurrently processed and orbital state vectors were generated. Solar activity data was updated as fast as possible.

Measured orientation data was supplied to the dynamics simulation, which then, after generating the complete dynamics forecast, checked the orbital data against measured state vectors. The best available solar data was then input to the simulation and the measured orbital data was reached against the predicted. Then the Cd multiplied by the reconstructed satellite cross sectional area term was varied until the orbital and attitude data matched. This is somewhat iterative, but seems to work well. After the attitude data is fit as well as possible, it becomes possible to evaluate the Cd or biases in our models.

Once a good fit is available, the Electrical power simulation is fed data on orientation angles and orbit in-order to construct the environmental conditions for the solar panels and the battery. This was then matched against the EPS currents, voltages and biases measured in the preflight or ground testing, and the biases in the simulation.

This data and approach was used to generate the results shown above for orbital lifetime and the time for power off-and-on-again. Since the fit between simulated and real data during the mission and afterwards was close, the approach was successful in deciphering observed anomalies. It also explained the occurrence of the key events and pretty successfully estimeted the lifetime of the satellite.

## 5. CONCLUSIONS

The Ofeq-2 mission accomplished its goals and revealed important factors to be considered in the design of future IAI satellites. To name just a few: Design for solar activity uncertainties, Protection of the satellite computer against radiation, Preparation for power outages and their effects. Of no less importance was the successful space worthiness testing and approval of systems and components, manufactured by IAI.


#### Acknowledgment

The authors acknowledge the significant contribution of Mr J. Wittenstein to the TLM data management and evaluation effort concerning the Ofeq-2 mission [3].


#### REFERENCES


1. "Ofeq-1, Preliminary Flight Evaluation Results", J. Wittenstein and M. Barlev, 30th Israel Annual Conference on Aviation and Astronautics, February 1989
2. "Stabilization and Control of Spacecraft", A.E. Bryson, AAS Guidance and Control Conference, 1983, Vol 44, AAS 83-087.
3. "Ofeq-2, Orbit and Attitude Flight Evaluation Report", J. Wittenstein, H. Shyldkrot, M. Grumer, J. Komem, O. Kubitski, J. Kronenfeld, 4th Annual AIAA / USU Conference on Small Satellites, Logan, Utah, August 28 - 30, 1990.

# EFFECTS OF SOLAR RADIATION PRESSURE TORQUE ON THE ROTATIONAL MOTION OF AN ARTIFICIAL SATELLITE

M. Cecília F.P.S. Zanardi, Msc
UNESP-FEG-DMA
C.P. 205
12500 - Guaratinguetá - SP - Brasil

Dr. Rodolpho Vilhena de Moraes
ITA-IEA-IEAB
Centro Técnico Aeroespacial
12225 - São José dos Campos - SP - Brasil

**Abstract**

The motion of an artificial satellite about its center of mass is studied considering torques due to the gravity gradient and direct solar radiation pressure. A model for direct solar radiation torque is derived for a circular cylinder satellite. An analytical solution is obtained by the method of variation of the parameters. This solution shows that the angular variables have secular variation but, the modulus of the rotational angular momentum, the projection of rotational angular momentum on the z-axis of the moment of inertia and inertial axis z, suffer only periodic variations. Considering a hypotetical artificial satellite, a numerical application is exhibited.

## 1. Introduction

The object of this paper is to analyse the influence of the torque due to the direct solar radiation pressure on the rotational motion of an artificial satellite. Gravity gradient torque is also considered and Andoyer's variables are used to describe the rotational motion. Solar radiation pressure torque is considered of second order with respect to the torque free motion and first order with respect to gravity gradient torque [2].

Euler's angles have been used to study the influence of the solar radiation pressure torque on the stability of the rotational motion of artificial satellites [3, 8, 9, 10].

In this paper a model for direct solar radiation pressure is derived, using the general expression given by Georgeovic [5] and reviewed by Tang [11]. Coefficients of specular and difuse reflection are assumed distinct for the various surfaces of the satellite and a general expression for the torque is computed for a circular cylinder satellite. Using cylindrical and polar coordinates the position of the surface elements are defined with respect to the geometric center of the satellite. The iluminated surfaces of the cylinder satellite are a circular flat surface and a portion of the cylinder surface. The components of the torque are obtained in the principal axis of inertia and expressed in terms of the Andoyer's variables. Shadow s effects are not considered in this paper. The derived general expression for the direct solar radiation torque can be used for any shape of satellite, however the integration of the function depending on the elements of the surface become more complicated.

The Lagrange's method of variation of parameter is applied to obtain an analytical solution for the system of equations describing the rotational motion. The solution is analysed in two ways: first the mean equations are obtained and the solution of these equations are shown then, we apply the method of sucessive approximation in the initial system of equations and another solution is obtained.

A numerical application is done to analyse the magnitude of the torques considered.

## 2. Solar Radiation Pressure Torque Model

The light pressure is created by the continuous impingement of a stream of photons upon an intercepting surface. The total change in momentum of all photons striking the surface is the solar radiation force and this force produces a torque in the satellite.

The free space intensity of the solar radiation per unit area, per unit of time, at the Earth's mean solar distance ($a_o$ = $1.496 \times 10^8$ km) is known as solar constant radiation ($S_o$). With sufficient accuracy we may take [5] :

$$S_o = 1.353 \times 10^6 \text{ Watts m}^{-2} \quad (1)$$

If the phenomenon is considered over long time period, it is necessary to include the change in the distance between the Earth and the Sun. In this paper the Earth-Sun distance is considered constant.

The intensity of the solar radiation flowing per area, per unit of time, at distance R, can be given by

$$\bar{S} = S_o \left(\frac{a_o}{R}\right)^2 \quad (2)$$

When the solar radiation flowing meets perpendicularly the surface of a body , the radiation pressure is given by :

$$p = \frac{\bar{S}}{c} = \frac{K}{R^2} \quad (3)$$

where c is the light's speed and K assumes the value [5]

$$K = 1.01 \times 10^{17} \text{ kg m s}^{-1} \quad (4)$$

According to Georgeovic [5] the solar radiation pressure torque is given by

$$\vec{M} = -\left(\frac{K}{R^2}\right) \iint \vec{r} \times [B(\theta)\, \hat{n} + b \cos\theta\, \hat{u}]\, dS \quad (5a)$$

where:

1) R is the Sun-satellite distance;

2) $\vec{r}$ gives the position of the surface element dS with respect the mass center of the satellite;

3) $\hat{n}$ is a unit vector along the outer normal;

4) $\hat{u}$ is a unit vector along the direction of flux;

5) $\cos\theta = \hat{u} \cdot \hat{n}$ (5b)

6) $B(\theta) = \frac{2}{3}\gamma(1-\beta)\cos\theta + 2\beta\gamma\cos^2\theta$ (5c)

In this paper it is assumed Lambert's law for the diffusely reflected photons.

7) $b = 1 - \beta\gamma$ (5d)

8) $\beta$ and $\gamma$ are, respectively, the coefficients of specular and difuse reflection.

In order to compute the general expression (5) it will be considered here an artificial Earth satellite of circular cylindrical shape, in an elliptical orbit. Moreover the following simplifications will be made:

1) the direction of the solar flux is given by the apparent motion of the Sun with respect to the Earth;

2) the Sun-satellite distance is constant;

3) the coefficients of specular and difuse reflections admit constant average values.

The inertial system considered is the Equatorial system with unit vectors $\hat{e}_X, \hat{e}_Y, \hat{e}_Z$ . The direction of the solar flux is given in function of the right ascension ( $\alpha_s$ ) and declination ( $\delta_s$ ) of the Sun. Therefore:

$$\hat{u} = \cos\delta_s \cos\alpha_s\, \hat{e}_X + \cos\delta_s \sin\alpha_s\, \hat{e}_Y + \sin\delta_s\, \hat{e}_Z \quad (6)$$

The components of the solar radiation torque will be expressed in the system Oxyz of the principal axis of inertia of the satellite with units vetors $\hat{e}_x$, $\hat{e}_y$, $\hat{e}_z$.

The position of this system relative to the inertial system is defined by matrices whose elements are function of the Andoyer's variables ( $l_i$ , $L_i$ ), i = 1,2,3 [1] defined in figure (1).

Therefore the direction $\hat{u}$ in the principal axis of inertia is given by:

$$\hat{u} = u_X\, \hat{e}_X + u_Y\, \hat{e}_Y + u_Z\, \hat{e}_Z \quad (7)$$

where $u_X$ , $u_Y$ , $u_Z$ are functions of I, J, $\alpha_s$, $\delta_s$ and $l_i$, where i = 1,2,3.

The iluminated surfaces of the cylinder satellite are the circular flat surface ($A_1$) and the portion of the cylindrical surface ($A_2$) limited between ($\lambda - 90°$) and ($90° + \lambda$), as showed in figure (2). The parameter is defined by:

$$\text{tg}\,\lambda = \frac{u_Y}{u_X} \quad (8)$$

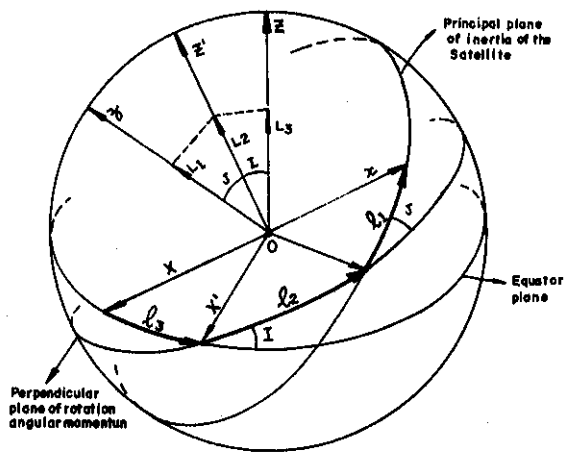


Figure (1). Andoyer's Variables $(l_i , L_i)$, i = 1,2,3, being $\cos J = L_1/L_2$ and $\cos I = L_3/L_2$ .

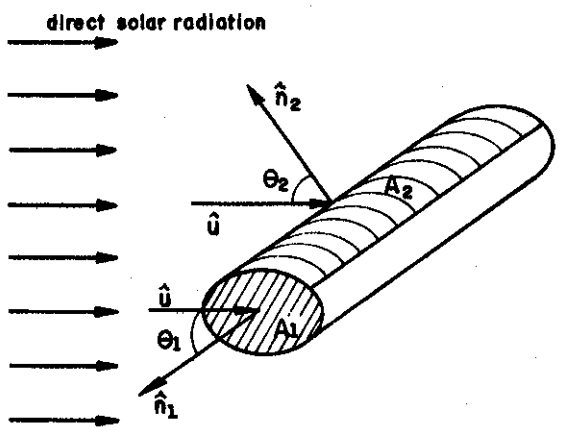


Figure (2) . The iluminated surfaces of the cilinder satellites $A_1$ and $A_2$.

For each surface, the vetors n and r can be expressed in cylindrical coordinates in the system of principal axis of inertia. Thus:

A) Surface $A_1$

$$\hat{n}_1 = \hat{e}_Z \qquad (9a)$$

$$\vec{r}_1 = s \cos \alpha \, \hat{e}_X + s \sin \alpha \, \hat{e}_Y + h/2 \, \hat{e}_Z$$

with:

$$0 \le \alpha \le 2\pi \qquad \text{and} \qquad 0 \le s \le \sigma$$

where h and are respectively the height and the radius of the cylinder.

B) Surface $A_2$

$$\hat{n}_2 = \cos \phi \, \hat{e}_X + \sin \phi \, \hat{e}_Y \qquad (10a)$$

$$\vec{r}_2 = \sigma(\cos \phi \, \hat{e}_X + \sin \phi \, \hat{e}_Y) + z \, \hat{e}_Z$$

with :

$$\lambda - 90° \le \phi \le 90° + \lambda$$

$$- h/2 \le z \le h/2$$

Thereafter, if circular cylindrical satellite is considered, the solar radiation pressure torque is given by :

$$\vec{M} = - (K/R^2) \{ \int_0^{\sigma}\int_0^{2\pi} [B_1(\theta_1) \, \vec{r}_1 \times \hat{n}_1 +$$

$$b_1 \cos \theta_1 \, \vec{r}_1 \times \hat{u}] \, s \, d\alpha \, ds +$$

$$\int_{-(90-\lambda)}^{90+\lambda}\int_{-h/2}^{h/2} [B_2(\theta_2) \, \vec{r}_2 \times \hat{n}_2 +$$

$$b_2 \cos \theta_2 \, \vec{r}_2 \times \hat{u}] \, \sigma \, dz \, d\alpha \} \qquad (11)$$

where :

$$B_i(\theta_i) = (2 \gamma_i/3) (1 - \beta_i) \cos \theta_i +$$

$$2 \beta_i \gamma_i \cos^2 \theta_i \qquad (12a)$$

$$b_i = 1 - \beta_i \gamma_i \qquad (12b)$$

$$i = 1,2$$

Here, $\beta_i$ and $\gamma_i$ are respectively the coefficients of specular and difuse reflection of the surface $S_i$ .

Substituting the expressions (7), (9) and (10) in the equations (11), and then integrating, the following expression for the solar radiation pressure torque (for circular satellites) are obtained :

$$\vec{M} = M_X \, \hat{e}_X + M_Y \, \hat{e}_Y \qquad (13)$$

where :

$$M_X = - m u_Y u_Z \quad (14a)$$

$$M_Y = m u_X u_Z \quad (14b)$$

with

$$m = (K/R^2)(\pi \sigma^2 h/2)(\beta_2 \gamma_2 - \beta_1 \gamma_1)$$

Equation (13) shows that the components of the solar radiation torque in the principal z-axis is zero.

### 3.Equations for the Rotational Motion

Considering the gravity gradient torque and the torque produced by direct solar radiation pressure, the equations for the rotational motion can be put in the following form:

$$\frac{dl_i}{dt} = \frac{\partial F}{\partial L_i} + P_i \quad (15a)$$

$$\frac{dL_i}{dt} = \frac{-\partial F}{\partial l_i} + S_i \quad (15b)$$

$i = 1,2,3$

where

1) $l_i$ and $L_i$ are the Andoyer's variables [1];

2) F is the Hamiltonian for the conservative problem. It will be considered in the Hamiltonian terms up to the order of the inverse of the cube of the distance from the center of the mass of the satellite to the Earth's center of mass. Also, terms to the order 2 in excentricity were considered. Therefore the Hamiltonian F can be written in the following form [7]

$$F = F_o(L_1, L_2, L_4) + F_1(l_i, L_i) \quad (16)$$

$i = 1,2...6$

where:

$$F_o = 1/2 \left\{ \left[ \frac{1}{C} - \frac{1}{2A} - \frac{1}{2B} \right] L_1^2 + 1/2 \left[ \frac{1}{A} + \frac{1}{B} \right] L_2^2 \right\} \quad (17a)$$

$$F_1 = 1/4 \left( \frac{1}{B} - \frac{1}{A} \right)(L_2^2 - L_1^2) \cos 2 l_1 + (\mu^4 M^7/L_4^7) \left[ \frac{2C - A - B}{2M} f_1(l_i, L_i) + \frac{A - B}{4M} f_2(l_i, L_i) \right] \quad (17b)$$

$i = 1,...,6$

and

a) M is the mass of the satellite;

b) $\mu$ is the product of the gravitational constant by the mass of the Earth;

c) A, B, C are the principal moments of inertia of the satellite ( for cylindrical satellite A = B and the Hamiltonian F is simplified);

d) $l_j$ and $L_j$ represent the Delaunay's variables for $j = 4,5,6$;

e) $f_1$ and $f_2$ are functions of the marked variables. These functions, expressed in terms of the mean anomaly, are shown in Zanardi [15].

3) $P_i$ and $S_i$ , coming from the solar radiation, are presented in Vilhena de Moraes [14] as follows :

$$P_1 = \frac{1}{L_2 \sin J}(M_X \cos l_1 - M_Y \sin l_1)$$

$$P_2 = - (M_X/L_2)\{ \text{cotg } J \cos l_1 + \text{cotg } I [\cos l_1 \cos l_2 - \sin l_2 \cos J \sin l_1]\} + (M_Y/L_2)\{\text{cotg } J \sin l_1 + \text{cotg } I [\sin l_2 \cos l_1 \cos J + \cos l_2 \sin l_1]\} - (M_Z/L_2)\{ \text{cotg } I \sin l_2 \sin J \}$$

$$P_3 = \frac{1}{L_2 \sin I}\{ M_X [\cos l_1 \cos l_2 - \sin l_1 \sin l_2 \cos J] - M_Y [\sin l_1 \cos l_2 + \cos l_1 \sin l_2 \cos J] + M_Z \sin l_2 \sin J\}$$

$$S_1 = M_Z$$

$$S_2 = M_Z \cos J + M_X \sin J \sin l_1 + M_Y \sin J \cos l_1$$

$$S_3 = M_X \{\sin I \cos l_1 \sin l_2 + \sin l_1 (\cos I \sin J + \sin I \cos J \cos l_2)\} + M_Y \{-\sin I \sin l_2 \sin l_1 + \cos l_1 [\cos I \sin J + \sin I \cos l_2 \cos J]\} + M_Z \{\cos J \cos I - \sin I \sin J \cos l_2\} \quad (18)$$

where:

a) $M_X$, $M_Y$, $M_Z$ are the components of the solar radiation pressure torque M, expressed in the principal axis of inertia system of the satellite;

b) $\cos J = L_1/L_2$ (19a)

c) $\cos I = L_3/L_2$ (19b)

It worth to mention that if the shadow's effect is neglected, P and Q can be included in the Hamiltonian.

Now we will solve the system (15), applying Lagrange's method of variation of parameter.

## 4. Integration of the Equations of Motion

Using Hori's method [6], the solution of the system (15), when $P_i = Q_i = 0$, was obtained by Zanardi [15] in the following form:

$$L_i = L_i^* + \delta L_i$$

$$l_i = l_i^* + n_i t + \delta l_i \quad (20)$$

$$i = 1,2,3$$

where :

a) $L_i^*$ and $l_i^*$ are constants;

b) $\delta L_i$ and $\delta l_i$ are periodic funtions

c) $n_j = n_{jo} + n_{jg}$ $\quad j = 1,2$

d) $n_3 = n_{3g}$

Here, $n_{jo}$ is given by the torque free motion and $n_{jg}$ is due to the gravity gradient torque.

Applying Lagrange's method in the system (15a) and (15b), by [13] we get :

$$\dot{L}_i^* = \bar{S}_i - \sum_{k=1}^{3} \{\bar{S}_k \frac{\partial(\delta \bar{L}_i)}{\partial L_k^*} + \bar{P}_k \frac{\partial(\delta L_i^*)}{\partial \sigma_k^*}\}$$

$$\dot{\bar{\sigma}}_i^* = \bar{P}_i + \bar{n}_i - \sum_{k=1}^{3} \{\bar{S}_k \frac{\partial(\delta \bar{\sigma}_i)}{\partial L_k^*} + \bar{P}_k \frac{\partial(\delta \bar{\sigma}_i)}{\partial \sigma_k^*}\} \quad (21)$$

$$i = 1,2,3$$

where:

a) the transformation of $l_i^*$ to $\sigma_i^*$, i = 1,2,3, is necessary to eliminate spurious mixed terms, being:

$$l_i^* = \sigma_i^* - \bar{n}_i t \quad (22)$$

b) $\bar{P}_i$, $\bar{S}_i$, $\bar{n}_i$ are $P_i$, $S_i$, $n_i$ written in the new variables $L_i^*$ and $\sigma_i^*$;

c) $\delta\bar{\sigma}_i$, $\delta\bar{L}_i$ are the periodic parts of the solution without solar radiation pressure expressed in terms of $L_i^*$ and $\sigma_i^*$.

The solar radiation pressure torque is considered of second order with respect to the free rotational motion. Thus neglecting coupling terms in system (21) :

$$\dot{L}_i^* = \bar{S}_i (\sigma_i^*, L_i^*, \alpha_s, \delta_s, m)$$

$$\dot{\sigma}_i^* = \bar{n}_i(L_i^*, m) + \bar{P}_i (\sigma_i^*, L_i^*, \alpha_s, \delta_s, m)$$

$$i = 1,2,3 \quad (23)$$

In the system (23) the variables $\alpha_s$, $\delta_s$ and $\sigma_i$, i=1,2,3, are always as arguments of the trigonometric terms.

The solution of the system (15) is given by (20), where $l_i^*$ and $L_i^*$ are the solution of the system (23).

It is important to note that :

$$\frac{dL_1^*}{dt} = 0 \qquad \Rightarrow L_1^* = \text{constant} \qquad (24)$$

and therefore, the solar radiation pressure doesn't influence the computation of the projection of rotational angular momentum on the axis z of the moment of inertia.

The solution of system (23), is obtained first eliminating the short periodic variables $\sigma_j^*$, $j = 1,2$ , and the long periodic variables $\sigma_3^*, \delta_s, \alpha_s$. Finally the method of sucessive approximations is applied.

**4.1 Preliminary Analysis**

Only secular terms will be considered. Therefore, this correspond to eliminate first the periodic variables $\sigma_1^*$, $\sigma_2^*$ and after the long periodic variables $\sigma_3^*$, $\lambda_s$, $\alpha_s$.

With short periodic variables $\sigma_1^*$, $\sigma_2^*$ eliminated, we have new variables $\bar{\sigma}_i$, $\bar{L}_i$ and the system (19) remains:

$$\frac{d\bar{L}_j}{dt} = 0 \qquad \bar{L}_j = 0 \qquad j = 1,2$$

$$\frac{d\bar{L}_3}{dt} = f_3\,(\bar{\sigma}_3, \bar{L}_i, m, \alpha_s, \delta_s) \qquad (25)$$

$$\frac{d\bar{\sigma}_i}{dt} = g_i\,(\bar{\sigma}_3, \bar{L}_i, m, \alpha_s, \delta_s)$$

$$i = 1,2,3$$

After the elimination of the long periodic variables $\bar{\sigma}_3$, $\alpha_s$, $\delta_s$, we have new variables $\bar{\bar{\sigma}}_i$, $\bar{\bar{L}}_i$ given by[8]:

$$\frac{d\bar{\bar{L}}_i}{dt} = 0 \qquad i = 1,2,3$$

$$\frac{d\bar{\bar{\sigma}}_1}{dt} = \bar{\bar{n}}_1 - \frac{m}{\bar{\bar{L}}_2 \sin \bar{\bar{J}}} \left\{ \frac{\sin 2\bar{\bar{J}}}{8} (3 \sin^2 \bar{\bar{I}} - 2) \right\}$$

$$\frac{d\bar{\bar{\sigma}}_2}{dt} = \bar{\bar{n}}_2 + \frac{m}{4\,\bar{\bar{L}}_2} \{\cos^2 \bar{\bar{J}} - \cos^2 \bar{\bar{I}} (2 + 3 \cos 2\bar{\bar{J}})\}$$

$$\frac{d\bar{\bar{\sigma}}_3}{dt} = \bar{\bar{n}}_3 + \frac{m \cos \bar{\bar{I}}}{8\,\bar{\bar{L}}_2} (3 \cos 2\bar{\bar{J}} + 1) \qquad (26)$$

where:

a) $\bar{\bar{n}}_i$ is $\bar{n}_i$ expressed in terms of $\bar{\bar{L}}_i$, i = 1,2,3

b) $\cos \bar{\bar{J}} = \bar{\bar{L}}_1/\bar{\bar{L}}_2$

c) $\cos \bar{\bar{I}} = \bar{\bar{L}}_3/\bar{\bar{L}}_2$

The solution of system (26) is :

$$L_i = \text{constant}$$

$$\bar{\bar{\sigma}}_i = \bar{\bar{n}}_i^* t + \sigma_{io}^* \qquad (27)$$

$$i = 1,2,3$$

where:

$$\bar{\bar{n}}_1^* = \bar{\bar{n}}_1 - \frac{m}{4\bar{\bar{L}}_2} \cos \bar{\bar{J}} (3 \sin^2 \bar{\bar{I}} - 2)$$

$$\bar{\bar{n}}_2^* = \bar{\bar{n}}_2 + \frac{m}{4\bar{\bar{L}}_2} \left[ \cos^2 \bar{\bar{J}} - \cos^2 \bar{\bar{I}} (2 + 3 \cos 2\bar{\bar{J}}) \right]$$

$$\bar{\bar{n}}_3^* = \bar{\bar{n}}_3 + \frac{m \cos \bar{\bar{I}}}{8\bar{\bar{L}}_2} (3 \cos 2\bar{\bar{J}} + 1) \qquad (28)$$

Therefore the rotational angular momentum ($L_2$) and its projection on the inertial axis z ($L_3$) doesn't suffer secular variations due to the solar radiation pressure torque.

The new variables $\bar{\sigma}_i$, $\bar{L}_i$ and the variables $\sigma_i^*$, $L_i^*$ are similar with exception of periodic terms.

### 4.2 Using the method of sucessive aproximations

The solution of system (23) will be obtained by the method of sucessive approximations.It will be considered the solution given in (27) to avoid the spurious Poisson terms. The variables $\alpha_s$, $\delta_s$ are function of the time and can be taken from the Astronomical Almanac [11].

Then, substituting the solution (27) in the system (23) and integrating then we obtain:

$$L_1^* = \text{constant} \qquad (29a)$$

$$L_j^* = L_{jo}^* + \delta L_j^* \qquad j = 2,3 \qquad (29b)$$

$$\sigma_i^* = (\bar{n}_i + \Delta\bar{n}_i)\, t + \sigma_{io}^* + \delta\sigma_i^* \qquad (29c)$$

$$i = 1,2,3$$

where :

a) $\delta L_j^*$, $\delta\sigma_i^*$ are periodic functions of the variables $\sigma_i^*$, $\alpha_s$, $\delta_s$;

b) $L_{jo}^*$, $\sigma_{io}^*$ are initial conditions;

c) $\bar{n}_i$ and $\Delta\bar{n}_i$ are secular effects in the variables respectively due the gravity gradient and direct solar radiation torques;

Therefore, the solar radiation pressure torque produce secular and periodic variations in the angular variables $\sigma_i^*$ and only periodic variations in the rotational angular momentum ($L_2^*$) and its projetion on the inertial axis z ($L_3^*$).

### 4.3 Solution of the Equations of Motion

The solution of rotational motion considering the torque produced by direct solar radiation pressure and the gravity gradient torque, given by the system (15), can be put in the following form:

$$L_1 = L_1^* + \delta L_1$$

$$L_j = L_{jo} + \delta L_j + \delta L_j^* \qquad j = 2,3$$

$$l_i = (n_i + \Delta n_i)\, t + \delta l_i + \delta l_i^* + l_{io}$$

$$i = 1,2,3$$

where

a) $\delta L_i$, $\delta l_i$, $n_i$ are the effects of the torque free motion and gravity gradient torque.

b) $\delta L_j^*$, $\delta l_i^*$, $\Delta n_i$,are the effects of the direct solar radiation torques.

## 5. Numerical Application

In order to analyse the order of magnitude of the gravity gradient torque and solar radiation pressure torque, let us consider an hypothetical satellite with orbital and physical elements similar to the elements of the "PEGASUS A" satellite [4,16]. Thus, we will assume the following values:

a) diameter $\sigma$ and height h :

$$\sigma = 4 \text{ m}$$

$$h = 18 \text{ m}$$

b) coefficients of specular and difuse reflection, $\beta_i$ and $\gamma_i$, in the circular flat surface (i = 1) and, in the lateral cylindrical surface (i = 2) :

$$\beta_1 = 0.1 \qquad \gamma_1 = 0.7$$

$$\beta_2 = 0.1 \qquad \gamma_2 = 0.5$$

c) parameter m given in (14c) :

$$m = -4.245 \times 10^{-11} \text{ kg km}^2\text{s}^{-1}$$

Initial values for the Andoyer's variables will be taken the followings :

$$L_1 = 0$$

$$L_2 = 9.7307 \times 10^{-3} \text{ kg km}^2\text{s}^{-1}$$

$$L_3 = -2.9956 \times 10^{-3} \text{ kg km}^2\text{s}^{-1}$$

$$l_1 = l_2 = 90^\circ \qquad l_3 = 276.42^\circ$$

$I = 107.93°$ $J = 90°$

Using the mentioned figures we can compute the magnitude of the solar radiation torque. Thus , for the component $L_3$ , we find for the most important long period term, an amplitude of about $10^{-12}$ kg $km^2$ $s^{-1}$ with a period of about 108300 days. This is of about $10^{-3}$ of the influence of the gravity gradient torque [16] (term with a period of 89 days). This influence, very small due to the dimensions of the satellite, can become important for big spatial stations.

## 6. Conclusions

The purpose of this paper was obtain an analytical solution for the rotational motion of an artificial satellite, considering the gravity gradient and direct solar radiation torques. The solution was shown and a model for solar radiation torque was presented. The components of the solar radiation torque were expressed in the system of the principal axis of inertia of the satellite. Considering a hypothetical artificial satellite, a numerical appllication shows that the magnitude of the solar radiation torque is about $10^{-3}$ of the magnitude of the gravity gradient torque.

## 7. References


[01] - Andoyer, H.: 1923, "Cours de Mecanique Celeste", Vol 1 Gauthier - Villard, Paris, p.54.

[02] - Beleskii, V. V.: 1966, "Motion of an Artificial Satellite about its center of Mass", Israel Program for Scientific Translations Ltda; Jerusalém.

[03] - Clancy, T. F. ; Mitchell, T. P.: 1964, AIAA Journal, vol 2, 3, 517

[04] - Cochran, V. E.: 1972, Celest. Mech., 6, 127.

[05] - Georgeovic, R. M.: 1973, The Journal of the Astron-Sci, vol XX, 5, 257

[06] - Hori, G.: 1966, Celest. Mech., 6, 127.

[07] - Kinoshita, H.: 1972, Publ. Astron. Soc. Japan, 24, 423.

[08] - Modi, V. J.: Kumar, K.: 1974, AIAA Journal, vol 12, 2.

[09] - Modi, V. J.: Pande, K. C.: 1973, Journal of Spacecraft and Rocket, vol 10, 9, 615.

[10] - Modi, V. J.; Pande, K. C.: 1975, Celest. Mech., vol 11, 2, 195.

[11] - The Astronomical Almanac for the year 1991, Washington, USA.

[12] - Tang, C. C. H.: 1981, The Journal of the Astron. Sci., vol XXIX, 2, 171.

[13] - Vilhena de Moraes, R.: 1981. Celest. Mech., 25, 281-292.

[14] - Vilhena de Moraes, R.: 1988, Anais do 7 Congresso Brasileiro de Automatica, vol 2, 986.

[15] - Zanardi, M. C.: 1983, Tese de Mestrado do Instituto Tecnológico de Aeronáutica, São José dos Campos, São Paulo, Brazil.

[16] - Zanardi, M.C.: 1986, Celest. Mech., 39, 147.

[17] - Zanardi M. C.: 1989, Solar Radiation Pressure Torque Model on a Circular Cylinder Satellite, in R. V. Martins, D. Lazzaro and W. Sessin (eds), Orbital Dynamics of Natural and Artificial Objects, Observatório Nacional, Rio de Janeiro, pp 145 - 152.

# Minimum Number of Satellites for Earth Coverage by a Constellation of Low-Orbit Satellites.

Dr.Marcel Sidi, Yoram Yaniv
Israel Aircraft Industries, MBT-Yehud, Israel

Abstract.

An analytical way for computing the minimum number of satellites in a Low-Orbit Multi-Satellite System with 100% coverage requirements is described. A Walker delta pattern constellation is assumed for a certain class of Earth Coverage definition.

An efficient numerical simulation has been prepared in order to check the analytical results; the agreement between the analytical results and the simulation was perfect.

Nomenclature.

GST - Ground station
Dd - ground distance from the GST
Rd -radius of circle for covered area around the GST
h - altitude of the satellite
Ds -ground distance of satellite coverage from subsatellite point
Rs -radius of circle for satellite coverage area
Inc -inclination of orbit plane
AN -number of satellites in one orbit plane (chain)
N -INTEGER(AN)+1
AM1 -number of chains for almost 100% coverage
M1 -INTEGER(AM1)+1
AM2 -number of chains for 100% coverage
M2 -INTEGER(AM2)+1
ANM100 -number of satellites for 100% coverage
ANM -number of satellites for almost 100% coverage
$\alpha$ -covered angle of satellite communication (antena or other instrumentation)
$\delta\alpha$ -minimum horizon angle for satellite/ground communication
Re -radius of earth globe
Cd -circle of desired ground coverage
Cs -circle of satellite ground coverage
Rc -satellite communication range
Rcmax -max satellite communic. range
AL ANT -half the antenna aperture

## 1. Introduction.

The importance of Low-Orbit, Low-Cost Multi-Satellite Systems for a variety of civil and military requirements is increasing constantly. Some of these requirements include communications, data relay, meteorology, surveillance and so on.

A principal advantage of a constellation of satellites is high reliability and survivability: the loss of a single satellite leads to a graceful degradation only. Moreover, the system is justifiable even with a preliminary smaller number of satellites, which increases gradually until the system is completed.

Depending on the specific mission, the necessary number of satellites may become quite large, especially for very low- altitude satellites. The normal trade-offs in designing a Multi-Satellite System (hereafter called MSS) is coverage (performance) versus the number of satellites (cost).

Numerous types of constellations have been treated [1] and we shall concentrate on the Walker delta pattern Constellation[2]. This constellation is based on a number of satellites equally distributed in some orbit planes having the same inclination, the ascending nodes of the orbit planes being equally spaced on the equator principal circle. In the analysis to follow, the Walker type constellation is very important, because all satellites in the same orbit plane, having the same altitude, will keep their relative position constant. However, the Earth Coverage definition, as treated in the present paper, is basically different from that of Reference 2.

Various procedures for spacing satellites of a constellation in space are based on powerful numerical optimization techniques [3]. For Low-Orbit Constellations, they can result in an unnecessarily large number of satellites. The present paper presents a very simple analytical way to predict the minimum number of satellites for a class of coverage, to be stated in the following section.

A powerful numerical simulation has been prepared in order to check the results. Moreover, the same simulation has been used to compute the degradation of the coverage index if the number of satellites is decreased, for instance, in order to decrease the cost of the Multi-Satellite System.

## 2. Statement of the problem.

A Low-Orbit Multi-satellite System is required to achieve a full (100%) desired coverage of a certain region around a Central Ground Station, hereafter called GST (Fig.1). Suppose the Desired Earth Coverage (hereafter called DEC) area on ground is a circle with radius Rd centered on the ground station. The Satellite Earth Coverage (hereafter called SEC) is the section of the earth which can be seen by the satellite with anyone of its specific instruments or antennae. Assuming that the Earth is an exact sphere, the SEC is a circle with radius Rs, centered at the sub-satellite point.

Direct Communication between satellites is prohibited; however, communication between satellites via the GST is allowed. With these geometrical constraints, communication between any two points inside the circle with radius Rd around the GST is to be continuous in time, which is the same as asking for a 100% coverage to be achieved within the DEC area.

Before we attempt the solution of the problem, some more definitions are required: all satellite orbits are circular with the same altitude. Any communication or observation from the satellites or to the satellites is practically possible for a minimum

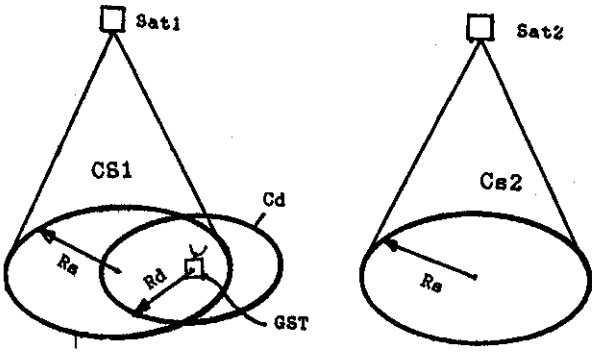


Figure 1

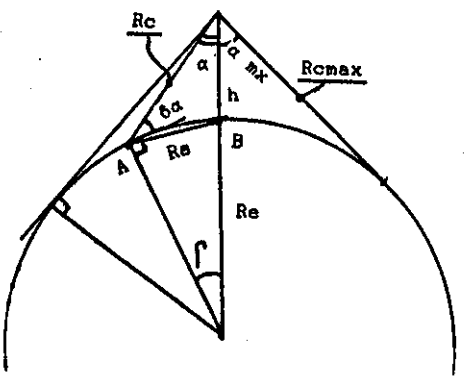


Figure 2

elevation angle δα above horizon, as shown in Fig.2. In fact, given δα and h, we can compute the effective coverage radius Rs for every one of the constellation satellites.

Given a Satellite Ground Covered Distance Ds, which is the length of the arc AB, the radius Rs is easily computed and is the length of the segment AB=Rs. The same is true for the Desired Ground Covered Distance Dd, and Rd, which are similarily computed.

For both cases, given the arc AB, which is the distances Ds (or Dd), the central Earth angle Γ is

known,hence also Rs (or Rd) can be computed.

## 3.Computation of the Minimum Number of Satellites.

Computation of the number of satellites for a full (100%) coverage is based on the following assumptions, the first two to be abandoned at a later stage.The assumptions are:

1.The earth globe is motionless around its polar axis.

2.The planes of the satellite orbits are inertially stationary.

3. Rs > Rd .

4.The inclination of the orbits is equal ,or greater,than the latitude of the GST.

With the above assumptions,suppose that the GST is located in one of the planes of the orbit constellation. When a satellite moves in its orbit, and the circle Cd is entirely inside circle Cs1 , (or Cs2), in Figure 1, then a 100% coverage does exist.For a continuous 100% coverage,more than one satellite is of course necessary in the same orbit plane.

The first question to be answered is what is the minimum number N of satellites needed on this plane only,so that 100% coverage is achieved

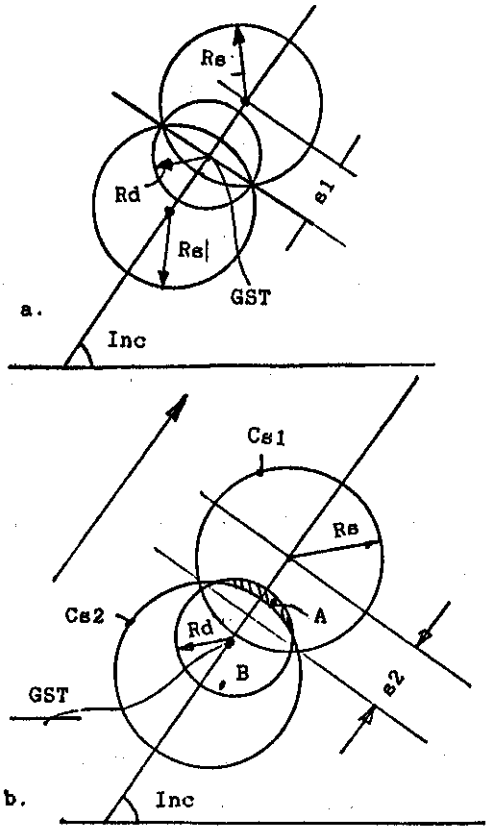


Figure 3

continuously.Accordingly to assumptions 1 and 2 ,the GST stays continuously in the plane of the orbits.Hence,in Figure 3,there are two extreme cases,which allow us to find the minimum permitted distance 2*s between the sub-satellite points of two adjacent satellites. In Figure 3,

$$s1=\sqrt{Rs^2-Rd^2} \qquad (1)$$

$$s2=Rs - Rd/2 \qquad (2)$$

The additional condition of Eq.(2) must be imposed,because ,for the extreme case shown in Figure 3b.Point A in the dashed area ,cannot communicate with point B ,because the GST is outside Cs1,hence ,s2 must be decreased.

(Direct communication between satellites is prohibited).Because of the the movement of both satellites,the dashed region will decrease and disappear.In the limit,the GST must lie on the circle CS1,and Eq.(2) follows. Finally, s=Min(s1,s2),so that the minimum distance between the sub-satellite points should be :

$$\text{Min Distance} = 2*s. \qquad (3)$$

Knowing the length of a great circle of the Earth,Le=2.π.Re, the minimum number of satellites in one plane should be :

$$AN = \frac{Le}{2*s} = \frac{\pi*Re}{s} \qquad (4)$$

AN need not be an integer.

Define N=INT(AN)+1 [If INT(AN)=AN then N=AN ].

The agglomeration of satellites in the same plane will be called "a chain of satellites". The next step will be to find the necessary number of chains,or planes of orbits,necessary to cover the entire globe strip, as in Figure 4.

The computation of the needed number of planes is also very simple:as per Figure 5,the covered distance on the equator circle is:

$$m = \frac{Rs}{\sin(Inc)} \qquad (5)$$

and the necessary number of chains (orbit planes) ,assuming coverage at the equator is required, will be:

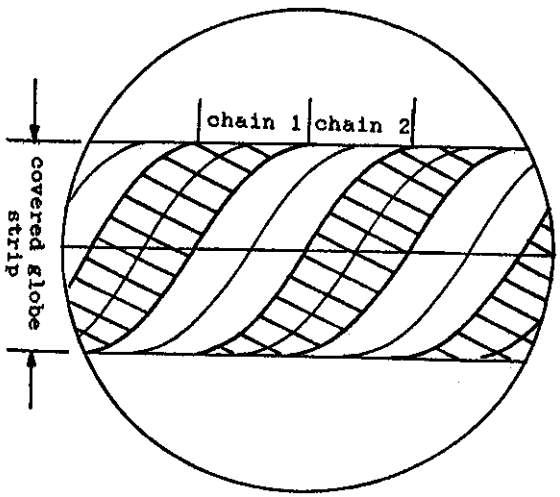


Figure 4

$$AM1 = \frac{2*RE*\pi}{2*2*m} = \frac{\pi*Re*\sin(Ic)}{2*Rs} \qquad (6)$$

In Figure 5a, small gaps remain uncovered. These uncovered regions can be cancelled by augmenting the number of chains (but with some unnecessarily multiply covered areas,as in Figure 5b):Eq.6 needs to be altered to:

$$AM2 = \frac{\pi*Re*\sin(Inc)}{2 * Rd} \qquad (7)$$

The needed number of satellites for a 100% coverage becomes:

$$ANM100 = AN*AM2 \qquad (8)$$

If the small uncovered gaps in Figure 5a are acceptable,then :

$$ANM = AN * AM1 < ANM100 \qquad (9)$$

Since according to Figure 4, the entire globe strip is covered, assumptions 1 and 2 can be removed:the relative motion between the GST and the chains and satellites is of no importance any more.A GST located anywhere inside the "globe strip",as in Figure 4,will be covered continuously in the entire desired ground area,as defined by the radius Rd.

AN,AM1,AM2,ANM and ANM100 are not, in general, integers. A simple way,but very expensive in number of satellites, is to increase AN,AM1 and AM2 to the nearest higher integer.An overdesign shall result.

Some numerical examples are given in Table 1.

Take, as an example, a MSS of orbits with an altitude of 1400 km.,and an inclination of 40°.The desired coverage region around the GST should be Rd=2000 km.,$\delta\alpha$=2°.

The number of satellites in one chain (plane) comes to be :

AN=7.65 ,N=8.

If the uncovered gaps in Figure 5a are permitted,then AM1=1.78,M1=2 (from Eq.6),and the total number of satellites will be NM=16 .(The unrounded number of satellites is only

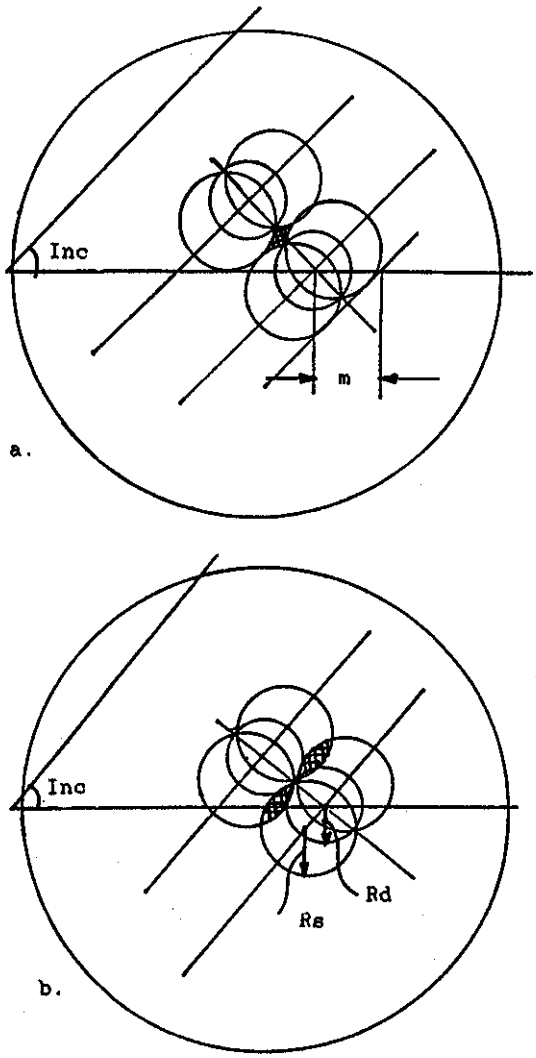


Figure 5

AN*AM1=13.61). Numerical simulation with two chains of eight satellites shows a coverage of 96.65 % only,which is expected.In case a 100% coverage is required,we find that AM2=3.22 (from Eq.7) so that M2=4,and four chains are necessary,with NM100=32.The calculated number is AN*AM2=24.63 satellites.Simulation showed a coverage of 100% at all times

during a period of 61 days.However, when the numerical simulation was carried with 3 chains of 8 satellites (24 satellites,close to the theoretical number AN*AM2=24.63), a coverage of 99.998% was demonstrated (See Figure 6).

On the same Figure 6, %COMM means the percentage of area of the circle Cd covered by circles Cs1. The averaging of the coverage percent is carried over a time period of 10(exp 6) sec=11.6 days.

The above simulations were carried for Ground Stations located 32° West,35° North, and 32° West,10° North,with similar results .

Some comments are mandatory on the results in Table 1.

The number of satellites in one plane increases with increasing Rd,as per Eq.(4),since s decreases with Rd in both Eqs. (1) and (2).

For the case in which the small uncovered gaps in Figure 5a are acceptable,the number of chains AM1 depends on Rs only,see Eq.(5).Hence, the number of satellites AN*AM1 always increase with increasing Rd.

For the case in which small uncovered gaps are not permitted,as in Figure 5b,the number of chains AM2 depends on Rd also,see Eq.(7); hence, ANM100,in Eq.(8),has a minimum dependant on Rd. (See Figure 7).

SATCOV.FOR(FINAL)

INCL= 0.400E+02 H= 0.600E+03 $\delta\alpha$ = 0.200E+01
RC MAX= 0.283E+04 ALMAX= 0.661E+02
RC= 0.262E+04 R= 0.244E+04 AL ANT =2 X 0.660E+02

| RD | AN | AM1 | NM | AN*AM1 | AM2(100%) | NM(100%) | AN*AM2(100%) |
|---|---|---|---|---|---|---|---|
| 0.500E+03 | 9.17 | 2.64 | 30 | 24.25 | 12.88 | 130 | 118.09 |
| 0.100E+04 | 10.35 | 2.64 | 33 | 27.36 | 6.44 | 77 | 66.67 |
| 0.150E+04 | 11.89 | 2.64 | 36 | 31.44 | 4.29 | 60 | 51.04 |
| 0.200E+04 | 14.42 | 2.64 | 45 | 38.13 | 3.22 | 60 | 46.43 |

INCL= 0.400E+02 H= 0.100E+04 $\delta\alpha$ = 0.200E+01
RC MAX= 0.371E+04 ALMAX= 0.598E+02
RC= 0.349E+04 R= 0.311E+04 AL ANT =2 X 0.598E+02

| RD | AN | AM1 | NM | AN*AM1 | AM2(100%) | NM(100%) | AN*AM2(100%) |
|---|---|---|---|---|---|---|---|
| 0.500E+03 | 7.00 | 2.07 | 24 | 14.49 | 12.88 | 104 | 90.18 |
| 0.100E+04 | 7.67 | 2.07 | 24 | 15.88 | 6.44 | 56 | 49.41 |
| 0.150E+04 | 8.48 | 2.07 | 27 | 17.56 | 4.29 | 45 | 36.42 |
| 0.200E+04 | 9.49 | 2.07 | 30 | 19.64 | 3.22 | 40 | 30.55 |
| 0.250E+04 | 10.81 | 2.07 | 33 | 22.38 | 2.58 | 33 | 27.86 |
| 0.300E+04 | 24.25 | 2.07 | 75 | 50.18 | 2.15 | 75 | 52.05 |

INCL= 0.400E+02 H= 0.140E+04 $\delta\alpha$ = 0.200E+01
RC MAX= 0.445E+04 ALMAX= 0.551E+02
RC= 0.423E+04 R= 0.362E+04 AL ANT =2 X 0.550E+02

| RD | AN | AM1 | NM | AN*AM1 | AM2(100%) | NM(100%) | AN*AM2(100%) |
|---|---|---|---|---|---|---|---|
| 0.500E+03 | 5.95 | 1.78 | 12 | 10.56 | 12.88 | 78 | 76.60 |
| 0.100E+04 | 6.42 | 1.78 | 14 | 11.43 | 6.44 | 49 | 41.37 |
| 0.150E+04 | 6.98 | 1.78 | 14 | 12.43 | 4.29 | 35 | 29.98 |
| 0.200E+04 | 7.65 | 1.78 | 16 | 13.61 | 3.22 | 32 | 24.63 |
| 0.250E+04 | 8.46 | 1.78 | 18 | 15.05 | 2.58 | 27 | 21.79 |
| 0.300E+04 | 9.90 | 1.78 | 20 | 17.61 | 2.15 | 30 | 21.25 |
| 0.350E+04 | 21.76 | 1.78 | 44 | 38.72 | 1.84 | 44 | 40.03 |

INCL= 0.400E+02 H= 0.180E+04 $\delta\alpha$ = 0.200E+01
RC MAX= 0.512E+04 ALMAX= 0.513E+02
RC= 0.490E+04 R= 0.403E+04 AL ANT =2 X 0.512E+02

| RD | AN | AM1 | NM | AN*AM1 | AM2(100%) | NM(100%) | AN*AM2(100%) |
|---|---|---|---|---|---|---|---|
| 0.500E+03 | 5.31 | 1.60 | 12 | 8.49 | 12.88 | 78 | 68.35 |
| 0.100E+04 | 5.68 | 1.60 | 12 | 9.09 | 6.44 | 42 | 36.60 |
| 0.150E+04 | 6.12 | 1.60 | 14 | 9.79 | 4.29 | 35 | 26.26 |
| 0.200E+04 | 6.62 | 1.60 | 14 | 10.59 | 3.22 | 28 | 21.32 |
| 0.250E+04 | 7.22 | 1.60 | 18 | 11.55 | 2.58 | 24 | 18.60 |
| 0.300E+04 | 7.93 | 1.60 | 18 | 12.69 | 2.15 | 24 | 17.03 |
| 0.350E+04 | 10.07 | 1.60 | 22 | 16.12 | 1.84 | 22 | 18.54 |
| 0.400E+04 | 44.20 | 1.60 | 90 | 70.71 | 1.61 | 90 | 71.16 |

Table 1

( Distances in kms ; Angles in degs.)

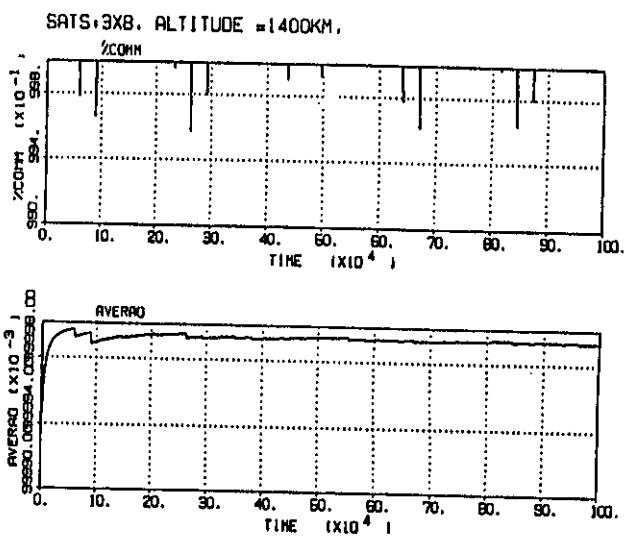


Figure 6

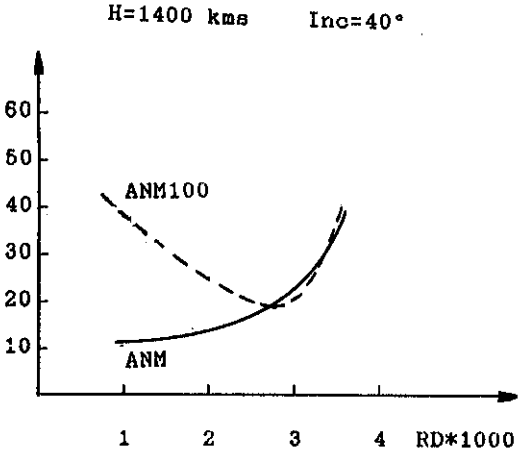


Figure 7

The same simulation can be used to compute the decrease in coverage percentage, if and when a decrease in the number of satellites should be necessary ,in order to decrease the cost of the Multi-Satellite System. This point will not be pursued in the present paper.

## 4. Summary.

The simple analytical method described above allows us to compute the minimum number of satellites needed in order to achieve a 100% coverage over a given distance from a specified ground station. The inclination of the orbit plane must be at least equal to the latitude of the GST, which can be situated anywhere within the covered global strip , as defined in Figure 4.

The simple, but very efficient numerical simulation that was prepared to check the coverage percentage, shows perfect agreement with the analytical results.

## References.

1. Wertz J.R., Larson W.J., "Space Mission Analysis and Design", 1991 ,KLUVER ACADEMIC PUBLISHERS, Dordrecht, Boston, London.

2. Walker J.G. Satellite Constellations, Journal of the British Interplanetary Society, 37:559-572, 1984 .

3. Dain J.E., Continuous Global N-Tuple Coverage with (2N+2) Satellites., J. Guidance, Vol.14, No 1, Jan.-Febr.1991

# DEVELOPMENT OF IR RADIATION SIMULATOR FOR SPACECRAFT THERMAL TESTING

Dr. Yoram Shimrony
Mr. Zachary Bachmutsky
Mr. Yaron Naimark
Dr. Sylvia Zalmanovich

IAI/MBT, Space Technology Dept., PO Box 105, Yehud 56000 ISRAEL

**ABSTRACT**

This paper describes the development of an IR Radiation Simulator conducted at MBT, a plant of Israel Aircraft Industries.

The development tackled a unique problem of creating uniform IR radiation fluxes onto irregular geometry of a spacecraft, the OFEQ satellite.

The thermal design of spacecraft and its verification by ground testing is one of the critical issues for achieving mission success in space.

The ground thermal tests include a thermal balance test and an acceptance test.

A Solar Simulator, in which the sun radiation existing in real space is being simulated, is the equipment regularly used for this purpose; it is, however, very expensive, and so are its operation and maintenance.

Another alternative, called IR Simulation, uses local infra-red sources, simulating the external radiated energy which is absorbed by different spacecraft surfaces and the simulation is conducted in iso-flux zones.

At MBT, an IR Simulator [of the latter type] has been developed and testing was carried out on an "OFEQ" Thermal Model (TM). For the TM's verification, it was subjected to a Solar Simulator test conducted in a European space center.

The IR Simulator development required the availability of adequate design tools and familiarity with the properties and the performance of the various thermal elements which are part of these IR tests. A Heat flux mapping software was developed for the heat sources' placement determination, for achieving flux uniformity; a special structure was designed and fabricated for zoning and for lamps and sensors attachment, and a special system was built for heat flux and temprature monitoring and control, to assure the satellite safety while under test. A special heat flux sensor was developed to measure the energy absorbed by the satellite surfaces, in a way independent of radiation wavelenghs, so that its measurements in testing using IR wavelengths will be equivalent to the real sun radiation effects.

The verification experiment was carried out in three phases. The results are presented below and their adequate conformance with the predicted parameters shows the developed technique to be a viable satellite thermal design verification tool.

## 1. INTRODUCTION

An important stage in a satellite development is the thermal testing, which includes verification of the thermal control system by a thermal balance test, and an acceptance test, checking the proper functioning of the satellite when subjected to its anticipated space extremest thermal environmental conditions.

Satellites' thermal environmental conditions include radiated heat fluxes, a cold surrounding, and total vacuum.

The a.m. tests take place in a vacuum chamber, providing the vacuum, which contains a cryogenic shroud simulating the cold surrounding and an IR simulator which simulated the heat fluxes.

The established method to simulate the heat fluxes impinging on the satellite's surfaces is to use a Sun Simulator, but due to program-related reasons, it was decided to achieve this goal using an IR Simulator.

This paper details the considerations, the design, the construction and the performance verification of the IR Simulator as built.

## 2. GOAL OF THE DEVELOPMENT

The goal of this effort was to develop a tool appropriate for verification of the design of the OFEQ satellite's thermal control system and to serve in the satellite's functional acceptance testing under the extremes of environmental conditions it is expected to encounter in orbit.

## 3. DESCRIPTION OF THE PROBLEM

The OFEQ is a low-orbit satellite, having an eight-faced blunt- pyramid shape on top of a short cylindrical ring with a base plate of uneven, complex surface both sides.

While orbiting, the satellite's external surfaces meet heat fluxes originating from three sources: sun radiation, earth radiation and albedo.

The heat quantities absorbed by the satellite's various external surfaces depend on the fluxes' intensities, their spectral composition, and on the thermo-optical properties of the surfaces themselves.

The satellite's thermal control system is tasked with operating various means so as to control the temperatures from not rising or decreasing out of the specified limits, and thus assure proper equipment functioning. This system makes use of heating blankets, insulation blankets, radiators and various paints and coatings which give the external and internal surfaces thermo-optical properties as specified.

In order to test the satellite's performance it must be subjected to the environmental conditions of space which it is designed to cope with; i.e., to be tested in the a.m. vacuum test set-up with the heat fluxes simulated properly. For simulating the energy absorbed from the heat fluxes, the satellite's external envelope was divided to iso-heat flux intensity zones, derived from the satellite's orbit parameters and the thermo-optical properties of the surfaces.

To these iso-heat flux intensity zones, heat fluxes correlating with the orbit conditions have to be applied. Of high importance are the means to measure the fluxes' intensities. These sensors must directly measure the absorbed energy, in order to be relieved from needing tiresome analysis for calculating the absorbed flux as a function of radiated wavelengths and the thermo-optical properties of the surface.

The installation supplying the fluxes onto the various zones should be closely fitting the satellite's form, it should also be insulated from the under-test equipment and avoid any mechanical contact. If unavoidable, any contact will be thermally insulated.

Another requirement is the prevention of radiation spillover between adjacent different-level iso-flux zones.

The division of the satellite's external envelope to the iso-flux zones is achieved by using specular baffles. Using these raises the secondary problems of somewhat blocking the cold shroud of the test chamber and, in addition, the baffles' temperatures might affect the satellite.

Another area of importance is the matching of the heat sources with their various characteristics to the specific requirements of the zones.

There are principally three types of IR sources: heating blankets, IR lamps and temperature-controlled surfaces. Each has its advantages and disadvantages, the most significant of which are as follows :

- The blankets supply uniform heat fluxes in accurate intensity, but they have to be glued to the satellite's surface, which cannot be done on all of its parts.
- Using lamps and proper design, a uniform flux intensity may be achieved employing various lamps quantities, flexibly located, and flexibly adjusted for power by varying the supply voltages. Using lamps relieves us of the need to directly contact the satellite's surfaces. Baffles help in separating the different zones.
  A difficulty with this method is the need to develop a flux intensity sensor able to measure the heat absorbed by the surface directly and accurately, and having its response time, appropriate for adjusting the lamps supply voltages used to get the required flux intensities. These sensors create some blocking between the lamps and the unit under test.
- The temperature controlled plates are used in areas having complex uneven surfaces where lamps and heating elements are inefficient. Using these plates does not necessitate measuring the fluxes and enables efficiently computing the absorbed heat quantities by proper computer programs.

For solving all the above, the IR methodology was thoroughly learnt and software was developed for mapping the heat fluxes on the satellite's iso-flux intensity surfaces.

Flux intensity sensors were developed and manufactured, having thermo-optical properties identical with their intended locations' surfaces.

The results obtained from running the computer programs were verified by a series of pilot tests performed on surfaces identical to the iso-intensity surfaces of the satellite.

Likewise, practices were developed in order to achieve good control of the various IR techniques and devices characteritiques. Following below is a description of the components developed and the techniques practiced.

## 4. INVESTIGATION OF FLUX GENERATION AND MEASUREMENT TECHNIQUES

### 4.1 Pilot Tests

The simulator has to provide to each defined thermal zone of the satellite a heat flux with a specified intensity distribution, e.g: a homogeneous heat intensity over a flat surface, or a parabolically shaped heat intensity distribution over a cylindrical surface.

Therefore main goal of the pilot tests was to achieve homogeneity of fluxes.

A laboratory pilot test bench was built with capability to measure high and low level heat flux intensities of different sources. One test bench was constructed around two adjacent trapezoidal plates and a second one was constructed around a cylindrical surface.

The first step was the calibration of heat flow transducer type LO-6-120-T made by HY-CAL Engineering, by comparing its measurements to the measurement in same conditions of a high sensitivity radiometer type RK-5720 made by LASER PRECISION Corp.

The second step was to study single IR sources performance at free air and inside specular baffled square tunnel of 405x405x500mm dimensions.

The following IR sources were tested:

1) RESEARCH Inc. Radiant Heating Unit : models 5236 and 5273.
2) PHILIPS lamp : IRK 13169X/98.
3) WATLOW Calrod Model RAN2510B.

The third step was to study IR source arrays' performance over the trapezoidal flat panels, the same as plates used on the satellite. The panel was surrounded along its perimeter with perpendicular-to-it specular baffles. The pilot rig included two such panels arranged as on the satellite. The tests were performed at two radiation intensity levels representing the sun and the earth radiations, for different arrangements of IR source arrays and baffles.

The best configurations, i.e., the ones producing the most homogenous patterns, were now tested in vacuum of less than $10^{-5}$mbar and with a shroud of 90K, under the following assumptions :

a) Heat flux can be accurately measured by a calorimetric method as follows:
A small Aluminum black plate with thermocouple in it and isolated of the environment, as a calorimeter, can measure the radiated heat flux as a function of T, when T (temperature of the plate) reaches steady state.

b) Homogenous distribution of heat flux intensity is indicated by comparison between the points' temperatures when in steady state.

The results confirmed the prediction for tests in atmospheric and vacuum conditions except for a slight boundary influence of the baffles.

The results of the best arrangements of 6 lamps and 3 lamps are presented in table 1 below for two intensity levels.

The fourth step was to study the ability of the IR source array to create the predicted distribution of heat flux intensity over a cylindrical surface. Using the method to measure radiant heat flux in atmosphere, performance of each of the above mentioned IR sources radiating on cylindrical surface were investigated. Both single large units

Table 1. Results of Heat Arrays Around Trapezoidal Flat Plates

| IR Sources | Height Over Panel [mm] | Heat Flux [W/m$^2$] | Measured Heat Flux Homogeneity | Calculated Heat Flux Homogeneity |
|---|---|---|---|---|
| 6 5236-5 lamps | 400 | 400 | ± 8% | ±5.5% |
| 6 5236-5 lamps | 400 | 40 | ±12% | ±5% |
| 3 "Philips" lamps | 400 | 400 | ± 9% | ±5% |
| 3 "Philips" lamps | 400 | 40 | ± 7% | ±5% |

(Calrod) and different arrangements of multiple lamps and specular baffles were tested. In order to confirm the obtained results in atmosphere the specific lamps arrangement had been tested in vacuum conditions. The shape of the obtained curves were similar to those obtained in the atmosphere tests.

The comparison of the pilot tests in the atmosphere and in the cold vacuum gave us the best solution of lamp array arrangement for the simulator construction.

## 4.2 The Developed Software

The specified flux over the isoflux zones has been produced by combinations of IR lamps. The flux intensities and lamps arrangement were calculated with the aid of a computer program developed at MBT, [1]. The program was based on the calculation features and assumptions as described for IRSIM, [2]: lamps were treated as point sources, the flux over the zone was considered either absorbed or reflected out of the system, and the field is isothermal. The results were in excellent agreement with published results [3].

The program treats each zone separately. The inputs to the program are: lamp definitions, lamps arrangement, geometry of the flux zone and baffle, spacecraft and baffles surface thermo-optical properties, and the position of the sensors.

The program treats specular planar baffles by creating images of the lamps at proper locations. For an arrangement of two or more baffles an infinite number of source images is created. The zone is divided into N*M grid points. For each point, the flux portion arriving from each source (or source image, if the point is located in the image's influence area) is evaluted and summed up.

For a trapezoid baffled zone, the optimal lamp arrangement has been decided upon by a trial and error procedure. After positioning the lamps, a further improvement in flux homogeneity over a part of the zone (for example - the area covered by a radiator) was achieved by adjusting the power supplied to each with an optimization routine.

The flux distribution over the trapezoid is shown in Figure 1.

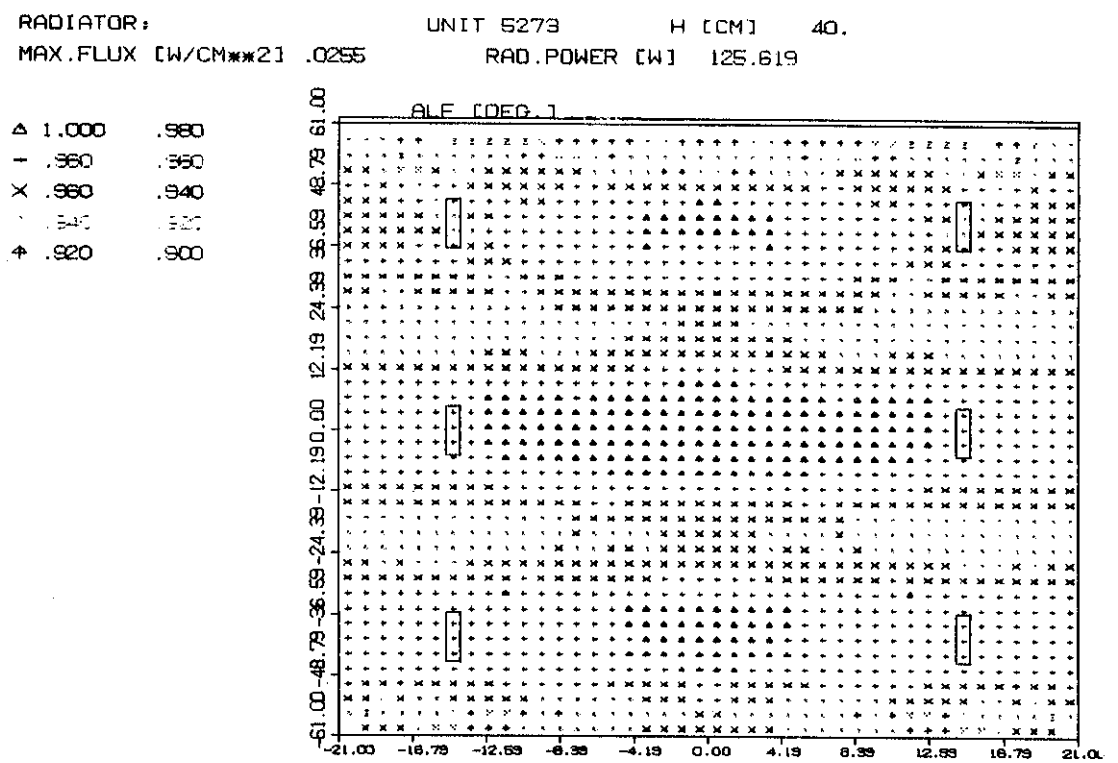


Figure 1. Heat Flux Distribution Over a Trapezoidal Surface, Using Six Lamps

## 4.3 Radiometers

The most difficult issue while choosing the heat flux generation method for thermal balance tests is to possess or acquire the ability to measure accurately the heat flux intensity absorbed by the spacecraft surfaces with minimal disturbances. In order to accomplish this requirement in a vacuum environment, two radiometers have been designed, one at Rafael and one at MBT. The designed radiometer was of the background monitored type, of the kind developed by others [4].

The radiometer has two main parts: a sensor plate and a body. The sensor plate is coated with the same optical properties as the surface whose flux it is intended to measure, and it has a heating element for calibration. The temperatures of the sensor plate and the body are monitored.

A thermal mathematical model, formulated for the radiometer and solved with SINDA, served for design purposes. The aim was to design a radiometer where most of the heat is radiated to the cold shroud and all heat losses interchange between one monitored part (the sensor plate) and the second monitored part (the body). The radiometers were then built, calibrated and tested versus heat fluxes of known intensity.

The calibration was intended to determine the coefficients for the conduction and radiation losses and the capacitance coefficient of the sensor plate.

The calibration constants were found with an optimization routine which searched for the minimum in the squares of the differences between the measured and the calculated fluxes. With these three constants and two temperatures, the absorbed flux could be calculated. The calibration method and program are described in [5].

# 5. THE DEVELOPMENT PATH

## 5.1 The Thermal Model (TM)

A Thermal Model Satellite (TM), which is a non-functional satellite, used to simulate the thermal behvaior of the real satellite was constructed. It consisted of the following equipment:

- Main Satellite's Structure
- Dummy electronic boxes containing heat generating circuits to simulate internal satellite heat dimension
- Thermal control elements of the satellite
- Thermocouples, attached in various model points identical with points of the Thermal Mathematical Model (TMM), used to compare the temperatures computed by the TMM and those actually measured on the TM.

A solar thermal balance test was performed at ITS's facilities in France in order to verify the functioning of the thermal control system; The TMM was updated according to the results and it was then used to determine correlation with the in-house-built IR simulator.

The Thermal Model (TM) was divided to 13 iso-flux-intensity surfaces, listed as follows:

- 8 sidewalls having trapezoidal shape;
- 3 sectors of a cylinder
- A lower base plate of complex surface texture;
- An upper segment having the form of a blunt cone.

It was decided not to expose the upper segment to IR Radiation since this surface is totally enveloped in insulation blankets and the radiation transmitted thru has a negligible effect.

## 5.2 The IR Simulator Construction

Two approaches to the configuration of the IR simulator were considered:

The first (IRS-1): A combination of heating blankets on part of the trapezoidal surfaces; IR lamps on the cylinderical sectors, and a temperature-controlled heating plate adjacent to the base plate;

The second (IRS-2): Arrays of lamps on the trapezoids, lamps on the cylinderical sectors, and same heating plate as above for the base.

Figure 2 shows this installation.

It was decided not to cool the baffles by active means. Their thermal finish was chosen to solve the following problems:

- The array of the baffles, being installed on the TM and very near to it, may create a secondary radiation effect on it
- The baffles' surfaces somewhat block the TM from the cold shroud.

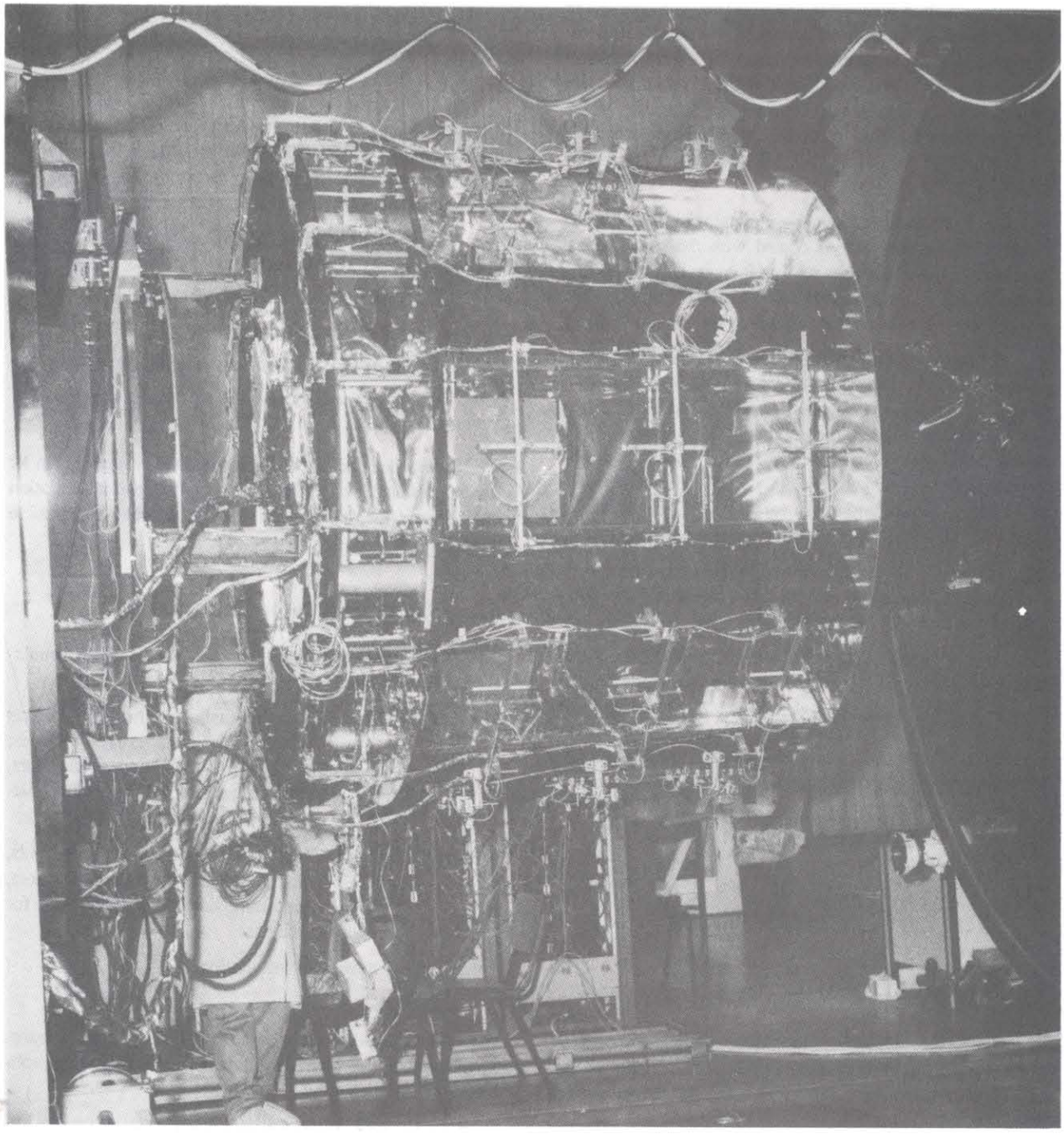

Figure 2. General View of the IR Simulator (Configuration 2) and the Thermal Model Satellite

Therefore, the selected thermal finishes were as follows;

- The baffles' surfaces facing the shroud were painted black (high emissivity) in order to increase the radiation link between the baffles and the shroud. In this way the baffles surfaces were somewhat cooled.
- The baffles' surfaces facing the TM were covered with reflective aluminized kapton tape. This achieved insulation (low emissivity), i.e, a weak radiation link between the baffles' surfaces and the TM and, additionally, they optically constitute a specular mirror, exploited to create a uniform heat flux.
- The complex shape of the bottom plate surface dictated usage of a controlled temperature plate.

## 6. TEST SET UP AND FACILITIES

The test set-up consisted of a vacuum chamber system, an adaptor mounting the TM onto the chamber's door and a lamp rig (together called "the Rig"), and measuring instruments, Following is their description.

### 6.1 Vacuum Chamber

The IR test was performed in MBT's vacuum chamber, dimensioned 2.8 X 3.60 M.

The environmental conditions inside the chamber were as follows: a pressure of $10^{-5}$mbar and the cryogenic shroud's temperature was 90K.

### 6.2 Rig Description

The RIG was built from the following main parts :

a) Adapting fixture for the Simulator installation on the Thermal Vacuum Chamber's door. It was intended also to accept the satellite and the lamp rig which had to be put on the satellite. The rig could perform leveling of the satellite.

b) The lamp rig.
This was constructed of specular baffles around iso-flux zones over the satellite. It supports the lamps and the radiometers. The rig construction enables flexibility in lamp arrangements.

The Rig rigidity provides differences of the clearance between the lamp rig and the satellite less than 2 mils per unit of length during continuous transition from vertical to horizontal position.

### 6.3 Heat Flux Measurement

93 flux sensors (radiometers) were positioned close to the surfaces of the satellite, based on the flux zones definitions. Each radiometer's thermal finish was the same as that of the surface that its flux it measured. Thus, a direct measurement of the heat absorbed by a particular surface was provided. The flux sensors were connected to the baffles using small and narrow brackets to minimize blockage between the lamp array and the satellite surfaces.

This measurement method reads the real values of flux absorbed by the TM surfaces, i.e. baffles' blockage and secondary radiation effects already included, but their own blockage is not yet compensated. Calculations show this effect to be 7% in the maximum condition.

### 6.4 Power Control And Data Acquisition System

A main console controller was connected to four controllers, each controlling 16 power supplies'.

A control system was developed, capable of the following :

- Supplying a stabilized power to either a single lamp or to a lamp array of a flux zone
- Supplying power to heating plate
- Alarm and protection, including open or short-circuited, load detection, shutdown, channel set-point level, and out-of-limit alarms

The data acquisition system sampled channels of thermocouples and current, then displayed both measured and calculated fluxes and power.

This output was displayed in tables and graphs on a monitor screen.

## 7. IR SIMULATOR TEST AND RESULTS

The step by step procedure of the IR Simulator test, using the TM for correlation, was performed in the following steps :

- Pump down (achieving the required vacuum).
- Cooling the shrouds.
- Supplying power to the thermal model.

  Supplying the power to the IR Simulator was performed, according to the two configurations mentioned above.

  * Supplying power to heating blankets or the lamp arrays (per configuration) on the trapeziodal panels.
  * Setting flux level on the TM surfaces by adjusting the lamps power until the desired average flux level on the radiometer was achieved.
  * Supplying power to the heating plate in order to achieve the predesigned temperature.
- Reaching a steady state conditions of the TM.
- Return to ambient conditions.

According to the first IR Simulator configuration (which was a combination of heating blankets, IR lamps and heating plates (IRS-1)), the TMM was updated using the following data:

- Power of heating blankets
- Absorbed heat fluxes
- Boundary temperature conditions.

Table 2 compares the average differences between the TM and the TMM's steady state temperatures (measured, and calculated), according to IRS-1. A difference of less than $5^0$C in temperature shows good correlation between TM and TMM. The table shows that the test met this criterion.

Table 2. Correlation Achieved Between TM and TMM, IRS-1

| Zones in Satellite | Differences Between Measured and Calculated Temperature |
|---|---|
| A | $1.5^0$C |
| B | $0.1^0$C |
| C | $2.9^0$C |
| D | $1.6^0$C |

The distribution of absorbed flux on a trapizoidal panel was 5% from the designed flux value.

According to the second simulator configuration (IRS-2) (which was a combination of lamp arrays on the trapeziodal panels and IR lamps on the cylindrical parts, and heating plates on the bottom surface) the TMM was updated using the following data :

- Absorbed heat fluxes
- Boundary temperature conditions.

Table 3 compares the average differences between TM and TMM steady state temperatures (measured and calculated), according to IRS-2. It shows a good correlation between the TM and the TMM.

Table 3. Correlation Achieved Between TM and TMM, IRS-2

| Zones in Satellite | Differences Between Measured and Calculated Temperature |
|---|---|
| A | $1.9^0$C |
| B | $2.1^0$C |
| C | $4.5^0$C |
| D | $0.3^0$C |

## 8. CONCLUSIONS

As a result of the tests undertaken, the following conclusions were arrived at :

- The IR simulator enables control of heat fluxes observed in the various satellite surfaces, and therefore is suitable for acceptance tests.
- The results of the balance tests achieved with the aid of the IR simulator, shows that a good correlation exists between the TM and TMM models.
  It seems that the good correlation is a result of the thermal mathematical model which was calibrated according to the solar test results, prior to the beginning of the development of the abovementioned IR simulator.
- It is possible to use the IR simulator for heat balance testing of satellites with a simple external configuration.
- It is very important to fit the IR sources to the satellite configuration.
  For this specific satellite, the IR simulator is based on the IRS-1 configuration.
  This configuration seems to be a suitable choice because it uses inexpensive hardware components,

it is simple to operate, and the results are easy to analyse.

- Every IR simulator is custom-made to satellite specifications.

## 9. PROGRAM OVERVIEW

The development of the IR Simulator including its various components was successful. Skills were acquired in the various IR techniques.

A surface absorbed heat flux-intensity sensor was developed, which measures the absorbed heat directly and avoids needing tiresome computations for getting these parameters. The knowledge, technology and skill acquired will enable testing future satellites thermal control systems reliably and in relatively low cost.

## LIST OF REFERENCES


1. Zalmanovich S., "Software for the Calculation of Infrared Flux Intensity", TR-1270-0000-15, IAI, MBT, 1990.
2. Rogers R.P., "IRSIM: A Program for Calculation of Infrared Flux Incident on a Spacecraft inside a Test Chamber", Proc. Int. Symp. Env. & Thermal Sys., 1983.
3. Donato M, Ruel C. and Harris A, "Absorbed Flux Predictions for Spacecraft IR Testing", 14'th Intersociety Conf. Env. Sys., 1984.
4. Ruel C., M. Larouche and M. Donate "Monitored Background Radiometer", 14th space simulation conference, 1986.
5. Zalmanovich S., "Calibration of radiometers" TR-1270-0000-08, IAI, MBT, 1990.
6. Naimark Y., "IR Simulator Tests - Final Report", TR-1820-0000-02, IAI, MBT.

# VERTICAL LANDING ON AN ASTEROID

D. Harel*
Technion - Israel Institute of Technology, Haifa 32000, Israel

M. Guelman**
RAFAEL, M.O.D., P.O. Box 2250, Haifa, Israel

## Abstract

This work is concerned with the final approach phase and vertical landing on an asteroid with a power limited, electrically propelled spacecraft. With gravitational effects taken into account, a new solution to the fuel optimal vertical landing on an asteroid was obtained. In this solution the spacecraft commanded acceleration is explicitly expressed as a function of vehicle velocity and time to go. Based on qualitative methods of analysis, the guidance strategy and the resulting trajectories were studied. It is shown that these fuel optimal trajectories effectively assure a vertical soft landing on the asteroid. Results of numerical simulations for the vertical landing starting from an elliptic orbit are presented.

## 1. Introduction

For the past thirty years, mission feasibility studies and trajectory analyses have been conducted to assess the possibility of a rendezvous with small celestial objects such as comets and asteroids. The interest in this kind of mission stemmed both from its scientific importance, and its possible practical applications. Asteroids form an ordered assemblage of protoplanetary fragments which seem to remain near the original locations of their formation between Mars and Jupiter. The compositional and structural variations of objects in the asteroid belt are thought to retain clues about the primordial conditions and processes that contributed to the formation of the solar system. In [1] was stated that an ideal mode of an asteroid mission for scientific purposes would be to achieve rendezvous with a diverse set of asteroids during a single mission and such a goal could be achieved employing electric propulsion. In this work were also presented the trajectory options available for a modified Mariner spacecraft mission to asteroids. In a completely different work [2] the placement of transmitters on selected asteroids to provide an independent navigation capability for interplanetary flight, similar to the Global Positioning System, was proposed. Missions for a comet-nucleus sample return mission using electric propulsion at very low thrust levels were studied in [3]. These are some of the many works published in recent years in this field. Furthermore, the Galileo spacecraft in its present flight is targeted to flyby one of more asteroids during its cruise to Jupiter [4]. This strong interest in a rendezvous with small celestial objects provided the motivation for the present work.

The rendezvous of a spacecraft with a nearly massless object presents significant challenges. Classical planetary encounter techniques, with their reliance upon the gravitational signature of the target body are ineffective. Furthermore, the long distances from earth make the use of autonomous guidance in the vicinity of the celestial body, a must. Use of on board instruments as a source of target relative information was considered the adequate solution [3]. Rendezvous missions to celestial objects are in general divided into a number of navigation and guidance phases. This work is concerned with the final approach phase and vertical landing on an asteroid with a power limited, electrically propelled spacecraft. With gravitational effects taken into account, an analytic solution to the fuel optimal vertical landing on an asteroid is obtained.

## 2. Problem Definition

Rendezvous and landing on a small celestial object without atmosphere are particular cases of the more general problems of transfer.

The optimal transfer problem can be defined in its most general form as follows: Given a vehicle in a central gravitational field at initial position $\vec{r}_o$ and velocity $\vec{v}_o$, transfer this vehicle to a final position $\vec{r}_f$ and velocity $\vec{v}_f$ at time $t_f$ while fuel expenditure is a minimum. The final $t_f$ can be given or free.

The system equations in vectorial form and cartesian coordinates are given by:

$$\dot{\vec{r}} = \vec{v} \tag{1}$$

$$\dot{\vec{v}} = \vec{a} - \frac{\mu \vec{r}}{r^3} \tag{2}$$

where $\vec{r}$, $\vec{v}$ and $\vec{a}$ are respectively the position, velocity and applied acceleration vectors of the vehicle under control and $\mu$ is the gravitational constant of the central body. The specific problem considered in this work is to find the required acceleration for the transfer of a spacecraft from an elliptic orbit about the celestial body to a soft landing on the body surface (zero relative velocity) along the local vertical, while fuel expenditure is minimized. The spacecraft employs an electric engine to generate the required accelerations.

## 3. Optimality Criterion

Electric engines generate thrust by accelerating charged particles through an electromagnetic field. In an electric engine, it is

---

* Graduate student, Faculty of Aerospace Engineering
** Chief Scientist, Missiles Division

possible to modify both the ejection speed $v_c$ and the mass flow rate $\dot{m}$, and therefore, to control independently the thrust T and power P, given by

$$T = -\dot{m}v_c \tag{3}$$

$$P = \frac{1}{2}|\dot{m}|v_c^2 \tag{4}$$

From these relations follows

$$\frac{1}{m_f} - \frac{1}{m_o} = \int \frac{a^2}{2P}\,dt \tag{5}$$

where m is mass and a=T/m is thrust acceleration. For a vehicle with electric propulsion, we have a limited power system. The optimal operating point of a Limited Power (LP) system uses the maximum power, and the optimization criterion to minimize the fuel is to minimize the quadratic performance index

$$J = \frac{1}{2}\int_{t_o}^{t_f} a^2 dt \tag{6}$$

The problem here considered is to transfer from state $(\vec{r}_o,\vec{v}_o)$ to state $(\vec{r}_f,\vec{v}_f)$ at time $t_f$ such that the performance index J is a minimum with $t_f$ free.

## 4. The Optimal Control

The maximum principle of Pontryagin is employed [5]. The Hamiltonian of the system is given by,

$$H = \vec{p}_r\cdot\vec{v} + \vec{p}_v\cdot(\vec{a} - \mu\vec{r}/r^3) + p_J a^2/2 \tag{7}$$

where vectors $\vec{p}_r$, $\vec{p}_v$, and scalar $p_J$ are the components of the adjoint vector and are defined by,

$$\dot{\vec{p}}_r = \frac{\mu}{r^3}\left[\vec{p}_v - 3(\vec{p}_v\cdot\vec{r})\frac{\vec{r}}{r^2}\right] \quad , \quad \vec{p}_r(t_f) = \vec{p}_{rf} \tag{8}$$

$$\dot{\vec{p}}_v = -\vec{p}_r \quad , \quad \vec{p}_v(t_f) = \vec{p}_{vf} \tag{9}$$

$$\dot{p}_J = 0 \quad , \quad p_J(t_f) = -1 \tag{10}$$

From (10) follows immediately,

$$p_J = -1 \tag{11}$$

The Hamiltonian is minimum with respect to a for:

$$\frac{\partial H}{\partial a} = -\vec{a} + \vec{p}_v = 0 \tag{12}$$

It follows then,

$$\vec{a} = \vec{p}_v \tag{13}$$

$\vec{p}_v$ is the so-called primer vector [5].

We shall now solve for $\vec{p}_v$ as a function of the state variables, their final values and time.

For the free time case

$$H^* = 0 \tag{14}$$

Substituting (3), and (9) into (7), it is obtained,

$$H^* = -\frac{1}{2}p_v^2 - \dot{\vec{v}}\cdot\vec{p}_v + \dot{\vec{p}}_v\cdot\vec{v} = 0 \tag{15}$$

Let us assume a solution for the vector $\vec{p}_v$ of the form

$$\vec{p}_v = f(t)\vec{v} \tag{16}$$

where f(t) is a scalar function of time, to be defined. Substituting (16) into (15) and rearranging,

$$-\vec{v}\left(\frac{1}{2}f^2(t) + \dot{f}(t)\right) = 0 \tag{17}$$

from where it follows,

$$\frac{1}{2}f^2(t) + \dot{f}(t) = 0 \tag{18}$$

Integrating wth c a constant of integration,

$$f(t) = \frac{2}{c+t} \tag{19}$$

Substituting (19) into (16),

$$\vec{p}_v = \frac{2}{c+t}\vec{v} \tag{20}$$

In Appendix I is shown that this particular solution for $\vec{p}_v$ effectively satisfies the adjoint equations (8) and (9).

The adjoint vector $\vec{p}_v$ as defined by (20) provides a particular solution for the optimal acceleration vector as a function of the vehicle velocity and time,

$$\vec{a}^* = \frac{2}{c+t}\vec{v} \tag{21}$$

This particular solution has two main characteristics:

1) The optimal acceleration vector is colinear with the vehicle velocity. The entire trajectory will in consequence rest in the plane defined by the initial vectors $\vec{r}_o$, $\vec{v}_o$. This optimal acceleration vector provides a solution only to two dimensional problems.

2) This solution includes a single free parameter c, besides the final time in order to match the required final conditions in position and velocity.

We shall now restrict our analysis to the two dimensional case.

## 5. The Two Dimensional Case

The system equations in polar coordinates for the two dimensional case with the acceleration as given in Eq. (21) are defined by,

$$\ddot{r}\dot{\theta} + 2\dot{r}\ddot{\theta} = \frac{2r\dot{\theta}}{c+t} \qquad (22)$$

$$\ddot{r} - r\dot{\theta}^2 = \frac{2\dot{r}}{c+t} - \frac{\mu}{r^2} \qquad (23)$$

where r and $\theta$ define the spacecraft position with respect to the central body as shown in Fig. 1.

Multiplying equation (22) by r and rearranging

$$\frac{dr^2\dot{\theta}}{dt} = \frac{2r^2\dot{\theta}}{c+t} \qquad (24)$$

The angular momentum

$$h = r^2\dot{\theta} \qquad (25)$$

Substituting (25) into (24) it follows,

$$\dot{h} = \frac{2h}{c+t} \qquad (26)$$

Integrating from initial conditons t=0, $h=h_o$, it is obtained,

$$h = h_o \frac{(c+t)^2}{c^2} \qquad (27)$$

It is worthwhile to remark that equation (27) is in fact equivalent to one of the known integrals of the general problem [5],

$$\vec{r} \times \vec{p}_r + \vec{v} \times \vec{p}_v = \text{constant} \qquad (28)$$

as can be readily verified.

From Eq. (27) follows that to transfer from an initial orbit with angular momentum $h_o$ to a final orbit with angular momentum $h_f$ at $t=t_f$, c is given by,

$$c = \frac{t_f}{(h_f/h_o)^{1/2}-1} \qquad (29)$$

For $h_f > h_o$ it follows $c > 0$ and consequently from equation (21), the commanded acceleration is positively aligned with the vehicle velocity.

For $h_f > h_o$, $c < 0$, and consequently the commanded acceleration is negatively aligned with the vehicle velocity. In particular, for the case of landing on the central body, $h_f = 0$, and $c = -t_f$. This specific case will be further developed here below.

Substituting $\dot{\theta}$ from equations (25) and (27) into (23) it follows,

$$\ddot{r} - \frac{h_o^2(c+t)^4}{r^3c^4} = \frac{2\dot{r}}{c+t} - \frac{\mu}{r^2} \qquad (30)$$

This nonlinear time varying differential equation for the range r has no known solution. In order to be able to further analyze the problem, qualitative methods of analysis will be employed.

## 6. Qualitative Analysis

We shall restrict our analysis to the particular case

$$c = -t_f \qquad (31)$$

Let us define instead of r and t two new variables p and $\sigma$, as follows:

$$p = r(t_f-t)^{-2/3} \qquad (32)$$

$$e^{-\sigma} = (t_f-t)/t_f \qquad (33)$$

With these new variables the following equation is obtained,

$$\frac{d^2p}{d\sigma^2} + \frac{5}{3}\frac{dp}{d\sigma} - \frac{14}{9}p + \mu p^{-2} - h_o^2 t_f^{-5/3} e^{-7\sigma/3} p^{-3} = 0 \qquad (34)$$

The qualitative analysis of equation (34), is performed in two steps. First the particular case $h_o=0$, corresponding to the single dimensional case, is considered. In this case, equation (34) becomes autonomous and well known methods of analysis can be employed [6]. The resulting trajectories and separatrices in the phase plane p, $dp/d\sigma$ are shown in Fig. 2. Two classes of trajectories can be distinguished:

I) $\lim_{\sigma\to\infty} p = \infty$, $\lim_{\sigma\to\infty} dp/d\sigma = \infty$,

II) $\lim_{\sigma\to\infty} p = 0$, $\lim_{\sigma\to\infty} dp/d\sigma \to -\infty$

These two trajectories classes appear in both sides of separatrix $S_1$, for the trajectories going to infinity, the exponential order of p is 2/3, i.e., for $\sigma \to \infty$, $p \simeq e^{2/3\sigma}$.

To determine the behavior of the original variables let us express the radial distance r and the radial relative velocity $\dot{r}$ in terms of p and $\sigma$,

$$r = t_f^{2/3} p e^{-2\sigma/3} \qquad (35)$$

$$\dot{r} = t_f^{-1/3}\left(\frac{dp}{d\sigma} - \frac{2}{3}p\right)e^{\sigma/3} \qquad (36)$$

According to the behavior of p for $\sigma \to \infty$, it follows by direct substitution [7], that for the trajectories of Class I,

$$\lim_{t\to t_f} r = r_f$$

$$\lim_{t\to t_f} \dot{r} = 0$$

Furthermore, for $t\to\infty$, $\dot{r} \simeq (t_f-t)$.

For trajectories of Class II

$$\lim_{t\to t_f} r = 0$$

$$\lim_{t\to t_f} \dot{r} = -\infty$$

Now, given initial conditons for $\dot{r}$, r, respectively, $\dot{r}_o$, $r_o$, it follows for p and dp/dσ,

$$p_o = t_f^{-2/3} r_o \qquad (37)$$

$$\left.\frac{dp}{d\sigma}\right|_o = t_f^{-1/3}\left(t_f \dot{r}_o + \frac{2}{3} r_o\right) \qquad (38)$$

For given initial $r_o$, $\dot{r}_o$, the initial conditions in the plane p, $\frac{dp}{d\sigma}$ are functions of $t_f$ Depending on the value of $t_f$, the initial conditions will give rise to trajectories either of Class I or II as shown in Fig. 3.

It follows, that there exists a value of $t_f$, $t_f^*$, such that

1) For $t_f < t_f^*$ $\lim_{t\to t_f} r = r_f$ , $\lim_{t\to t_f} \dot{r} = 0$

2) For $t_f \to t_f^*$ $\lim_{t\to t_f} r = 0$ , $\lim_{t\to t_f} \dot{r} = \infty$

This result indicates that the optimal guidance law effectively achieves a soft rendezvous at $r = r_f$ provided $t_f < t_f^*$.

Once the particular $h_o = 0$ has been analyzed, the general case as defined by equation (34) is now considered.

Since the nonlinear time varying term that depends on $h_o$ includes also an exponentially decreasing factor, unless $p\to 0$, it is straightforward to show that this term will not affect the behavior of p and dp/dσ for $\sigma\to\infty$.

For $p\to 0$, a more elaborate analysis as performed in [7], shows that in this case also, as for the particular case previously studied, $dp/d\sigma\to-\infty$ for $\sigma\to\infty$.

Summarizing then, since the same behavior for $\sigma\to\infty$ is obtained as for the single dimensional case the same conclusion follows: The optimal guidance law as defined in (21) with $c = -t_f$ achieves a soft rendezvous at $r = r_f$ provided $t_f < t_f^*$.

Now, the approach angle σ as defined by

$$\sigma = \operatorname{atan} \frac{r\dot{\theta}}{\dot{r}}$$

with r and h as previously defined is such that,

$$\lim_{t\to t_f} \alpha = 0$$

Consequently, the landing trajectory is tangent to the radius vector, or, in other terms, the final landing approach is made along the local vertical.

## 7. Numerical Results

To achieve the desired $r_f$, it is necessary to determine, at guidance initiation, the correct value of $t_f$. Since there is no closed form solution for the equations of motion, $t_f$ is determined by an iterative process.

As an application example, the case of landing of a spacecraft parked in an elliptic orbit about an asteroid with a 20 Km. diameter and gravitational constant $\mu = 3900$ is considered. The optimal guidance law and the iterative process to determine the required $t_f$ to achieve a soft landing at $r_f = 10$ Km. are employed. The spacecraft trajectory is depicted in Figs. 4a and 4b. Range and velocity relative to the asteroid are depicted in Figs. 5 and 6, respectively. As can be seen, the spacecraft effectively achieves a soft landing along the local vertical. The optimal guidance law first reduces range, even at the expense of increasing the vehicle velocity and only towards the final approach, velocity is brought to zero. This is clearly reflected in the spacecraft acceleration and the resulting cost, as depicted in Figs. 7 and 8, respectively.

## 8. References


1. Sauer, C.G., Chen-Wan, L.Y., "Multiple Main-Belt Asteroid Mission Options for a Mariner Mark II Spacecraft", Paper 89-434, AAS/AIAA Astrodynamics Conference, Stowe, Vermont, August 1989.

2. Jee, J.R., Khatib, A.R., Muellerschoen, R.J., Williams, B.G., Vincent, M.A., "Preliminary Performance Analysis of an Interplanetary Navigation System Using Asteroid Based Beacons", Journal of Guidance and Control, Vol. 11, No. 2, March-April 1988, pp. 103-109.

3. Noton, M., Salehi, S.V., Elliot, C.A., "Low Thrust Navigation for a Comet-Nucleus Sample Return Mission", Second International Symposium on Spacecraft Flight Dynamics, Darmstadt, Germany, October 1986, pp. 81-89.

4. Murrow, D.W., Chodas, P.W., Kallemeyn, P.H., "Galileo Asteroid Encounter Navigation", Paper 89-406, AAS/AIAA Astrodynamics Conference, Stowe, Vermont, August 1989.

5. Marec, J.P., Optimal Space Trajectories, Elsevier Co., Amsterdam, 1979.

6. Cesari, L., Asympotic Behavior and Stability Problems in Ordinary Differential Equations, Springer-Verlag, Berlin, 1959.

7. Harel, D., "Vertical Landing on an Asteroid", M.Sc. Thesis, Faculty of Aerospace Engineering, Technion, September 1990 (in Hebrew).

## Appendix I

Differentiating p with respect to time and introducing into (8),

$$p = \frac{2\mu r/r^3}{t + c} - \frac{2v}{(t+c)^2} \qquad (I.1)$$

Differentiating $p_r$ with respect to time

$$\dot{p}_r = \frac{2\mu}{r^3}\left\{\frac{v}{(t+c)} - \frac{3(r\cdot v)r}{(t+c)r^2}\right\} \qquad (I.2)$$

Once $p_v$ from (18) is introduced into (8), it can be readily seen that it is identical to (I.2), effectively verifying the adjoint equations.

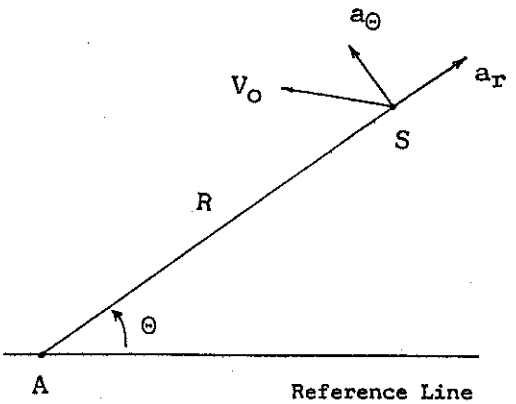


Fig. 1: Relative Geometry

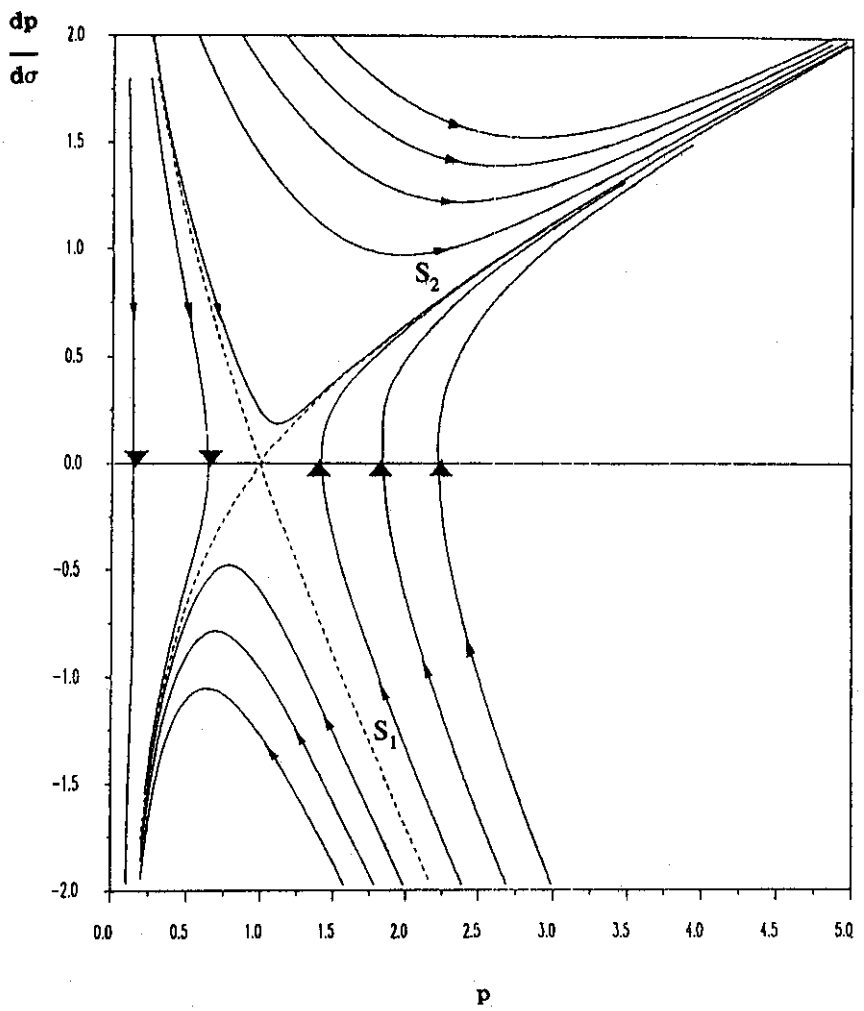


Fig. 2: Phase plane trajectories

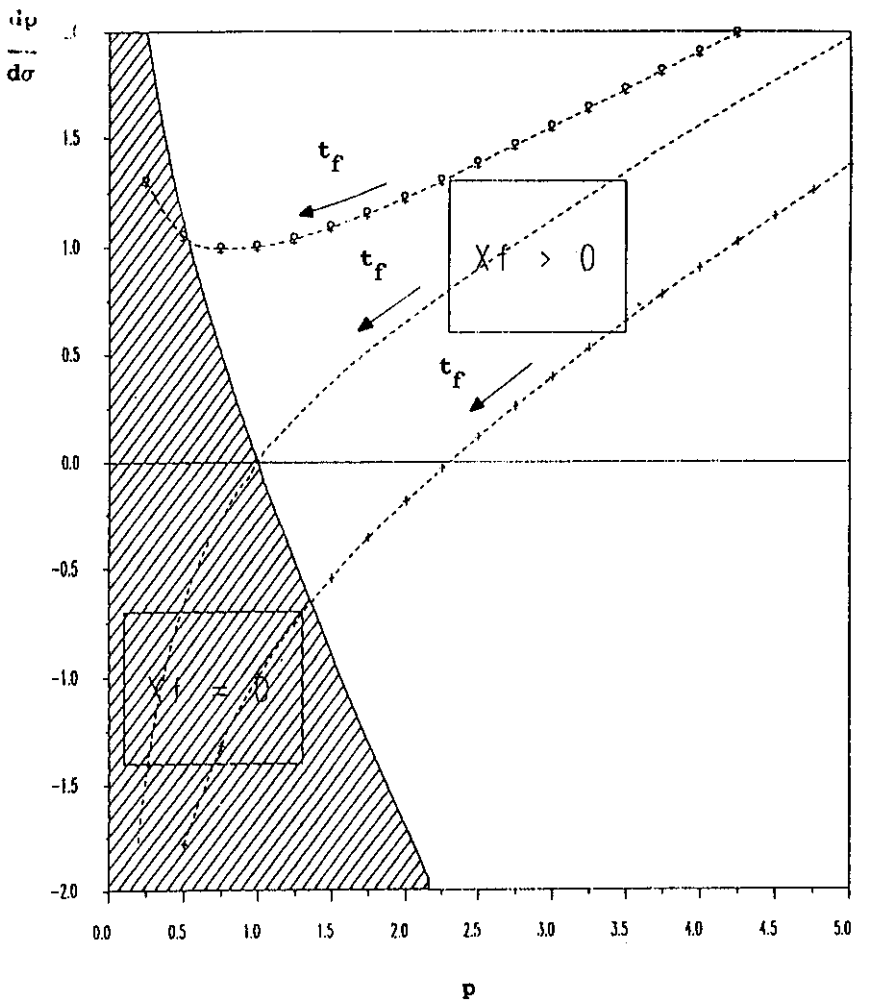


Fig. 3: Phase plane division

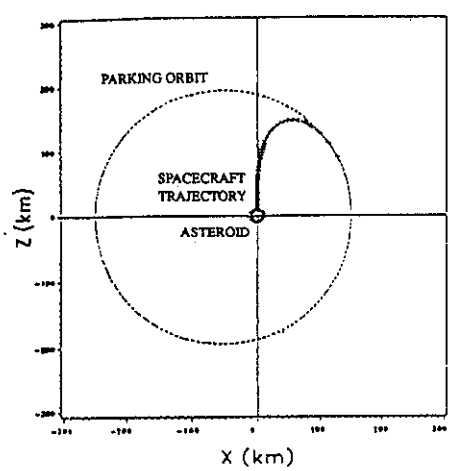


Fig. 4: Spacecraft trajectory

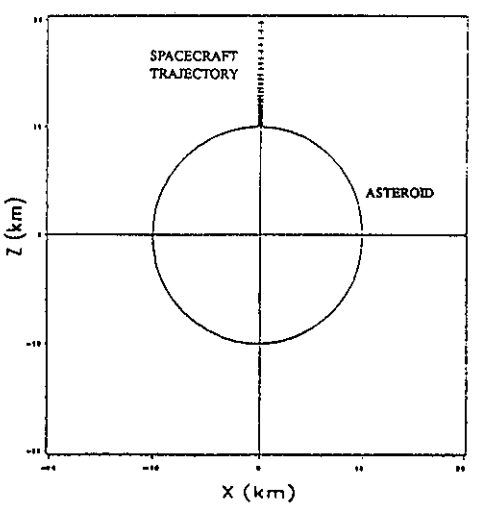


Fig. 4a: Spacecraft final approach

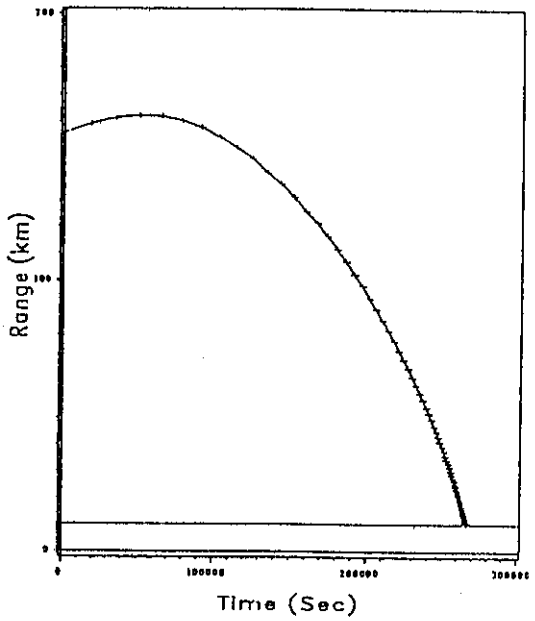


Fig. 5: Spacecraft asteroid range

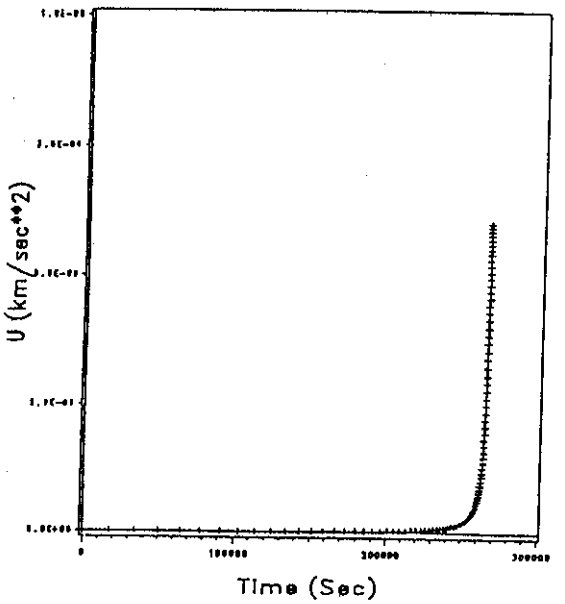


Fig. 7: Spacecraft acceleration

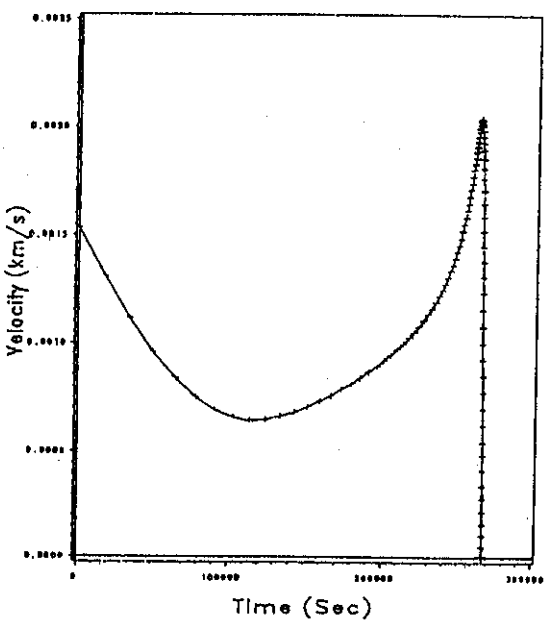


Fig. 6: Spacecraft asteroid relative velocity

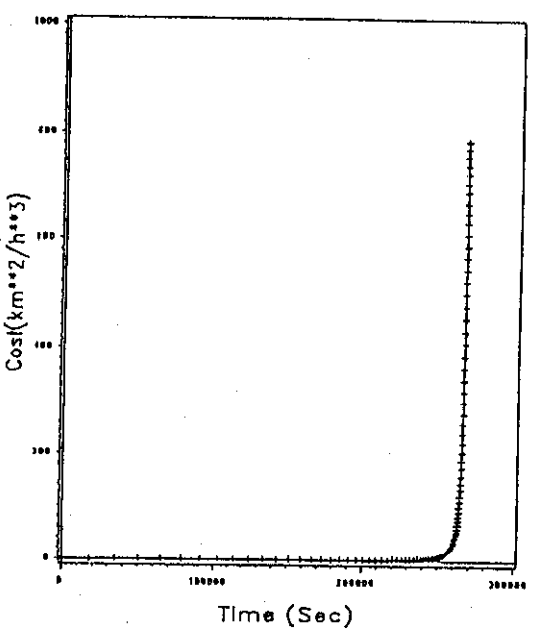


Fig. 8: Cost vs. time

# SOLAR SAIL ATTITUDE CONTROL INCLUDING ACTIVE NUTATION DAMPING IN A FIXED-MOMENTUM WHEEL SATELLITE

Dr. Ruth Azor
IAI - MBT, Systems and Space Technology
P. O. B. 105, Yahud 56000, Israel

## Abstract

In geostationary cruise of a momentum biased satellite, it is necessary to stabilize the roll/yaw attitude due to disturbances, caused mainly by solar pressure. This work presents a roll/yaw control, which is obtained by the use of solar arrays and fixed flaps as actuators, with a horizon sensor for roll measurement. The design also includes an active nutation damping.

## 1 Introduction

This work deals with the stabilization of a geostationary satellite with a fixed momentum wheel. Actually, the problem is to stabilize the roll/yaw attitude in the presence of solar pressure. The roll/yaw control is obtained by the use of solar arrays and fixed flaps, and a horizon sensor for roll measurement. It also includes active nutation damping.

The damping torques are obtained by the momentum wheel in the pitch axis, taking advantage of products of inertia between the pitch axis and the roll or yaw axis.

This paper describes a solar disturbance (due to solar arrays and flaps) model development, a definition of solar sailing torques capability due to energy efficiency, an approximate solar moment model for the roll/yaw control and, finally, the roll/yaw and active nutation damping control loops.

The design of roll/yaw attitude control, in this work, is obtained by combining solar sailing with just a horizon sensor for roll measurement and the nutation damping in roll/yaw axes by the momentum wheel (in pitch). In other communication sattelite designs, gyros and/or star sensors and/or sun sensors ([1],[2]) are used in addition to a horizon sensor. Skewed bias momentum wheels ([3]) or double gimball momentum wheels ([4]), are used instead of one fixed-momentum wheel, and solar sailing is replaced by thrusters ([5]). It should be noted that the nutation damping design is also applicable when thrusters are used for roll/yaw control.

## 2 Model for Solar Moments on Solar Arrays and Flaps

The solar arrays and flaps are described in figure 1.

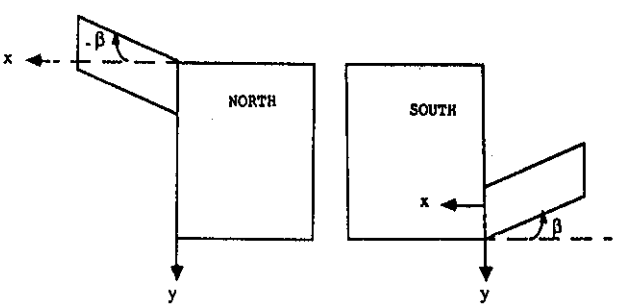


Figure 1: South and North Arrays and Flaps

The Y-axis of the arrays coordinate system coincides with the pitch axis of the satellite, on which the momentum wheel is fixed. The Z-axis completes the X,Y-axes to a right handed system. When Z is directed towards the sun, the system is defined as a "sun coordinates system".

The general formula of the solar force on a surface is ([9]):

$$F = -P \cdot A \cdot \cos\theta \cdot (1-\rho_s) \cdot \vec{S} + 2[\rho_s \cdot \cos\theta + \frac{1}{3} \cdot \rho_d] \cdot \vec{N} \quad (1)$$

where :

$P$ - radiation pressure coefficient $(4.6 \cdot 10^{-6} Kg/ms^2)$

$A$ - surface area

$\vec{S}$ - unit vector from surface to sun.

$\vec{N}$ - the normal to the surface

$\rho_s$ - specular reflection coefficient

$\rho_d$ - diffusive reflection coefficient

It can be shown ([7]) that the solar force in "sun coordinates" is of the form:

$$F = -P \cdot A \cdot U_z \cdot cos(\gamma+\delta) \cdot \{(1-\rho_s) \cdot \begin{bmatrix} 0 \\ U_y \\ U_z \end{bmatrix} + 2[\rho_s \cdot U_z \cdot cos(\gamma+\delta) + \frac{1}{3} \cdot \rho_d] \begin{bmatrix} \sin(\gamma+\delta) \\ 0 \\ \cos(\gamma+\delta) \end{bmatrix} \} \quad (2)$$

where :

$A$ - surface area ($A_p/A_f$-panel/flap)

$\rho_s$ - specular reflection coefficient ($\rho_{sp}/\rho_{sf}$-panel/flap)

$\rho_d$ - diffusive reflection coefficient ($\rho_{dp}/\rho_{df}$-panel/flap)

$(0, U_y, U_z)$ - unit vector from surface to the sun in "sun coordinates"

and: $\delta = 0, \pm\beta$ ; $\gamma = \gamma_n, \gamma_s$

For each surface the solar force is computed, from which the solar moment is obtained. By summing all these moments, the solar moments in the X,Y,Z axes (in "sun coordinates") are obtained:

$$\begin{aligned} T_x &= T_{xsp} + T_{xnp} + T_{xsf} + T_{xnf} \\ T_y &= T_{ysp} + T_{ynp} + T_{ysf} + T_{ynf} \\ T_z &= T_{zsp} + T_{znp} + T_{zsf} + T_{znf} \end{aligned} \quad (3)$$

$T_{xsp}, T_{ysp}, T_{zsp}, T_{xsf}, T_{ysf}, T_{zsf}, T_{xnp}, T_{ynp}, T_{znp}, T_{xnf}, T_{ynf}, T_{znf}$ are the solar moments in the X,Y,Z axes, caused by the south and north panels and flaps. The solar moments $T_x, T_y, T_z$ are functions of the surfaces parameters and $\gamma_s$, $\gamma_n$ and $\beta$, where $\gamma_s$ and $\gamma_n$ are the rotation angles $\gamma_s, \gamma_n$ of the south and north panel, respectively, around the Y axis from state of maximum sun and $\beta$ is the angle between the flap and panel's normal.

It can be proved ([7]) that:

(a) When the sun is in the orbit plane, the solar forces in the $Y$-axis are zero, i.e., $F_{ysp}, F_{ynp}, F_{ysf}, F_{ynf} = 0$.

- If $\gamma_n = -\gamma_s$ then: $T_x = 0$, $T_z \neq 0$,

which means that in such a case there is a solar moment just in the $Z$-axis (sun direction).

$T_z$ is called the "windmill torque" and $T_x$ is called the "unbalance torque".

- If $\gamma_n = \gamma_s$, then neither $T_x$ nor $T_z$ is identically zero.

(b) If the sun is not in the orbit plane, again, $T_x$ and $T_z$ are not identically zero.

The solar sailing torques capability is a function of all the parameters mentioned above and the required efficiency loss, which is defined by:

$$L_{oss} = \frac{2 - \cos(\gamma_n) - \cos(\gamma_s)}{2} \cdot 100 \quad (4)$$

Figure 2 presents the solar sailing capability due to efficiency loss.

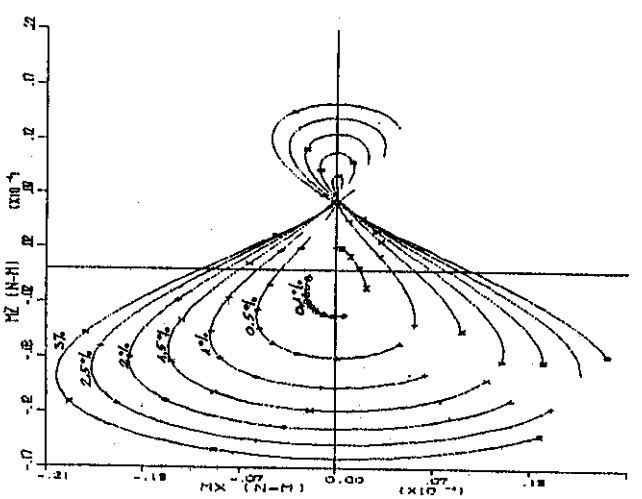

Figure 2: Solar Sailing Torques Capability (sun coordinates)

# 3 Approximate Solar Moments Model for Roll/Yaw Control

Various approximate models can be obtained, according to the assumptions.
(a) If in the system equations (2), the approximations $\cos\gamma \approx 1, \sin\gamma \approx \gamma$, for small $\gamma$ are used, and all other terms of order greater than 2 are neglected, then the solar moments may be approximated by:

$$\begin{aligned} T_x &\approx A_x \cdot X \cdot Y + B_x \cdot Y + C_x \cdot X + D_x \qquad (5) \\ T_z &\approx A_z \cdot ({\gamma_s}^2 + {\gamma_n}^2) + B_z \cdot Y + C_z \cdot X + D_z \end{aligned}$$

where:

$$\begin{aligned} X &= \gamma_n - \gamma_s \\ Y &= \gamma_n + \gamma_s \end{aligned}$$

This system can be solved by an iterative process.
(b) With additional assumptions that $\rho_{sf}, \rho_{nf} = 0$, another approximation for the solar moments is:

$$\begin{aligned} T_x &\approx a_x \cdot X \cdot Y + b_x \cdot Y + c_x \cdot X + d_x \qquad (6) \\ T_z &\approx a_z \cdot X + b_z \cdot Y \end{aligned}$$

This system has two solutions. The one which gives lower efficiency loss, is chosen.
(c) If, in addition, one assumes that $X_f, Y_f \ll Z_f, Y_p$, where $(X_f, Y_f, Z_f), (0, Y_p, 0)$ are the radius vectors of the flaps and panels, respectively, another approximate model can be obtained, which is of the form:

$$\begin{aligned} T_x &= A \cdot X \cdot Y + B \cdot Y \\ T_z &= A \cdot X \qquad (7) \end{aligned}$$

This system has one solution for $\gamma_n$ and $\gamma_s$.
It can be shown that in the last approximate model (c), a pure "windmill moment" when $\gamma_n = -\gamma_s$, and a pure "unbalance moment" for $\gamma_n = \gamma_s$, are obtained.

In figure 3 the solar moments Tx,Tz from the full model and those from the approximate one (b), can be seen.

$$\begin{aligned} A_p &= 6.48\ m^2 \\ A_f &= 1.00\ m^2 \\ Loss &= 1.00\ \% \\ \rho_{sp} &= 0.10 \\ \rho_{dp} &= 0.10 \\ \rho_{sf} &= 0.10 \\ \rho_{df} &= 0.10 \end{aligned}$$

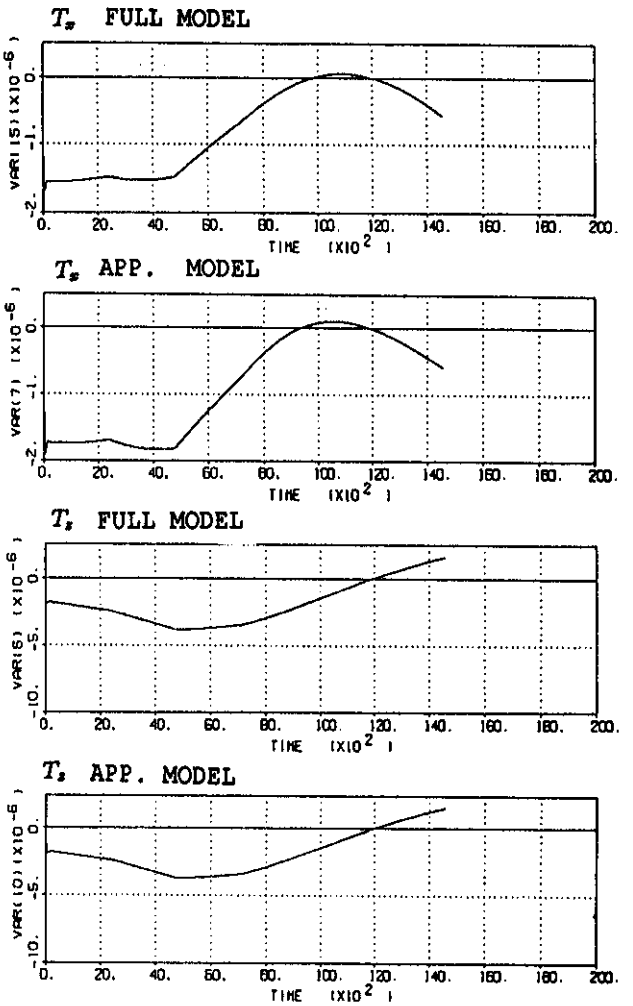


Figure 3: $T_x, T_z$ from the Full and Approximate Models. (sun elevation 23°)

# 4 Roll/Yaw Control

It can be shown that Euler's equations for the roll/yaw axes, in the frequency domain, are:

$$\begin{bmatrix} \tilde{M}_{sx} \\ \tilde{M}_{sz} \end{bmatrix} = \begin{bmatrix} I_{xx}S^2 + \omega_0 h - K_x & hS \\ -hS - K_z & I_{zz}S^2 + \omega_0 h \end{bmatrix} \begin{bmatrix} \tilde{\varphi} \\ \tilde{\psi} \end{bmatrix} \quad (8)$$

where:

$\tilde{M}_{sx}, \tilde{M}_{sz}$ - solar disturbance moments in frequency domain

$\tilde{M}_{cx}, \tilde{M}_{cz}$ - control moments, such that $\tilde{M}_{cx} = K_x(S)\tilde{\varphi}(S)$ $\tilde{M}_{cz} = K_z(S)\tilde{\varphi}(S)$

$h$ - momentum wheel

$I_{xx}, I_{zz}$ - diagonal moments of inertia

$\omega_0$ - orbital rate ($7.210^{-5}$ r/s for geosynchronous orbit)

In designing the control torques for the roll/yaw axes, the fact that only the roll angle can be measured is to be considered, and a choice is to be made between treating sensor noise and nutation damping.
It should be noted that if the control torques, in the frequency domain, are of the form:

$$\begin{aligned} \tilde{M}_{cx} &= -K(1+\tau \cdot S)\tilde{\varphi}(S) \\ \tilde{M}_{cz} &= \alpha \cdot K(1+\tau \cdot S)\tilde{\varphi}(S) \end{aligned} \quad (9)$$

a horizon sensor's noise of $0.1°$ ($3\sigma$) requires a moment of $1. \cdot 10^{-4}$[Nm], which is 20 times more than the solar sailing torques capability, but can not be reduced by a factor of 20, because it leads to instability. Therefore, the obvious conclusion is to treat the noise by the loop control and the nutation to be damped by the fixed momentum wheel. This is the situation in the roll axis. In the yaw axis, the bandwidth is smaller ($3 \cdot 10^{-4}$ r/s) than that of the roll axis ($2.3 \cdot 10^{-2}$ r/s),which enables the use of a filter (at $(2 \cdot 10^{-3}$ r/s) for the derivative.

Therefore, the control torques, in the time domain, are ([6]) :

$$\begin{aligned} M_{cx}(t) &= -K_1\varphi(t) \\ M_{cz}(t) &= K_2\varphi(t) - K_3\frac{1}{\omega_0}\dot{\psi}(t) \end{aligned} \quad (10)$$

and the nutation is damped by the momentum wheel. In equations (7), $K_1, K_2$ are computed by:

$$\begin{aligned} K_1 &= \frac{M_{sx}(\infty)}{\varphi(\infty)} - \omega_0 h \\ K_2 &= \frac{\psi(\infty)\omega_0 h - M_{sx}(\infty)}{\varphi(\infty)} \end{aligned} \quad (11)$$

and $K_3$ is defined by the maximum moment caused by the nutation.
The roll $\varphi$ is measured by the horizon sensor and filtered.
$\dot{\psi}$ can be estimated from $\varphi$, as will be shown latter.
If, for example:

$$\begin{aligned} M_{sx} &= 8 \cdot 10^{-6} \quad Nm \\ M_{sz} &= 8 \cdot 10^{-6} \quad Nm \\ \varphi(\infty) &= 0.03° \\ \psi(\infty) &= 0.45° \\ h &= 20 \quad Nms \\ \omega_0 &= 7.2 \cdot 10^{-5} \quad r/sec \end{aligned}$$

then: $K_1 = 0.014$ ; $K_2 = 0.007$
If the highest moment caused by nutation is less than $2. \cdot 10^{-6}$[Nm] and the highest nutation is $0.015°$, then $K_3$ is :
$K_3 = 2 \cdot 10^{-6}/(0.015 \cdot \pi/180.) = 0.0076$
In the proposed torques control (7):

$$\begin{aligned} \varphi &= \mathcal{L}^{-1}\{\tilde{\varphi}_m \cdot \frac{0.1}{S+0.1} \cdot \frac{0.002}{S+0.002}\} \\ \frac{1}{\omega_n} \cdot \dot{\psi} &= \mathcal{L}^{-1}\{\tilde{\varphi}_m \cdot \frac{S}{0.002} \cdot \frac{0.1}{S+0.1} \cdot \frac{0.002}{S+0.002}\} \end{aligned} \quad (12)$$

Theoretically, if the control torques capability is large enough, the required performance is reached, as shown in figure 4.

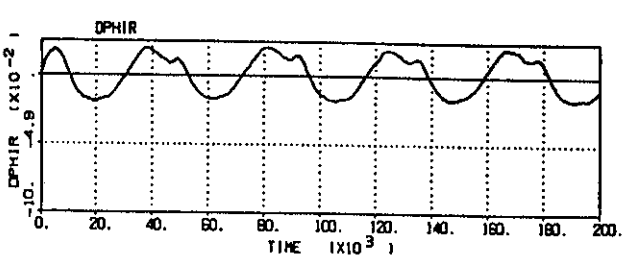


Figure 4: Roll/Yaw Performances (Sun Elevation 23°)

In the above mentioned references the same accuracy was obtained with other combinations of hardware.

However, if only a limited control capability (up to $5. \cdot 10^{-6}$ Nm), caused by flap area of 1 $m^2$ and efficiency loss of 1%, is available, maximum roll angle of 0.2° (for sun elevation 23° can be achieved, which is good enough for mission requirement.

# 5 Active Nutation Damping

In the above roll/yaw control loops, the roll/yaw angles converge even if the initial nutation is due to 0.5°, however the process lasts about 160,000 sec. In order to improve the nutation damping, the momentum wheel in the pitch axis is used, taking advantage of the products of inertia between the pitch axis and the roll/yaw axis ([8]).

Suppose that there is a product of inertia between pitch axis and the yaw axis, then the inertia matrix of the body is:

$$\begin{bmatrix} Ixx & 0 & 0 \\ 0 & Iyy & -Iyz \\ 0 & -Iyz & Izz \end{bmatrix} \tag{13}$$

The equation of motion is

$$M = H + wxH = H_\omega + H_b + \omega x(H_\omega + H_b) \tag{14}$$

In our case:

$$H_\omega = \begin{bmatrix} 0 \\ h \\ 0 \end{bmatrix} \tag{15}$$

$$H_b = \begin{bmatrix} Ixx & 0 & 0 \\ 0 & Iyy & -Iyz \\ 0 & -Iyz & Izz \end{bmatrix} \begin{bmatrix} \omega_x \\ \omega_y \\ \omega_z \end{bmatrix}$$

By using the linear approximation:

$$\begin{bmatrix} \omega_x \\ \omega_y \\ \omega_z \end{bmatrix} = \begin{bmatrix} \dot{\varphi} - \omega_0 \psi \\ \dot{\theta} - \omega_0 \\ \dot{\psi} + \omega_0 \varphi \end{bmatrix} \tag{16}$$

and converting to the frequency domain, the following system is obtained:

$$\begin{bmatrix} \varphi \\ \theta \\ \psi \end{bmatrix} = \tag{17}$$

$$\begin{bmatrix} p_{11} & p_{12} & p_{13} \\ p_{21} & p_{22} & p_{23} \\ p_{31} & p_{32} & p_{33} \end{bmatrix} \begin{bmatrix} M_x + I_{yz} \\ M_y - h \\ M_z \end{bmatrix} \tag{18}$$

where,

$$\begin{bmatrix} M_x + I_{yz} \\ M_y - h \\ M_z \end{bmatrix} = \begin{bmatrix} M_{sx} + M_{cx} \\ M_{sy} + M_{cy} + damper \cdot \varphi \\ M_{sz} + M_{cz} \end{bmatrix} \tag{19}$$

and $M_{sx}, M_{sy}, M_{sz}$ are the solar disturbance torques, $M_{cx}, M_{cy}, M_{cz}$ are the control torques, $P_{ij}$ are functions (in the frequency domain) of $I_{xx}, I_{yy}, I_{zz}, I_{yz}, \omega_x, \omega_y, \omega_z$ and $h$.

The diagram block of the roll/yaw control and the active nutation damping is given in figure 5.
In figure 5, $P_x$ and $P_z$ are derived from equation (8):

$$\begin{aligned} P_x(S) &= -K_1 \qquad (20) \\ P_z(s) &= K_2 - K_3 \cdot \frac{S}{0.002} \cdot \frac{0.1}{S+0.1} \cdot \frac{0.002}{S+0.002} \end{aligned}$$

and $P_y(S)$ is defined by:

$$P_y(S) = I_{yy} \cdot (-\omega_n^2 - 2 \cdot \zeta \cdot \omega_n \cdot S - \frac{0.2 \cdot \omega_n^3}{S} \tag{21}$$

where: $\omega_n = 0.05\ r/s \ ; \ \zeta = 1$
Lets consider for example:

$$\begin{aligned} I_{xx} &= 764 \quad Kgm^2 \\ I_{yy} &= 339 \quad Kgm^2 \\ I_{zz} &= 955 \quad Kgm^2 \\ I_{yz} &= 20 \quad Kgm^2 \\ h &= -20 \quad Nms \\ \omega_0 &= 7.2 \cdot 10^{-5} \quad r/s \\ damper &= 10 \end{aligned}$$

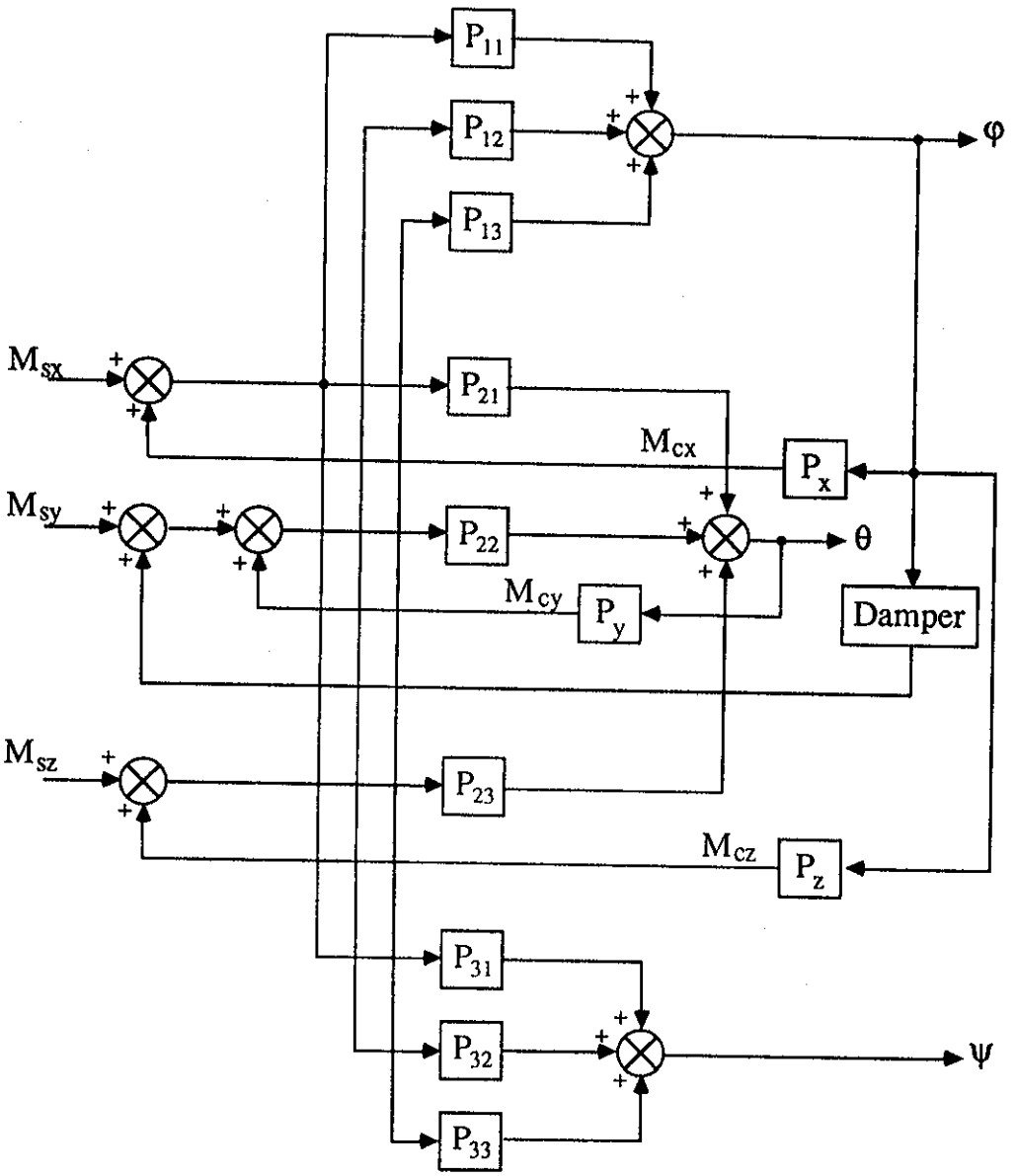


Figure 5: Block Diagram of The Roll/Yaw Control and active nutation damping loops

In figure 6 the time response in the roll angle, is shown for two cases:
(a) The loop does not include nutation damping
(b) The loop includes nutation damping

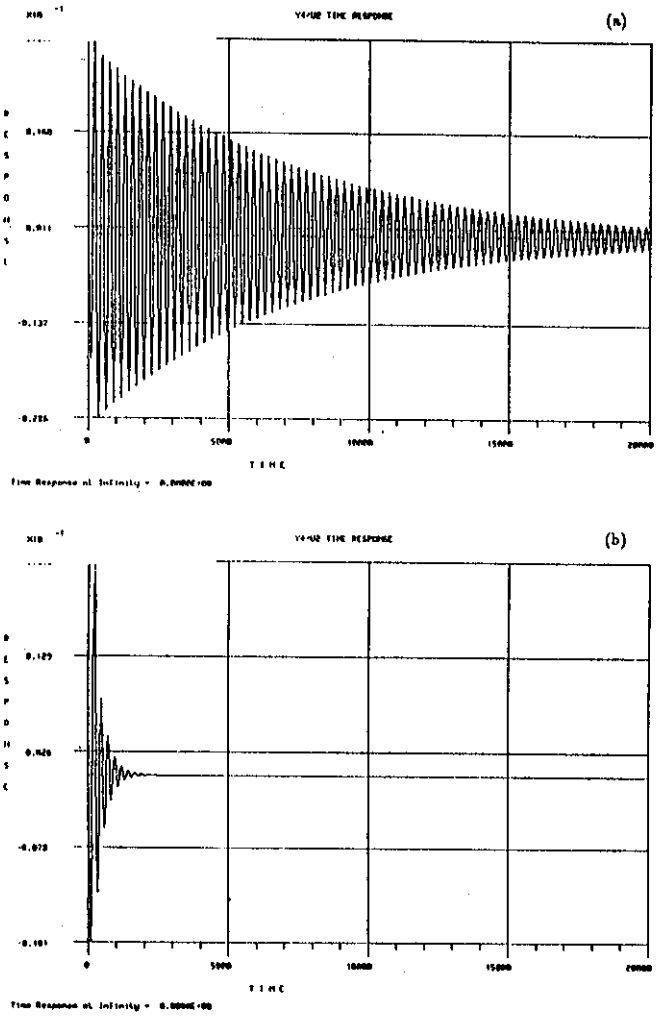


Figure 6: Time Response for Roll Angle (a) without Damper; (b) with Damper

It should be noted that the active nutation damping can be designed due to $I_{xz}$ instead $I_{yz}$.

# References


[1] J. Lievere - Solar Sailing Attitude Control of Large Geostationary Satellite, IFAC, Aut. Control in Space, France, 1985.

[2] T. Duhmael, A.Benoit - New Aocs Concepts for Artemis and Drs, Matra Espace. Presented at ESA International Conference - to be printed.

[3] B. Wie, J.A. Lehner, C.T. Plescia - Roll/Yaw Control of Flexible Spacecraft using Skewed Bias Momentum wheels, American Institute of Aeronautics and Astronautic, 1984.

[4] L. Mazzini, A. Ritorto, E. Astin - Attitude Control Design in the DRTM Satellites, Alenia Spazio, Italy. Presented at ESA International Conference - to be printed.

[5] R.P. Iwens, A.W. Fleming, V.A. Spector - Precision Attitude Control with a Single Body-Fixed Momentum Wheel, AIAA, Mechanical and Control of Flight Conference, No. 74-894.

[6] R. Azor - Roll/Yaw Control by Solar Sail Arrays, IAI-MBT, RT-P910-0000-20, 1990.

[7] R. Azor - Solar Arrays Model IAI-MBT, RT-P910-0000-21, 1990.

[8] R. Azor - Active Nutation Damping in Roll/Yaw axes , IAI-MBT, 266(3791)899-PR, 1990.

[9] J. R. Wertz - Spacecraft Attitude Determination and Control

# INTERACTIVE METHOD FOR PLANNING CONSTRAINED, FUEL OPTIMAL, ORBITAL PROXIMITY OPERATIONS

A. Abramovitz and A. Grunwald
Faculty of Aerospace Engineering
Technion - Israel Institute of Technology
Haifa, Israel

## Abstract

An interactive technique for planning fuel optimal rendezvous trajectories in the proximity of the space station is presented. The approach employed provides a method for determining the spatial constrained impulsive maneuver between two completely arbitrary chaser and target trajectories, to be executed in a limited task time. The proximity operations are described by the relative motion equations. The optimization method is based on the primer vector and its extension to non-optimal trajectories. The optimal number, direction and magnitude of the impulses could thus be found. A variety of different design examples has been presented, by which the tool was evaluated. In many cases a fuel saving of up to 30% could be accomplished by adding an intermediate impulse. Similar fuel savings could be achieved by initial and final arcs. Most of the optimal solutions were quite counter-intuitive, and could not have been found without the use of the optimizations tools implemented herein. Operating the system was proved to be very easy, and did not require any previous in depth knowledge of the relevant theoretical background. Trade-off studies of fuel consumption versus task time were obtained with this method.

## 1. Introduction

The space station will function as a platform for research and experiments in the close micro g environment of the Earth and will serve as an orbital operations centre for missions to nearby and far away destinations. The station is planned to become operational in less than ten years, and soon afterwards, the dense traffic of space vehicles in its proximity will raise problems quite different from the ones encountered in ordinary design of space trajectories. The main difference will result from the stringent safety constraints imposed by the complex type of maneuvers executed by the variety of spacecraft co orbiting with the space station in close vecinity. Besides this, the well known demand for optimization of fuel consumption will have an even stronger validity because of the large number of maneuvers involved and the repeatable character of some of them.

Among the orbital operations typical to the space station environment, this research deals with rendezvous maneuvers, in which a chaser spacecraft, initially moving along a specified trajectory, has to meet with a target spacecraft moving along a different trajectory. Rendezvous is distinguished from interception by the fact that the chaser has to adjust its velocity with the target, so that after the meeting, they continue to move together along the latter's trajectory. Moreover, the approach must lead to the docking points of the target, at the correct angular orientation, while the relative velocity is within a safe range.

In the crowded, multi-vehicle surrounding mentioned above, planning each maneuver has to take into account the complex interface with the neighbouring trajectories. Therefore, an on-site, orbital stand alone, trajectory planning capability is needed in each spacecraft. Such a tool may help overcome the difficulties related to orbital rendezvous, that originate from the counter-intuitive character of relative orbital motion together with the demand to satisfy the spatial constraints.

The method proposed here attempts to find a solution to these difficulties by means of a graphical system that displays the trajectories as well as the constraints and a fuel optimization indicator, while facilitating planning through an interactive process. The usefulness of graphical interactive orbital trajectory design has been demonstrated by Grunwald and Ellis [1].

## 2. Analytical Background

This research is based on two main analytical components:

a. the relative motion that describes the proximity operations, based on ref [2].
b. the fuel optimization method, based on the primer vector theory developed by Lawden [3] and extended to non-optimal trajectories by Lion and Handelsman [4].

These issues are briefly described in this section.

### 2.1 Proximity Operations and Relative Motion

The maneuvers of a spacecraft orbiting in the vecinity of the space station are called proximity operations, and are characterized by relative distances of less than 1500 m, relative velocities of less than 0.5 m/sec and mission times smaller than half the station's orbital period. The most typical proximity operations are station keeping with co-orbiting spacecraft, rendezvous, arrival and departure, docking (with its precise demands for angular orientation and relative velocity), berthing and also astronauts' EVA (Extra Vehicular Activity) performed with the aid of the MMU (Manned Maneuvering Unit).

Maneuvers of many space vehicles in a dense environment impose safety constraints, such as collision avoidance along the trajectory, clearance from LSS (Large Space Structures), avoidance of plume impingement and arrival and departure with permitted velocities and directions. Authors of references [5], [6] and [7] have checked different strategies for maneuvers in the proximity of LSS, that satisfy the collision avoidance constraint. Numerous numerical simulations resulted in necessary and sufficient conditions that assure the fulfilment of these constraints. Optimization of the fuel consumption was recomended as a continuation of their investigations.

The most natural way to describe proximity operations is by the relative motion between the vehicles, since their trajectories are very similar and only the relative separation is significant to the maneuver. Clohessy and Wiltshire [2], Hill [8] and Wheelon [9] developed the equations of motion of a spacecraft in a coordinate system attached to a satellite moving in a circular orbit. The inverse square law gravitational force function acting on the spacecraft is linearized about the center of the satellite. In this system, the axis pointed in the direction of motion is called V-bar, or s parameter, while the axis pointing away from the attraction centre is called R-bar, or r parameter (see Fig. 1). $\bar{\rho}$ is the relative position

vector. The forward solution for the relative motion, considering that the initial position and velocity are given, receives the form:

$$\begin{Bmatrix} s(t) \\ r(t) \\ \dot{s}(t) \\ \dot{r}(t) \end{Bmatrix} = \begin{bmatrix} 1 & D & E & C \\ 0 & A & C & B \\ 0 & F & H & G \\ 0 & I & G & J \end{bmatrix} \begin{Bmatrix} s_0 \\ r_0 \\ \dot{s}_0 \\ \dot{r}_0 \end{Bmatrix} \qquad (1)$$

while the initial velocity can be calculated, given the initial and final position, from:

$$\begin{Bmatrix} \dot{s}_0 \\ \dot{r}_0 \end{Bmatrix} = \begin{bmatrix} P & Q & P & L \\ L & K & L & M \end{bmatrix} \begin{Bmatrix} s_0 \\ r_0 \\ s(t) \\ r(t) \end{Bmatrix} \qquad (2)$$

The coefficients A, B, ... P are trigonometric functions of the mean motion n and the time parameter t, defined by:

$$A = 4 - 3\cos(nt) \qquad F = 6n[\cos(nt) - 1] \qquad K = \frac{CD - AE}{BE + C^2}$$

$$B = \frac{1}{n}\sin(nt) \qquad G = \frac{C}{BE + C^2} \qquad L = 2\sin(nt)$$

$$C = \frac{2}{n}[1 - \cos(nt)] \qquad H = 4\cos(nt) - 3 \qquad M = \frac{E}{BE + C^2} \qquad (3)$$

$$D = 6[\sin(nt) - nt] \qquad I = 3n*\sin(nt) \qquad Q = \frac{AC + BD}{BE + C^2}$$

$$E = \frac{1}{n}[4\sin(nt) - 3nt] \qquad J = \cos(nt) \qquad P = \frac{B}{BE + C^2}$$

As a result of using relative coordinates, the calculation of the trajectory is much simplified, especially compared to the "Gauss problem". But, on the other hand, the relative motion has a counter intuitive character, thus making the task of piloting a spacecraft according to visual cues (i.e. as seen through the window) practically impossible. Fig. 2 shows the relative motion caused by a positive V bar burn, which, intuitively, should have brought the vehicle ahead, in the direction of the burn. In yfact, this burn causes an increase in the orbital velocity, which brings the spacecraft to a higher orbit, with a bigger period, finally keeping the spacecraft behind its expected position. Therefore, a graphical computerized tool is needed for planning complex, multiple burn maneuvers.

### 2.2 Fuel Optimization and the Primer Vector

Minimizing fuel consumption in a central, inverse square law gravity field is one of the fundamental concerns of optimization of space trajectories. The motivation for fuel minimization, besides the high cost of lifting it into orbit, is based on the fact that the life cycle span of a spacecraft depends mostly on the fuel left for trajectory corrections and manuevers. This dependency strenghtens in lower orbits, due to the atmospheric drag.

Rocket propulsion is usually described by impulses, which alter the magnitude and direction of the velocity, so that the trajectory is a succession of impulses followed by coast sections. Optimizing the fuel consumption of an impulsive trajectory means finding the number, magnitude and direction of the impulses needed for performing a transfer, intercept or rendezvous maneuver with minimum fuel (known as "Lawden problem"). Neustadt [10] and Stern and Potter [11] have established that the number of impulses required for an unconstrained, free time, minimum fuel trajectory is equal to or less than the number of state variables needed to define the final point of the trajectory. Therefore, a maximum number of six impulses is needed for a three dimensional trajectory, while in the case of a planar trajectory up to four impulses are required for minimizing the fuel consumption.

In this research, the fuel optimization method is based on Lawden's primer vector, since this method does not assume an initial number of impulses, but allows finding this parameter, together with their time and location. Lawden [3] treated the problem of minimizing the fuel consumption as a Mayer problem of the calculus of variations. He formulated the equations of motion for rocket trajectories, the Hamiltonian and the necessary conditions, and found that the Lagrange multipliers of the velocity have a dominant role in the necessary conditions. With these multipliers he composed a vector, which he named the primer vector, and expressed the necessary conditions by means of this vector, as follows:

1. The primer vector and its first derivative must be continuous everywhere along the trajectory.
2. The thrust vector must be parallel to the primer vector at all waypoints (points of impulses activation).
3. The magnitude of the primer vector must be less than one everywhere, except for the waypoints, where it must be equal to one.
4. The first derivative of the primer vector must be zero at all intermediate waypoints.

The primer vector distribution, $\vec{p}$, and its first derivative, $\dot{\vec{p}}$, for circular trajectories, can be calculated as follows:

$$\vec{p} = \begin{Bmatrix} \lambda_s = -2a\sin f + 2b\cos f - 3cf + d \\ \lambda_r = a\cos f + b\sin f + 2c \\ \lambda_z = k_1\cos f + k_2\sin f \end{Bmatrix} \qquad (4)$$

$$\dot{\vec{p}} = \begin{Bmatrix} \dot{\lambda}_s = -n(a\cos f + b\sin f + c) \\ \dot{\lambda}_r = n(a\sin f - b\cos f + 3cf - d) \\ \dot{\lambda}_z = n(k_1\cos f - k_2\sin f) \end{Bmatrix} \qquad (5)$$

where $f = nt$ is the true anomaly and the constants $a, b, c, d, k_1, k_2$ must be calculated from the initial conditions. It is important to note, regarding these equations, that the out-of-plane components of the primer and its derivative are independent of the planar ones, and can be treated separately. The primer must be evaluated apart, for each section of the trajectory.

Fig. 3 shows five possible distributions of the primer vector, for a two-impulse trajectory, where:
- primer a describes an optimal trajectory.
- primers b, c and d describe trajectories which are close to optimal, each having a different character, as will be explained later.
- primer e describes a trajectory which is far from being optimal.

Further on, Lion and Handelsman [4] extended the definition of the primer vector to non optimal trajectories and showed that its distribution can give an indication about the way to improve the fuel consumption. By comparing between a two-impulse section and a section with an additional intermediate waypoint, they found criterions for adding waypoints, initial or final coasts, that minimize the fuel consumption. Moreover, they

formulated expressions for the change in time or position of the impulses, which, if executed in small steps, can assure the optimization. As a result of this contribution, the primers of fig. 3 can be interpreted as follows:

- primer b indicates that an intermediate impulse will always reduce the fuel consumption. The time of this impulse should be the time when the primer is maximal and its direction, the direction of the primer vector at this time.
- primer c indicates that an initial coast will always reduce the fuel consumption.
- primer d indicates that a final coast will always reduce the fuel consumption.

The explicit expressions for the change in the time and position of an intermediate waypoint, which appear in ref. [4], are functions of the primer vector's first derivative, thus expressing Lawden's fourth necessary condition.

Several works have used similar methods for fuel optimization:

Prussing [12] and [13] treated minimum fuel fixed-time rendezvous in the proximity of a circular orbit, and separated the maneuvers according to the number of impulses (2, 3 and 4).

Jezewski and Rozendaal [14] treated rendezvous between three dimensional trajectories, with practical application to the Apollo program. They showed that a considerable amount of fuel can be saved by adding impulses.

Gross and Prussing [15] treated free-time rendezvous between circular orbits, where ratio of radiuses is much bigger than unity.

Prussing and Chiu [16] treated fixed time rendezvous, as a function of the phase angle. They showed that if the time is sufficient, than Hohmann transfer is optimal.

None of these works deal with any kind of constraints.

## 3. Problem formulation

The purpose of this research is to develop an interactive graphical tool for planning time-limited rendezvous trajectories between space vehicles that orbit in the proximity of the space station. The resultant trajectories must satisfy the spatial constraints assuring collission avoidance and must have an optimal fuel consumption. Some of the practical applications may be:

transfer of crew between neighbouring vehicles, where the time limitation can originate from the limited amount of oxygen for breathing, batteries, navigation precision, or from the need to perform an urgent operation, such as rescue.

- transfer of equipment, with an unmanned spaceship.
- free flyers maintenance.

The chaser, target and rendezvous trajectories discussed herein are two dimensional and limited to the station's orbital plane, but are not otherwise limited in their shape. Fig. 4 describes graphically a typical testcase in which the location of the chaser and the target at initial task time, $t_0$, and final time, $t_f$, are given, so that their trajectories are fully defined. The mission total task time is $t_{task}=t_f-t_0$. The coordinate system, (s,r), is attached to the space station which is placed in a circular orbit, 480 km above the Earth. The chaser leaves its original trajectory at time $t_1$, when the initial impulse $\Delta V_1$ is applied, adjusts the rendezvous trajectory at $t_2$, with the intermediate impulse $\Delta V_2$, and reaches the target trajectory at $t_3$, where the final impulse $\Delta V_3$ adjusts its velocity, according to the target's velocity. In this case the rendezvous trajectory is composed of an initial coast along the chaser trajectory ($t_0<t<t_1$), two sections, a final coast along the target trajectory ($t_3<t<t_f$), and three impulses. The second section of the rendezvous trajectory does not fulfil the spatial constraint, so that even if this solution is fuel optimal, another one, with a higher fuel consumption, must be found.

Finding a fuel optimal trajectory means finding a trajectory in which the sum of the impulses applied is minimal, including the last one. Taking into account the last impulse is specific to rendezvous maneuvers, while for interception cases, this last impulse is ignored.

An additional demand for the required method is that it must be simple enough to be implemented and used with reasonable hardware, so that it can be operated in each vehicle, in orbit, without the need of a wide academic background in the field.

The basic assumptions made in this research were:

- motion in a central inverse square law gravity field, that yields Keplerian trajectories; no perturbations were considered;
- two dimensional motion, limited to the orbital plane of the space station;
- limited task time;
- propulsion achieved by impulses, with no limitations on their number, magnitude or direction; no disturbing forces (like drag, third body attraction, etc.) were considered;
- motion in almost circular trajectories, with negligible excentricity;
- linear problem in which the fuel consumption [kg] is proportional to the sum of the impulses [m/sec].

## 4. Method of Solution

Planning a complex maneuver, which is fuel optimal and fulfils the spatial constraints, turns out to be a difficult task. Therefore the approach of this method is to use an interactive graphic system, which displays simultaneously the maneuver, the spatial constraints, the cost function (the sum of the impulses applied), together with an optimization pointer and the primer vector distribution. The solution is obtained by means of an iterative process, whose logic flowchart is described in fig. 5.

The optimization method is based on the primer vector theory, which does not take into account any constraints. Due to the extension of the primer vector to non-optimal trajectories, an optimization pointer is built, which indicates the change of time and location of the intermediate waypoints, that assures minimizing the fuel consumption. This pointer exists only when the trajectory is not optimal. The optimal solution is obtained with the interactive aid of the operator, by moving the waypoints, according to the pointer and so that it by-passes the constraints. Although the solution may be composed of up to four waypoints, only one is active each time. This way, finding the constrained optimal solution is a simple and straight-forward process.

Lawden's four necessary conditions for optimality are satisfied for the computation of the primer vector distribution, for each section apart, as follows:

First condition is obvious from the equations of the primer vector (4).

second and third conditions, applied at each of the two waypoints of the section, allow evaluating the constants a, b, c, d of equation (4).

fourth condition is implemented in the extension of the primer to non optimal trajectories, and therefore in the optimization pointer.

This method is especially suitable for cases in which the fuel optimal solution does not satisfy the spatial constraints, so that a constrained sub optimal solution is required.

The graphic display contains clear and simple symbols, which are meant to help the operator in the iterative process of solution.

The graphic program was implemented on a PC (IBM compatible) in Microsoft C and MetaWindows graphic package. Due to the relative simplicity of the equations, the interactivity is felt even with an IBM PC XT. The program is built to process events caused by the operator, with the aid of the mouse or the keyboard.

## 5. Typical Applications and Results

The method presented here is general and is not restricted to specific chaser or target trajectories or to a given number of impulses. The few following examples, cited from Abramovitz [17], are meant to demonstrate the utility of the method in saving significant amounts of fuel in rendezvous maneuvers that must satisfy a spatial constraint. Moreover, it is demonstrated that, in certain cases, adding an intermediate impulse may reduce the total fuel consumption.

In these examples it was assumed that the space station is located at the origin of the (s,r) coordinate system, although every other location is legitimate. No distances or dimensions are given for the figures, they are treated generically. Most of the distances in the proximity operations following are less than 500 m, and the space station is assumed to be a square of 200x200 m.

### 5.1 Stationary Chaser and Target with Trajectory Beginning and Ending along the V-bar

Fig. 6.a shows a two impulse rendezvous between a stationary chaser, coinciding with the space station, and a target that moves from a location before the station to one behind it. Since the primer distribution was not optimal, an intermediate waypoint was added, and its optimal location was found with the help of the optimization pointer. The optimal solution (see fig. 6.b) consists of three impulses and the resultant trajectory is very close to the original one. Despite the additional impulse, a 20% reduction of the impulsive cost was achieved.

### 5.2 Chaser and Target Trajectory Begin and End along the V-bar

Fig. 7.a shows a two impulse rendezvous between a chaser that moves from a location before the space station to a location after the station. The target moves from the chaser arrival point to its departure point, similarly to the previous case. Intuitively, the best strategy might be to stop the motion of the chaser at its initial location, with the impulse $I_2$ (first impulse out of two), to wait for the target to reach this point, and then to continue with it, while catching with the target's velocity with impulse $II_2$ (second impulse out of two). But the primer for this strategy is far from being optimal, and it shows that an intermediate impulse will reduce the fuel consumption. The intermediate waypoint was taken to its optimal position, with the help of the optimization pointer, and the final solution, which has three impulses (see fig. 7.b), has a total impulsive cost 20% lower than the "intuitive" two impulse one. It is probably very unlikely to find this optimal solution without using the primer and the optimization pointer.

The task time in the previous example was equal to half the station's orbital period. Fig. 8 shows the influence of the task time on the percentage of fuel saved by adding a third impulse, and specifically, that the saving is bigger than 20% for $0.5<t_{task}<0.9$. If the task time can be controlled, than, by this graph, a task time can be chosen so that the fuel saving is bigger than a threshold value. In this way, the worthiness of adding the third impulse, which is itself a complicated and risky maneuver, can be evaluated versus the choice of a certain task time. This kind of trade-off study may be very important in cases with great repeatability.

### 5.3 Hohmann Rendezvous

Hohmann rendezvous is the fuel optimal rendezvous between vehicles orbiting in circular trajectories, when the task time equals half the orbital period of the average trajectory (see Billik and Roth [18]). For Hohmann rendezvous, a specific phase angle must develop between the two vehicles. The waiting time that brings the vehicles to the appropriate phase angle depends on the trajectory radiuses, in such a way that the closer they are, the higher this time can be. This is the main obstacle in using Hohmann maneuver for proximity operations. A possible solution is the bi-elliptic maneuver. Fig. 9 shows the Hohmann rendezvous in relative coordinates. Its characteristic features are:

- the chaser is located $\Delta r=r_{chaser}$ beneath the V-bar, the target $\Delta r=r_{target}$ above;
- task time equals half the station's orbital period;
- chaser and target relative trajectories are straight lines (circular in absolute coordinates);
- chaser's departure point is right beneath the target's arrival point;
- the impulses are parallel to the V-bar and in the same direction;
- primer equals unity everywhere;

Deviations from Hohmann rendezvous may originate from:

- incorrect task time;
- incorrect relative positions (incorrect phase angle);
- harm of the spatial constraint.

The following sections present Hohmann-like maneuvers caused by these reasons.

### 5.4 Hohmann-like rendezvous because of incorrect task time

When the task time is bigger than half the orbital period and the chaser and target positions fit to the Hohmann requirements, a two-impulse maneuver that uses all the available time is not fuel optimal (see primer in fig. 10). A rendezvous with an impulsive cost identical to Hohmann can be achieved by:

- initial and final coast for equal periods, so that the remaining time equals half the period; the resultant trajectory is identical to Hohmann, in shape and impulsive cost (see fig. 11);
- three-impulse maneuver that uses all the available

time; this bi elliptic maneuver has an impulsive cost identical to Hohmann (see fig. 12).

When the task time is smaller than half the orbital period, the optimal maneuver uses all the available time and two impulses. The impulsive price is higher than Hohmann's (see fig. 13).

### 5.5 Hohmann-like rendezvous because of incorrect relative positions

Incorrect relative positions may result in long waiting times, which are practically part of the task time. On the other hand, a small delay in executing the maneuver may result in missing it, and having to wait a long time. For all this cases, a trade off between the waiting time and the impulsive cost must be done. The following examples demonstrate the utility of the method for this goal.

In a Hohmann rendezvous expressed in relative coordinates only the s coordinates change (see fig. 14). A certain position on this graph, relating to a certain relative position, develops in time by moving along a diagonal parallel to the lineal ones. The graph shows domains for relative positions before and after Hohmann.

Fig. 15 shows the situation for the position marked by "1" in fig. 14. The primer indicates that a final coast is necessary, resulting in a 3% fuel reduction (see fig. 16). The spatial constraint can be by passed from the right or the left side (see fig. 17 and 18). None of them is optimal (note the primers), they both fulfil the spatial constraint in a fuel optimal way, and the right by-pass is 94% more fuel expensive. Fig. 19 shows the total impulsive cost for the relative positions along the lineal diagonal of fig. 14. The two impulses maneuver are the cheapest, but do not fulfil the spatial constraint in the period of 20 minutes around Hohmann time. In the extremal parts of this period, three impulses by-passing the constraint from the right are optimal, while for the central part of the period, three impulses with a left by pass are optimal. In this constrained case, the total impulsive cost determines that:

no maneuver should be executed in the period of 15 minutes after Hohmann time; the proper strategy is to reach 20 minutes, and use two impulses; this is against the intuition, by which the impulsive cost grows with time and the maneuver should be executed imediatelly; if the maneuver must be executed at least 15 minutes before Hohmann time, than a two impulse maneuver should be executed 20 minutes before Hohmann time, although before Hohmann time, the impulsive cost goes down with the time.

## 6. Conclusions

The method presented, with its graphic interactive display of the primer vector distribution and the optimization pointer, was found to be most efficient in planning constrained, fuel optimal rendezvous maneuvers. Fuel savings of up to 30% were obtained. The optimal number of impulses could be easily found. The optimization pointer helped in finding optimal solutions, especially in the constrained cases.

Most of the solutions that were obtained have a counter intuitive character, so that finding them without these tools would have been difficult.

Although the method is based on necessary but not sufficient conditions, in all cases checked, only one optimal solution was found.

The method can be used for preparing contours of potential times and locations of the intermediate waypoints. These contours can help in studying the trade-offs of fuel consumption versus task time.

Operating the system was proved to be very easy, and did not require any previous in-depth knowledge of the relevant theoretical background.

The interactivity of the method helps familiarizing with the counter intuitive character of constrained relative motion, so that the tool created can be used as a training aid.

Although implemented for planar motion only, the method can be easily expanded to three dimensional maneuvers, since the out-of-plane component of both the relative motion and the primer vector is independent of the two planar ones.

A further continuation of this research must include automatic planning with the aid of heuristic design rules, found by experienced operators.

## References


1. Grunwald, A.J. and Ellis, S., "Interactive Orbital Proximity Operations Planning System," *NASA Technical Paper* 2839, Ames Research Center, Moffet Field, California, 1988.

2. Clohessy, W.H. and Wiltshire, R.S., "Terminal Guidance System for Satellite Rendezvous," *Journal of the Aerospace Sciences*, Sept. 1960, pp. 653-658, 674.

3. Lawden, D.F., *Optimal Trajectories for Space Navigation*, Butterworths, London, 1963.

4. Lion, P.M. and Handelsman, M., "The Primer Vector on Fixed-Time Impulsive Trajectories," *AIAA Journal*, Vol. 6, Jan. 1968, pp. 127-132.

5. Stern, S.A. and Soileau, K.M., "Operational Implications for Path-Constrained Rendezvous," *AIAA Paper* 85-1918, 1985.

6. Stern, S.A. and Fowler, W.T., "Path-Constrained Maneuvering near Large Space Structures," *Journal of Spacecraft*, vol. 22, No. 5, Sept. Oct. 1985, pp. 548-553.

7. Soileau, K.M. and Stern, S.A., "Path Constrained Rendezvous: Necessaryand Sufficient Conditions," *Journal of Spacecraft*, Vol. 23, No. 5, Sept.-Oct. 1986, pp. 492-498.

8. Hill, G.W., "Researches in the Lunar Theory," *American Journal of Mathematics*, Vol. 1, No. 1, 1878, pp. 5-26.

9. Wheelon, A.D., "Midcourse and Terminal Guidance," *Space Technology*, John Willey & Sons, New York, 1959.

10. Neustadt, L.W., "Optimization, A Moment Problem and Nonlinear Programming," *SIAM Journal on Control*, Vol. 2, No. 1, 1964, pp. 33-89.

11. Stern, R.G. and Potter, J.E., "Optimization of Midcourse Velocity Corrections," Proceedings of the IFAC Symposium on Automatic Control," in "*Peaceful Uses of Automation in Outer Space*," Plenum Press, New York, 1965.

12. Prussing, J.E., "Optimal Four Impulse Fixed Time Rendezvous in the Vicinity of a Circular Orbit," *AIAA Journal*, Vol. 7, No. 5, May 1969, pp. 928 935.

13. Prussing, J.E., "Optimal Two and Three Impulse Fixed Time Rendezvous in the Vicinity of a Circular Orbit," *AIAA Journal*, Vol. 7, No. 5, May 1969, pp. 928 935.

14. Jezewski, D.J. and Rozendaal, H.L., "An Efficient Method for Calculating Optimal Free-Space N-Impulsive Trajectories," *AIAA Journal*, Vol. 6, No. 11, Nov. 1968, pp. 2160-2165.

15. Gross, L.R. and Prussing, J.E., "Optimal Multiple Impulse Direct Ascent Fixed Time Rendezvous," *AIAA Journal*, Vol. 12, No.7, July 1974, pp. 885 889.

16. Prussing, J.E. and Chiu, J.H., "Optimal Multiple-Impulse Time-Fixed Rendezvous between Circular Orbits," *Journal of Guidance, Control and Dynamics*, Vol. 9, No. 1, Jan.-Feb. 1986, pp. 17-22.

17. Abramovitz, A., "Interactive Method for Planning Constrained, Fuel Optimal Orbital Proximity Operations," M. Sc. Thesis, Technion - Israel Institute of Technology, July 1991. (in Hebrew)

18. Billik, B.H. and Roth, H.L., "Studies Relative to Rendezvous between Circular Orbits," *Astronautica Acta*, Vol. 13, Jan.-Feb. 1967, pp. 23-36.

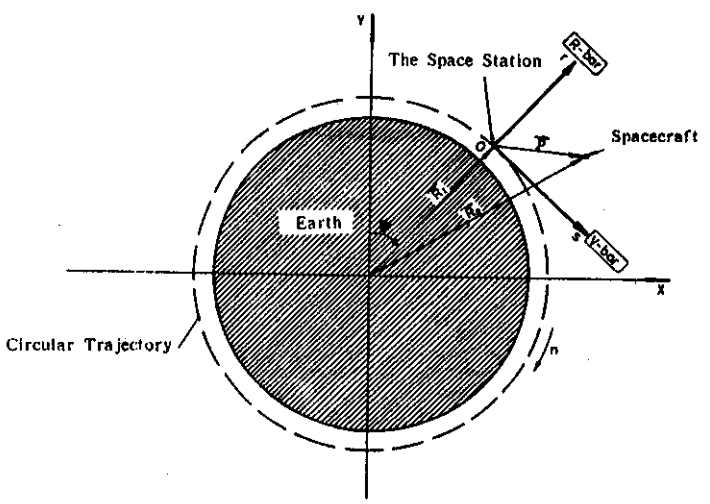


Fig. 1: Definition of relative motion's coordinate system

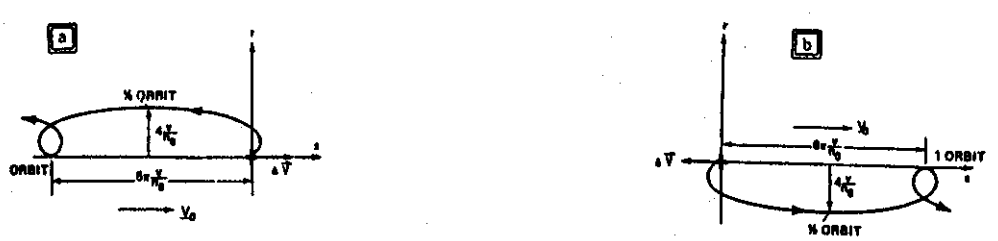


Fig. 2: Relative motion after V-bar burn
a. positive V-bar burn
b. negative V-bar burn

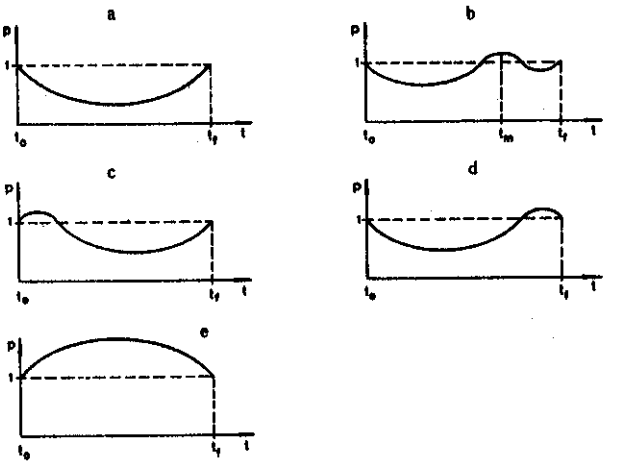


Fig. 3: Possible primer distributions

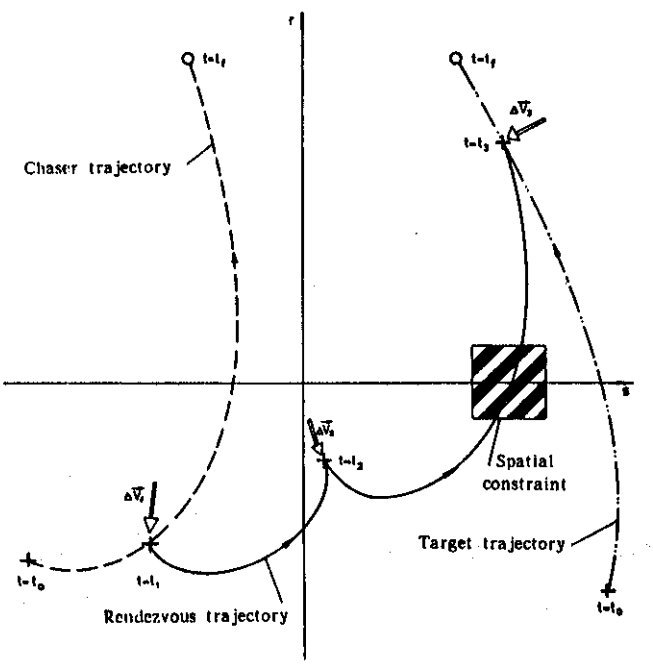


Fig. 4: Graphical presentation of a planar rendezvous composed of three impulses

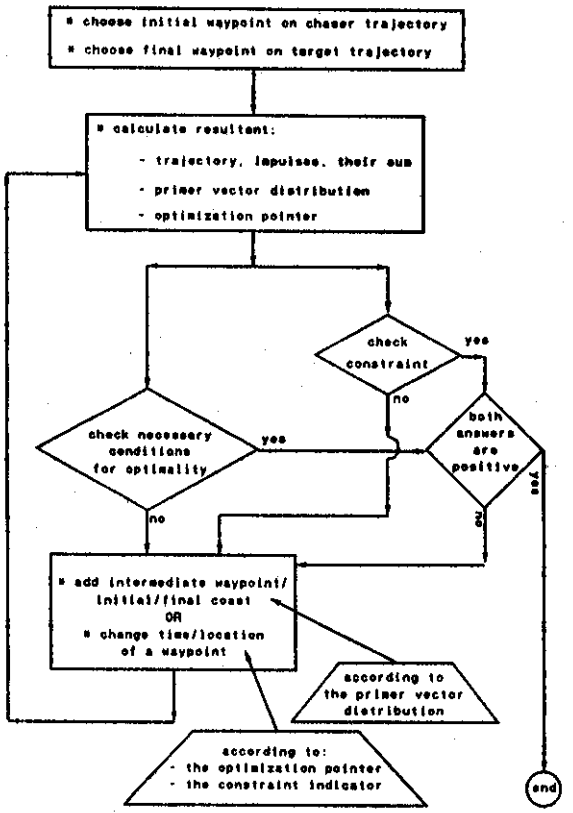


Fig. 5: Logic flowchart of the software

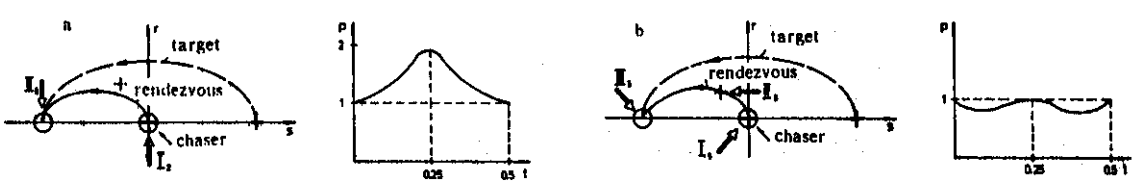


Fig. 6: Rendezvous between a stationary chaser and a target with trajectory beginning and ending along the V-bar

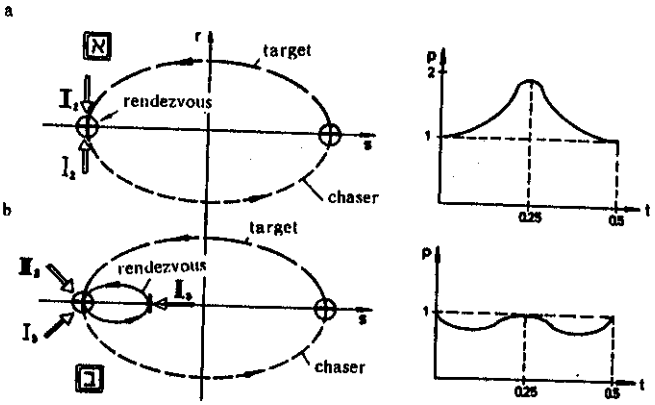


Fig. 7: Rendezvous between a chaser and a target having identical trajectories, with common endpoints, in different directions

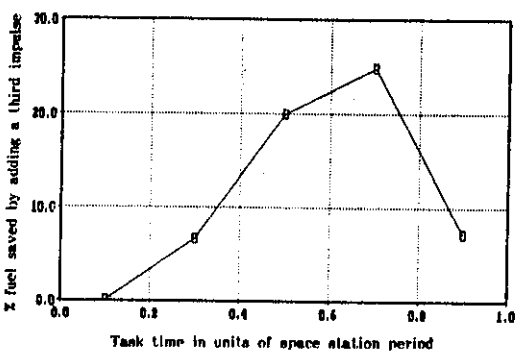


Fig. 8: Fuel saved as a result of adding a third impulse, versus task time

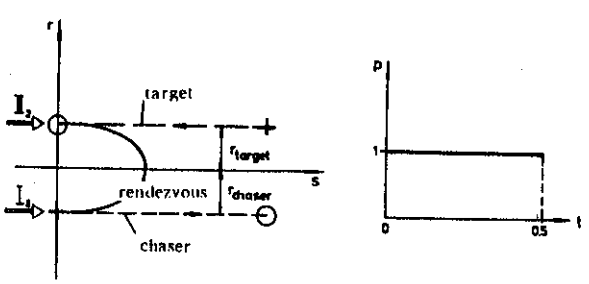


Fig. 9: Hohmann rendezvous in relative coordinates

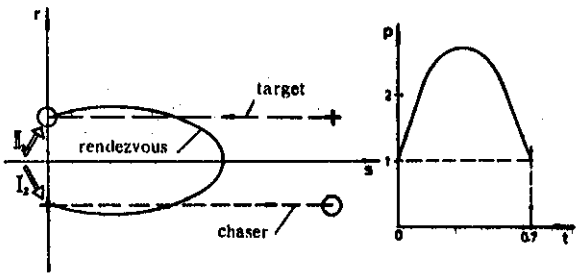


Fig. 10: Hohmann like rendezvous with task time bigger than half a period

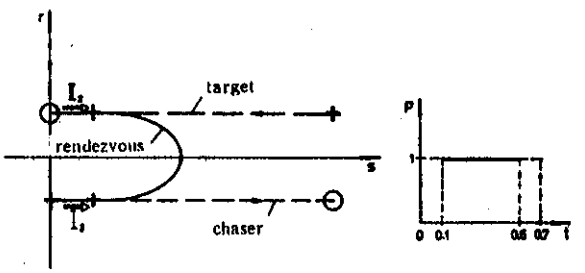


Fig. 11: Hohmann-like rendezvous with initial and final coast

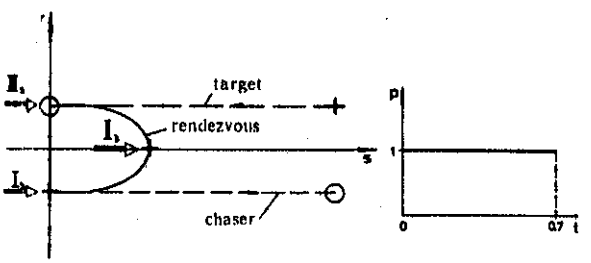


Fig. 12: Hohmann-like rendezvous with intermediate waypoint

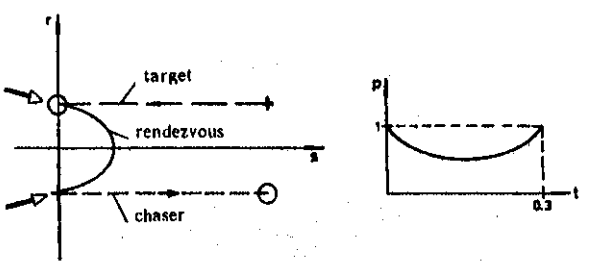


Fig. 13: Hohmann like rendezvous with task time smaller than half a period

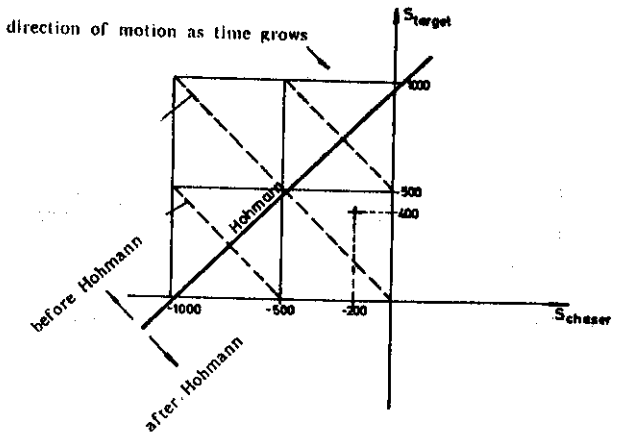


fig. 14: Plot of relative positions of chaser and target in the neighbourhood of the Hohmann positions, for a task time of half a period

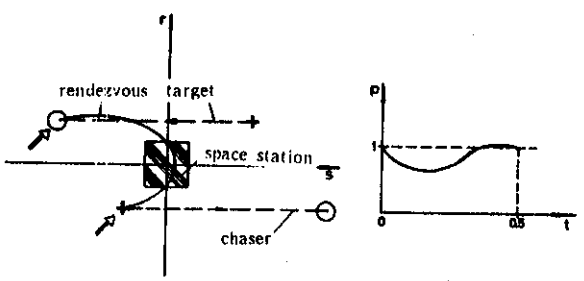


Fig. 15: Hohmann like rendezvous as a result of incorrect initial positions two impulses trajectory

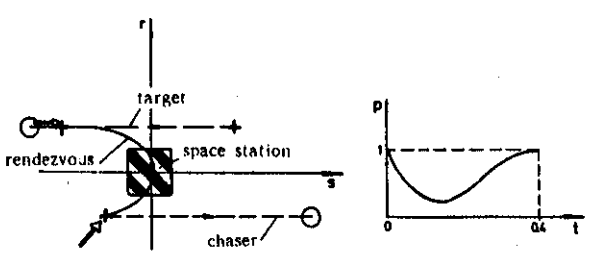


Fig. 16: Hohmann like rendezvous as a result of incorrect initial positions improved trajectory with final coast

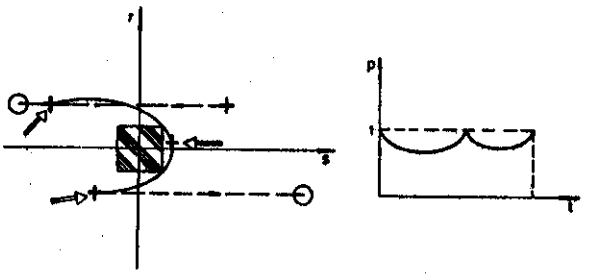


Fig. 17: Hohmann like rendezvous as a result of incorrect initial positions - trajectory by-passes constraint from the right side

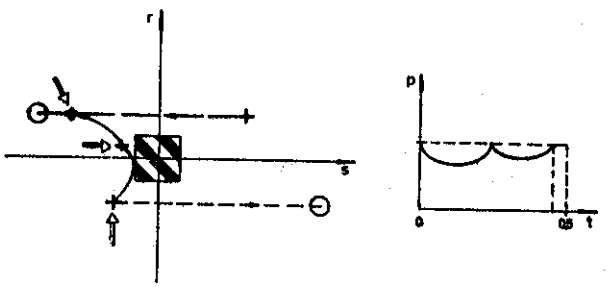


Fig. 18: Hohmann like rendezvous as a result of incorrect initial positions - trajectory by-passes constraint from the left side

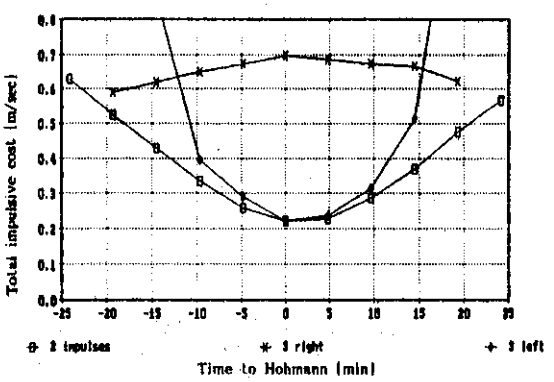


Fig. 19: Total impulsive cost versus time to Hohmann trade-off, for chaser and target on the lineal diagonal of fig. 14

# STUDENTS' ROCKET "TECHNION 90"

Project Team*
Faculty of Aerospace Engineering
Technion - Israel Institute of Technology
Haifa 32000, Israel

On August 22, 1990, fourteen Technion students and their advisors watched as the highlight of a long year of labor came true. The two-stage sounding rocket "Technion 90" was successfully launched, accelerating towards the blue skies, followed by a long tail of flame and smoke (Fig. 1).

The 360 cm long 16 cm diameter rocket (see details in Fig. 2) was propelled by two solid propellant motors containing 44.3 kg of propellant (39 kg in the first motor and 5.3 kg in the second motor) providing total impulse of over 100,000 N-s. The overall launch weight of 113 kg was divided into two motors and a payload. The payload included meteorological instruments for measuring atmospheric pressure and temperature, an accelerometer for recording vehicle acceleration during flight, a telemetry system for real-time transmission of the measured data to the ground station, and a radar transponder allowing for continuous tracking of the vehicle and payload trajectory. Motor chamber pressure of the two stages was monitored and transmitted as well. Two nickel-cadmium battery packages with a total output of 56 W were installed in the rocket to provide the necessary operating power for the telemetry and radar transponder.

The rocket was tracked by both radar and a number of high- and low-speed cameras to provide actual trajectory data and visualize special events.

Operation included sliding separation and jettison of the first stage after burnout, pyrotechnic separation of the second stage from the payload followed by parachute ejection after achieving peak altitude, and slow descent of the payload to the ground.

The sounding rocket project was one of a number of subjects offered to the 4th year Aerospace

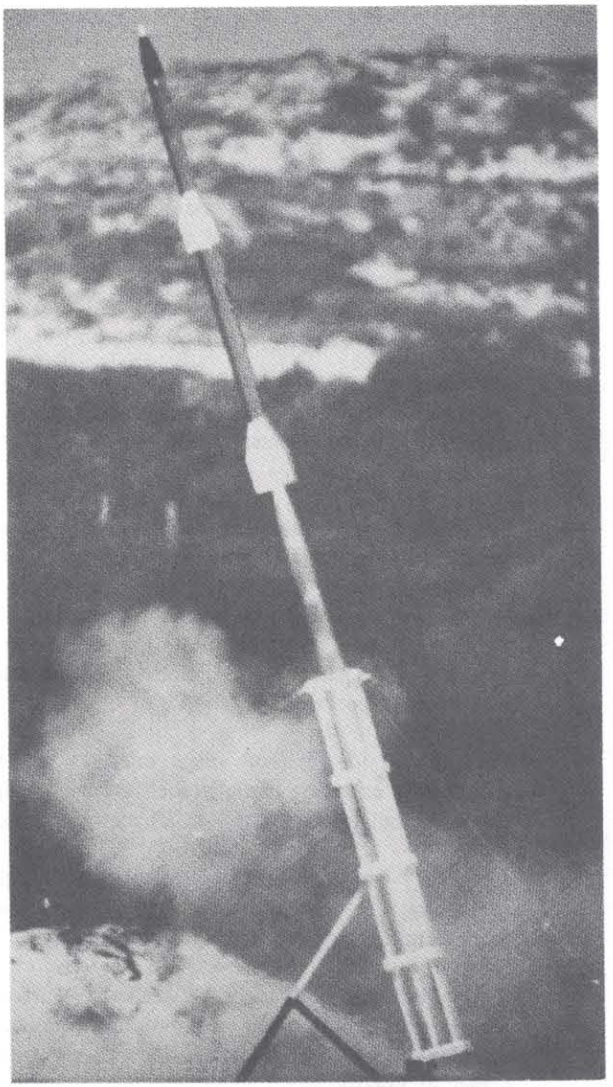

Fig. 1: Student rocket "Technion 90" takes-off.

*Participating Students: Daniel Alkalai, Oren Barak, Shirley Barkai, Ben-Zvi Buchris, Ofer Caspi, Vitali Cohen, Lior Fisher, Efraim Fishles, Izhak Greenbaum, Yaniv Kor-Al, Odet Lupo, Ziv Nir, Ruth Rivlin, Avi Wise.

Project Supervisors: Professor Alon Gany, Israel Aharon, Dr. Jonah Manela and Professor Yaakov M. Timnat (during design phase).

Engineering students for selection as a design project according to the undergraduate study program. Most design projects in the Faculty of Aerospace Engineering are basically "paper projects" which end on the drawing board. The rocket project gave the participants a unique opportunity to exercise the practical aspects of their theoretical studies as well as to face the real-world problems in carrying out a complete engineering project with very realistic constraints of time, money, coordination and integration.

The objective of this project was to design, build and successfully launch an instrumented sounding rocket.

The students who participated in the project were divided into seven 2-person teams, each of them assumed responsibility for one of the major efforts:

* Propulsion - design and performance prediction of the motors.

* Structure - design of specific rocket elements such as motor case and fins, accounting for strength requirements and manufacturing limitations.

* Aerodynamics - design of rocket outfit, solution of stability problems, and prediction of vehicle trajectory.

* Separation and Parachuting - design of separation sections and parachute ejection, and prediction of parachute performance.

* Payload - design of the interior of the instrument capsule, participation in the design, assembly and packaging of the telemetry system.

* Launcher - concept and design of the launcher accounting for strength requirements, manufacturing limitations and ease of assembly.

* Integration - coordination between the different teams, responsibility for assembly drawings, and calculation of overall dimensions, weight and center of gravity.

Weekly meetings with the project advisors were initially used to evaluate conceptual ideas and to deliver specific information to the students. In the later stages of the project detailed design drawings and calculations made by different teams were discussed thoroughly. Manufacturing and machining of the majority of the rocket parts were done at the Faculty's machine-shop. Professional aid as well as

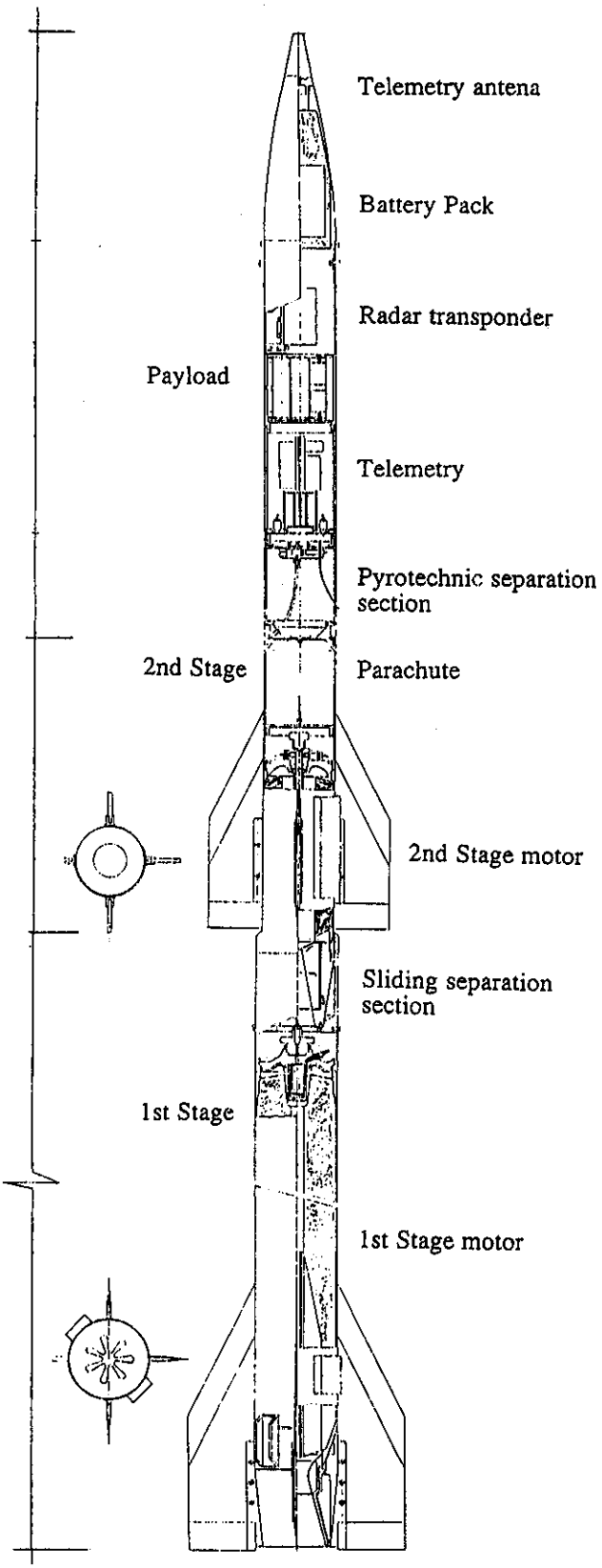


Fig. 2: Assembly drawing of the rocket.

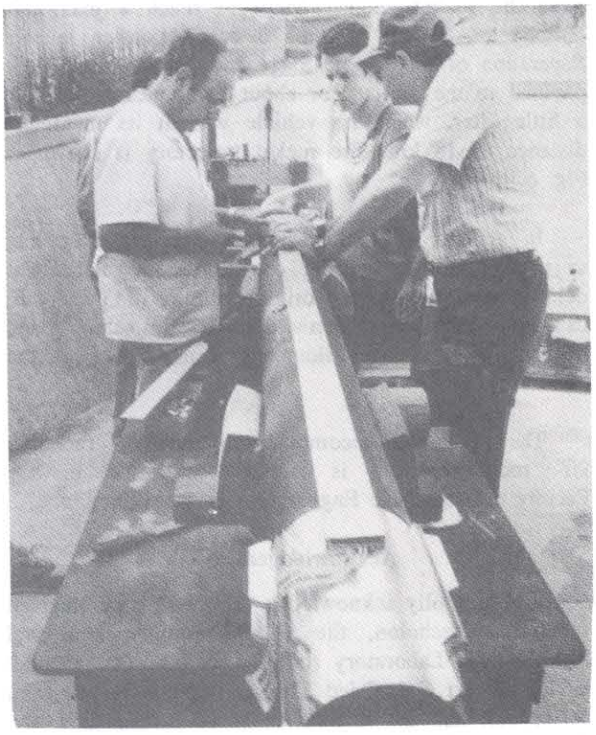

Fig. 3: Integration phase at the Faculty's Propulsion Lab.

support with special equipment, electronics and the launching procedure were willingly provided by potential employers of the graduating students, particularly Rafael, Israel Military Industries (IMI), and the Airforce, who considered the project as an excellent experience towards future engineering challenges.

During the development stage 28 aerodynamic tests were performed in the Faculty's wind tunnels, using precise small-scale models of the rocket. The data gathered in these tests were used to determine the different aerodynamic coefficients as well as aerodynamic stability.

The two motors were static-fired in order to find-out the thrust and pressure versus time characteristics.

The pyrotechnic separation system and the parachute ejection procedure were tested as well.

The preparations for launching included a two-week extensive integration effort at the Faculty's Propulsion Laboratory (Fig. 3). Final assembly and system testing including a general rehearsal of the firing procedure took place at the launching site, where the students spent a few days (Fig. 4). At

Fig. 4: Project team and the rocket at the launching site.

last, the rocket was positioned on the launcher and connected to the ignition wires (Fig. 5).

Actual launching sequence followed closely the plan and predictions: First stage ignition was followed by 7 seconds of motor burning which brought the rocket to its highest speed of 720 m/s at an altitude of 3 km. After burnout and separation of the first stage, the second stage continued to gain altitude, unpropelled, for another 23 seconds. Ignition and 3 second burning of the second stage gave the rocket another boost to reach a maximum altitude of 21 km about 70 seconds after launch. Separation of the second stage and parachuting of the payload to the ground for about 5 minutes took place a little after, when the vehicle was at its maximum distance of 18 km. The rocket trajectory is shown in Fig. 6.

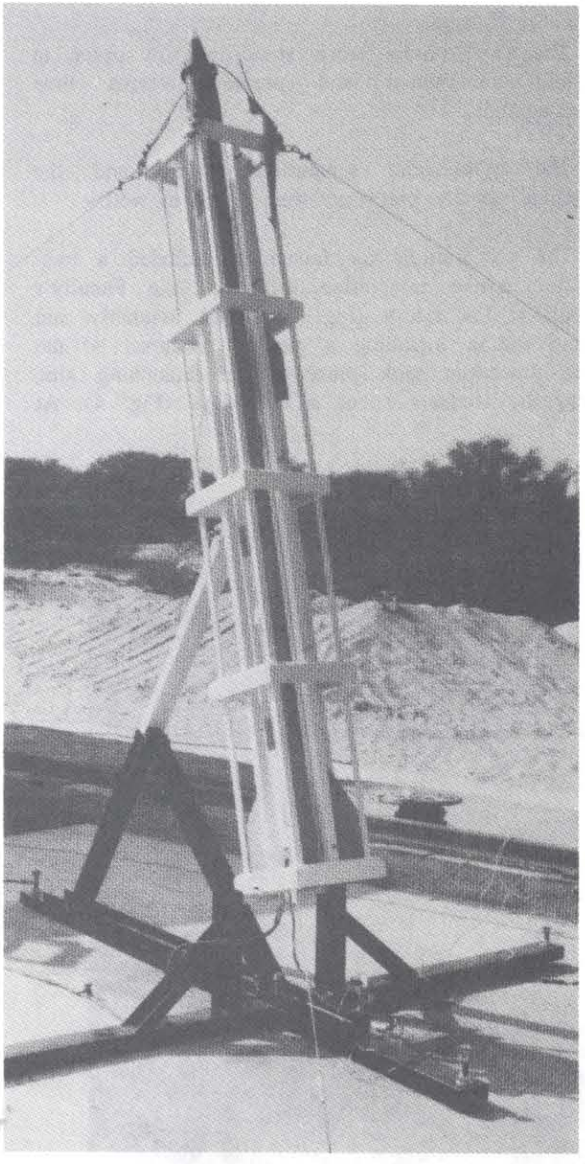

Fig. 5: "Technion 90" on the launcher.

In general all rocket systems operated according to plan, although ignition of the second stage was delayed compared to the original timing of 5 seconds, causing deviation from optimal trajectory and reduction of a few kilometers from the predicted altitude.

The successful accomplishment of the "Technion 90" rocket project is another milestone in the Faculty of Aerospace Engineering of the Technion.


### Acknowledgement

We greatfully acknowledge the support we received from the Technion, the Faculty's technicians and Aerodynamic Laboratory staff, as well as the personal aid of Robert Gal, Oded Chipser, Amnon Netzer, and colleagues, and the important aid of Rafael, IMI, the Airforce, Yeda Computers, and ATS. The photographs were taken by Yair Nahor.


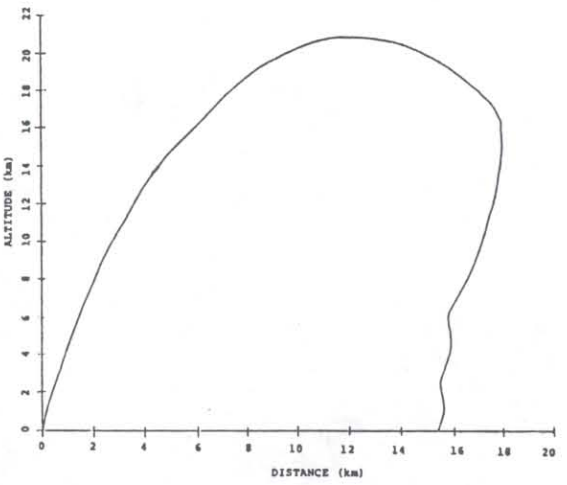


Fig. 6: Actual rocket and payload trajectory.





TECHNION — ISRAEL INSTITUTE OF TECHNOLOGY

THE S. NEAMAN INSTITUTE

FOR ADVANCED STUDIES IN SCIENCE & TECHNOLOGY

TECHNION CITY, HAIFA 32000, ISRAEL . TEL. 237145 / 292329 . FAX 231889